LARGE EDDY SIMULATION OF THE UPPER ATMOSPHERIC SURFACE LAYER

By

Xiaoming Cai

B. Sc. (Mechanics) Fudan University, P.R. China, 1982

M. Sc. (Applied Mechanics) Fudan University, P.R. China, 1985

A THESIS SUBMITTED IN PARTIAL FULFILLMENT OF

THE REQUIREMENTS FOR THE DEGREE OF

DOCTOR OF PHILOSOPHY

in

THE FACULTY OF GRADUATE STUDIES

MATHEMATICS, INSTITUTE OF APPLIED MATHEMATICS

We accept this thesis as conforming

to the required standard

.....

.....

.....

.....

THE UNIVERSITY OF BRITISH COLUMBIA

July 1993

In presenting this thesis in partial fulfilment of the requirements for an advanced degree at the University of British Columbia, I agree that the Library shall make it freely available for reference and study. I further agree that permission for extensive copying of this thesis for scholarly purposes may be granted by the head of my department or by his or her representatives. It is understood that copying or publication of this thesis for financial gain shall not be allowed without my written permission.

(Signature) Xiang Cai

Department of Mathematics

The University of British Columbia
Vancouver, Canada

Date July 15, 1993

DE-6 (2/88)

Abstract

The von Kármán constant (κ) and the Monin-Obukhov similarity formulation occupy very important positions in the theoretical framework of the atmospheric surface layer (ASL). Measurements, however, provide a great scatter in their estimates mainly because the requirements of neutrality (only for estimate of κ), stationarity and horizontal homogeneity in the real atmospheric boundary layer (ABL) are hardly achieved. Therefore, a long-time dispute over the value of the von Kármán constant applicable in the neutral-static-stability ABL has not been settled yet; another controversy concerns the form of the universal Monin-Obukhov similarity functions in very unstable conditions.

A numerical tool, three-dimensional large eddy simulation (LES), is adopted to simulate turbulence in the ABL, with a fine resolution in the ASL, so that an "*a priori* value" of the von Kármán constant and the Monin-Obukhov similarity formulas can be derived from the resolved-scale turbulence in the upper surface layer (USL). Only an ideal geometry, flat but rough surface, is treated. Horizontal homogeneity of all dependent mean variables is assumed except the mean pressure, which is the driving mechanism of the whole turbulent boundary layer due to the geostrophic flow aloft. Smagorinsky's sub-grid scale (SGS) model is adopted.

In the present study, the Smagorinsky-model Reynolds number (Re_{SM}) is proposed for a LES adopting the Smagorinsky SGS model. This number is shown to be an independent model parameter, which determines the statistics of resolved scale (RS) turbulence in the USL. If Re_{SM} is smaller than a critical value, RS fields are damped out. This fact establishes a criterion for a LES adopting the Smagorinsky SGS model.

For a neutral-static-stability ABL, the present study uses grid spacings that fall within

the inertial subrange of the USL turbulence in order to follow the assumption of the Smagorinsky SGS model. Other specifications of grid spacing are also used to show the influence of grid spacing and validity of Re_{SM}. The largest computation involves $64 \times 64 \times 50$ grids. The average of the velocity fields over the whole horizontal plane and time domain yields a logarithmic velocity profile in the USL, from which the von Kármán constant can be derived. The value of κ found in the study ranges from 0.17 to 0.35, depending on the value of Re_{SM} when the domain size and the Rossby number are fixed. Other quantities in the USL, such as profiles of $\langle \tilde{u}^2 \rangle / u_*^2$, $\langle \tilde{v}^2 \rangle / u_*^2$, $\langle \tilde{w}^2 \rangle / u_*^2$, $-\langle \tilde{u}\tilde{w} \rangle / u_*^2$ and $-\langle \tilde{v}\tilde{w} \rangle / u_*^2$, also exhibit a very strong dependence on Re_{SM}.

For an unstable ABL, in which an additional turbulent sensible heat flux is imposed on the surface, profiles of the mean velocity in the USL yield a Monin-Obukhov similarity formula for the dimensionless momentum flux. For $-5 < z/L < -1$, where L is the Monin-Obukhov length, the formula gives smaller values of $\phi_m(z/L)$ than existing empirical formulas, but close to Carl *et al.*'s $-1/3$ power law (1973). LES results of $\sigma_{\tilde{\theta}}/T_{*,s}$ fit the empirical similarity formulas fairly well, and derive a power law exponent of about -0.4, which is smaller than $-1/3$. Similarity results for $\sigma_{\tilde{w}}/u_*$ in the USL has also been examined.

Table of Contents

List of Tables

List of Figures

List of Abbreviations

2D	two-dimensional
3D	three-dimensional
ABL	atmospheric boundary layer
ASL	atmospheric surface layer
CBL	convective atmospheric boundary layer
CPU	central processing unit
DNS	direct numerical simulation
EAM	ensemble-average model
ECR	energy-containing range
EL	entrainment layer
FCL	free convection layer
ITCE	International Turbulence Comparison Experiment
ISR	inertial subrange
JASIN	Joint Air-Sea INteraction experiment
KE	kinetic energy
KONTUR	CONvection and TURbulence experiment
LES	large eddy simulation
ML	mixed layer
N-S	Navier-Stokes
ODE	ordinary differential equation
PDE	partial differential equation
RAMS	Regional Atmospheric Modeling System
RS	resolved-scale
SGS	subgrid-scale
SL	surface layer
SM	Smagorinsky-model
TBL	turbulent boundary layer
TKE	turbulence kinetic energy
USL	upper atmospheric surface layer

List of Symbols

$\bar{\cdot}$	averaging operator (ensemble averaging or spatial filtering)
$[\,\cdot\,]$	horizontal averaging of a RS quantity
$\langle\cdot\rangle$	horizontal and then time averaging of a RS quantity
$\{\cdot\}$	domain averaging of a RS quantity
$\tilde{\cdot}$	fluctuations of a RS quantity about $[\,\cdot\,]$
a, b, C, C_i	constants
C_p	specific heat of dry air
C_s	model constant in the Smagorinsky SGS model
C_{ϕ_h}	coefficient of the power law for ϕ_h in the FCL
C_{ϕ_m}	coefficient of the power law for ϕ_m in the FCL
C_{σ_w}	coefficient of the power law for σ_w in the FCL
C_{σ_θ}	coefficient of the power law for σ_θ in the FCL
$D(= D_x D_y h)^{1/3}$	characteristic length scale of simulation domain
D_x, D_y, D_z	length of simulation domain in the x, y or z direction
E	turbulent kinetic energy
E_M	domain-averaged kinetic energy of mean velocity
E_R	domain-averaged RS TKE
E_s	SGS TKE
$F, \mathcal{F}$	functional form
$\mathcal{F}^{(i)}$	similarity functional form in the inner layer
$\mathcal{F}^{(o)}$	similarity functional form in the outer layer
$f(= 2\Omega \sin\phi)$	Coriolis parameter
f_i	normalized frequency for measured turbulence spectra in the ML
$f_i^{(c)}$	smallest value of f_i in the ISR for ML turbulence
$f_s^{(c)}$	smallest value of f_i in the ISR for SL turbulence
$G(= \lvert\vec{G}\rvert)$	magnitude of the geostrophic wind
$\vec{G}$	geostrophic wind vector
G_i	x_i-component of geostrophic wind
g	acceleration due to gravity

$H_i^{(s)}$	SGS turbulent sensible heat flux
H_ρ	density scale height of the earth
h	height of the ABL
h_E	height of the turbulent Ekman layer, i.e., neutral-static-stability ABL
h_b	height of the SGS buffer layer
h_s	height of the SL
h_ν	height of a laminar Ekman layer
$h_{\nu,e}$	height of a turbulent Ekman layer modelled with a constant effective eddy coefficient
$i = \sqrt{-1}$	imaginary unit
k	wavenumber
k_1, k_2	vertical grid index corresponding to the lower and upper level of a region from which LES results in the USL are obtained
$L(= -u_*^3/\kappa\beta\overline{w'\theta'}_0)$	Monin-Obukhov length
L_{ij}	Leonard stress tensor
$L^{(i)}$	length scale in the inner layer
$L^{(o)}$	length scale in the outer layer
$\mathcal{L}$	integral length scale
$\mathcal{L}_{ij}$	integral length scale tensor
l	mixing length
$N(= N_x N_y N_z)$	total number of grid points in the simulation domain
N_x, N_y, N_z	number of grid points in the x, y or z direction
$N_{BV}(= \sqrt{\beta\Gamma})$	Brunt-Väisälä frequency
N_{Z_i}	number of vertical grid points in the region: $0 \leq z \leq Z_i$
N_{h_E}	number of vertical grid points in the region: $0 \leq z \leq h_E$
n	frequency in Hertz
$Pr_s(= \nu_s/\eta_s)$	SGS Prandtl number
p	pressure
p_0	regionally averaged pressure

$p_{0,0}$	regionally averaged pressure at the surface
$\breve{p}$	pressure deviation from p_0
$\bar{p}$	averaged pressure: ensemble average of $\breve{p}$, or spatially filtered $\breve{p}$
Q	heat energy per unit mass
q	velocity scale of turbulence intensity
R	ratio of $\overline{w'\theta'}_i$ to $\overline{w'\theta'}_0$
R_d	gas constant of dry air
$R_{f,s}$	SGS flux Richardson number $(= \beta\partial\Theta/\partial z/(Pr_s s^2))$
R_{ij}	two-point correlation function tensor of velocity fluctuations
Re	Reynolds number based on a characteristic velocity and a characteristic length
Re_{DNS}	mathematical Reynolds number for a DNS $(= UD/\nu_{DNS})$
Re_{EAM}	mathematical Reynolds number for an EAM $(= UD/\nu_{EAM})$
Re_{LES}	mathematical Reynolds number for a LES $(= UD/\nu_{LES})$
Re_{SM}	Smagorinsky-Model Reynolds number $(= (D/C_s\Delta_0)^2)$
$Re_{SM,cr}$	critical Smagorinsky-Model Reynolds number
Re_{cr}	critical Reynolds number for transition from laminar to turbulent flow
Re_t	critical Reynolds number for fully developed turbulence
$Re_*(= u_*/\sqrt{\nu f})$	Reynolds number for an Ekman layer based on friction velocity
$Ro(= G/fz_0)$	surface Rossby number based on G and z_0
$Ro_D(= G/fD)$	Rossby number based on G and D
$Ro_*(= u_*/fz_0)$	surface Rossby number based on u_* and z_0
r_{ij}	two-point correlation coefficient tensor of velocity fluctuations
S_H	heat sources per unit mass per unit time
S_a	turbulence spectrum for variable a
$S_\Theta(= S_H\Theta/C_pT)$	"temperature sources" per unit time
$s(= \sqrt{2s_{ij}s_{ij}})$	scalar of deformation rate
s_{ij}	tensor of deformation rate
T	absolute temperature of dry air

T_0	regionally averaged absolute temperature of dry air
$T_{*,s}(=\overline{w'\theta'}_0/u_*)$	temperature scale in the SL
t	time
t_1, t_2	time interval over which time averaging is taken for LES results
$t_N(=1/N_{BV})$	reciprocal of the Brunt-Väisälä frequency
$t_f(=2\pi/f)$	time scale of inertial oscillation due to the Coriolis force
$t_*(=Z_i/w_*)$	convection time scale in a CBL
U	characteristic wind speed
$\vec{U}$	mean wind vector
U_g	x-component of geostrophic wind
u	velocity component in the x direction
u_f	velocity scale in the free convection regime
u_i	velocity vector in the x_i direction
$\bar{u}_i$	averaged velocity component in the x_i direction: ensemble average of u_i, or spatially filtered u_i
u_0, v_0	amplitudes of velocity fluctuations of inertial oscillation due to the Coriolis force
$\bar{u}$	averaged velocity component in the x direction: ensemble average of u, or spatially filtered u
$\langle u \rangle$	horizontal and time average of RS velocity component in the x direction
$\tilde{u}$	$\bar{u}$'s fluctuations about $\langle u \rangle$
$-\overline{u_i'u_j'}$	kinematic Reynolds stress tensor
$\overline{u_i'^2}$	turbulent velocity variances
$\overline{u_i'^2}_0$	turbulent velocity variances at the surface
$\overline{u'^2}$	turbulent velocity variance of u component
$\overline{u_i'\theta'}$	turbulent kinematic heat flux
$-\overline{u_s'w_s'}$	x-component of kinematic SGS shear stress on the x-y plane
$\langle \tilde{u}_i^2 \rangle$	variances of RS velocity fluctuations
$\langle \tilde{u}^2 \rangle$	variances of RS velocity fluctuations in the x direction

$-\langle\tilde{u}\tilde{w}\rangle$	x-component of kinematic RS shear stress on the x-y plane
u_*	friction velocity
u_{*r}	estimate of friction velocity based on RS motions
u_{*0}	estimate of friction velocity based on SGS model
V_g	y-component of geostrophic wind
v	velocity component in the y direction
$v^{(i)}$	velocity scale in the inner layer
$v^{(o)}$	velocity scale in the outer layer
$\bar{v}$	averaged velocity component in the y direction: ensemble average of v, or spatially filtered v
$\langle v\rangle$	horizontal and time average of RS velocity component in the y direction
$\tilde{v}$	$\bar{v}$'s fluctuations about $\langle v\rangle$
$\overline{v'^2}$	turbulent velocity variance of v component
$-\overline{v_s'w_s'}$	y-component of kinematic SGS shear stress on the x-y plane
$\langle\tilde{v}^2\rangle$	variances of RS velocity fluctuations in the y direction
$-\langle\tilde{v}\tilde{w}\rangle$	y-component of kinematic RS shear stress on the x-y plane
w	velocity component in the z direction
$\bar{w}$	averaged velocity component in the z direction: ensemble average of w, or spatially filtered w
w_*	convective velocity scaling, defined by $w_* = (\beta\overline{w'\theta'}_0 Z_i)^{1/3}$
$\langle w\rangle$	horizontal and time average of RS velocity component in the z direction
$\tilde{w}$	$\bar{w}$'s fluctuations about $\langle w\rangle$
$\overline{w'^2}$	turbulent velocity variance of w component
$\overline{w'\theta'}$	turbulent sensible heat flux
$\overline{w'\theta'}_0$	turbulent sensible heat flux at the surface
$\overline{w'\theta'}_i$	turbulent sensible heat flux at the inversion base
$\langle\tilde{w}^2\rangle$	variances of RS vertical velocity fluctuations
$\langle\tilde{w}\tilde{\theta}\rangle$	RS turbulent sensible heat flux

x_i or x, y, z	space variables of the coordinate system
Z_i	height of the inversion base, or height of a CBL
z_0	roughness length
$z_{0,r}$	roughness length estimated from LES
z_1	height of the first vertical grid
α_R	Rayleigh friction relaxation coefficient as a function of z
$\alpha_R^{(0)}$	value of α_R at the top of simulation domain
α_{dv}	turning angle between mean velocity shear vector and $\vec{G}$
α_v	turning angle between mean velocity vector and $\vec{G}$
$\alpha_{v,0}$	value of α_v at the surface
α_τ	turning angle between shear stress vector and $\vec{G}$
$\alpha_{\tau,0}$	value of α_τ at the surface
$\beta(= g/\Theta_0)$	buoyancy parameter
Γ	lapse rate of potential temperature profile in the inversion layer
$\Delta = (\Delta_x \Delta_y \Delta_z)^{1/3}$	length scale of mesh spacing
Δ_i	mesh spacing in the x_i direction
$\Delta_x, \Delta_y, \Delta_z$	mesh spacing in the x, y or z direction
$\Delta_{z,1}$	first vertical mesh spacing
$\Delta_{z,typ}$	typical value of Δ_z
Δ_0	typical value of Δ
$\Delta h_i, \delta h_i$	length scale of the EL
δh_i^+	ratio of the depth of the EL to that of the CBL
δ_{ij}	Kronecker delta
ϵ	turbulent dissipation rate
ϵ_{ijk}	alternating unit tensor
$\zeta(= z/L)$	normalized height by the Monin-Obukhov length
η	molecular thermal diffusivity for Θ
η_e	effective thermal diffusivity for Θ
η_s	SGS eddy thermal diffusivity for Θ
Θ	potential temperature

Θ_0	potential temperature at the surface; or regionally averaged potential temperature
$\bar{\Theta}$	averaged potential temperature: ensemble average of Θ, or spatially filtered Θ
$\langle\Theta\rangle$	horizontal and time average of RS potential temperature
Θ_f	temperature scale in the free convection regime
$\Theta_*(=\overline{w'\theta'}_0/w_*)$	temperature scale in the ML
$\tilde{\theta}$	$\bar{\Theta}$'s fluctuations about $\langle\Theta\rangle$
$\overline{\theta'^2}$	variance of temperature fluctuations
$\langle\tilde{\theta}^2\rangle$	variance of RS temperature fluctuations
κ	von Kármán constant
κ_{LES}	von Kármán constant evaluated from LES
κ_0	von Kármán constant input as the boundary conditions at the surface
λ	wavelength in meter
$\lambda_i^{(c)}$	largest wavelength of the ISR eddies for the ML turbulence
$\lambda_s^{(c)}$	largest wavelength of the ISR eddies for the SL turbulence
ν	kinematic viscosity of air
ν_{DNS}	order of effective viscosity for a DNS
ν_{EAM}	order of effective viscosity for an EAM
ν_{LES}	order of effective viscosity for a LES
ν_e	effective eddy viscosity
ν_s	eddy viscosity of SGS motions for LES
$\vec{\xi}$	space variable vector in correlation functions or correlation coefficients
$\xi = \lvert\vec{\xi}\rvert$	space distance in correlation functions or correlation coefficients
ξ_x, ξ_y	space variable component of $\vec{\xi}$ in the x and y directions
Π	Exner function $(= C_p(p/p_{0,0})^{R/C_p})$
ρ	density of dry air
ρ_0	regionally averaged density of dry air

$\sigma_{u_i}(=\sqrt{\overline{u_i'^2}})$	standard deviation of u_i's fluctuations
σ_u	standard deviation of u'
σ_v	standard deviation of v'
σ_w	standard deviation of w'
$\sigma_{\tilde{u}}(=\sqrt{\langle\tilde{u}^2\rangle})$	standard deviation of $\tilde{u}$
$\sigma_{\tilde{v}}(=\sqrt{\langle\tilde{v}^2\rangle})$	standard deviation of $\tilde{v}$
$\sigma_{\tilde{w}}(=\sqrt{\langle\tilde{w}^2\rangle})$	standard deviation of $\tilde{w}$
$\sigma_{\tilde{u},max}$	maximum of $\sigma_{\tilde{u}}$
$\sigma_{\tilde{v},max}$	maximum of $\sigma_{\tilde{v}}$
$\sigma_{\tilde{w},max}$	maximum of $\sigma_{\tilde{w}}$
$\sigma_\theta(=\sqrt{\overline{\theta'^2}})$	standard deviation of θ's fluctuations
$\sigma_{\tilde{\theta}}(=\sqrt{\langle\tilde{\theta}^2\rangle})$	standard deviation of θ's fluctuations
τ_{ij}	kinematic stress tensor
$\tau_{uw}(=\tau_{13})$	x-component of kinematic shear stress on the x-y plane
$\tau_{vw}(=\tau_{23})$	y-component of kinematic shear stress on the x-y plane
$\tau_{uw,0}$	value of τ_{uw} at the surface
$\tau_{vw,0}$	value of τ_{vw} at the surface
τ_0	magnitude of kinematic shear stress at the surface $(=\sqrt{\tau_{uw,0}^2+\tau_{vw,0}^2})$
$\tau_{\tilde{u}\tilde{w}}(=-\langle\tilde{u}\tilde{w}\rangle)$	x-component of kinematic RS shear stress on the x-y plane
$\tau_{\tilde{v}\tilde{w}}(=-\langle\tilde{v}\tilde{w}\rangle)$	y-component of kinematic RS shear stress on the x-y plane
$\tau_{ij}^{(s)}$	kinematic SGS stress tensor
$\tau_{ij}^{(s,2)}$	SGS stress tensor in Leonard's model
ϕ	latitude on the earth; functional form
ϕ_h	Monin-Obukhov similarity function for heat flux
ϕ_m	Monin-Obukhov similarity function for momentum flux
$\phi_\epsilon(=\kappa z\epsilon/u_*^3)$	normalized TKE dissipation in the SL
$\phi_\epsilon^i(=\kappa Z_i\epsilon/u_*^3)$	normalized TKE dissipation in the ML
$\Omega_i, \vec{\Omega}$	angular velocity vector of the earth's rotation
$\vec{\Omega}_3, \vec{\Omega}_{12}$	projection of angular velocity vector of the earth's rotation onto the x_3-axis, and onto the x_1-x_2 plane, respectively
$\Omega = \lvert\vec{\Omega}\rvert$	magnitude of angular velocity of the earth's rotation

Acknowledgment

I would very much like to thank my supervisor, Dr. Douw Steyn, for his guidance and support throughout my program, providing personal funding through several research assistantships, as well as his suggestions and constructive criticism. I also thank Dr. Ian Gartshore, my co-supervisor, who provides useful comments on this project and supervised the first year of my program while Dr. Steyn was on his sabbatical leave. My thanks are extended to the other members of my committee, Drs. Brian Seymour and Gregory Lawrence. As my graduate advisor in the Institute of Applied Mathematics in the first two years of my program, Dr. Seymour helped me to schedule courses and provided a partial research assistantship for the first year.

I wish to thank the following organizations who funded this work: The University of British Columbia offered two year of personal support via its University Graduate Fellowship; The Department of Mathematics provided personal funding through several Teaching Assistantships. The Department of Geography provided office space. The Natural Science and Engineering Research Council (NSERC) funded much of the operating costs for computer resources via grants to my supervisor, which made this research possible. University Computing Services of UBC provided partial computing resources for numerical simulation.

The following people assisted this work in various ways: Roger Pielke of the Atmospheric Science Department at Colorado State University provided the numerical model (CSU-RAMS). Peter Jackson was extremely helpful and generous with his time and knowledge in helping with the use of RAMS code. Tom Nicol and Susan Ng of University Computing Services of UBC provided a useful support to set up the numerical

computation on IBM AIX operating system. Mark Hadfield helped with initial trial of large eddy simulation with RAMS model.

I have also benefitted from discussions with Dr. Roland Stull at the Department of Meteorology, University of Wisconsin, Madison.

Lastly I should thank my wife, Xian (Zhang), for her companionship and persistent encouragement throughout the program of study.

Chapter 1

Introduction

Turbulence is a complex but common form of fluid motion, and has been considered the most difficult research topic in the area of fluid dynamics. Turbulence has been the subject of scientific study for at least a century. During this period, various ideas and techniques have been proposed to tackle this extremely complicated problem; all of them have in common their complexity, as well as inabilities to solve the problem universally. The most basic question of how to define turbulence is even uncertain.

Extremely schematically, two opposing points of view have been advocated: "*statistical*" and "*structural*". The first one comes from Taylor and Kolmogorov in the nineteen-thirties and nineteen-forties and assumes that all fluctuating quantities are random functions satisfying homogeneity[1] and isotropy[2]. Models of this type try to solve the evolution of *ensemble-averaged* quantities of turbulent flows by parameterizing higher moments through lower ones, which is sometimes called *phenomenological modelling* or *ensemble-average model* (EAM). It is well known that this parameterization includes many uncertainties. The most successful statistical model is therefore homogeneous isotropic turbulence (Hinze, 1975; Panchev, 1971). For some inhomogeneous flows in practical applications, this type of models can be adopted to calculate the mean quantities for simple turbulent shear layers such as jets, wakes, mixing layers or boundary layers on flat plates (Patankar, 1980; Rodi, 1980). But, the statistical models can never answer the question of how turbulence is generated, developed and dissipated.

[1]Here, homogeneity means statistical invariance under linear transformation.
[2]Isotropy means statistical invariance under rigid rotation.

The second type of model, developed in the past several decades, considers turbulence from a purely deterministic point of view, by studying either the behaviour of dynamical systems or the stability of flows in various situations. The fundamental assumption is that turbulence, no matter how fully developed it is, always obeys the Navier-Stokes (N-S) equations, the continuity equation and the energy conservation equation. Under certain conditions, the deterministic three-dimensional (3D) solutions can evolve with time in a very complicated way due to nonlinear interactions. The theoretical description of this behavior is impossible now, but is stimulated by the development of the so-called "*dynamical systems approach*", which deals with *chaos phenomenon*, the temporal complexity exhibited by the evolution of an ordinary differential equation (ODE) system with only few degrees of freedom[3]. There is enough evidence now that low-dimensional[4] temporal chaos has provided new as well as useful ideas and tools for analyzing early stages of transition[5] in some types of flows (Sreenivasan, 1985). One type of advance made in low-dimensional chaos that has found some application in turbulence is the invention of several dynamical measures such as Liapunov exponents (Keefe, Moin and Kim, 1992; Liapunov, 1966). Fully developed turbulence has millions of degrees of freedom (Constantin et al., 1985), and, in addition, exhibits spatial complexity which the dynamical systems approach is not able to handle. Therefore, there is a huge gap between realistic continuum models of fluid systems, such as the N-S equations with appropriate boundary conditions, and ODE dynamical system with only few degrees of freedom. This spatial complexity may exist in the form of a "*coherent structures*" a large scale ordered eddy or vortex that persistently appears, disappears and reappears. Such structures evolve

[3]Degree of freedom is sometimes called "dimension", not to be confused with space dimension. Generally speaking, for a set of ODE system, degree of freedom corresponds to the number of equations. There is no strict definition of "degree of freedom" for a set of partial differential equation (PDE) system. For a discretized PDE system, however, degree of freedom corresponds to the number of spatial grids.

[4]of small degrees of freedom

[5]from a laminar flow to a turbulent flow

in space and time typically in a complicated fashion, often exhibiting a repetitive cycle of events, such as lift, oscillation and ejection of longitudinal boundary layer streaks, followed by sweep and reformation. Flow visualization by injected dye, smoke, hydrogen bubbles *etc.* has revealed persistent organized structures in many flows (Brown and Roshko, 1974; Kline et al., 1967). It is generally accepted that these structures give important contributions to energy generation and transport in turbulent flows (Cantwell, 1989).

In the past decade, another way that has emerged to reveal these coherent structures is numerical simulation. Direct Numerical Simulation (DNS)[6] is based on the N-S equations, while Large eddy simulation (LES) is based on the grid-volume-averaged N-S equations with parameterization of the subgrid-scale (SGS) stress tensor. The number of numerical grids required by a DNS is of the order of degrees of freedom of turbulence[7] to be simulated. Therefore, DNS can only be applied to relatively low Reynolds number cases, (Coleman, Ferziger and Spalart, 1990; Coleman, Ferziger and Spalart, 1992; Kim, Moin and Moser, 1987; Spalart, 1988). LES is free of this constraint and it has been widely adopted in many engineering applications and geophysical flows (Moeng, 1986a; Moeng, 1986b; Moin and Kim, 1985; Schmidt and Schumann, 1989).

Success of LES mainly depends on whether the SGS parameterization well describes the momentum interaction occurring between resolved-scale (RS) eddies and SGS eddies. The Smagorinsky SGS model (Smagorinsky, 1963) is one of the simplest SGS models and it is based on the assumption that the grid spacing falls into the inertial subrange (ISR) of the turbulence spectrum. A model constant C_s, which represents the ratio of mixing length in the SGS model to the grid spacing, is to be determined by analysis or numerical experiment. Lilly (1967) provided a theoretical estimate of 0.17 for this value, assuming

[6]also called Full Turbulence Simulation, or FTS

[7]Degrees of freedom of turbulence is approximately of the order of $Re^{9/4}$, where Re is based on characteristic large scales, D and U, see Reynolds (1989).

turbulence to be homogeneous and isotropic, with no discretization error. Taking into account some discretization error, this value must be revised to the range from 0.20 to 0.22 (Deardorff, 1971). Applying the value of $C_s \sim 0.2$ to turbulence driven by thermal convection yields a satisfactory agreement with observations (Deardorff, 1972; Mason, 1989). When this value is applied to inhomogeneous boundary layer turbulence in which only shear production dominates, the resolvable scale motions were found to be damped out (Deardorff, 1970c; Mason and Callen, 1986). Smaller values of C_s, *e.g.*, 0.1 in Deardorff (1970c), have to be adopted to sustain the RS eddies.

Not only can LES reveal the details of turbulent structures, but also it can produce mean statistical quantities of the flow, some of which can not be derived from the aforementioned phenomenological models. One such quantity which can be calculated by LES is the numerical value of the von Kármán constant κ.

The von Kármán constant is a fundamental parameter in the mean velocity structure of a turbulent flow near a wall, and occupies an important position in turbulence theory. The value of κ had only been determined by experiment through the past several decades because no alternative was available. Wind tunnel experiments, in which the Reynolds numbers[8] are usually of the order of 10^5 to 10^6, suggest that $\kappa \approx 0.4$ (Hinze, 1975).

There is still some doubt about value of the von Kármán constant (κ) applicable in the neutral-static-stability[9] atmospheric boundary layer[10] (ABL) and whether very high Reynolds numbers and rough boundaries associated with the atmosphere may produce values of κ different from those observed in engineering applications. Measurement of

[8]This Reynolds number is usually denoted by Re_δ, which is based on the characteristic velocity U and the boundary layer depth δ.

[9]Neutral-static-stability means the air is neutrally stable when it has no motion; in other words, its potential temperature Θ is constant in whole atmospheric boundary layer. For simplicity, neutral-static-stability is referred to as "neutral", and neutral-static-stability atmospheric boundary layer is referred to as "neutral atmospheric boundary layer ".

[10]The atmospheric boundary layer is the lowest portion of the atmosphere, which intensively exchanges momentum as well as heat and mass with the earth's surface. The height of the ABL may vary from a few hundred meters to more than one thousand meters.

turbulent structures of the atmospheric boundary layer, especially the atmospheric surface layer[11] (ASL), has been greatly developed in the past several decades. Most of the observations are conducted below about 30 m, the easiest attainable height range for measurement in the ASL. Under neutral conditions, velocity profiles have been shown to have a logarithmic form from several meters above the ground to the top of the ASL. However, the value of the von Kármán constant estimated from the observations is too scattered to be satisfactory, because the real ABL rarely meets the requirements of neutrality, stationarity and horizontal homogeneity. A very carefully designed observation of the ABL was carried out in Kansas in 1968. This experiment provided very detailed data which for many years have been and still are the source of information on the ASL, but it surprisingly yielded an unexpectedly low value of $\kappa = 0.35$, which gave great impetus to the debate on the value of κ (see, *e.g.*, Dyer (1974), Wieringa (1980), Wieringa (1982), Wyngaard et al. (1982)). The true value of κ is still hotly debated in the meteorological community. In the recent Tenth American Meteorological Society Symposium on Turbulence and Diffusion, Frenzen and Vogel (1992a) estimated $\kappa = 0.381 \pm 0.017$, and a panel discussion headed by Businger gave no conclusion on this topic.

With dramatically increasing power of computers, the potential capability of LES to resolve eddies close to the wall and therefore to evaluate the von Kármán constant emerges. There have been many DNS and LES approaches for near wall turbulent structures of channel flows (Kim, Moin and Moser, 1987; Moin and Kim, 1982), but few for turbulence in the ASL. One objective of the present work is to explore the extent to which the logarithmic region of the ASL can be modelled and the von Kármán constant determined using LES.

The present study views LES of a neutral ABL as a non-linear system of PDEs similar

[11]The height of the atmospheric surface layer is defined as that elevation above the ground below which the stress magnitude varies by less than 20% (Lumley and Panofsky, 1964); or, to a good approximation, the lowest 10% of the whole ABL (Sorbjan, 1989).

to the N-S equations. It is assumed that the behavior of the RS motions mainly depends on the ratio of advection term to the SGS diffusion term. If the Smagorinsky SGS model is employed, a Smagorinsky-Model Reynolds number (or SM-Reynolds number) Re_{SM} can be defined by this study to represent the magnitude of this ratio (see the definition in (2.86) on page 38). One of the feature of LES[12] is that as Re_{SM} is sufficiently large, the solution of the system must fall into a non-linear unstable regime, with which no existing mathematical theory is able to deal. The unstable solution is typically represented by eddy-like structures with continuous spectra, which are characteristics of turbulence. Due to nonlinear interactions among these eddies and the presence of SGS diffusion, the solution does not possess any spatial or temporal singularity; a statistical equilibrium state can be reached as time approaches infinity. If Re_{SM} is smaller than a critical value, say $Re_{SM,cr}$, only trivial solutions can exist — these do not include unstable modes with a continuous spectrum. Based on the definition of the SM-Reynolds number and above arguments, too large a value of C_s will cause too small an Re_{SM}, and unstable RS eddies will be damped out if the number of grids is not large enough. Deardorff (1970c) adopted 6720 as total number of grids, which corresponds to about 19 grid points in each direction. This resolution is far coarser than the ideal one which would resolve all eddies between the energy-containing range (ECR) and the ISR, a wavenumber span of more than two decades. However, using a smaller value of C_s (equivalently increasing the value of Re_{SM}) makes it possible for Deardorff to run his LES. Mason and Callen (1986) adopted more grid points, i.e., $40 \times 40 \times 32$ in three respective directions. They found that a C_s as large as 0.2 allowed the RS eddies to be sustained but a larger C_s caused the decay of the RS eddies. In other words, the value of Re_{SM} in their case was larger, but not *much* larger than $Re_{SM,cr}$. In this situation, the RS motions must be SM-Reynolds

[12]Because the present study adopts the Smagorinsky SGS model, the word "LES" hereafter stands for LES with the Smagorinsky SGS model, unless otherwise specified.

number dependent. This dependence will be alleviated as Re_{SM} becomes very large and an asymptotic state will be reached as $Re_{SM} \to \infty$. This asymptotic state is considered as the aim of LES by the present study.

Turbulence statistics in an unstable ABL with geostrophic wind remain difficult to measure, especially far from the surface. In this case, LES is a useful supplemental tool for investigating the turbulence structure and statistics of the ABL because it is relatively easy for LES to resolve layers higher than easily attainable measurement levels. The pioneering LES work by Deardorff (1972), adopting a total of 32,000 grid points, simulated an unstable ABL with the geostrophic wind. Different values of the stability parameter, $|Z_i/L| = 0$, 1.5, 4.5 and 45 (Z_i is the height of the unstable ABL and L is the Monin-Obukhov length), were used to obtain turbulence statistics above the ASL. Most subsequent LES approaches to the unstable ABL are without the presence of the geostrophic wind; this ABL is called a pure convective boundary layer (CBL). Continuing from the work of Deardorff (1972), the present study refines resolution in the ASL so that turbulence in the upper surface layer (USL) can be resolved, and verifies surface layer (SL) similarity for dimensionless momentum flux profile, variances of temperature fluctuations and vertical velocity fluctuations through LES output in the USL.

This thesis is organized as follows. In chapter 2, I give a brief account of DNS, LES and EAM; I list governing PDEs, the SGS model and boundary conditions; then I define the SM-Reynolds number and rationalize its definition; finally I discuss discretization and certain criteria regarding grid size and domain size.

Chapter 3 turns to analysis of LES results of a neutral ABL; I recall the scaling analysis for the neutral ABL and some sufficient conditions for the logarithmic velocity profile; I briefly review some measurement results for the neutral ABL; then I show my LES results of the logarithmic profile of the mean velocity, the so-called "SGS buffer layer", estimates of the von Kármán constant and its dependence on the SM-Reynolds

number, and some other turbulence statistics in the USL; I also present some mean profiles of turbulence statistics in the whole ABL and compare them with observation or previous LES, to demonstrate the credibility of my LES.

In chapter 4, I give the analysis of LES results of an unstable ABL; I outline the scaling analysis for the unstable ABL, the Monin-Obukhov similarity work and corresponding empirical formulas; then I present my LES results of SL similarity for the dimensionless momentum flux $\phi_m(\zeta)$, the dimensionless standard deviation of RS temperature fluctuations $\sigma_{\tilde{\theta}}/T_{*,s}$, and the dimensionless standard deviation of RS vertical velocity fluctuations in the USL.

The last chapter, chapter 5, contains a summary of the present research work and some suggestions for further research on this topic.

Chapter 2

Large Eddy Simulation and Subgrid Scale Model

2.1 Direct Numerical Simulation, Large Eddy Simulation and Ensemble-average Model

Turbulent flow is one of the most complex phenomena found in nature; it is a 3D, time-dependent interchange of energy and momentum between vortices of different sizes and life-times. Since there is no evidence of any physical difference between a fluid in turbulent flow and the same fluid in laminar flow, the N-S equations that govern laminar flows can be used to represent those smallest eddies in turbulent flows. From the viewpoint of the solutions to PDEs, the Navier-Stokes equations along with the continuity equation completely describe incompressible laminar flows with sufficiently small Reynolds number $Re = UD/\nu$ (where U is the characteristic velocity of the flow, D the characteristic length and ν the kinematic viscosity of the fluid). While the existence and uniqueness of the solution for small Re problems have already been proven (Ladyzhenskaya, 1969), there are no similar results for large Re problems[1].

From the perspective of dynamical system approach, the development during the past two or three decades has shed some light on the behavior of the fluid flows characterized by large Re. It has been shown that deterministic nonlinear dynamical systems with a few (but not less than three) degrees of freedom can exhibit chaotic behavior, or sensitive

[1] A nonstationary boundary-value problem for the two-dimensional (2D) N-S equations has a unique solution for all instants of time. For the 3D problem, if the external force can be derived from a potential and if the Reynolds number is small at the initial time, its solution is unique. In the general 3D case, the uniqueness of the solution cannot be asserted.

dependence on initial conditions (Lichtenberg and Lieberman, 1982). One example is the Lorenz system of three nonlinear ordinary differential equations (ODEs) (Lorenz, 1963). Bifurcation theory applied to simplified model problems yields predictions that are amazingly close to real fluid phenomena and lead one to believe that transition to chaos can follow some rather generic patterns (Gollub, Benson and Steinman, 1979; Ruelle, 1980). The question arises as to whether the results from ODEs can be applied to the very complicated N-S equations. In contrast to the output of low-dimensional systems, turbulence governed by the N-S equations could have a very large (potentially infinite) number of degrees of freedom, since the N-S equations are partial differential equations and represent a flow in a continuum. In spite of these difficulties, some have speculated that the chaotic phenomena and the *strange attractors* found in simple ODE systems could also be characteristics of turbulence (Holmes, 1989).

A short-cut to reveal some of the turbulent structure is to numerically solve the N-S equations along with continuity equation, ignoring questions concerning the existence or otherwise of unique solutions. It is expected that numerical simulation can create all types of phenomena observed in nature, such as transitions from laminar flow to turbulent flow, and the development of turbulent structures and even the so-called "*coherent structures*". The difficulty encountered here is that existing computers do not have enough power to allow the resolution of all sizes of turbulent eddies exhibited by real flows. An accurate simulation of a flow problem requires a very large number of degrees of freedom and the long time runs necessary to correctly simulate the evolution of turbulent structures are rather expensive in computer time.

In order to overcome this difficulty, the N-S equations are subjected to various averaging schemes. Depending on which averaging scheme is employed, the numerical methods which deal with turbulence characteristics can be classified as: DNS, LES and EAM.

2.1.1 Direct Numerical Simulation

DNS has been developed to reveal details of flow structures down to the smallest eddies. DNS is a 3D time-dependent numerical simulation. The main idea of this method is to assume that the size of the smallest eddies in any turbulent flow is of the order of the Kolmogorov microscale[2] (Batchelor, 1960), and to specify the number of grids in space so that these eddies can be resolved. The eddy flow embedded in such a fine mesh system can be well described by the N-S equations, without any parameterization. Once the simulated results (3D, time-dependent eddy fields) are obtained, the average fields (zero-moment statistics) and all higher moment fields can be produced by simple statistical calculations. Unfortunately, on today's biggest computers, DNS can only be applied to very small Reynolds number problems, because the necessary number of mesh points is roughly given by (Reynolds, 1989)

$$N = O(Re^{\frac{9}{4}}), \tag{2.1}$$

where the Reynolds number is defined based on the bulk velocity and the characteristic length of the flow. This relation is extremely restrictive of much development of DNS. In spite of this restriction, more and more DNS approaches still appear because of the development of computer technology. These range from homogeneous isotropic turbulent flow to channel flow and the turbulent Ekman layer (Clark, Ferziger and Reynolds, 1978; Coleman, Ferziger and Spalart, 1990; Coleman, Ferziger and Spalart, 1992; Gerz, Schumann and Elghobashi, 1989; Holt, Koseff and Ferziger, 1989; Kim, Moin and Moser, 1987; Lesieur, Metais and Laroche, 1989; Spalart, 1989). These approaches remain confined to flows with very low Reynolds number, of the order of 10^3 for homogeneous isotropic

[2]The Kolmogorov microscale can be derived from dimensional analysis as follows. It is assumed that in the dissipation subrange, there are only two important parameters, ν and ϵ, which is the dissipation rate of the turbulent flow. The length scale corresponding to the eddy size in the dissipation subrange must be a function of ν and ϵ. Applying corollary 2 in appendixB yields that this length scale must be of the form of $(\nu^3/\epsilon)^{1/4}$.

turbulence for example, if the Reynolds number is defined as $Re_T = q^4/(\epsilon\nu)$, where q is the velocity scale of turbulent kinetic energy (TKE) and ϵ the rate of dissipation of TKE per unit mass. Most of these flows are in the transition regime. Because of the Reynolds number restriction, it is believed that DNS will not be widely applied to practical problems unless computer speed is enhanced tremendously.

2.1.2 Ensemble-Average Models

In contrast, from a practical viewpoint, EAM provides a simple and powerful tool to obtain solutions to many simple flows. In an EAM, all effects due to turbulent eddies are parameterized by the specified kinematic Reynolds stresses $-\overline{u_i'u_j'}$ or other important correlations. The model needs only a small number of mesh points; however, it often seems that the parameters specifying the model closure have to be adjusted to match observational data for each application. In other words, EAMs are not fully universal.

According to whether of not the eddy viscosity assumption is used as a basic closure scheme, EAM models can be divided by two groups, namely, *eddy-viscosity models* and *shear-stress models.* In eddy viscosity model, Reynolds turbulence stresses arising from the ensemble averaging procedure are modeled by:

$$-\overline{u_i'u_j'} = \nu_e(\frac{\partial \bar{u}_i}{\partial x_j} + \frac{\partial \bar{u}_j}{\partial x_i}) - \frac{2}{3}\delta_{ij}E \tag{2.2}$$

where ν_e is referred to as the effective turbulent viscosity, δ_{ij} the Kronecker delta, $\bar{u}_i$ the ensemble-averaged velocity component and E represents the TKE. The order of the unknown ν_e suggested by experiments is (Tennekes and Lumley, 1972):

$$\nu_e \propto UL \tag{2.3}$$

where L and U are the characteristic length scale and the velocity scale of the ECR eddies, respectively. To parameterize ν_e, zero-equation models (*e.g.*, the mixing length

model), one-equation models (*e.g.*, equation for TKE) or two-equation models (*e.g.*, k-ε model) can be adopted (Rodi, 1980). The shear-stress model, however, abandons the assumption (2.2) and employs either algebraic or PDE equations for $-\overline{u_i'u_j'}$ (Launder, 1989).

In general, predictions of current eddy-viscosity models agree fairly well with experimental data for simple flows, such as 2D boundary layers, jets, wakes, mixing layers, channel flows and tube flows, and some 3D flows without strong swirl and density variations (Rodi, 1980); predictions of current shear-stress models agree fairly well with experimental data for recirculating flows (Launder, 1989). However, these "good predictions" are based on different *empirical* choices of model constants for different flows. Those constants are not truly universal but functions of characteristic flow parameters. Existing EAMs were shown to be less than universal at the 1980-81 Stanford meeting on Computation of Complex Turbulent Flows (Kline, Cantwell and Lilley, 1981). Furthermore, model effectiveness did not necessarily increase with increasing model complexity.

2.1.3 Large Eddy Simulation

From the above discussion, the major disadvantage of DNS is that it can only deal with the low Reynolds number problems using currently available computers, and the major defect of EAMs is that they are not truly universal for different turbulent flows and are even inapplicable to some flows. LES, however, has advantages over both DNS and EAM; it employs a mesh resolution coarser than that used by DNS but fine enough to resolve the large-scale eddies in the ECR, and parameterizes those eddies whose sizes are smaller than the mesh spacing. This parameterization is called SGS model; it reduces cost so that it can be applied to relatively high Reynolds number problems, or even to some complicated ABL problems.

As an example, in Smagorinsky's scheme (Smagorinsky, 1963), the SGS parameterizations are as follows:

$$\tau_{ij}^{(s)} = 2\nu_s \cdot s_{ij} - \frac{2}{3}E_s, \tag{2.4}$$

$$\nu_s = (C_s\Delta)^2 s, \tag{2.5}$$

$$s_{ij} = \frac{1}{2}(\frac{\partial \bar{u}_i}{\partial x_j} + \frac{\partial \bar{u}_j}{\partial x_i}), \tag{2.6}$$

$$s^2 = 2s_{ij} \cdot s_{ij}, \tag{2.7}$$

where $\tau_{ij}^{(s)}$ is the SGS shear stress tensor, E_s is the SGS TKE, $\bar{u}_i$ is the RS velocity, the parameter Δ is a length scale related to the mesh spacing; C_s is a constant to be determined by numerical experiments. The mesh size must be chosen so that the parameterized eddies behave like homogeneous isotropic turbulence and therefore have more universal properties. In this sense, LES models are more universal than EAMs.

It is worth noting that, from a mathematical point of view, the closure scheme (2.4) in LES is formatted the same as that in EAM, namely, (2.2), even though they are derived from totally different averaging processes. However, the behavior of their solutions will be different because of the order of the magnitude of the "eddy viscosity". It is assumed that the deformation rate s in (2.5) has an order of U/L because of (2.6) and (2.7). Compared with (2.3) in an EAM, the magnitude of "eddy viscosity" in LES with the Smagorinsky SGS model is

$$\nu_s \propto \Delta_0^2 \frac{U}{L}.$$

where Δ_0 is a typical value of Δ in (2.5). This therefore yields

$$\frac{\nu_s}{\nu_e} \propto (\frac{\Delta_0}{L})^2.$$

If the two closure schemes (EAM's and LES's) are substituted in the averaged N-S equations, the corresponding stress-flux terms

$$-\frac{\partial \overline{u_i' u_j'}}{\partial x_j} = \frac{\partial}{\partial x_j}(2\nu_\alpha s_{ij}) - \frac{2}{3}\frac{\partial E_\alpha}{\partial x_j} \qquad \alpha = e, s$$

will have different orders of magnitude relative to other terms in the equations. The two closures therefore yield solutions with different stabilities because of the different magnitudes of diffusion terms, or, different magnitudes of the mathematical model Reynolds numbers. In general, EAM runs in a "mathematically stable regime", while LES runs in a "mathematically unstable regime". This issue will be discussed in more details later in section 2.3.

To summarize, DNS resolves almost all sizes of eddies, while EAM parameterizes almost all sizes of eddies. As far as LES is concerned, it has been suggested that a good rule of thumb is that 80% of the TKE should be contained in the resolved eddies and 80% of the dissipation should be in subgrid eddies (Ferziger, 1977).

2.1.4 Historical Survey of LES

The first application of LES was made by Deardorff (1970c) who studied the plane Poiseuille flow. His pioneering paper provided many of the foundations of this subject and influenced much subsequent work. Deardoff has also performed LES studies of atmospheric turbulence (Deardorff, 1970a; Deardorff, 1972; Deardorff, 1973).

Following Deardorff's work, Schumann (1975) divided SGS stresses into a locally isotropic part and an inhomogeneous part and adopted a separate PDE for the SGS TKE. However, this extra PDE did not significantly improve the results over the LES using the Smagorinsky SGS model.

Reynolds and Ferziger at Stanford University began work in 1972 and have concentrated on developing the fundamental formulation of SGS schemes, with systematic

extension to more complex flows. The use of spectral methods was introduced by them (Mansour, Reynolds and Ferziger, 1979; Moin, Reynolds and Ferziger, 1978). They carried out interesting tests of the eddy viscosity SGS models by comparing LES predictions, based on a coarse mesh, with DNS of homogeneous turbulence on a finer mesh (Clark, Ferziger and Reynolds, 1978; McMillan and Ferziger, 1979). An excellent LES of a turbulent channel flow (Moin and Kim, 1982), a DNS of a channel flow (Kim, Moin and Moser, 1987) and interesting DNSs of the turbulent ABL (Coleman, Ferziger and Spalart, 1990; Coleman, Ferziger and Spalart, 1992) were also reported. The NASA Ames group has also specialized in DNS of simple flows (Spalart, 1988; Spalart, 1989). Leslie and his group at Queen Mary College in London began in 1976 to look at a number of issues, including the use of turbulence theories in developing SGS models (Antonopaulos-Domis, 1981; Leslie and Quarini, 1979; Love and Leslie, 1977).

With the development of research on LES models, its application to the atmosphere, especially to the microscale problems, has been carried out by many meteorologists. One of the major groups is the National Center for Atmosphere Research (NCAR). Its work includes:

- Neutral ABL (Deardorff, 1970a; Deardorff, 1972);
- The convective ABL (or called CBL) decay (Brost and Nieuwstadt, 1986);
- Clear CBL dynamics (Deardorff, 1972; Moeng, 1984; Moeng and Wyngaard, 1984; Moeng and Wyngaard, 1986; Moeng and Wyngaard, 1988);
- Cloud CBL dynamics (Deardorff, 1980; Moeng, 1986a; Moeng, 1986b; Moeng and Randall, 1984; Smolarkiewicz and Clark, 1985; Smolarkiewicz and Clark, 1986);
- Passive scalar dispersion in the CBL (Wyngaard, 1984a; Wyngaard, 1984b);

- Use of LES results to test ensemble-average parameterization (Moeng and Wyngaard, 1986; Moeng and Wyngaard, 1989; Wyngaard, 1985).

In the Netherlands, Nieuwstadt and his colleagues concentrated on buoyant scalar dispersion in the CBL (van Haren and Nieuwstadt, 1989; Nieuwstadt and de Valk, 1987), and also conducted a LES on the CBL decay (Nieuwstadt and Brost, 1986).

In England, Mason carried out studies of the Smagorinsky model's coefficient C_s in Equation (2.5) (Mason and Callen, 1986), as well as the application of LES to the CBL (Mason, 1989), neutral ABL (Mason and Thomson, 1987; Mason and Thomson, 1992) and the stably-stratified ABL (Mason, 1990).

A German group led by Schumann has been active following his fundamental approach on SGS modelling (Schumann, 1975). Ebert, Schumann and Stull (1989) used LES results of the CBL to directly determine the so-called transilient matrix, proposed by Stull (1984), Stull and Hasagawa (1984) in the Transilient Turbulence Theory. They also analyzed the coherent structure of the CBL in detail (Schmidt and Schumann, 1989), carried out LES of the CBL with chemical reactions (Schumann, 1989), and performed LES in a domain bounded by a rigid adiabatic lid and a wavy lower surface whose height varied sinusoidally through a single cycle across the domain (Krettenauer and Schumann, 1992). They also conducted a DNS on stratified homogeneous turbulent shear flows (Gerz, Schumann and Elghobashi, 1989).

A group at Colorado State University has also conducted LES which has been introduced into its RAMS (Regional Atmospheric Modelling System) code. Application to the clear CBL was carried out by Chen and Cotton (1986), to passive scalar dispersion by Cotton et al. (1987). Hadfield, Cotton and Pielke (1991), Hadfield, Cotton and Pielke (1992) have performed LES over a flat surface with horizontal variations in surface heat flux, and Walko, Cotton and Pielke (1992) examined the effects of hilly terrain on the

CBL using LES.

Several other researchers have performed a variety of LES studies. For example, Sykes and Henn (1989) studied free and sheared convective flow between moving flat plates. Miyake, Kajishima and Hamaogi (1989) simulated a channel flow with fluid injection or a sink on one wall; Bader and Horst (1988) and Sykes, Lewellen and Henn (1988) used LES to evaluate dispersion of passive tracers; Lesieur, Metais and Laroche (1989) carried out a LES of stably stratified homogeneous turbulence and coherent structures in the mixing layer; Dang and Teissedre (1989) studied the energy exchange between resolved and unresolved scales in LES of homogeneous turbulence by using DNS; Shaw and Schumann (1992) applied LES to an atmospheric surface layer in which the lower third of the domain is occupied by a drag layer and heat sources to represent a forest; Sykes, Henn and Lewellen (1993) conducted a LES to study the structure of the boundary layer close to the surface under free-convection conditions. Other LES approaches have been reviewed in the following papers: Herring (1979), Ferziger and Leslie (1979), Voke (1983), Wyngaard (1984c), Yoshizawa (1986), Young (1988), Schmidt and Schumann (1989) and Reynolds (1989).

2.1.5 A General Evaluation of LES

Based on previous studies using LES, one can list the advantages of LES as follows:

- Simulated flow fields can provide information on the statistics of large eddies which cannot be reflected by EAMs;
- The results of the averaged quantities derived from LES agree well with many measurements;
- As far as the model constants in various LES applications are concerned, LES is highly universal because it uses fewer model constants than EAMs. For example,

only one constant appears in the Smagorinsky model (2.4) to (2.7), while there are normally 5 constants in the k-ϵ closure model often employed in EAMs. In addition, the SGS modelling constant C_s can be theoretically derived (Lilly, 1967).

- LES handles the CBL very well, despite the fact that the mean velocity gradient is almost zero whereas EAM fails to deal with this case.

Another potential of LES is to study the closure problems in EAM. For example, using LES output, Moeng and Wyngaard (1986) calculated the pressure-scalar covariances, which dominate the Reynolds flux equations but are impossible to measure directly. They used the LES model results to evaluate existing EAMs (Moeng and Wyngaard, 1989).

In spite of its successes, LES still remains underutilized because the successes are based on a high resolution of the flows, and hence very high computational costs. For example, Moeng and Wyngaard (1988) used $96 \times 96 \times 96 \simeq 10^6$ grid points; each time step, corresponding to 1 second of real time, consumes about 36 seconds CPU time on a CRAY-XMP. In order to obtain a satisfactory results for about 1.6 hours of real time, about 57.6 hours of CPU time were consumed on a CRAY-XMP! The largest computation of the present study involves $64 \times 64 \times 50 \simeq 2 \times 10^5$ grid points and each time step of 1.5 seconds of real time costs about 24 seconds CPU time on an IBM RISC 6000/560 workstation. In contrast,an EAM can simulate the same problem for the same time period with less than 1% of that computing time.

Because of this fact, LES cannot be used as a prediction tool at present. But, one must realize that field experiments cannot provide enough data owing to limitations of cost and instrumentation; even well-designed laboratory experiments are similarly limited. Fortunately, LES may compensate for these shortages. Such excellent examples of LES are the ABL studies of Deardorff (1974a), Deardorff (1974b).

2.2 Governing equations and subgrid scale model

2.2.1 Partial differential equations for the ABL

Flows in the ABL have to follow three basic conservation laws: conservation of mass, conservation of momentum and conservation of energy. The set of governing equations can therefore be derived based on these three laws. The equation that results from the law of conservation of mass is called the continuity equation:

$$\frac{\partial \rho}{\partial t} + \frac{\partial(\rho u_j)}{\partial x_j} = 0, \tag{2.8}$$

where ρ is the air density, u_i the velocity vector, x_i the spatial coordinates with x_3 vertically upwards, and t is the time.

Equations of motion are the mathematical expressions of the conservation law of momentum. The equations of motion in a noninertial reference frame rotating with the earth are given by

$$\frac{\partial u_i}{\partial t} + u_j \frac{\partial u_i}{\partial x_j} = -\frac{1}{\rho}\frac{\partial p}{\partial x_i} + \nu \frac{\partial^2 u_i}{\partial x_j^2} - g\delta_{i3} - 2\epsilon_{ijk}\Omega_j u_k \qquad (i = 1, 2, 3), \tag{2.9}$$

where p is the pressure, ν the kinematic viscosity of air, g the gravity acceleration of the earth, ϵ_{ijk} the alternating unit tensor, and Ω_j the angular velocity vector of the earth's rotation.

The conservation law of energy is the First Law of Thermodynamics. One of its expressions is

$$\delta Q = C_p dT - \frac{1}{\rho} dp, \tag{2.10}$$

where δQ is the quantity of heat energy entering unit mass, C_p the heat capacity at constant pressure per mass, T the absolute temperature. One defines the potential

temperature Θ for an air mass with temperature T and pressure p through a reference pressure $p_{0,0}$

$$\Theta = T(\frac{p_{0,0}}{p})^{R_d/C_p}, \tag{2.11}$$

where $p_{0,0}$ is usually taken as 1000 mbar, and R_d is the gas constant. For dry air under standard conditions, $R_d = 287\text{m}^2\text{s}^{-2}\text{K}^{-1}$. . Substituting (2.11) into (2.10) yields another form of the energy conservation law:

$$C_p T \frac{d\Theta}{\Theta} = \delta Q.$$

Therefore, the equation of Θ can be derived:

$$\frac{\partial \Theta}{\partial t} + u_j \frac{\partial \Theta}{\partial x_j} = \frac{\Theta}{C_p T} S_H,$$

or

$$\frac{\partial \Theta}{\partial t} + u_j \frac{\partial \Theta}{\partial x_j} = S_\Theta, \tag{2.12}$$

where S_H is the total source of heat energy per unit mass per unit time, and $S_\Theta (= S_H \Theta / C_p T)$ is the corresponding source of potential temperature per unit time. In a laminar atmospheric flow, major contributors to S_H include radiative flux convergence, dissipation of heat by molecular diffusion and latent heat.

Finally, the equation of state is included to close the PDE system:

$$p = \rho R_d T. \tag{2.13}$$

The PDE system (2.8), (2.9), (2.11), (2.12) and (2.13) has 7 equations, while involving 7 variables: u_i $(i = 1, 2, 3)$, ρ, T, Θ and p. Therefore, this PDE system is closed.

Simplification of the equations

Some assumptions are made to simplify the above basic equations:

i) f-plane assumption:

The term $2\epsilon_{ijk}\Omega_j u_k$ can be denoted in the form of vectors as $2\vec{\Omega} \times \vec{U}$, if Ω_i is denoted by $\vec{\Omega}$ and u_i by $\vec{U}$. By setting x_3 to the vertical direction at a place of a latitude ϕ on the earth, the angular velocity vector $\vec{\Omega}$ can be projected onto the x_3-axis and onto the horizontal plane, and $\vec{\Omega}_3$ and $\vec{\Omega}_{12}$ are obtained, respectively. Letting $f = 2\Omega \sin\phi$, referred to as the Coriolis parameter, one obtains $2\vec{\Omega}_3 = (0, 0, 2\Omega \sin\phi) = (0, 0, f)$. Since $\vec{\Omega}_3$ is perpendicular to the horizontal plane and the mean wind $\vec{U}$ is parallel to the plane, $\vec{\Omega}_3 \times \vec{U}$ will be parallel to the horizontal plane and $\vec{\Omega}_{12} \times \vec{U}$ will be in the vertical direction as a vertical acceleration. In mid-latitude regions, the magnitude of $\vec{\Omega}_3 \times \vec{U}$ is almost the same as that of $\vec{\Omega}_{12} \times \vec{U}$, but their importance in their respective momentum equations is not the same. Compared with other terms in the vertical momentum equation, $\vec{\Omega}_{12} \times \vec{U}$ is negligible (Sorbjan, 1989). Therefore, one obtains

$$2\vec{\Omega} \times \vec{U} \approx 2\vec{\Omega}_3 \times \vec{U} = (-fv, fu, 0), \tag{2.14}$$

or, equivalently,

$$2\epsilon_{ijk}\Omega_j u_k \approx -f u_j \epsilon_{ij3}. \tag{2.15}$$

ii) Incompressibility approximation

As long as the ABL depth (its typical value is 1 km) is much smaller than the density scale height $H_\rho = |(1/\rho_0)(\partial\rho/\partial z)_0|^{-1} \approx 8$ km, where the subscript $_0$ denotes the value at the earth surface, the air can be approximated as incompressible (Pielke, 1984) and:

$$\frac{\partial u_i}{\partial x_i} = 0. \tag{2.16}$$

iii) Boussinesq approximation

For simplicity, the thermodynamic variables are decomposed into two parts: the regional mean variables[3] and the perturbation part; namely

$$\frac{\partial p}{\partial x_i} = \frac{\partial p_0}{\partial x_i} + \frac{\partial \breve{p}}{\partial x_i} \quad , \quad \rho = \rho_0 + \breve{\rho}, \tag{2.17}$$

$$T = T_0 + \breve{T} \quad , \quad \Theta = \Theta_0 + \breve{\Theta}, \tag{2.18}$$

where the subscript $_0$ represents the regional mean quantities, and $\breve{}$ represents the perturbation about the regional means. The perturbation parts are assumed to be much smaller than the regional average parts. It is also assumed that the ABL is horizontally homogeneous and the above reference variables satisfy:

$$-\frac{1}{\rho_0}\frac{\partial p_0}{\partial x_i} - g\delta_{i3} + fG_j\epsilon_{ij3} = 0, \tag{2.19}$$

where G_1 and G_2 are components of the geostrophic wind[4]. These yield, to the first order of perturbation quantities,

$$\begin{aligned} \frac{1}{\rho}\frac{\partial p}{\partial x_i} + g\delta_{i3} &= \frac{1}{\rho_0 + \breve{\rho}}[\frac{\partial p_0}{\partial x_i} + \frac{\partial \breve{p}}{\partial x_i} + (\rho_0 + \breve{\rho})g\delta_{i3}] \\ &\approx (\frac{1}{\rho_0} - \frac{1}{\rho_0}\frac{\breve{\rho}}{\rho_0})(\frac{\partial p_0}{\partial x_i} + \frac{\partial \breve{p}}{\partial x_i} + \rho_0 g\delta_{i3} + \breve{\rho}g\delta_{i3}) \\ &\approx \frac{1}{\rho_0}\frac{\partial \breve{p}}{\partial x_i} + \frac{\breve{\rho}}{\rho_0}g\delta_{i3} + fG_j\epsilon_{ij3}. \end{aligned} \tag{2.20}$$

From (2.11), (2.13), (2.17) and (2.18), one obtains to the first order,

$$\frac{\breve{\rho}}{\rho_0} \approx (1 - \frac{R_d}{C_p})\frac{\breve{p}}{p_0} - \frac{\breve{\Theta}}{\Theta_0}.$$

[3]Regional mean value refers to horizontal average over a region whose horizontal dimension is comparable to the domain size of this LES study, for example, four or five kilometers. For the pressure field, pressure gradient, rather than pressure, is subjected to this averaging procedure, because a linear distribution of pressure field (constant pressure gradient) is the driving force of the neutral ABL.

[4]The geostrophic wind is usually 2D, parallel to the horizontal plane, which implies that $G_3 = 0$.

Since the ABL depth (its typical value is 1 km) is much smaller than the density scale height $H_\rho \approx 8$ km, the value of $\breve{p}/p_0$ can be ignored compared with $\breve{\rho}/\rho_0$ (Pielke, 1984). The above approximation can be written as

$$\frac{\breve{\rho}}{\rho_0} \approx -\frac{\breve{\Theta}}{\Theta_0}.$$

Substituting this into (2.20) yields

$$-\frac{1}{\rho}\frac{\partial p}{\partial x_i} - g\delta_{i3} \approx -\frac{1}{\rho_0}\frac{\partial \breve{p}}{\partial x_i} + g\frac{\breve{\Theta}}{\Theta_0}\delta_{i3} - fG_j\epsilon_{ij3}. \tag{2.21}$$

After applying approximations i) to iii), the basic equations become:

$$\frac{\partial u_i}{\partial x_i} = 0, \tag{2.22}$$

$$\frac{\partial u_i}{\partial t} + u_j\frac{\partial u_i}{\partial x_j} = -\frac{1}{\rho_0}\frac{\partial \breve{p}}{\partial x_i} + \nu\frac{\partial^2 u_i}{\partial x_j^2} + g\frac{\breve{\Theta}}{\Theta_0}\delta_{i3} - f(G_j - u_j)\epsilon_{ij3} \quad i = 1,2,3 \tag{2.23}$$

$$\frac{\partial \Theta}{\partial t} + \frac{\partial \Theta}{\partial x_j} = \eta\frac{\partial^2 \Theta}{\partial x_j^2} + \text{other source terms}, \tag{2.24}$$

where η is the molecular thermal diffusivity of potential temperature. If "other source terms" are known, the above five equations includes five unknowns $(u_i, \breve{p}, \breve{\Theta})$, and so are a closed set. The present work only investigates an idealized situation, in which no cloud, water vapor, or chemical reactions occur in the ABL. There is also no radiative flux convergence within the region. Therefore, the "other source terms" in the potential temperature equation (2.24) can be eliminated. The equations can be solved if combined with proper boundary conditions, from the viewpoint of initial-value and boundary-value PDE.

2.2.2 The Smagorinsky Model

Averaging processes

It is noted that the averaging procedure can be defined in many different ways, and introduces many difficulties for nonlinear problems. Generally speaking, three averaging

procedures are well recognized: ensemble averages, time averages and space averages. If ϕ is a flow variable, it can be decomposed as follows no matter what kind of averaging process is taken:

$$\phi(x_i, t) = \bar{\phi}(x_i, t) + \phi'(x_i, t), \tag{2.25}$$

where $\bar{\phi}$ is the averaged component and $\phi'(x_i, t)$ is the residual field.

Ensemble average

Ensemble averaging has the following properties (Hinze, 1975):

$$\phi = \bar{\phi} + \phi', \qquad \overline{a\phi + b\psi} = a\bar{\phi} + b\bar{\psi}, \tag{2.26}$$

$$\overline{\frac{\partial \phi}{\partial t}} = \frac{\partial \bar{\phi}}{\partial t}, \qquad \overline{\frac{\partial \phi}{\partial x_i}} = \frac{\partial \bar{\phi}}{\partial x_i}, \tag{2.27}$$

$$\overline{\bar{\phi}\psi'} = 0, \qquad \overline{\phi'} = 0, \tag{2.28}$$

$$\overline{\bar{\phi}\bar{\psi}} = \bar{\phi}\bar{\psi}, \qquad \bar{\bar{\phi}} = \bar{\phi}, \tag{2.29}$$

where ψ is any other flow variable, and a and b are constants. Applying ensemble averaging to equation (2.22) to (2.24) yields

$$\frac{\partial \bar{u}_j}{\partial x_j} = 0, \tag{2.30}$$

$$\begin{aligned} \frac{\partial \bar{u}_i}{\partial t} + \bar{u}_j \frac{\partial \bar{u}_i}{\partial x_j} &= -\frac{1}{\rho_0}\frac{\partial \bar{p}}{\partial x_i} + g\frac{\bar{\Theta}}{\Theta_0}\delta_{i3} - f(G_j - \bar{u}_j)\epsilon_{ij3} \\ &\quad + \nu\frac{\partial^2 \bar{u}_i}{\partial x_j^2} - \frac{\partial \overline{u_i' u_j'}}{\partial x_j}, \end{aligned} \tag{2.31}$$

$$\frac{\partial \bar{\Theta}}{\partial t} + \bar{u}_j \frac{\partial \bar{\Theta}}{\partial x_j} = \eta \frac{\partial^2 \bar{\Theta}}{\partial x_j^2} - \frac{\partial \overline{u_j' \theta'}}{\partial x_j}. \tag{2.32}$$

In the momentum equation the unknowns $-\overline{u_i' u_j'}$ are called Reynolds stress terms and in the potential temperature equation, the unknowns $\overline{u_j' \theta'}$ are called turbulent kinematic heat flux.

Time average and space average

Time or space averaging is very different from ensemble averaging. Firstly, unlike the latter, they are not unique in the sense that the averaged value depends on the choice of the moving filter F in the definition:

$$\bar{\phi}(t, x_i) = \int_{-\infty}^{+\infty} \phi(\tau, x_i) F(t - \tau) d\tau, \tag{2.33}$$

or

$$\bar{\phi}(t, x_i) = \iiint_{-\infty}^{+\infty} \phi(t, \xi_i) F(x_i - \xi_i) d\xi_i. \tag{2.34}$$

(2.33) is time averaging, while (2.34) is space averaging; LES adopts the latter. F is usually taken as a symmetric function of its argument $r_i = x_i - \xi_i$ with an integral of unity which has a maximum at the origin and tends to zero as $r = \sqrt{r_i r_i} \gg \Delta$, where Δ is of the order of the grid spacing. One can therefore think of $\bar{\phi}(t, x_i)$ as a local spatially averaged field. A common form for F is the top-hat function, which is defined as

$$F(x_i, \xi_i) = \begin{cases} 1/(\Delta_1 \Delta_2 \Delta_3) & |x_i - \xi_i| \leq \Delta_i/2 \quad \text{for all } i = 1, 2, 3 \\ 0 & \text{otherwise,} \end{cases} \tag{2.35}$$

while another example is the Gaussian filter, which is defined as

$$F(x_i, \xi_i) = (\frac{6}{\pi \Delta_i})^{\frac{1}{2}} \exp[-\frac{6(x_i - \xi_i)^2}{\Delta_i^2}]. \tag{2.36}$$

The properties of time or space averaging are:

$$\overline{\phi'} \neq 0, \qquad \bar{\bar{\phi}} \neq \bar{\phi}, \tag{2.37}$$

$$\overline{\bar{\phi}\psi'} \neq 0, \qquad \overline{\bar{\phi}\bar{\psi}} \neq \bar{\phi}\bar{\psi}, \tag{2.38}$$

while (2.26) and (2.27) are still satisfied. This presents difficulties when applying time or space averaging to the governing equations.

Applying spatial average operator to equation (2.22) to (2.24) yields

$$\frac{\partial \bar{u}_i}{\partial x_i} = 0, \tag{2.39}$$

$$\begin{aligned}\frac{\partial \bar{u}_i}{\partial t} + \frac{\partial \bar{u}_i \bar{u}_j}{\partial x_j} &= -\frac{1}{\rho_0}\frac{\partial \bar{p}}{\partial x_i} + g\frac{\bar{\Theta}}{\Theta_0}\delta_{i3} - f(G_j - \bar{u}_j)\epsilon_{ij3} \\ &\quad + \nu\frac{\partial^2 \bar{u}_i}{\partial x_j^2} + \frac{\partial \tau_{ij}^{(s)}}{\partial x_j},\end{aligned} \tag{2.40}$$

$$\frac{\partial \bar{\Theta}}{\partial t} + \frac{\partial \bar{u}_j \bar{\Theta}}{\partial x_j} = \eta\frac{\partial^2 \bar{\Theta}}{\partial x_j^2} - \frac{\partial H_j^{(s)}}{\partial x_j}, \tag{2.41}$$

where $\tau_{ij}^{(s)} = -(\overline{u_i u_j} - \bar{u}_i \bar{u}_j)$ is an unknown stress tensor, $H_j^{(s)} = \overline{u_i \Theta} - \bar{u}_i \bar{\Theta}$ are sensible heat fluxes. Closure of these unknowns will be left to the next section.

Another form of momentum equation was proposed by Leonard (1974):

$$\begin{aligned}\frac{\partial \bar{u}_i}{\partial t} + \frac{\partial \overline{\bar{u}_i \bar{u}_j}}{\partial x_j} &= -\frac{1}{\rho_0}\frac{\partial \bar{p}}{\partial x_i} + g\frac{\bar{\Theta}}{\Theta_0}\delta_{i3} - f(G_j - \bar{u}_j)\epsilon_{ij3} \\ &\quad + \nu\frac{\partial^2 \bar{u}_i}{\partial x_j^2} + \frac{\partial \tau_{ij}^{(s,2)}}{\partial x_j},\end{aligned} \tag{2.42}$$

where $\tau_{ij}^{(s,2)} = -(\overline{\bar{u}_i u_j'} + \overline{u_i' \bar{u}_j} + \overline{u_i' u_j'})$. Note that $\overline{\bar{u}_i u_j'}$ and $\overline{u_i' \bar{u}_j}$ do not disappear because of (2.38). The difference $\tau_{ij}^{(s,2)} - \tau_{ij}^{(s)} = L_{ij} = \overline{\bar{u}_i \bar{u}_j} - \bar{u}_i \bar{u}_j$ is called the Leonard stress term. Leonard (1974) proved that L_{ij} is responsible for significant energy extraction from the large scales due to triple correlations of these motions.

One has the option of calculating the term $\overline{\bar{u}_i \bar{u}_j}$ in (2.42) explicitly with double application of the averaging operator, or, as Deardorff (1971) has done, to incorporate $\tau_{ij}^{(s)}$ in a modelling assumption. In the present work, the latter option is adopted with the Smagorinsky SGS model.

In this thesis, subscript $_s$ or superscript $^{(s)}$ is usually adopted to denote a SGS quantity. For example, $\tau_{ij}^{(s)}(= -\overline{u_i u_j} + \bar{u}_i \bar{u}_j)$ denotes the SGS shear stress tensor; $-\overline{u_s' w_s'}(= -\overline{uw} +$

$\bar{u}\bar{w}$) represents the SGS shear stress component $\tau_{13}^{(s)}$, which is also denoted by $\tau_{uw}^{(s)}$ or SGS τ_{uw}; $\overline{u_s'^2}(= -\overline{u^2} + \bar{u}^2)$ represents the SGS velocity fluctuations of u component.

For simplicity, the bars on top of the first moment variables denoting spatial average operator defined by (2.34) are dropped hereafter.

The SGS model

Noting that $\tau_{ij}^{(s)}$ expresses the effect of the SGS eddies on the RS eddies, this effect is represented as an additional "viscosity". Namely, using the Smagorinsky SGS eddy viscosity ν_s, one writes

$$\tau_{ij}^{(s)} = -\frac{2}{3}E_s\delta_{ij} + 2\nu_s s_{ij}, \tag{2.43}$$

$$s_{ij} = \frac{1}{2}(\frac{\partial u_i}{\partial x_j} + \frac{\partial u_j}{\partial x_i}), \tag{2.44}$$

where E_s is the SGS TKE defined by $E_s = \frac{1}{2}(\overline{u_i^2} - \overline{u_i}^2)$, and s_{ij} the RS strain rate tensor.

To derive the closure scheme for ν_s, it is proper to assume that the grid spacing Δ is in the inertial subrange, and therefore ν_s must be a function of Δ and turbulence dissipation rate ϵ only. Dimensional analysis tells us that

$$\nu_s = C\Delta^{4/3}\epsilon^{1/3}, \tag{2.45}$$

The local equilibrium assumption is made to relate ϵ to the RS components[5] ; namely,

$$\epsilon = \tau_{ij}^{(s)}\frac{\partial u_i}{\partial x_j}. \tag{2.46}$$

Substituting (2.43), (2.44) into (2.46) and combining (2.45) yield

$$\nu_s = (C_s\Delta)^2 s, \tag{2.47}$$

[5]The RS TKE is not necessarily dissipated through the local SGS dissipation, but it is a good approximation for homogeneous turbulence. In some part of the ABL where transport of TKE is much smaller than dissipation rate of TKE, this assumption can also be valid (Stull, 1988).

$$s^2 = 2s_{ij}s_{ij}. \tag{2.48}$$

Note that after substituting $\tau_{ij}^{(s)}$ into the momentum equations one can absorb the E_s term into the pressure gradient term. E_s is therefore not explicitly calculated in computation.

A similar parameterization can be constructed for the sensible heat flux, $H_j^{(s)} = \overline{u_i\Theta} - u_i\Theta$:

$$H_j^{(s)} = -\eta_s \frac{\partial \Theta}{\partial x_j}, \tag{2.49}$$

$$\eta_s = 3.0\nu_s. \tag{2.50}$$

The ratio η_s/ν_s was determined empirically by Deardorff (1972) who found that a ratio smaller than 3 led to excessive intensity at the larger wavenumbers in the temperature spectrum at interior levels.

2.2.3 Boundary conditions and initial conditions

Height of the ABL

The ABL height, h, is separately defined for the neutral ABL and the unstable ABL. For the neutral ABL, this height is denoted by h_E; relevant external parameters are the Coriolis parameter f, the geostrophic wind speed U_g and the roughness length z_0. A dependent parameter is the friction velocity $u_* = \sqrt{\tau_0}$, where τ_0 is the kinematic shear stress at the surface. The set of parameters forms two length scales: either (U_g/f, z_0) or (u_*/f, z_0). Observations indicate that the length scale u_*/f is the most relevant one when considering h_E. The empirical relation is (Nieuwstadt and van Dop, 1982)

$$h_E \approx 0.3\frac{u_*}{f}. \tag{2.51}$$

For an unstable ABL, the inversion layer, typically represented by a large positive gradient of potential temperature, confines the development of turbulence in the ABL.

This layer acts as a lid on the top and thus defines the height of the ABL, denoted by Z_i.

Upper boundary conditions

Above the height of the ABL, the flow is considered as being 2D on a horizontal plane, and is assumed to be no vertical wind shear and no turbulence. This assumption yields the balance between the pressure gradient and the Coriolis force:

$$-\frac{1}{\rho_0}\frac{\partial p_0}{\partial x_i} - g\delta_{i3} + fG_j\epsilon_{ij3} = 0, \tag{2.52}$$

Through these equations, the pressure gradient and the geostrophic velocity component are related to each other. As vectors, they are perpendicular to each other. The upper boundary conditions for horizontal velocity components u, v and w are:

$$u(x,y,z)|_{z\to\infty} = U_g, \tag{2.53}$$

$$v(x,y,z)|_{z\to\infty} = V_g, \tag{2.54}$$

$$w(x,y,z)|_{z\to\infty} = 0. \tag{2.55}$$

where $U_g = G_1$ and $V_g = G_2$. A more realistic way of improving this is to specify a finite height, say $D_z(\geq h)$, above which the assumption (2.52) holds. The boundary conditions are thus written as:

$$u(x,y,z)|_{z=D_z} = U_g, \tag{2.56}$$

$$v(x,y,z)|_{z=D_z} = V_g, \tag{2.57}$$

$$w(x,y,z)|_{z=D_z} = 0. \tag{2.58}$$

It is noted that equation (2.52) has the same form as equation (2.19), which governs the regional mean pressure gradient *inside* the ABL. Therefore, specification of boundary

conditions for velocity components with the values of geostrophic wind components implies a specification of a pressure gradient acting upon air inside the ABL. This fact can be seen from the derivation of equation (2.23). The term $-fG_j\epsilon_{ij3}$ on the right-hand side was obtained from $-(1/\rho_0)\partial p_0/\partial x_i$ because of (2.52). The pressure gradient is a driving force of the ABL turbulence. Unlike the mean pressure gradient in a turbulent channel flow which is parallel to the mean flow, it is perpendicular to the mean wind above the ABL (the geostrophic wind). The kinetic energy (KE) of flow in the ABL is obtained from the work done by the mean pressure gradient, transferred to eddies of different sizes through the cascade of TKE and eventually dissipated into heat.

Lower boundary conditions

It is assumed that the lower boundary is a rough layer with a constant roughness length z_0. For a neutral ABL, the velocity profile near the surface obeys the so-called "law of the wall" in which the roughness length z_0 and friction velocity u_* determine the velocity:

$$u(x,y,z) = \frac{u_*}{\kappa_0}\ln\frac{z}{z_0}. \tag{2.59}$$

where κ_0 is the value of the von Kármán constant in the specification of the lower boundary conditions[6]. This yields the boundary conditions for the velocity components:

$$u(x,y,z)|_{z=z_1} = \frac{u_*}{\kappa_0}\ln\frac{z_1}{z_0}\cos\alpha_{v,0}, \tag{2.60}$$

$$v(x,y,z)|_{z=z_1} = \frac{u_*}{\kappa_0}\ln\frac{z_1}{z_0}\sin\alpha_{v,0}, \tag{2.61}$$

$$w(x,y,z)|_{z=z_1} = 0, \tag{2.62}$$

[6]It is shown in chapter 3 that the effects of accuracy of κ_0 and z_0 on the RS turbulence in the USL are very small.

where z_1 is the height at which the lower boundary is located and $\alpha_{v,0}$ denotes the angle from the x-axis to the wind direction at the surface. (2.60) and (2.61) imply that $z_1 > z_0$.

For an unstable ABL, the lower boundary conditions for the velocity components can be derived from the Monin-Obukhov similarity formulas (Paulson, 1970):

$$u(x,y,z) = \frac{u_*}{\kappa_0}[\ln\frac{z}{z_0} - \Psi_u(\frac{z}{L})], \tag{2.63}$$

$$\Theta(x,y,z) = \Theta_0 + \frac{\alpha_\Theta T_{*,s}}{\kappa_0}[\ln\frac{z}{z_0} - \Psi_\Theta(\frac{z}{L})], \tag{2.64}$$

$$T_{*,s} = \frac{\overline{w'\theta'}_0}{u_*}, \tag{2.65}$$

where $\alpha_\Theta = 0.74$ (Businger et al., 1971). For the *unstable regime*,

$$\Psi_u(\frac{z}{L}) = 2\ln\frac{1+x_u}{2} + \ln\frac{1+x_u^2}{2} - 2\arctan x_u + \frac{\pi}{2}, \tag{2.66}$$

$$\Psi_\Theta(\frac{z}{L}) = 2\ln\frac{1+x_\Theta^2}{2}. \tag{2.67}$$

where $x_u = (1-15z/L)^{1/4}$ and $x_\Theta = (1-9z/L)^{1/4}$. In consequence, the boundary condition for the velocity components and the potential temperature are as follows:

$$u(x,y,z)|_{z=z_1} = \frac{u_*}{\kappa_0}[\ln\frac{z_1}{z_0} - \Psi_u(\frac{z_1}{L})]\cos\alpha_{v,0}, \tag{2.68}$$

$$v(x,y,z)|_{z=z_1} = \frac{u_*}{\kappa_0}[\ln\frac{z_1}{z_0} - \Psi_u(\frac{z_1}{L})]\sin\alpha_{v,0}, \tag{2.69}$$

$$w(x,y,z)|_{z=z_1} = 0, \tag{2.70}$$

$$\Theta(x,y,z)|_{z=z_1} = \Theta_0 + \frac{\alpha_\Theta T_{*,s}}{\kappa_0}[\ln\frac{z_1}{z_0} - \Psi_\Theta(\frac{z_1}{L})]. \tag{2.71}$$

The present study does not deal with the stably stratified ABL.

Lateral boundary conditions

The present work only investigates a very idealized situation in which turbulence in the ABL is horizontally homogeneous and extends to infinity on horizontal planes. In other words, statistics will be the same at all points on the horizontal plane at height z. Mathematically, a Cauchy problem can be proposed in the x and y directions. It is noted that LES solves a nonlinear PDE in a turbulent regime, in which detailed "accurate" solutions cannot be achieved. In other words, long-time behavior of the *detailed structure* of the solution can not be accurately simulated. However, statistics of the solution are still very useful for practical problems.

Is is assumed that the turbulent flow is confined by $0 \leq z \leq h$ in the vertical direction; the size of the largest eddies in the ABL is therefore of order h. These eddies make major contributions to two-point correlations of velocity fluctuations $R_{ij}(\vec{\xi}) = \overline{u_i'(\vec{x})u_j'(\vec{x}+\vec{\xi})}$ with a scale of order h, where $\vec{x}$ denotes any point in the ABL, and $\vec{\xi}$ is a vector lying on a horizontal plane. As $|\vec{\xi}|$ tends to infinity, the value of the correlation is expected to approach zero. This can be interpreted as a diminished correlation of turbulent structure between two points in space as their distance increases. For 3D, stationary, homogeneous and isotropic turbulence, the correlation function is a function of $\xi = |\vec{\xi}|$ only and an integral length scale can be defined as:

$$\mathcal{L}_{ij} = \int_0^\infty \frac{R_{ij}(\xi)}{\overline{u_i'^2}\ \overline{u_j'^2}} d\xi. \tag{2.72}$$

Denoting the order of $\mathcal{L}_{ij}$ by $\mathcal{L}$, one expects that $\mathcal{L} \sim h$ in the case of the ABL for the reason that largest eddies in the ABL are of the size of h.

Instead of solving (2.39) to (2.41) in a domain with infinite size in the horizontal direction, they are solved in a finite domain $\Omega = \{(x,y,z)|0 \leq x \leq D_x, 0 \leq y \leq D_y, 0 \leq z \leq D_z\}$, where D_x, D_y and D_z are the length, width and depth of the domain. As discussed above, in order to take into account the largest possible eddies, one must

choose :

$$D_x \geq \mathcal{L},\ D_y \geq \mathcal{L}, \quad \text{and } D_z \geq \mathcal{L}. \tag{2.73}$$

The lateral boundary conditions for velocity components are crucial to LES of turbulence, especially in LES studies of shear dominated turbulence. Shear turbulence is produced by instabilities of the mean shear flow and develops as it is advected downstream by the mean flow. If the boundary conditions for the velocity components of the inflow are imposed as smooth profiles, one needs a section of domain in which turbulence is allowed to be initially produced and then fully developed. This is a "transition to turbulence" problem. The length scale of the transition section would have to be so large that the computations would be impossible in today's computers. To solve this difficulty, periodic boundary conditions for the velocity components and for potential temperature are imposed in both x and y directions. These boundary conditions allow fully developed turbulence that is advected out of the domain to re-enter the domain and thus allow the maintenance of turbulent intensity. In fact, this study adopts this cyclic horizontal boundary condition for all variables.

One difficulty that arises from periodic boundary condition is that the technique may contradict the *irregularity* of turbulence if it allows periodic variations to be sustained as possible solutions. This question cannot be answered analytically. Examining two-point correlation functions of RS velocity fluctuations of LES output, however, may provide an answer (see page 114 for details).

Initial conditions

To generate fully developed turbulence as quickly as possible, random initial disturbances with finite amplitudes are added to the initial velocity mean field. The amplitudes

are specified as functions of z, given by

$$C_i U_g \frac{27}{4}\frac{z}{h}(1-\frac{z}{h})^2 \qquad i=1,2,3$$

where $C_1 = 0.06$ and $C_2 = C_3 = 0.03$ are three constants, and h is taken as 1000 m. These values are in fairly reasonable range. As stated by Reynolds (1989), for homogeneous isotropic turbulence, where the decay history is to a large degree set by the initial state, the initial conditions are very important; for homogeneous shear flow, the developed spectrum and its statistics are less sensitive to the initial field; inhomogeneous flows, such as the channel flow, establish their own steady-state spectrum and hence the initial conditions are not important at all. The ABL flows are subjected to external forces — pressure gradient associated with the geostrophic wind, and/or buoyancy force associated with the surface heat flux — which make it similar to a channel flow in the sense that both flows have energy flux from large scale motions. At a sufficiently long time, the self-generated and self-sustained turbulence has no memory of initial conditions and reaches a statistically stationary state. In other words, the ABL turbulence statistics of LES is insensitive to its initial conditions.

Descriptions of the code of this study and its numerical scheme can be seen in appendix A.

2.3 The Smagorinsky-Model Reynolds number

By adopting the the Smagorinsky SGS model and omitting the buoyancy force term and the molecular viscosity diffusion term, the momentum equations (2.40) becomes

$$\underset{\mathrm{I}}{\frac{\partial \hat{u}_i}{\partial \hat{t}}} + \underset{\mathrm{II}}{\hat{u}_j\frac{\partial \hat{u}_i}{\partial \hat{x}_j}} = \underset{\mathrm{III}}{-\frac{1}{\hat{\rho}_0}\frac{\partial \hat{p}}{\partial \hat{x}_i}} \underset{\mathrm{IV}}{- \hat{f}(\hat{G}_j - \hat{u}_j)\epsilon_{ij3}} + \underset{\mathrm{V}}{\frac{\partial}{\partial \hat{x}_j}(\hat{\nu}_s\frac{\partial \hat{u}_i}{\partial \hat{x}_j})}, \tag{2.74}$$

$$\hat{\nu}_s = (C_s\hat{\Delta})^2[\frac{\partial \hat{u}_i}{\partial \hat{x}_j}(\frac{\partial \hat{u}_i}{\partial \hat{x}_j} + \frac{\partial \hat{u}_j}{\partial \hat{x}_i})]^{1/2}, \tag{2.75}$$

where ˆ in this section denotes a dimensional variable.

Solution to the laminar Ekman layer

Consider the simplest situation in which $\hat{\nu}_s = \hat{\nu}$ constant, flow is steady with no turbulence and no variation on the horizontal plane, and $\hat{w} = 0$. The equation (2.74) becomes

$$0 = -\hat{f}(\hat{G}_j - \hat{u}_j)\epsilon_{ij3} + \frac{\partial}{\partial \hat{x}_j}(\hat{\nu}\frac{\partial \hat{u}_i}{\partial \hat{x}_j}), \tag{2.76}$$

or

$$0 = -\hat{f}(\hat{V}_g - \hat{v}) + \frac{\partial}{\partial \hat{z}}(\hat{\nu}\frac{\partial \hat{u}}{\partial \hat{z}}), \tag{2.77}$$

$$0 = \hat{f}(\hat{U}_g - \hat{u}) + \frac{\partial}{\partial \hat{z}}(\hat{\nu}\frac{\partial \hat{v}}{\partial \hat{z}}). \tag{2.78}$$

Its solution was found in 1905 by Ekman:

$$\hat{U} = \hat{U}_g - e^{-\pi\hat{z}/\hat{h}}(\hat{U}_g \cos\frac{\hat{z}}{\hat{h}}\pi + \hat{V}_g \sin\frac{\hat{z}}{\hat{h}}\pi), \tag{2.79}$$

$$\hat{V} = \hat{V}_g - e^{-\pi\hat{z}/\hat{h}}(\hat{V}_g \cos\frac{\hat{z}}{\hat{h}}\pi - \hat{U}_g \sin\frac{\hat{z}}{\hat{h}}\pi), \tag{2.80}$$

$$\hat{h} = \pi\sqrt{2\hat{\nu}/\hat{f}}. \tag{2.81}$$

It is noted that $\hat{h}$ is the only length scale in the problem.

Although the solution (2.79) and (2.80) does not depend on the Reynolds number $Re = \hat{G}\hat{h}/\hat{\nu} = \pi\hat{G}/\sqrt{\hat{\nu}\hat{f}/2}$, where $\hat{G} = \sqrt{\hat{U}_g^2 + \hat{V}_g^2}$, the N-S-like equations (2.74) are unstable as Re exceeds a critical value, say Re_{cr} (Brown, 1974). As Re increases, the relative importance of $\hat{\nu}$ becomes weaker, the flow evolves in a very complicated way due to non-linear interactions, and the flow becomes turbulent. When Re is large enough, say $Re > Re_t$, a turbulent field is fully developed; (2.81) no longer holds and the length

scale $\hat{u}_*/\hat{f}$ is becomes important. This scale relates to the height of the turbulent Ekman layer, which is about $0.3\hat{u}_*/\hat{f}$ as suggested by observations (Nieuwstadt and van Dop, 1982).

Definition of the Smagorinsky-Model Reynolds number

If the horizontal plane is effectively infinite in extent, no characteristic horizontal length scale is introduced. The present LES adopts finite horizontal domain sizes, which are not very large due to limitation of computer, and therefore introduces a characteristic horizontal length scale; in the vertical direction, however, the length scale is $\hat{h}_E$, which is defined by the Ekman spiral. Taking into account both horizontal domain size and vertical length scale $\hat{h}_E$, the characteristic length scale of LES is defined as

$$\hat{D} = (\hat{D}_x \hat{D}_y \hat{h}_E)^{1/3}. \tag{2.82}$$

Equation (2.74) is similar to the N-S equations except for the second term on the right-hand side, which plays the role of a driving force. In a turbulent channel flow, for example, the driving force is replaced by a constant horizontal pressure gradient. By analogy, one analyzes qualitatively the importance of $\hat{\nu}_s$ and therefore of the coefficient C_s. In this study, it is assumed that in the momentum equation (2.74), $\hat{u}_i$ has the order of $\hat{G}$, which is the magnitude of the geostrophic wind, $\hat{x}_i$ has the order of $\hat{D}$, and $\hat{\nu}_s$ given by (2.75) has the order of $(C_s\hat{\Delta}_0)^2\hat{G}/\hat{D}$, where $\hat{\Delta}_0$ is the typical size of $\hat{\Delta}$. Therefore, the order of the advection term (term II in equation (2.74) is

$$\hat{u}_j \frac{\partial \hat{u}_i}{\partial \hat{x}_j} \sim \frac{\hat{G}^2}{\hat{D}}, \tag{2.83}$$

the order of the Coriolis force term (term IV in equation (2.74) is

$$-\hat{f}(\hat{G}_j - \hat{u}_j)\epsilon_{ij3} \sim \hat{f}\hat{G}, \tag{2.84}$$

and the order of the SGS diffusion term (term V in equation (2.74) is

$$\frac{\partial}{\partial \hat{x}_j}(\hat{\nu}_s \frac{\partial \hat{u}_i}{\partial \hat{x}_j}) \sim \frac{1}{\hat{D}}(C_s\hat{\Delta}_0)^2 \frac{\hat{G}}{\hat{D}}(\frac{\hat{G}}{\hat{D}}) = (C_s\hat{\Delta}_0)^2 \frac{\hat{G}^2}{\hat{D}^3}. \tag{2.85}$$

Since the magnitude of the ratio of the advection term to the molecular diffusion term in the N-S equations gives the definition of the Reynolds number, which determines the stability of the flow, the magnitude of the ratio of the advection term to the *SGS* diffusion term in equation (2.74) yields the definition of the *Smagorinsky-Model Reynolds number*, or *SM-Reynolds number*:

$$\frac{\text{Advection term}}{\text{SGS Diffusion term}} \sim \frac{\hat{G}^2/\hat{D}}{(C_s\hat{\Delta}_0)^2\hat{G}^2/\hat{D}^3} = (\frac{\hat{D}}{C_s\hat{\Delta}_0})^2 = Re_{SM}. \tag{2.86}$$

This number determines the *mathematical stability*[7] of the LES model adopting the Smagorinsky SGS parameterization. The magnitude of the ratio of the advection term to the Coriolis term in equation (2.74) defines the *domain Rossby number*:

$$\frac{\text{Advection term}}{\text{Coriolis term}} \sim \frac{\hat{G}^2/\hat{D}}{\hat{f}\hat{G}} = \frac{\hat{G}}{\hat{f}\hat{D}} = Ro_D. \tag{2.87}$$

After normalization with the length scale $\hat{D}$, velocity scale $\hat{G}$, equations (2.74) become

$$\frac{\partial u_i}{\partial t} + u_j \frac{\partial u_i}{\partial x_j} = -\frac{\partial p}{\partial x_i} - \frac{1}{Ro_D}(G_j - u_i)\epsilon_{ij3} + \frac{1}{Re_{SM}}\frac{\partial}{\partial x_j}(\hat{\nu}_s \frac{\partial u_i}{\partial x_j}), \tag{2.88}$$

where $t = \hat{t}/(\hat{D}/\hat{G})$ and $p = \hat{p}/(\hat{\rho}_0\hat{G}^2)$. It is therefore concluded that *for LES flows to be formally similar with each other for an ABL flow, identity of both Re_{SM} and Ro_D is required.*

Model Reynolds number for DNS, LES and EAM

DNS attempts to solve the problem deterministically by employing an "effective viscosity" $\hat{\nu}_d = \hat{\nu}$. Its "mathematical Reynolds number" or DNS "model Reynolds number"

[7]Mathematical stability refers to the stability of a mathematical model, such as a LES model or a EAM model, due to intrinsic nonlinear characteristics.

is defined as $Re_{DNS} = Re = \hat{U}\hat{D}/\hat{\nu}$, where $\hat{D}$ and $\hat{U}$ are the characteristic length and velocity of the flow, respectively. In LES, however, those small eddies[8] have to be explicitly modelled, for example, as given by (2.43), (2.44), (2.47) and (2.48). Compared with DNS, LES has a larger "effective viscosity", $\hat{\nu}_{LES} \approx \hat{\nu}_s \gg \hat{\nu}_{DNS} = \hat{\nu}$, and equivalently, a smaller "mathematical Reynolds number", $Re_{LES} = \hat{U}\hat{D}/\hat{\nu}_{LES} \ll Re = \hat{U}\hat{D}/\hat{\nu}$.

In an EAM, an "effective viscosity" $\hat{\nu}_{EAM}$ is also employed, but for the same turbulent flow, it is much larger than $\hat{\nu}_{LES}$ in LES models. The mathematical Reynolds number in EAM models is $Re_{EAM} = \hat{U}\hat{D}/\hat{\nu}_{EAM} \ll Re_{LES}$. Generally, the orders of the "effective viscosities" for the three models are:

$$\hat{\nu}_{EAM} \sim \hat{D}\hat{U}, \tag{2.89}$$

$$\hat{\nu}_{LES} \sim (C_s\hat{\Delta}_0)^2\frac{\hat{U}}{\hat{D}}, \tag{2.90}$$

$$\hat{\nu}_{DNS} = \hat{\nu}, \tag{2.91}$$

where $\hat{\Delta}_0$ is the typical value of grid spacing. Therefore, one obtains

$$Re_{EAM} = \frac{\hat{U}\hat{D}}{\hat{\nu}_{EAM}} \sim O(1), \tag{2.92}$$

$$Re_{LES} = \frac{\hat{U}\hat{D}}{\hat{\nu}_{LES}} \sim O[(\frac{\hat{D}}{C_s\hat{\Delta}_0})^2] = O(Re_{SM}), \tag{2.93}$$

$$Re_{DNS} = \frac{\hat{U}\hat{D}}{\hat{\nu}_{DNS}} = Re. \tag{2.94}$$

It is also concluded that

$$\frac{\hat{\nu}_{EAM}}{\hat{\nu}_{DNS}} \sim Re, \tag{2.95}$$

$$\frac{\hat{\nu}_{EAM}}{\hat{\nu}_{LES}} \sim (\frac{\hat{D}}{C_s\hat{\Delta}_0})^2 = Re_{SM}, \tag{2.96}$$

[8]smaller that grid spacing, still playing an important role in exchanging momentum, dissipating KE *etc.*

$$\frac{\hat{\nu}_{LES}}{\hat{\nu}_{DNS}} \sim Re(\frac{C_s\hat{\Delta}_0}{\hat{D}})^2 \sim \frac{Re}{Re_{SM}}. \tag{2.97}$$

Estimate (2.92) shows that the order of model Reynolds number of an EAM is very small, and therefore may imply the mathematical stability of the solution to the EAM (although there is no theoretical proof). Equation (2.94) reveals that DNS possesses the same stability as real flows. If a real flow is in the turbulent regime, DNS also runs in the turbulent regime. In a LES with the Smagorinsky SGS model, its mathematical Reynolds number Re_{LES} is of the order of Re_{SM}, with the magnitude between Re_{EAM} and Re_{DNS}.

Applying the same procedure of dimensional analysis as that for LES model to DNS of an Ekman layer, two non-dimensional parameters are obtained: $Ro_D = \hat{G}/\hat{f}\hat{D}$ and $Re = \hat{G}\hat{D}/\hat{\nu}$. The Ekman layer becomes turbulent as the Reynolds number Re exceeds a critical number, Re_{cr}. The statistical properties of RS turbulence will be Reynolds number dependent unless the Reynolds number is so large that the turbulence statistics approach asymptotic values. Spalart (1989) used DNS to investigate an Ekman-layer-like turbulent flow, and Coleman, Ferziger and Spalart (1990) conducted a DNS for a turbulent Ekman layer with very low Reynolds numbers ($Re \sim 500$).

By analogy to a DNS, LES must be run in a "turbulent regime" to show a continuous spectrum for the RS motions. If $Re_{SM} \rightarrow 0$, the "simulated flow" becomes stable and "laminar"; when $Re_{SM} > Re_{SM,cr}$, the "simulated flow" becomes unstable and "turbulent". The statistical properties of RS turbulence is SM-Reynolds number dependent except when Re_{SM} is large enough.

This approach clearly shows that Re_{SM} is not only a mathematical stability criterion for a LES which employs the Smagorinsky SGS model, but it is also the dimensionless parameter on which the statistics of RS turbulent eddies depend.

2.4 Discretization and criterion of grid resolution

Rewriting the set of partial differential equations derived in the last section as follows:

$$\frac{\partial u_j}{\partial x_j} = 0, \tag{2.98}$$

$$\begin{aligned}\frac{\partial u_i}{\partial t} + \frac{\partial u_i u_j}{\partial x_j} &= -\frac{1}{\rho_0}\frac{\partial p}{\partial x_i} + g\frac{\Theta}{\Theta_0}\delta_{i3} - f(G_j - u_j)\epsilon_{ij3} \\ &\quad + \nu\frac{\partial^2 u_i}{\partial x_j^2} + \frac{\partial \tau_{ij}^{(s)}}{\partial x_j},\end{aligned} \tag{2.99}$$

$$\frac{\partial \Theta}{\partial t} + \frac{\partial u_j \Theta}{\partial x_j} = \eta\frac{\partial^2 \Theta}{\partial x_j^2} - \frac{\partial H_j^{(s)}}{\partial x_j}, \tag{2.100}$$

$$\tau_{ij}^{(s)} = -\frac{2}{3}E_s\delta_{ij} + 2\nu_s s_{ij}, \tag{2.101}$$

$$s_{ij} = \frac{1}{2}(\frac{\partial u_i}{\partial x_j} + \frac{\partial u_j}{\partial x_i}), \tag{2.102}$$

$$\nu_s = (C_s\Delta)^2 s, \tag{2.103}$$

$$s^2 = 2s_{ij}s_{ij}, \tag{2.104}$$

$$H_j^{(s)} = -\eta_s\frac{\partial \Theta}{\partial x_j}, \tag{2.105}$$

$$\eta_s = 3.0\nu_s. \tag{2.106}$$

In this section, the discretization of the PDEs will be discussed.

It is recalled in section 2.2.2 on page 28 that the derivation of ν_s in the Smagorinsky model (2.103) requires that the grid spacing Δ must be in the inertial subrange of turbulence spectrum. This requirement is referred to as the "*ISR rule*" hereafter, and it becomes effectively a criterion for choosing the grid size. For ABL turbulence, the ISR

can be identified in the observational curves of the power spectra of velocity components. It is known that a *necessary condition* for an ISR of homogeneous and isotropic turbulence is $-5/3$ power law of velocity spectra. There is no sufficient condition to identify the ISR for practical purposes. The present study assumes that a $-5/3$ power law of velocity spectra is a sufficient condition for the existence of an ISR as an approximation.

2.4.1 Mixed layer

Figure 2.1 presents observed velocity spectra after Kaimal et al. (1976). f_i is defined by $f_i = nZ_i/U$, where $U = U(z)$ is the mean speed at the height where the measurement was taken and n is the frequency of signals in Hertz. All spectra collapse into a single curve in the ISR ($f_i \geq 20$ for u and v, and varying with z/Z_i for w), but at lower frequencies the curves separate as a function of z/Z_i. It is also seen that the $-2/3$ laws[9] extend to lower frequencies as the height z/Z_i increases for all three spectra.

To find the spectral density as a function of eddy size, one must interpret f_i, the normalized frequency of the time series measured at a fixed point in the ABL, as meaning wavenumber or wavelength of the turbulent eddies. Since the measurements of turbulence spectra are based on the Taylor hypothesis which assumes that "frozen turbulent eddies" are passing the anemometer, n/U can therefore be interpreted as wavenumber $k/(2\pi)$, namely,

$$\frac{n}{U} = \frac{k}{2\pi}.$$

Replacing n by f_i yields

$$f_i = \frac{kZ_i}{2\pi},$$

[9]Traditionally, turbulence spectra in the ABL are plotted as $nS(n)$ vs. n in log-log coordinates; if $S(n)$ follows a $-5/3$ power law, $nS(n)$ will exhibit a $-2/3$ power law.

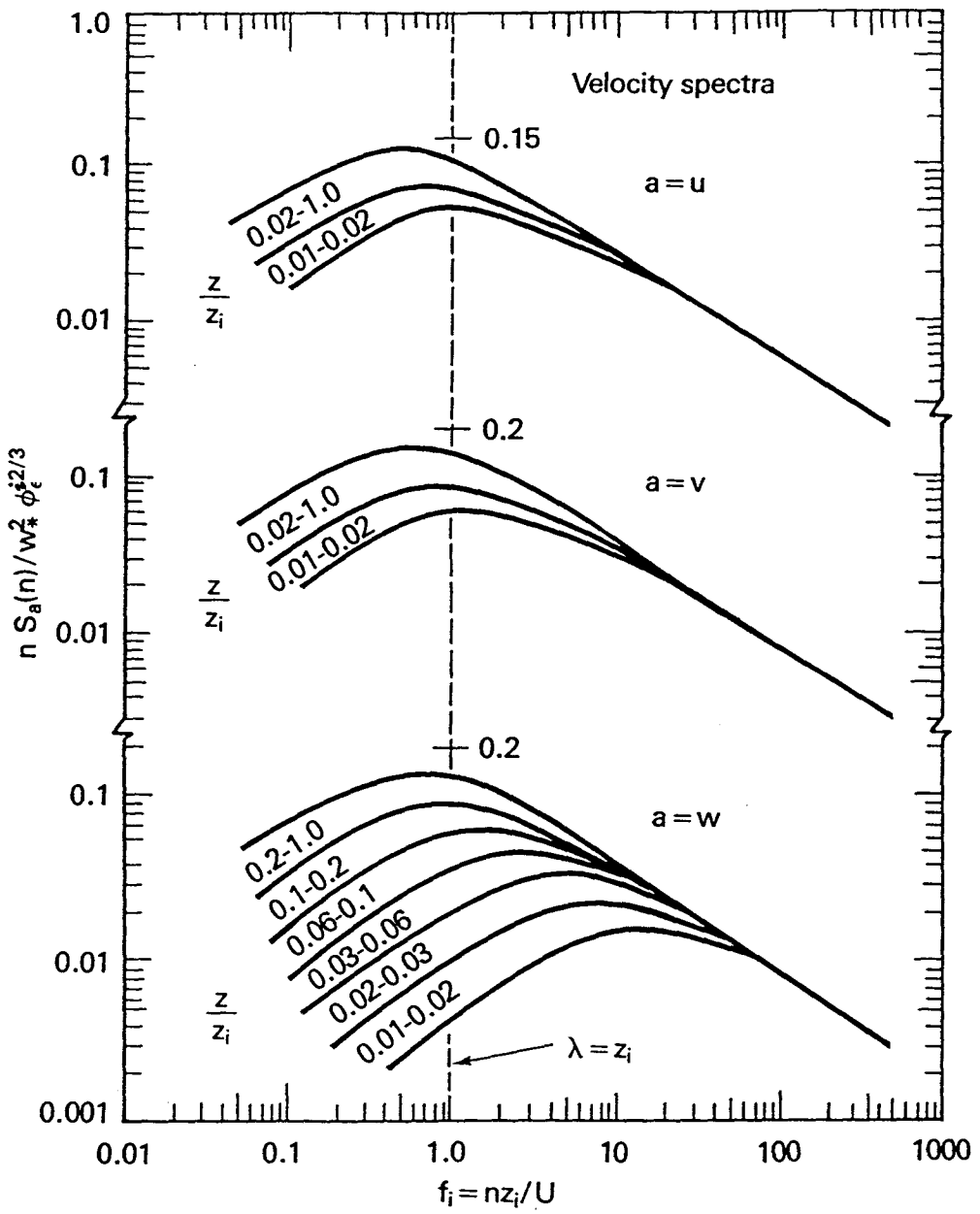

Figure 2.1: Universal curves for velocity spectra expressed in ML similarity coordinates. The function $\phi_\epsilon^i (= \kappa Z_i \epsilon / u_*^3)$ in the spectral normalization is the dimensionless energy dissipation rate. (After Kaimal *et al.*, 1976).

which is the dimensionless wavenumber (normalized by $1/Z_i$). By introducing the wavelength $\lambda = 2\pi/k$, one obtains

$$f_i = \frac{Z_i}{\lambda}. \tag{2.107}$$

Therefore, for a value of $f_i \approx 5$, for example, the corresponding wavelength is about $\lambda \approx 0.2Z_i$. The value of f_i at which the ISR starts is denoted by $f^{(c)}_{i,u_i}$, and the value of corresponding wavelength by $\lambda^{(c)}_{i,u_i}$, in which u_i is referred to as u, v or w, for $i = 1, 2, 3$.

Some useful information is provided by figure 2.1. For the power spectra of u and v, small variations with z/Z_i are found. This is the reason that Kaimal *et al.* only classified the spectra into two categories: $z/Z_i \in [0.01, 0.02]$ and $z/Z_i \in [0.02, 1.0]$. The difference in the peak values[10] is not significant, which implies that the typical size of the (energy-containing) horizontal velocity fluctuations is less influenced by the wall (compared with that of w). The value of $f^{(c)}_{i,u}$ or $f^{(c)}_{i,v}$ indicated by the figure is about 20, corresponding to

[10]Most of measured turbulence spectra are presented as $fS_a(f)$ vs. f in log-log coordinates. This presentation has the advantage of showing the inertial subrange of velocity spectra as a $-2/3$ line on the graph. Unfortunately, the area under the curve is no longer proportional to the corresponding velocity variance (Stull, 1988). Furthermore, the peak of the spectrum associated with the production of turbulence and usually the largest eddy sizes is not clear from such a presentation.

It is proved here that **for $fS_a(f)$ vs. f under log-log coordinates, the location of peak value for $S_a(f)$ is at the place where the curve has a slope of 1.**

At the peak value of $S_a(f)$, it suffices

$$\frac{dS_a(f)}{df} = 0. \tag{2.108}$$

Let

$$x = \ln(f) \qquad \text{and} \qquad F(x) = \ln(fS_a(f)). \tag{2.109}$$

Taking derivative with respect to f for both sides of the second equation in (2.109) yields:

$$F'(x)\frac{dx}{df} = \frac{1}{fS_a(f)}[S_a(f) + fS_a'(f)]. \tag{2.110}$$

Using (2.108), one obtains

$$F'(x) = 1. \tag{2.111}$$

It is therefore concluded that the frequency of the peak value of $S_a(f)$ is located at the left-side of the peak value of $fS_a(f)$.

$\lambda_{i,u}^{(c)}$ or $\lambda_{i,u}^{(c)} \approx 0.05Z_i$; but in most part of the mixed layer (ML) where $z/Z_i \in [0.02, 1.0]$ it seems to be a good approximation that $f_{i,u}^{(c)}$ or $f_{i,v}^{(c)} \approx 10$ which corresponds to $\lambda_{i,u}^{(c)}$ or $\lambda_{i,v}^{(c)} \approx 0.1Z_i$. As seen in the figure, however, the power spectra of w show a wide spread with z/Z_i and the position of the spectral peak shifts to increasingly lower values of λ as z/Z_i deceases. The value of $f_{i,w}^{(c)}$ varies with z/Z_i and shifts to the larger values as one approaches the surface. Table 2.1 gives a list of approximate values of $f_{i,u}^{(c)}$, $f_{i,v}^{(c)}$, $f_{i,w}^{(c)}$,

Table 2.1: Values of $f_{i,u}^{(c)}$, $f_{i,v}^{(c)}$, $f_{i,w}^{(c)}$, $\lambda_{i,u}^{(c)}/Z_i$, $\lambda_{i,v}^{(c)}/Z_i$ and $\lambda_{i,w}^{(c)}/Z_i$ as functions of z/Z_i.

z/Z_i	$f_{i,u}^{(c)}$	$\lambda_{i,u}^{(c)}/Z_i$	$f_{i,v}^{(c)}$	$\lambda_{i,v}^{(c)}/Z_i$	$f_{i,w}^{(c)}$	$\lambda_{i,w}^{(c)}/Z_i$
0.2 - 1.0					10	0.1
0.1 - 0.2					10	0.1
0.06 - 0.1	10	0.1	10	0.1	10-20	0.05
0.03 - 0.06					20-30	0.03-0.05
0.02 - 0.03					30-50	0.02-0.03
0.01 - 0.02	20	0.05	20	0.05	50-70	0.014-0.02

$\lambda_{i,u}^{(c)}/Z_i$, $\lambda_{i,v}^{(c)}/Z_i$ and $\lambda_{i,w}^{(c)}/Z_i$ as functions of z/Z_i.

The grid spacing can then be determined by the observational information provided by figure 2.1. In the horizontal directions, if one takes the largest wavelength of the inertial subrange eddies as the marginal value, $0.1Z_i$, and a typical value of Z_i as 1000 m, then the largest wavelength of the horizontal velocity fluctuations in the ISR is about 100 m. This determines that the grid size must be equal to or smaller than 50 m, because at least two mesh points are needed to resolve a wave.

In the vertical direction, it has already been shown that the value of $f_{i,w}^{(c)}$ (therefore the value of $\lambda_i^{(c)}$) varies significantly with height in the ABL. A non-uniform mesh will therefore be the best choice in the vertical direction. For example, in the region of $z/Z_i \in [0.2, 1.0]$, Δ_z can be chosen as about $0.5\lambda_{i,w}^{(c)} \approx 0.1Z_i$ (assuming that $f_{i,w}^{(c)} \approx 5$); in

the region of $z/Z_i \in [0.01, 0.02]$, Δ_z can be chosen as about $0.5\lambda_{i,w}^{(c)} \approx 0.005Z_i$ (assuming that $f_{i,w}^{(c)} \approx 100$). In consequence, using the value of Z_i of 1000 m, the former region will adopt $\Delta_z \approx 100$ m and the latter region will adopt $\Delta_z \approx 5$ m.

2.4.2 Surface layer

Generalized spectral curves for u, v and w in the ASL are shown in figure 2.2 obtained by Kaimal et al. (1972). The curves for $z/L = 0$ (the neutral case) are of interest. The value of f at which the ISR starts is denoted by $f_{u_i}^{(c)}$, and the value of corresponding wavelength by $\lambda_{s,u_i}^{(c)}$. No matter whether the neutral limit is taken on the stable side ($z/L > 0$) or on the unstable side ($z/L > 0$), the curves collapse to a universal line in the ISR. The value of $f_{s,u}^{(c)}$ in the neutral case is about 0.5. A big difference can be seen in the value of $f_{s,v}^{(c)}$ between the ASL here and the ML discussed above. In the ML, $f_{i,v}^{(c)} \approx f_{i,u}^{(c)}$; in the ASL, as shown in figure 2.2, a larger value of $f_{s,v}^{(c)} \approx 1$ is found, and an approximated value of $f_{s,w}^{(c)}$ is also about 2.

Based on the observational values of $f_{s,u}^{(c)}$, $f_{s,v}^{(c)}$ and $f_{s,w}^{(c)}$, one obtains the maximum wavelengths of the "ISR eddies":

$$\lambda_{s,u}^{(c)} \approx \frac{z}{0.5} = 2z, \tag{2.112}$$

$$\lambda_{s,v}^{(c)} \approx \frac{z}{1} = z, \tag{2.113}$$

$$\lambda_{s,w}^{(c)} \approx \frac{z}{2} = 0.5z. \tag{2.114}$$

Notice that all wavelengths are linearly proportional to the height z. It is impossible to design a mesh that has variant Δ_x and Δ_y changing with height. Therefore, it is inevitable to include some of the larger eddies outside of the ISR into the SGS model as z approaches to the surface. This basically violates the ISR rule. However, one can examine how serious the violation is. It is assumed that a uniform horizontal mesh

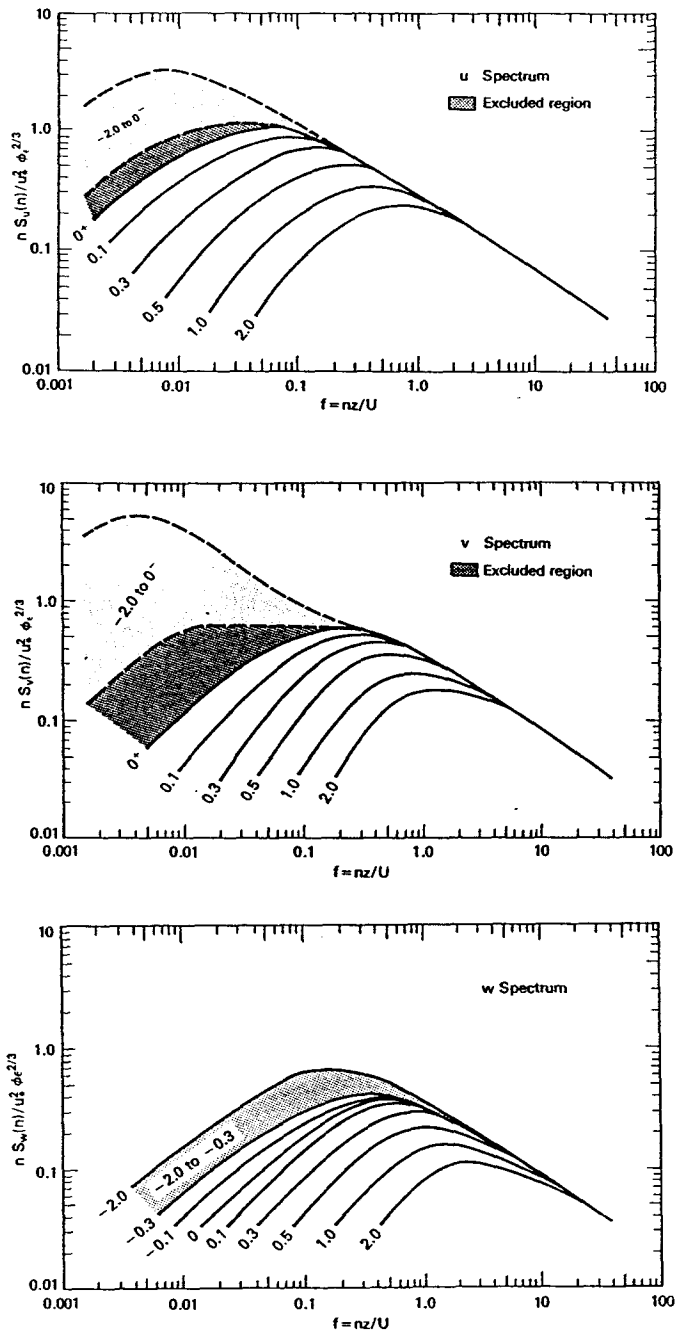

Figure 2.2: Universal curves for velocity spectra expressed in SL similarity coordinates. The function $\phi_\epsilon (= \kappa z \epsilon / u_*^3)$ in the spectral normalization is the dimensionless energy dissipation rate. (After Kaimal *et al.*, 1972).

spacing Δ_x, Δ_y and Δ_z are adopted. The shortest wavelength it can resolve is $2\Delta_x$; therefore, if $2\Delta_x = \lambda_{s,u}^{(c)}$, from (2.112), one obtains

$$z_c(u) \approx \Delta_x, \tag{2.115}$$

where $z_c(u)$ represents the height above which the largest size of u fluctuations in the ISR can be resolved by the mesh. Similar results can be obtained for the velocity fluctuations of v and w, from (2.113) and (2.114), respectively:

$$z_c(v) \approx 2\Delta_y, \tag{2.116}$$

$$z_c(w) \approx 4\Delta_z. \tag{2.117}$$

It is therefore ensured that, from (2.115), (2.116) and (2.117), the requirements of the ISR rule can be achieved in the region where $z > z_c = \max\{z_c(u_i), i = 1,2,3\} = \max\{\Delta_x, 2\Delta_y, 4\Delta_z\}$.

2.4.3 Grid spacing and Domain size

In the present simulations, the typical horizontal grid spacing of 60 m $\times$ 30 m is adopted as the reference grid specification for most runs (see table 3.4 on page 66). To resolve turbulent eddies in the ASL, the present study specifies the first vertical grid spacing of 2 m. The vertical grid spacing is non-uniform, given by an expansion rate of 1.2 up to a maximum grid spacing of 60 m (see table 2.2). Compared with the results discussed above, the resolution in the horizontal directions is about on the margin of the requirement of the ISR rule in the ML for the grid size. In the ASL, however, from (2.115) and (2.116), it yields that $z_c(u) \approx 60$ m and $z_c(v) \approx 60$ m. The effects of grid spacing on LES results will be shown in chapter 3 and chapter 4. As for the resolution in the vertical direction, an almost uniform grid spacing of 60 m in the ML is smaller than the value of 100 m, required by the ISR rule. In figure 2.3, some data in table 2.1 are drawn:

Table 2.2: Specification of the grid spacings in the z direction. i denotes the grid number along vertical direction; $z(i)$ is the height of i-th vertical grid; $\Delta_z(i) = z(i+1) - z(i)$ is the grid spacing in the vertical direction.

i	1	2	3	4	5	6	7	8	9	10	11
$z(i)$	1.0	3.1	5.8	8.9	12.7	17.3	22.7	29.3	37.1	46.5	57.8
$\Delta_z(i)$	2.1	2.6	3.2	3.8	4.5	5.5	6.5	7.8	9.4	11.3	13.6
i	12	13	14	15	16	17	18	19	20	21	22
$z(i)$	71.4	87.7	107.2	130.6	158.8	192.5	233.0	281.8	340	400	460
$\Delta_z(i)$	16.3	19.5	23.4	28.1	33.8	40.5	48.8	57.2	60.0	60.0	60.0
i	23	24	25	26	27	28	29	30	31	32	33
$z(i)$	520	580	640	700	760	820	880	940	1000	1060	1120
$\Delta_z(i)$	60.0	60.0	60.0	60.0	60.0	60.0	60.0	60.0	60.0	60.0	60.0
i	34	35	36	37	38	39	40	41	42	43	44
$z(i)$	1180	1240	1300	1360	1420	1480	1540	1600	1660	1720	1780
$\Delta_z(i)$	60.0	60.0	60.0	60.0	60.0	60.0	60.0	60.0	60.0	60.0	60.0
i	45	46	47	48	49	50					
$z(i)$	1840	1900	1960	2020	2080	2140					
$\Delta_z(i)$	60.0	60.0	60.0	60.0	60.0						

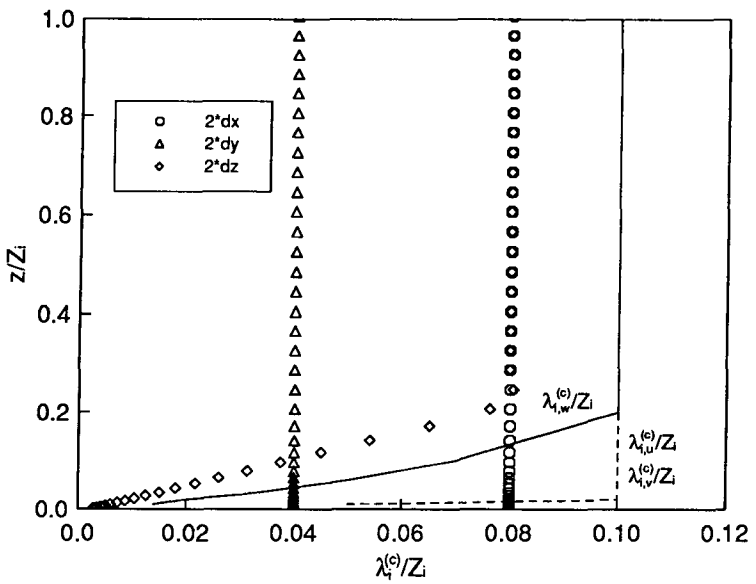

Figure 2.3: Profiles of $\lambda_i^{(c)}/Z_i$ as function of z/Z_i. Solid line represents the value of $\lambda_{i,w}^{(c)}/Z_i$ as a function of z/Z_i, while dashed line represents the value of $\lambda_{i,u}^{(c)}/Z_i$ or $\lambda_{i,v}^{(c)}/Z_i$ as a function of z/Z_i. Diamonds denote the values of $2\Delta_z/Z_i$, circles denote the values of $2\Delta_x/Z_i$ and the triangles denote the values of $2\Delta_y/Z_i$.

the solid line represents the value of $\lambda_{i,w}^{(c)}/Z_i$ as a function of z/Z_i, while the dashed line represents the value of $\lambda_{i,u}^{(c)}/Z_i$ or $\lambda_{i,v}^{(c)}/Z_i$ as a function of z/Z_i. Any point $(\lambda_i^{(c)}/Z_i, z/Z_i)$ located above or to the left of the lines corresponds to a grid spacing at z/Z_i which falls into the ISR of respective turbulence component. Therefore, $2\Delta_z/Z_i$ should be assigned above or to the left of the solid line, while $2\Delta_x/Z_i$ and $2\Delta_y/Z_i$ should be assigned above or to the left of the dashed line. In this figure, the diamonds in figure 2.3 represent the values of $2\Delta_z/Z_i$ adopted in this study,[11] which should be above or to the left of the solid line to meet the requirement of the ISR rule; the circles represent the values of $2\Delta_x/Z_i$ and the triangles represent the values of $2\Delta_y/Z_i$, which should be above or to the left of the dashed line to meet the requirement of the ISR rule. Figure 2.3 shows that the above-mentioned specification of grid spacing is satisfactory to resolve the ISR eddies in

[11]The value of Z_i is taken as 1500 m, which is the typical height of a CBL in summertime (Garratt, 1992).

most part of the CBL except very close to the surface.

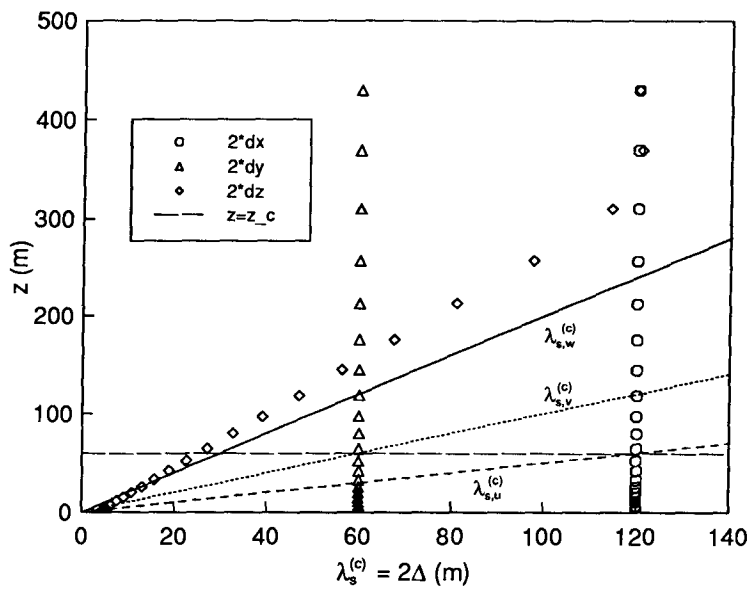

Figure 2.4: Profiles of $\lambda_s^{(c)}$ as function of z. Solid line represents the value of $\lambda_{s,w}^{(c)}$ as a function of z, dotted line represents the value of $\lambda_{s,v}^{(c)}$, and dashed line represents the value of $\lambda_{s,u}^{(c)}$. Diamonds denote the values of $2\Delta_z$, circles the values of $2\Delta_x$ and the triangles the values of $2\Delta_y$.

For the ASL, figure 2.4 shows the requirements for wavelengths by the ISR rule, i.e., equation (2.112), (2.113) and (2.114). The solid line represents the value of $\lambda_{s,w}^{(c)}$ as a function of z, the dotted line represents the value of $\lambda_{s,v}^{(c)}$, and the dashed line represents the value of $\lambda_{s,u}^{(c)}$. The regions above these lines are the ones which fall into the ISR of respective turbulence component. For the grid sizes the present work adopts, the same symbols as those in figure 2.3 are used to denote $2\Delta_x$, $2\Delta_x$ and $2\Delta_z$. For the x-component, $2\Delta_x$ (circles) do not fall into the inertial subrange unless $z \geq 60$ m; for the y-component, $2\Delta_x$ (triangles) do not fall into the inertial subrange unless $z \geq 60$ m; for the z-component, $2\Delta_z$ (diamonds) do not fall into the inertial subrange unless $z \geq$ about 40 m. It is thus concluded that when $z \geq 60$ m or so, the grid configuration mentioned above satisfies the ISR rule.

In section 2.2.3 on page 33, the requirements for the domain size were discussed in detail. The major conclusion is, in order to take into account the largest possible eddies, one must choose $D_x \sim h$ and $D_y \sim h$. Further constraints on the size of D_x and D_y are:

$$D_x \geq \mathcal{L}, \text{ and } D_y \geq \mathcal{L},$$

where $\mathcal{L}$ is the order of integral length scales.

To limit the computational effort, a relatively small number of grid points was used, namely, $24 \times 24 \times 50$, $32 \times 32 \times 50$ or $64 \times 64 \times 50$. These correspond to horizontal dimensions of 1440 m $\times$ 720 m, 2100 m $\times$ 1050 m or 3840 m $\times$ 1920 m, respectively. The vertical dimension of the calculation domain is 2140 m. Limited by total number of grids, LES cannot resolve both large and small eddies. To take into account the eddies in the ISR, LES has to lose its resolution of the largest eddies whose sizes are proportional to the ABL depth; to take into account those largest eddies, LES has to lose its resolution of small eddies that reside in the ISR. Previous LESs of the ABL only paid attention to those largest eddies, ignoring the resolution of "ISR eddies". For example, Moeng (1984) adopted $\Delta_x = \Delta_y = 156$ m and an equal value of $\Delta_z = 40$ m to simulate a CBL. Mason and Thomson (1987) conducted LESs of the neutral ABL and used $\Delta_x = 600$m, $\Delta_y = 300$ m and $\Delta_{z,1} = 11$ m in his case A, where $\Delta_{z,1}$ is the first vertical grid spacing, $\Delta_x = 150$m, $\Delta_y = 75$ m and $\Delta_{z,1} = 6$ m in case B, and $\Delta_x = 75$m, $\Delta_y = 37.5$ m and $\Delta_{z,1} = 4$ m in case C. The present study adopts relatively small grid sizes in order to resolve turbulence in the USL and it inevitably, but not seriously, loses resolution of the large eddies.

The criteria for a LES are listed as follows:

CR1 grid size must fall into the ISR of the turbulence so that the Smagorinsky SGS model can be employed properly;

CR2 Re_{SM} must be larger than $Re_{SM,cr}$ so that the model runs in turbulent regime and the behavior of RS fields is turbulent;

CR3 C_s must be large enough so as to eliminate grid-mode TKE[12] accumulation.

As long as the grid spacing is determined under the first criterion **CR1**, the second criterion **CR2** can be achieved either by increasing the number of grids, or by reducing the value of C_s while checking if the third criterion **CR3** is satisfied.

It is interesting to examine such a simulation: its domain size falls into the ECR, but its grid spacing is larger than the size of eddies in the inertial subrange due to limitation of the total number of grids. To satisfy **CR2**, the only way is to reduce the value of C_s, while it may conflict with **CR3**. Figure 2.1 and figure 2.2 show that the order differences between the largest ECR eddies and the largest ISR eddies are about two decades, noticing that the frequency of the peak value of S_a is smaller than that of nS_a.[13] In other words, if grid spacing falls into the ISR and the domain size includes the most-energetic eddies, D/Δ will be at least of the order of 10^2. With $C_s = 0.2$, say, the value of Re_{SM} is about 250,000.

Another simulation is also interesting: **CR1** is met, but the domain size is not large enough to include all ECR eddies. D/Δ_0 in this case is also small owing to the limitation of possible grids and it causes a small Re_{SM}. Reducing the value of C_s can obtain a larger value of Re_{SM} so as to meet **CR2**, but it may violate **CR3**.

[12]Grid-mode TKE is the TKE component whose wavelength is 2Δ, where Δ is the grid spacing.
[13]see the footnote on page 44.

Chapter 3

Large Eddy Simulation of a Neutral Atmospheric Boundary Layer

3.1 Scalings and dimensional analysis

In this chapter, a horizontally homogeneous ABL under adiabatic and barotropic conditions is investigated by LES. The surface heat flux and evaporation are taken as zero so that conditions are neutral; the ABL is in the Northern Hemisphere; there is no thermal wind and no mean streamline curvature and the surface is homogeneously rough, with a constant length scale z_0; there is no cloud, no moisture in the ABL; it is further assumed that the wind above the ABL is geostrophic, determined by the balance between the horizontal pressure gradient and the Coriolis force; for simplicity, the geostrophic wind is taken to be along the x-axis of LES model.

The most important dynamical characteristic of the whole ABL is the balance between the Coriolis force term $-f(G_j - u_j)\epsilon_{ij3}$ (see equation (2.99)) and the vertical momentum flux gradient, which results in a length scale related to the depth of the layer. The ABL under this situation is also called *the Ekman Layer*, because Ekman provided an analytic solution for a laminar model for it (see equation (2.79) and (2.80)). The development of the theoretical analysis on this topic had been slow for several decades, partially because of a lack of applications and partially because there were no enough experimental data for the entire ABL. The situation with regard to data acquisition has gradually changed in the last two and three decades, but there are still demands for more data and for less scattered data. The surface layer, in which fluxes do not deviate too far from their

surface values and where the shear is large and the generation of TKE the greatest, is about 10 per cent of the ABL depth. Measurements in this layer are relatively attainable and have been carried out frequently, which stimulates the advancement of theoretical analysis of the ASL (Sorbjan, 1989).

3.1.1 Laminar Ekman layer

Consider a simple situation in which the flow is steady, there is no turbulence, no variation on the horizontal plane, and $w = 0$. Its solution is given by (2.79), (2.80) and (2.81); they are re-written here with ˆ dropped:

$$U = U_g - e^{-\pi z/h_\nu}(U_g \cos \pi \frac{z}{h_\nu} + V_g \sin \pi \frac{z}{h_\nu}), \tag{3.1}$$

$$V = V_g - e^{-\pi z/h_\nu}(V_g \cos \pi \frac{z}{h_\nu} - U_g \sin \pi \frac{z}{h_\nu}), \tag{3.2}$$

$$h_\nu = \pi\sqrt{2\nu/f}, \tag{3.3}$$

where the length scale h_ν represents the height of the laminar Ekman layer. Since $\nu \approx 1.5 \times 10^{-5}\ m^2 s^{-1}$ and $f = 10^{-4} s^{-1}$, the height of the laminar Ekman layer $h_\nu \approx 1.72$ m. One can assume a very simple EAM for a turbulent Ekman layer by replacing ν with an effective *constant eddy viscosity* ν_e. If $\nu_e \approx 10\ m^2 s^{-1}$ and $f = 10^{-4}\ s^{-1}$, then $h_{\nu,e} \approx 1400$ m. This gives a way to estimate the order of the effective eddy viscosity through the height of the turbulent Ekman layer. But the solution given by (3.1) to (3.3) does not agree well with observations. For example, the angle between the shear stress vector and the geostrophic wind vector, α_τ, can be derived from (3.1) and (3.2)[1]:

$$\alpha_\tau = \arctan \frac{\tau_{vw}}{\tau_{uw}} = \arctan \frac{\nu \partial V/\partial z}{\nu \partial U/\partial z} = \arctan \frac{\cos(\pi z/h_\nu) - \sin(\pi z/h_\nu)}{\cos(\pi z/h_\nu) + \sin(\pi z/h_\nu)}. \tag{3.4}$$

[1]For simplicity, the geostrophic wind is taken to be along x-axis; i.e., $U_g = G$, $V_g = 0$.

As $z \to 0$, one obtains

$$\alpha_{\tau,0} = \frac{\pi}{4}. \tag{3.5}$$

However, in the turbulent Ekman layer, observations consistently suggest a much smaller value of $\alpha_{\tau,0}$ than $\pi/4$ (Brown, 1974). It is shown that the assumption of the EAM model with a constant eddy viscosity is too simple to represent the complicated turbulent Ekman layer.

3.1.2 Scaling in the turbulent Ekman layer

The solutions of a laminar Ekman layer, (3.1) and (3.2), are independent of the Reynolds number $Re = Gh_\nu/\nu = \sqrt{2}\pi G/\sqrt{\nu f}$. This does not imply that the solutions are unique for any value of the Reynolds number, recalling that equation (2.76) is a simplified form of the full equation (2.74). As the Reynolds number is larger than a critical value, say Re_{cr}, the solutions given by (3.1) and (3.2) becomes unstable and cannot be observed in a real ABL. When Re is large enough, say $Re > Re_t$, a turbulent Ekman layer is fully developed, and its scaling is different from that of the laminar Ekman layer.

Smooth surface

When the ground surface is smooth, the molecular viscosity coefficient ν is not important in momentum transferring processes of the turbulent Ekman layer except in the viscous sublayer in the near-surface region. The independent external parameters are: the Coriolis parameter f, the molecular viscosity coefficient ν and the friction velocity u_*. An asymptotic matching processes applied to a turbulent flow can yield approximate solutions. It is assumed that, in a turbulent Ekman layer with a smooth surface, when the Reynolds number is large enough, the whole layer is separated into two layers: the

outer layer, in which the effects of ν is omitted, and the *inner layer*, in which the effects of f is omitted.

Based on this assumption, independent external parameters[2] are f and u_* in the outer layer. Including any concerned variable ϕ and spatial variable z, the parameter group becomes $(\phi, z; f, u_*)$[3] , which involves two independent units: (L, T). Based on corollary 2 in appendix B, a single-variable function is obtained:

$$\frac{\phi}{L^{(o)\alpha} v^{(o)\beta}} = F^{(o)}(\frac{z}{L^{(o)}}),$$

where $L^{(o)} = u_*/f$, $v^{(o)} = u_*$, α and β are constants appropriate for dimensional homogeneity of the variable ϕ, and $F^{(o)}$ denotes an undetermined function. If $\phi = u$, then

$$\frac{u - U_g}{u_*} = F^{(o)}(\frac{z}{u_*/f}), \tag{3.6}$$

which is sometimes called *the velocity-defect law.*

In the inner layer, independent external parameters are ν and u_*. Including any concerned variable ϕ and spatial variable z, the parameter group becomes $(\phi, z; \nu, u_*)$, which involves two independent units: (L, T). Based on corollary 2 in appendix B, a single-variable function is also obtained:

$$\frac{\phi}{L^{(i)\alpha} v^{(i)\beta}} = F^{(i)}(\frac{z}{L^{(i)}}),$$

where $L^{(i)} = \nu/u_*$, $v^{(i)} = u_*$, and α and β are constants appropriate for dimensional homogeneity of the variable ϕ and $F^{(i)}$ denotes an undetermined function. If $\phi = u$, then

$$\frac{u}{u_*} = F^{(i)}(\frac{z}{\nu/u_*}), \tag{3.7}$$

which is referred to as *the law of the wall.*

[2]External parameters are referred to those global parameters which do not depend upon any spatial variable x_i nor upon temporal variable t.

[3]Semicolon is used to divide external parameters and other variables.

The velocity-defect law (3.6) and the law of the wall (3.7) can be *matched* in an overlapped region (Tennekes and Lumley, 1972). Let

$$z^{(i)} = \frac{z}{L^{(i)}} \qquad \text{and} \qquad z^{(o)} = \frac{z}{L^{(o)}}.$$

Taking derivatives with respect to z for (3.6) and (3.7), respectively, yields

$$\frac{du}{dz} = \frac{u_*^2}{\nu}\frac{dF^{(i)}}{dz^{(i)}}, \tag{3.8}$$

$$\frac{du}{dz} = f\frac{dF^{(o)}}{dz^{(o)}}. \tag{3.9}$$

Anticipating a logarithmic wind profile, (3.8) and (3.9) can be rearranged as:

$$\frac{z}{u_*}\frac{du}{dz} = z^{(i)}\frac{dF^{(i)}}{dz^{(i)}} = \mathcal{F}^{(i)}(z^{(i)}), \tag{3.10}$$

$$\frac{z}{u_*}\frac{du}{dz} = z^{(o)}\frac{dF^{(o)}}{dz^{(o)}} = \mathcal{F}^{(o)}(z^{(o)}), \tag{3.11}$$

where $\mathcal{F}^{(i)}$ and $\mathcal{F}^{(o)}$ are two undetermined functions, and thus

$$\mathcal{F}^{(i)}(z^{(i)}) = \mathcal{F}^{(o)}(z^{(o)}). \tag{3.12}$$

A double-limit process $z^{(i)} \to \infty$ and $z^{(o)} \to 0$ with a fixed z in the "*matched layer*" is taken. This limit process can be achieved by allowing the ratio of the inner variable $z^{(i)}$ to the outer variable $z^{(o)}$ to approach infinity:

$$\frac{z^{(i)}}{z^{(o)}} = \frac{u_*^2}{\nu f} = Re_*^2 \to \infty,$$

where $Re_* = u_*/\sqrt{\nu f}$. Under this limit process, "we will have a trivial result ($\mathcal{F}^{(i)}(z^{(i)})$, $\mathcal{F}^{(o)}(z^{(o)}) \to 0$, or ∞) *unless* $\mathcal{F}^{(i)}(z^{(i)})$, $\mathcal{F}^{(o)}(z^{(o)})$ become *asymptotically independent* of their arguments in the limit process envisaged. Hence, to the first order approximation (3.10) and (3.11) must involve the same universal constant. It is concluded that for $z^{(i)} \gg 1$ and $z^{(o)} \ll 1$, the wind shear is

$$\frac{z}{u_*}\frac{du}{dz} = \frac{1}{\kappa}. \tag{3.13}$$

Here, κ is the von Kármán constant; its value has to be determined experimentally" (Tennekes and Lumley, 1972).

Rough surface

The exact same results can be obtained for a rough surface with a roughness length scale z_0. If ν/u_* is replaced by the roughness length z_0, and it is defined that

$$z^{(i)} = \frac{z}{L^{(i)}} = \frac{z}{z_0} \qquad \text{and} \qquad z^{(o)} = \frac{z}{L^{(o)}} = \frac{z}{u_*/f},$$

one obtains the same form as (3.10) and (3.11):

$$\frac{z}{u_*}\frac{du}{dz} = z^{(i)}\frac{dF^{(i)}}{dz^{(i)}} = \mathcal{F}^{(i)}(z^{(i)}), \tag{3.14}$$

$$\frac{z}{u_*}\frac{du}{dz} = z^{(o)}\frac{dF^{(o)}}{dz^{(o)}} = \mathcal{F}^{(o)}(z^{(o)}). \tag{3.15}$$

Then the double-limit process $z^{(i)} \to \infty$ and $z^{(o)} \to 0$ is taken under the condition

$$\frac{z^{(i)}}{z^{(o)}} = \frac{u_*}{fz_0} = Ro_* \to \infty, \tag{3.16}$$

where Ro_* is the surface Rossby number based on u_*. The analysis also yields the logarithmic velocity profile involving the von Kármán constant:

$$\frac{u}{u_*} = \frac{1}{\kappa}\ln\frac{z}{z_0} \qquad (z/z_0 \gg 1 \quad \text{and} \quad zf/u_* \ll 1). \tag{3.17}$$

3.1.3 Sufficient conditions for the logarithmic velocity profile

Much work has been done on the logarithmic wind profile in a wall-bounded turbulent flow. The logarithmic velocity profile occurs in a turbulent boundary layer (TBL) over a rough or smooth plate with no pressure gradient, in a turbulent pipe flow and also, in the ABL. No *a priori* justification has been given for the necessary and sufficient conditions of the logarithmic profile. Here, a review is given for some sufficient conditions.

Mixing length assumption

For a wall-bounded turbulent flow, Prandtl proposed a hypothesis that the eddy viscosity ν_e is proportional to a length scale, l, and the surface friction velocity, u_* (Schlichting, 1979, Chapter 19):

$$-\overline{u'w'} = \nu_e \frac{du}{dz}, \tag{3.18}$$

$$\nu_e \sim l u_*. \tag{3.19}$$

It was further assumed that

$$l = \kappa z, \tag{3.20}$$

where κ is a constant (the von Kármán constant) and z is the distance to the wall. An additional assumption is that there exists a "constant-stress" layer, $0 \leq z \leq h_s$, throughout which the shear stress is approximately constant, i.e.,

$$-\overline{u'w'} = -\overline{u'w'}_0 = \rho u_*^2, \tag{3.21}$$

where $\overline{u'w'}_0$ is the shear stress at the wall. Substitution of (3.19) to (3.21) into (3.18) gives

$$\frac{du}{dz} = \frac{u_*}{\kappa z}, \tag{3.22}$$

and its integration yields a logarithmic velocity profile:

$$\frac{u}{u_*} = \frac{1}{\kappa} \ln z + \text{constant}. \tag{3.23}$$

As a conclusion, this set of sufficient conditions for a logarithmic velocity profile is:

- eddy viscosity assumption (3.18);
- Prandtl's mixing length hypothesis (3.19) and (3.20);
- assumption of a "constant-stress" layer.

Asymptotic matching theory

In section 3.1.2, the application of asymptotic matching theory applied to the Ekman layer yielded another set of sufficient conditions for a logarithmic velocity profile:

- the Reynolds number (or equivalently the surface Rossby number in a rough-surface case) is sufficiently large;
- ν (or z_0 in a rough-surface case) is dropped from the external parameter group in the outer layer; f is dropped from the external parameter group in the inner layer;
- there exists an overlap layer where the asymptotic matching process is applied.

Dimensional analysis

It is possible to apply a dimensional analysis to derive the logarithmic profile. Taking a smooth surface as an example. It is assumed that ν is excluded from the external parameter group in the outer layer, and f is excluded from the external parameter group in the inner layer. An additional assumption is that as the Reynolds number exceeds a critical value, there exists an overlap layer where both assumptions of the inner layer and the outer layer are met. This implies that in the overlap layer *both* ν and f are excluded from the external parameter group, leaving only one external parameter, u_*, which represents the momentum flux through the layer. Therefore, the only possible functional form for the velocity profile can be written as:

$$u = F(u_*, z) \qquad \text{or} \qquad \mathcal{F}(u, u_*, z) = 0. \tag{3.24}$$

While the functional form of these three variables does not imply a logarithmic relation between u and z. This relation can be derived by writing a functional form as follows:

$$\frac{du}{dz} = F(u_*, z) \qquad \text{or} \qquad \mathcal{F}(\frac{du}{dz}, u_*, z) = 0. \tag{3.25}$$

Two independent physical units, (L,T), are involved. Based on theorem 1 in appendix B, one obtains

$$\mathcal{F}(\frac{z}{u_*}\frac{du}{dz}) = 0, \tag{3.26}$$

which then obviously yields a logarithmic velocity profile:

$$\frac{z}{u_*}\frac{du}{dz} = \text{constant}.$$

3.2 Some measurements

Measurements of the ASL below 30 m have been conducted in the most detail. The tasks in this layer include measurement of the velocity profile, value of the von Kármán constant, variances (or standard deviations) of the velocity fluctuations, shear stresses, and power spectra of the velocity fluctuations. Notable measurement programs are: The 1953 Great Plains Turbulence field Program (Lettau and Davidson, 1957), the 1967 Wangara Experiment (Clarke et al., 1971), the 1968 Kansas Field Program (Businger et al., 1971; Haugen, Kaimal and Bradley, 1971), the 1973 Minnesota Experiment (Izumi and Caughey, 1976) and the 1976 Australian International Turbulence Comparison Experiment (Dyer, Garratt and Francey, 1981; Garratt et al., 1979). These and numerous other observational studies have provided substantial experiment data and a significant increase of our knowledge of the ABL, including the ASL.

Logarithmic wind profile and the von Kármán constant

Most observations showing logarithmic velocity profiles were carried out below 30 m or so. It is shown, however, by Thuillier and Lappe (1964) and Carl, Tarbell and Panofsky (1973) that logarithmic velocity profiles have been observed up to 150 m. Unfortunately, no well-instrumented towers are located over completely homogeneous terrain in the

world. Most such towers are built either in urban areas or in places surrounded by complex terrain. For this reason there is no enough data to test the height of applicability of the logarithmic velocity profile.

Table 3.1: Estimates of the von Kármán constant κ from measurements

Author(s)	κ	Comment
Goddard (1970)	0.41	
Dyer & Hicks (1970)	0.41	Also see Dyer (1974)
Hicks (1970)	0.42($\pm$0.02)	No detail provided
Businger *et al.* (1971)	0.35	See, *e.g.*, Wieringa (1980)
Pruitt *et al.* (1973)	0.42	0.39 by Kondo & Sato (1982)
Frenzen(1973)	0.35($\pm$0.01)	$\alpha_u = 0.55$ was assumed
Frenzen(1974)	0.36($\pm$0.01)	See Garratt (1974)
Högström (1974)	0.35($\pm$0.03)	$\alpha_u = 0.55$ was assumed
Hicks (1976)	0.4	
Garratt(1977)	0.415($\pm$0.02)	inferred from C_f data
Wieringa (1980)	0.41	Re-analysis of the Kansas data used by Businger *et al.* (1971)
Francey & Garratt(1981)	0.38($\pm$0.04)	$\phi_m(\zeta) = (1 - 15.5\zeta)^{-1/4}$ was used
Shirasawa (1981)	0.42($\pm$0.03)	$\lvert\zeta\rvert \leq 0.1$ or 0.03
Kondo & Sato(1982)	0.39($\pm$0.03)	$\lvert R_i\rvert \leq 0.02$ or 0.05
Dyer & Bradley (1982)	0.385($\pm$0.021)	0.4 was suggested
Telford (1982)	0.37	"Theoretical Value"
Frenzen & Hart (1983)	0.41	$\alpha_u = 0.52$ was assumed
Högström (1985)	0.4($\pm$0.011)	0.36 suggested by Telford & Businger (1986)
Högström (1986)	0.39($\pm$0.01)	
Högström (1988)	0.4	
Zhang (1988)	0.4	
Frenzen & Vogel (1992)	0.38($\pm$0.017)	

As for the value of the von Kármán constant, measurements exhibit a great scatter. A chronological list of the value of κ is shown in table 3.1. In general, the values of κ fall in the range of 0.35 to 0.43. The large value of 0.43 has been frequently reported by

Russian atmospheric scientists. The low value of 0.35 was obtained by Businger et al. (1971) from the Kansas experimental data, which has been considered to be very carefully conducted. Among the various values of κ listed in table 3.1, some were evaluated from the measurements without adequate accounts of instrumental errors, and some approaches of the evaluation of κ are questionable.

Many authors such as Shirasawa (1981) and Kondo and Sato (1982) adopted the so-called "wind-profile approach"; assuming the boundary layer to be a near-neutral, and κ is calculated from the measured wind profile. In fact true neutrality rarely happens in the ABL. This approach, therefore, gives errors associated with the deviation from neutrality. According to Kondo and Sato (1982), a small deviation from neutrality can cause significant errors in the estimates of κ (see table 3.2, in which L, called the Monin-Obukhov length, is defined by (4.4).

Table 3.2: Relative errors of estimated value of κ due to deviation from neutrality when the wind profile approach is adopted (see Kondo and Sato, 1982).

$\zeta(= z/L)$	-0.061	-0.026	0.03	0.086
Error %	-17.6	-8.6	12.4	28.8

Other workers such as Frenzen (1973), Frenzen (1974) and Högström (1974) adopted the so-called "*dissipation (ϵ) approach*". This approach, however, starts with the TKE budget equation, assuming negligible pressure-velocity correlations and TKE redistribution, and under the condition of neutrality, it derives a formula for the von Kármán constant:

$$\kappa = \frac{u_*^3}{\epsilon z}, \tag{3.27}$$

where ϵ is the viscous energy dissipation rate. Here, the value of ϵ can be determined

from the ISR of the power spectra of velocity fluctuations. In this case, another universal constant, α_u, has to be measured. Again, as shown in table 3.3, a slight deviation from neutrality can give a significant effect on the estimated value of κ (Frenzen and Hart, 1983; Wyngaard and Cote, 1971).

Table 3.3: Relative errors of estimated value of κ due to deviation from neutrality when the dissipation (ϵ) approach is adopted (see Wyngaard and Cote, 1971).

$\zeta(=z/L)$	-0.05	-0.02	-0.01	0.01	0.02	0.05
Error %	10.30	5.60	3.50	24.50	37.90	68.20

Variances of the velocity fluctuations

In the ASL, the Coriolis parameter f is not important so that nondimensional variances of velocities at the surface, σ_u/u_* (i=1,2,3) are about constants. Observations in the ASL (Panofsky and Dutton, 1984) suggest that

$$\sigma_u/u_* = 2.39 \pm 0.03, \tag{3.28}$$

$$\sigma_v/u_* = 1.92 \pm 0.05, \tag{3.29}$$

$$\sigma_w/u_* = 1.25 \pm 0.03. \tag{3.30}$$

3.3 LES results for the upper surface layer

Specification of LES cases

Three types of domain size (see table 3.4) have been adopted to examine LES results of resolved turbulent statistics in the USL. For all LES cases, the geostrophic wind is

Table 3.4: Specification of domain size and grid spacing for LESs of a neutral ABL. D_x, D_y and D_z are domain sizes in the x, y and z direction, respectively; N_x, N_y and N_z are the grid numbers in the x, y and z direction, respectively; Δ_x and Δ_y are the grid spaings in the x and y direction, respectively; nn is a few digits that stand for the value of C_s.

Run	Domain	D_x(m)	D_y(m)	D_z(m)	N_x	N_y	N_z	Δ_x(m)	Δ_y(m)
N16Ann	A	960	480	2140	16	16	50	60	30
N24Ann	A	960	480	2140	24	24	50	40	20
N32Ann	A	960	480	2140	32	32	50	30	15
N24Bnn	B	1440	720	2140	24	24	50	60	30
N32Bnn	B	1440	720	2140	32	32	50	45	12.5
N24Cnn	C	3840	1920	2140	24	24	50	160	80
N64Cnn	C	3840	1920	2140	64	64	50	60	30

specified as:

$$(U_g, V_g) = (10 \text{ m/s}, 0). \tag{3.31}$$

It is shown later in this chapter that the height of the ABL h_E is about 1000 m if the geostrophic wind speed is 10 m/s. The largest domain, D, has the ratio $D_x/h_E \approx 4$ and $D_y/h_E \approx 2$, which allow the largest eddies to develop, while the smallest, A, cannot resolve these large eddies, but it produces fairly satisfactory results in the USL. In addition, under neutral conditions, those large eddies are of small magnitude[4], and will not play important roles in momentum transfer in the whole layer. Therefore, domain A may still be meaningful for LES of the USL.

The parameters for model runs are shown in table 3.5. The value of Re_{SM} is based on the length scale of domain size, $D = (D_x D_y h_E)^{1/3}$, and the typical grid size, $\Delta_0 = (\Delta_x \Delta_y \Delta_{z,typ})^{1/3}$, where $\Delta_{z,typ} = 0.5 \max\{\Delta_z(i)\} = 30$ m (see table 2.2 on page 49).

[4]LES of a whole neutral ABL by Mason and Thomson (1987) shows no evidence for *any distinctly roll-like motions* which are the largest eddies in the ABL. DNS conducted by Coleman, Ferziger and Spalart (1990) also confirmed this conclusion.

Table 3.5: Parameters for each run. N_x and N_y are the grid numbers in the x and y direction; N_{h_E} is the grid number in the vertical direction within the ABL; h_E is the height of the ABL; C_s is the Smagorinsky SGS model constant; $\Delta_0 = (\Delta_x \Delta_y \Delta_{z,typ})^{1/3}$ is the typical vertical grid size which is taken as 30 m; $D = (D_x D_y h_E)^{1/3}$; $Re_{SM} = [D/(C_s \Delta_0)]^{2/3}$; $Ro_D = U_g/(fD)$; z_0 is the roughness at the surface.

Run	N_x	N_y	N_{h_E}	h_E	C_s	Δ_0	D	Re_{SM}	Ro_D	z_0
N16A05	16	16	32	830	0.050	37.8	730	147500	138	0.10
N16A06	16	16	32	830	0.060	37.8	730	102400	138	0.10
N24A078	24	24	32	830	0.078	28.8	730	104100	138	0.10
N24A1	24	24	32	830	0.100	28.8	730	63300	138	0.10
N24A15	24	24	32	830	0.150	28.8	730	28100	138	0.10
N24A2	24	24	32	830	0.200	28.8	730	15800	138	0.10
N32A08	32	32	32	830	0.080	23.8	730	145200	138	0.10
N32A1	32	32	32	830	0.100	23.8	730	92900	138	0.10
N32A12	32	32	32	830	0.120	23.8	730	64500	138	0.10
N32A15	32	32	32	830	0.150	23.8	730	41300	138	0.10
N24B052	24	24	36	970	0.052	37.8	1000	255900	100	0.10
N24B06	24	24	36	970	0.060	37.8	1000	195200	100	0.10
N24B08	24	24	36	970	0.080	37.8	1000	109800	100	0.10
N24B1	24	24	36	970	0.100	37.8	1000	70300	100	0.10
N32B06	32	32	36	970	0.060	31.2	1000	286400	100	0.10
N32B08	32	32	36	970	0.080	31.2	1000	161100	100	0.10
N32B1	32	32	36	970	0.100	31.2	1000	103100	100	0.10
N32B12	32	32	36	970	0.120	31.2	1000	71600	100	0.10
N24C06	24	24	42	1080	0.060	72.7	2000	209700	50	0.10
N64C06	64	64	42	1080	0.060	37.8	2000	775300	50	0.10
N64C075	64	64	42	1080	0.075	37.8	2000	496200	50	0.10
N64C1	64	64	42	1080	0.100	37.8	2000	279100	50	0.10
N64C15	64	64	42	1080	0.150	37.8	2000	124000	50	0.10
N64C2	64	64	42	1080	0.200	37.8	2000	69800	50	0.10
N32B08z01	32	32	36	970	0.080	31.2	1000	161100	100	0.01
N32B08z05	32	32	36	970	0.080	31.2	1000	161100	100	0.05
N32B08z5	32	32	36	970	0.080	31.2	1000	161100	100	0.50

$Ro_D = U_g/fD$ is the domain Rossby number based on domain size D. Since U_g and f are fixed for all runs, the domain Rossby number is constant for fixed domain size, and varies with only domain size. h_E is the height of the neutral ABL. It is noted that h_E is adopted as a representation of characteristic length in the vertical direction. Its determination is based on shear stress profile in the whole ABL, and is given in section 3.4.1 on page 100.

Statistical averaging operator for LES output

As introduced before, the symbol $[\cdot]$ denotes an average over a horizontal plane, or, in the simulation domain, over $N_x \times N_y$ grid points in a horizontal plane. Hence, any variable can be decomposed into two parts, i.e., horizontal average and fluctuation:

$$\phi(t,x,y,z) = [\phi](t,z) + \tilde{\phi}(t,x,y,z). \tag{3.32}$$

The fluctuation part $\tilde{\phi}(t,x,y,z)$ carries information on RS turbulence, from which the LES results are derived. For example, $[\tilde{u}_i^2](t,z)$ $(i = 1,2,3)$ is RS variance of the velocity fluctuation; $[\tilde{u}_i\tilde{u}_j](t,z)$ $(i \neq j)$ is RS kinematic shear stress; *etc.*. Taking averages of $[\phi](t,z)$ over a vertical direction yields the domain-averaged quantity:

$$\{\phi\}(t) = \frac{1}{h}\int_0^h [\phi](t,z)dz, \tag{3.33}$$

which is a function of time. Another notation, $\langle\cdot\rangle$, is introduced here, which denotes an average over (i) the horizontal plane, and (ii) a time interval $[t_1, t_2]$:

$$\langle\phi\rangle(z) = \frac{1}{t_2 - t_1}\int_{t_1}^{t_2} [\phi](t,z)dt.$$

If the time interval, $t_2 - t_1$, is large enough to include all important scales in the problem and the time variation of quantities of interest is considered to be *stationary* within the time interval, such an averaged quantity is a statistical description of the vertical distribution of ABL turbulence.

The statistical results presented in this paper are taken according to the following procedure:

1st-moment quantities Variable is $\phi(t,x,y,z)$, for example. Two basic steps are necessary:

1. an instantaneous, horizontal average is taken to derive $[\phi](t,z)$.
2. a time average is taken to derive $\langle\phi\rangle(z)$:

$$\langle\phi\rangle(z) = \frac{1}{t_2 - t_1}\int_{t_1}^{t_2}[\phi](t,z)dt.$$

2nd(or higher)-moment quantities Variables are $\phi_1(t,x,y,z)$ and $\phi_2(t,x,y,z)$ (and $\phi_3(t,x,y,z)$...) , for example. Four basic steps are necessary:

1. an instantaneous, horizontal average is taken to derive $[\phi](t,z)$.
2. instantaneous fluctuations are derived from

$$\tilde{\phi}(t,x,y,z) = \phi(t,x,y,z) - [\phi](t,z).$$

3. an instantaneous, horizontal average is taken to derive $[\tilde{\phi}_1\tilde{\phi}_2](t,z)$ (or $[\tilde{\phi}_1\tilde{\phi}_2\tilde{\phi}_3](t,z)$).
4. a time average is taken to derive $\langle\tilde{\phi}_1\tilde{\phi}_2\rangle(z)$:

$$\langle\tilde{\phi}_1\tilde{\phi}_2\rangle(z) = \frac{1}{t_2 - t_1}\int_{t_1}^{t_2}[\tilde{\phi}_1\tilde{\phi}_2](t,z)dt$$

$$\text{(or} \qquad \langle\tilde{\phi}_1\tilde{\phi}_2\tilde{\phi}_3\rangle(z) = \frac{1}{t_2 - t_1}\int_{t_1}^{t_2}[\tilde{\phi}_1\tilde{\phi}_2\tilde{\phi}_3](t,z)dt).$$

Time scaling of the Coriolis force

Domain-averaged RS TKE is defined as

$$E_R(t) = \sum_{i=1}^{3}\frac{1}{2}\{\tilde{u}_i^2\}, \tag{3.34}$$

and the domain-averaged KE of mean velocity is defined as:

$$E_M(t) = \sum_{i=1}^{3} \frac{1}{2}\{[u_i]^2\}. \tag{3.35}$$

By ignoring the shear stress terms and the advection terms, a simplified model of momentum equations (2.74) can be written as

$$\frac{\partial u}{\partial t} = f(v - V_g), \tag{3.36}$$

$$\frac{\partial v}{\partial t} = -f(u - U_g). \tag{3.37}$$

If one assumes a solution of the form

$$u = U_g + u_0 e^{i\omega t}, \tag{3.38}$$

$$v = V_g + v_0 e^{i\omega t}, \tag{3.39}$$

where $i = \sqrt{-1}$, u_0 and v_0 are the amplitudes of the fluctuations and ω is the unknown frequency, substitution of (3.38) and (3.39) into (3.36) and (3.37) gives

$$i\omega u_0 = f v_0, \tag{3.40}$$

$$i\omega v_0 = -f u_0, \tag{3.41}$$

from which one obtains

$$\omega = f. \tag{3.42}$$

The frequency in (3.38) and (3.39) is therefore f, and the corresponding time period is $2\pi/f$. Figure 3.1 shows the time variation of $E_M(t)$ calculated from the case N16A06. The lower abscissa represents the real time simulated in seconds, and the upper abscissa is the corresponding CPU time in seconds on an IBM RISC 6000/560 workstation. It is noted that the period of the sinusoid variation in figure 3.1 is roughly equal to but

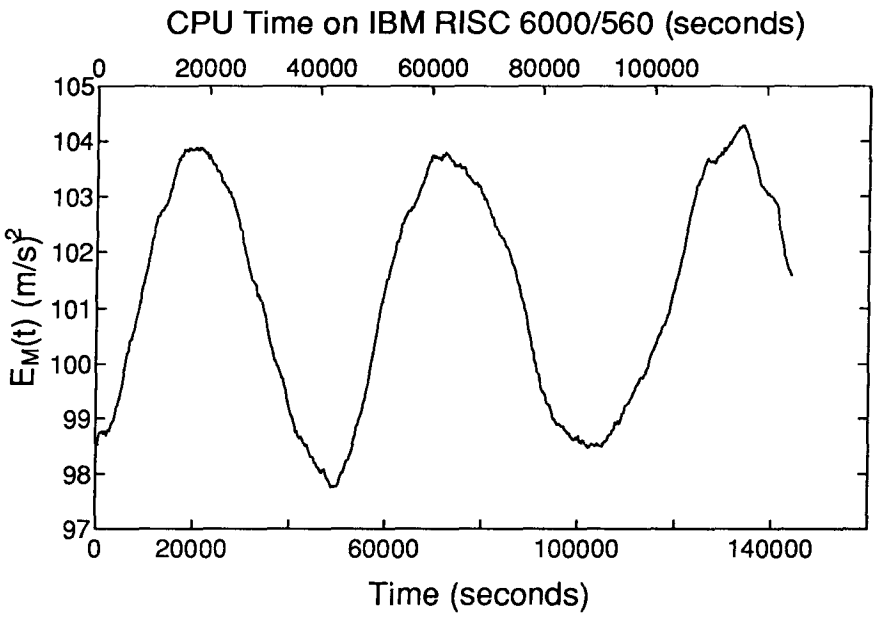

Figure 3.1: Time variation of the total KE averaged over the whole domain for case N16A06.

a little smaller than $2\pi/f \approx 6.28 \times 10^4$ seconds, and the magnitude of this variation is about 3% of mean KE.

After the initial perturbation, LES model runs until a statistically stationary state has been reached, as indicated by the time variation of domain integrated quantities. For example, RS TKE summed over the whole domain is one of the indicators. Figure 3.2 shows the time variation of domain-averaged RS TKE, $E_R(t)$, calculated from the case N16A06. The figure shows that $E_R(t)$ reaches a statistical steady state in a very short time after a randomly disturbed initial velocity field. The variation with a period of about $2\pi/f$ can not be seen clearly in the figure. As illustrated in figure 3.1, the amplitude of the variation is about 3 (m/s)^2, which is much greater than domain-averaged RS TKE, of the order of 0.04 (m/s)^2, which implies that the inertial variation is filtered by the averaging process involved in calculating $E_R(t)$. The statistics involving the horizontal components

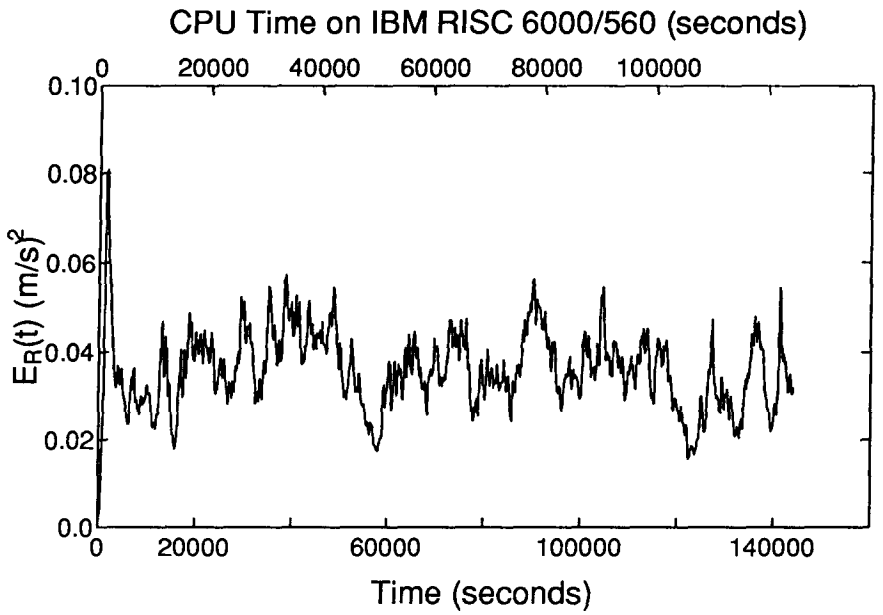

Figure 3.2: Time variation of the RS TKE averaged over the whole domain for case N16A06.

of motion have the fluctuations $(\tilde{u}, \tilde{v})$ relative to the instantaneous horizontal average $([u], [v])$ rather than about the average value over space and time $(\langle u \rangle, \langle v \rangle)$. Therefore, a major influence of the Coriolis force is on the inertial adjustment of the mean flow.

The ASL, where the time scale of turbulent eddies is much smaller than $t_f = f^{-1}$, is affected very little by the Coriolis force. Take for example the largest possible eddy (therefore, the longest time scale) in the ASL: its length scale is about $0.1h_E$, where h_E denotes the height of the Ekman layer, and its velocity scale is about u_*; using the observational relation $h_E \approx 0.3u_*/f$ (Nieuwstadt and van Dop, 1982), the time scale is about $0.1h_E/u_* \approx 0.1 \times 0.3/f = 0.03t_f = 300$(sec). This implies that taking a time average over at least $2\pi/f$, as recommended by Mason and Thomson (1987), is not strictly necessary for the investigation of SL turbulence. Furthermore, in some part of the SL in which local equilibrium prevails, time scales are even shorter. This means

that small eddies respond quickly to changing conditions in the mean flow. Small eddies are therefore always in approximate equilibrium with local conditions in the mean flow. However, in order to take into account the possible effects of the large eddies of the size of h_E on the turbulent statistics of the ASL, the present study still average the results over at least $t_f = f^{-1}$ seconds in the time domain for most LES runs.

3.3.1 Logarithmic profile of the mean speed

SGS buffer layer

The results for the averaged speed profile, defined by $|\mathbf{v}|(z) = \sqrt{\langle u \rangle^2 + \langle v \rangle^2}$ are presented here. Figure 3.3 shows an example of the mean speed profile under a semi-log

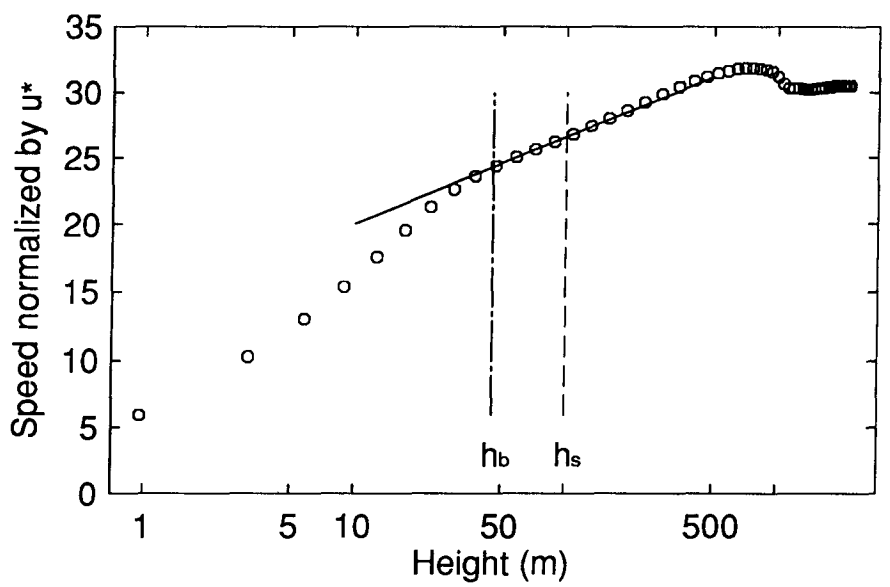

Figure 3.3: An example of the velocity profile derived from LES (case N64C06).

coordinate. This figure exhibits a logarithmic portion for the wind speed, located not immediately above the surface, but at some height above the surface, denoted by h_b, as shown in the figure. The region below h_b is referred to as the *SGS buffer layer.* The logarithmic portion extends to the top of the ASL, h_s, defined as $0.1h_E$, where h_E is the

height of the ABL. A question arises why the logarithmic profile can not be extended down to the surface as measurements suggest.

One of the most difficult problems to approach through LES is the presence of a solid boundary. For a TBL over a smooth plate, for example, in the region very close to a smooth boundary, turbulence is partially or totally suppressed and a thin "*viscous sublayer*" separates the surface and the turbulent layer aloft (with a logarithmic velocity profile) but transfers the same amount of momentum flux. The thickness of the viscous sublayer becomes thinner as the Reynolds number increases. For a rough surface, if the Reynolds number is large, no viscous sublayer is observed, and the logarithmic velocity profile can then be extended very close to the top of the roughness elements. In either case, the size of the eddies in the region of the logarithmic profile increases with the height. However, LES, employing a finite number of mesh points, has to adopt artificial conditions for *mean* velocity components at the first vertical grid, because this elevation is within the logarithmic region and no specification of the *true velocity fluctuations* is possible at this height. The wall-function is often adopted as the artificial condition.

For a TBL over a smooth plate, DNS, adopting a very fine mesh, resolves the viscous sublayer, and is thereby able to reproduce the whole layer. LES, however, is not capable of resolving the viscous sublayer if the Reynolds number of a smooth case is very large. By setting the first vertical grid of the simulation domain in the logarithmic profile region, LES adopts the universal logarithmic law as the boundary condition for the velocity components. Again, no velocity fluctuations are introduced at the boundary. The velocity boundary conditions are correct for the mean velocity components at the first vertical grid point. The mean velocity components above the boundary must depend on (i) the SGS viscosity if SGS motions dominate; (ii) RS momentum flux if RS motions dominate. (iii) both SGS viscosity and RS momentum flux if SGS and RS motions are competitive. In the region near the surface, since no fluctuations are specified for the

velocity components on the boundary, RS motions must be significantly suppressed while SGS motions prevail. Therefore, the dynamics in the region is mainly determined by the SGS turbulence model, and the same is true of the velocity profile.

For a TBL over a rough plate, both DNS and LES must place the numerical boundary in the logarithmic profile region. The same difficulty is encountered at the lower boundary.

Effects of roughness length z_0 on LES of USL

Two different roughness lengths are involved in LES of the USL: one is the roughness length z_0 in (2.60) and (2.61) as an external parameter specified through the lower boundary condition; the other is the value obtained by extrapolating the logarithmic velocity profile to intercept $u = 0$. This intercept is denoted by $z_{0,r}$. It is implicit in figure 3.3 that the value of $z_{0,r}$ is about 0.01 m, much smaller than the specified value of $z_0 = 0.1$ m, namely,

$$z_{0,r} < z_0. \tag{3.43}$$

It is assumed in this study that the specification of z_0 at the first vertical grid does not significantly influence the evaluation of the von Kármán constant. To examine this assumption, four LES cases with different value of z_0 have been carried out: $z_0 = 0.01$, 0.05, 0.1 and 0.5. The speed profiles of these four cases are shown in figure 3.4, where the speed is normalized by u_* and z by h_E. Profiles are almost parallel to each other in the ASL, and therefore the slopes of the logarithmic portion are approximately the same. In figure 3.5, those profiles are plotted under the coordinate of u/u_* vs. z/z_0. Without the defects of the SGS buffer layer, the velocity profile

$$\frac{u}{u_*} = \frac{1}{\kappa} \ln \frac{z}{z_0}$$

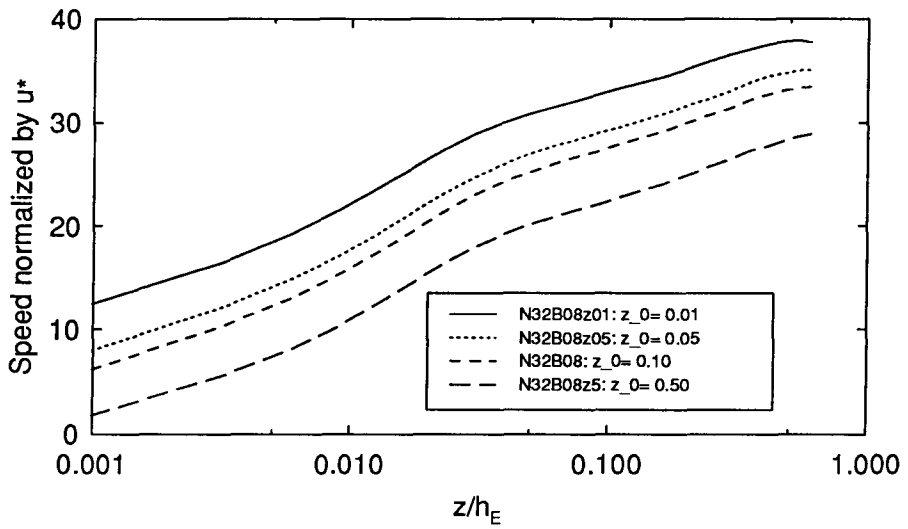

Figure 3.4: The velocity profiles derived from LES with different value of z_0 as the boundary condition at the surface. In the legend, z_0 represents z_0.

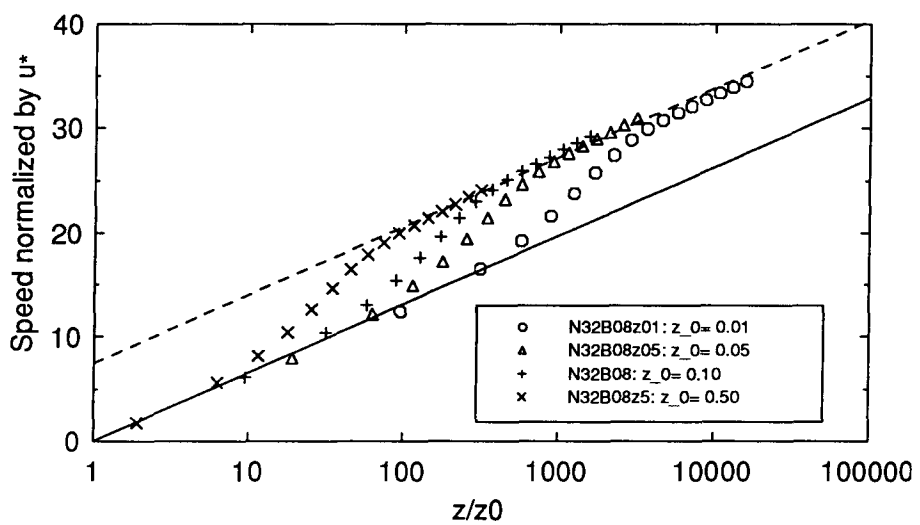

Figure 3.5: u/u_* vs. $\log z/z_0$ for different value of z_0 as the boundary condition at the surface. In the legend, z_0 represents z_0. The solid line is: $u/u_* = (1/\kappa_0)\ln(z/z_0)$; the dashed line is: $u/u_* = (1/\kappa_0)\ln(z/z_{0,r})$.

must correspond to the solid line in this figure. The dashed line in the figure is obtained from LES, represented by

$$\frac{u}{u_*} = \frac{1}{\kappa_{LES}} \ln \frac{z}{z_{0,r}},$$

where κ_{LES} is the value estimated from the dashed line. The offset from the solid line is determined by the "quality" of the SGS model and is independent of the boundary value of z_0. The performance of the SGS model in the near-wall region for a high Reynolds number flow is still an open question. The present study does not concentrate on this topic.

Some weaknesses in LES have been seen arising from the representation of turbulence near the wall. To improve these, the so-called "stochastic backscatter" was proposed in recent years. See, *e.g.*, Leith (1990), Chasnov (1991), Mason and Thomson (1992) for further details.

Effects of κ_0 on LES of USL

The lower boundary conditions for mean velocity components are given by (2.60) to (2.62), in which two constants, κ_0 and z_0, are specified. For simplicity, the x-axis is aligned with the surface wind direction; this assumption will not affect the following analysis. Thus, (2.61) and (2.62) are trivial; (2.60) becomes

$$\frac{u(x,y,z)|_{z=z_1}}{u_*} = \frac{1}{\kappa_0} \ln \frac{z_1}{z_0}, \tag{3.44}$$

where $z_1 = 0.95$ m is the height of the first vertical grid, which is fixed for all LES runs in the present study; $\kappa_0 = 0.35$, and $z_0 = 0.01$, 0.05, 0.1 and 0.5 as discussed above.

It is obvious that varying z_0 while fixing κ_0 is equivalent to varying κ_0 while fixing z_0 for the present LES model. As long as the value of the right-hand side of (3.44) is the

same for a pair of different values of (κ_0, z_0):

$$A = \frac{1}{\kappa_0} \ln \frac{z_1}{z_0},$$

these boundary conditions are identical, because κ_0 and z_0 are not used anywhere else in the LES model. If $z_0^{(i)}$ denotes the i-th value in the number set (0.01, 0.05, 0.1, 0.5), and $A^{(i)}$ denotes the value of A when $\kappa_0 = 0.35$ and $z_0 = z_0^{(i)}$:

$$A^{(i)} = \frac{1}{\kappa_0} \ln \frac{z_1}{z_0^{(i)}},$$

then another number set for $\kappa_0^{(i)}$ is obtained from the following equation:

$$A^{(i)} = \frac{1}{\kappa_0^{(i)}} \ln \frac{z_1}{z_0},$$

with fixed value of $z_0 = 0.1$. Table 3.6 shows that value of $\kappa_0^{(i)}$ varies from 0.17 to 1.22 if

Table 3.6: Equivalent varying-values of $\kappa_0^{(i)}$, with $z_0 = 0.1$, for the cases N32B08z01, N32B08z05, N32B08 and N32B08z5.

LES run		N32B08z01	N32B08z05	N32B08	N32B08z5
$A^{(i)}$		13.02	8.43	6.45	1.85
κ_0 fixed &	κ_0	0.35	0.35	0.35	0.35
$z_0^{(i)}$ varied	$z_0^{(i)}$	0.01	0.05	0.1	0.5
z_0 fixed &	z_0	0.1	0.1	0.1	0.1
$\kappa_0^{(i)}$ varied	$\kappa_0^{(i)}$	**0.17**	**0.27**	**0.35**	**1.22**

the value of z_0 is considered to be "fixed".

It has already been shown in figure 3.4 that the slope of the logarithmic portion of LES speed profile is almost independent of the value of z_0. Based on the argument discussed above, it is also concluded that the slope of the logarithmic portion of LES speed profile is almost independent of the value of κ_0.

Friction velocity

Friction velocity, as a controlling parameter in the ASL, cannot be specified beforehand, but rather has to be calculated through the model. By definition, u_* must be derived from the shear stress at the wall:

$$u_{*0}^2 = \sqrt{(\tau_{uw,0}^{(s)})^2 + (\tau_{uw,0}^{(s)})^2} \tag{3.45}$$

where $\tau_{uw,0}$ and $\tau_{vw,0}$ are the kinematic shear stress[5] components in the x and y direction, respectively, at the surface. LES produces two kinds of shear stresses at the same place: RS one and SGS one. At the wall, RS shear stress is zero; in the interior, the total shear stress is equal to the sum of the two parts, but SGS stress diminishes dramatically away from the boundary and total shear stress is almost equal to RS one. Figure 3.14 on page 88 shows an example of the vertical distributions of the shear stresses. A near-constant momentum flux region is observed sufficiently close to the boundary ($< 0.1h_E$), at the top of which SGS contribution is very small and RS shear stresses are almost at their maxima. Therefore, one can also calculate another value of friction velocity, being referred to as u_{*r}, through RS shear stresses:

$$u_{*r}^2 = \max_{z\in[0,h_E]}\{\sqrt{\langle\tilde{u}\tilde{w}\rangle^2 + \langle\tilde{v}\tilde{w}\rangle^2}\}. \tag{3.46}$$

u_{*r} and u_{*0} usually have slightly different values; the former is more sensitive to SM-Reynolds number than the latter, because the existing SGS buffer layer damps the influence of the eddies from the outer layer.

Effects of Re_{SM} on the velocity profile

In figure 3.6, a comparison of the logarithmic portion of mean speed among five

[5]The kinematic stress includes $1/\rho$. In the rest of this thesis, shear stresses always mean kinematic quantities, unless otherwise specified.

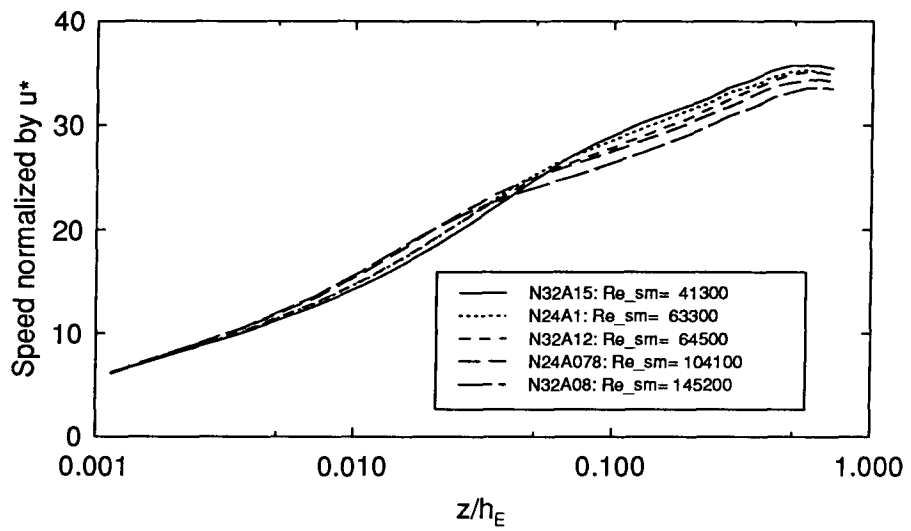

Figure 3.6: The velocity profiles for domain A.

different SM-Reynolds number cases (domain A) is illustrated. As shown in figure 3.6, the SGS buffer layer becomes shallower with increasing SM-Reynolds number. Compared with case N24A1 which adopts 24 by 24 grid points in horizontal directions and $C_s = 0.1$, case N32A12 adopts a larger value of $C_s = 0.12$, but it has more gird points than case N24A1 and therefore it has a larger value of Re_{SM}. Figure 3.6 shows clearly the dependence of profiles on the SM-Reynolds number, which supports the proposal of Re_{SM}.

For domain B, mean speed profiles in the ASL are presented in figure 3.7, which also demonstrates a clear dependence of the logarithmic portion on the SM-Reynolds number.

3.3.2 Investigation of the von Kármán constant

The von Kármán constant can be calculated from the slope of the logarithmic portion of the wind speed profile. The region over which κ is evaluated is taken as $0.05 \leq z/h_E \leq 0.1$. In fact, figure 3.14 on page 88, figure 3.17 on page 90 and figure 3.18 on page 91 show that in the region $0.05 \leq z/h_E \leq 0.1$, RS shear stresses $\langle \tilde{u}\tilde{w} \rangle$ are near their maxima,

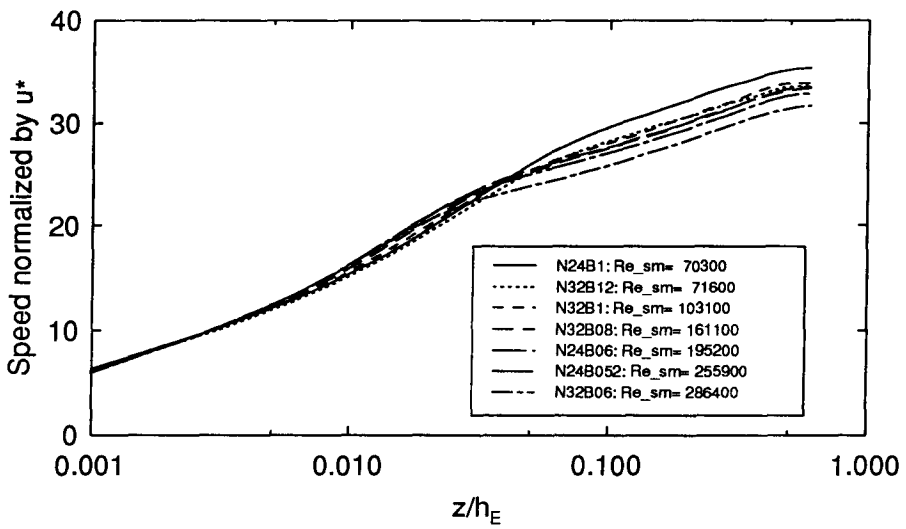

Figure 3.7: The velocity profiles for domain B.

which ensures that RS components are dominant in this region. Also, in figure 3.6 and figure 3.7, logarithmic profiles are displayed in the region $0.05 \leq z/h_E \leq 0.1$, which guarantees the region to be within the ASL.

Evaluation procedure

The evaluation of the von Kármán constant over time interval $[t_1, t_2]$ involves two averaging processes:

- $[t_1, t_2]$ is divided into N sub-intervals, each of length $0.03t_f$, which is the time scaling of surface layer eddies; time averages are taken for velocity profiles at each i-th sub-interval; based on the logarithmic portion of the averaged profile, the von Kármán constant is evaluated in this time sub-interval:

$$\frac{u_k^{(i)}}{u_{*r}} = \frac{1}{\kappa_{LES}^{(i)}} \ln z_k - \frac{1}{\kappa_{LES}^{(i)}} \ln z_{0,r} \qquad k = k_1, k_2 \tag{3.47}$$

where $^{(i)}$ indicates the i-th sub-interval, and k_1 and k_2 are the vertical grid index corresponding to $0.5h_s$ and h_s, respectively. The least square method is adopted to

derive a value for $\kappa_{LES}^{(i)}$.

- a further time averaging process is taken over these N sub-intervals to obtain a value for κ_{LES}:

$$\kappa_{LES} = \frac{1}{N}\sum_i \kappa_{LES}^{(i)}, \tag{3.48}$$

and also the standard deviation for the estimate.

The effects of Re_{SM} on κ_{LES} for a fixed domain size

In the ideal case, LES-estimated values of κ_{LES} should be close to those observed in the ASL and independent of numerical specifications, such as SGS model, grid size and domain size. In practice, due to the limitation in computer size, domain size and the total number of grids cannot be very large so that their influence on the evaluated κ_{LES} cannot be ignored. In order to understand how serious this influence is and what relation can be established, an important parameter, Re_{SM}, is proposed in section 2.3. It should be pointed out again that the length scale of domain size, expressed as $(D_x D_y h_E)^{1/3}$, in the definition of Re_{SM} is suitable for a group of cases in which the ratios of the three domain dimensions are fixed.

Figure 3.8 shows the estimated values of the von Kármán constant as a function of SM-Reynolds number for domain A. The triangles represent the average values taken over f^{-1} and error bars indicate standard deviations with time. The value of u_* involved in the calculation of κ_{LES} is u_{*r}. One of the reasons for adopting the local value rather than the surface friction velocity u_{*0} is that the value of u_{*0} is apparently underestimated by LES. The circles are the corresponding κ_{LES} values when the surface friction velocity u_{*0} was used in the estimation. In this group of simulations, there is no significant difference between adopting u_{*r} and adopting u_{*0}.

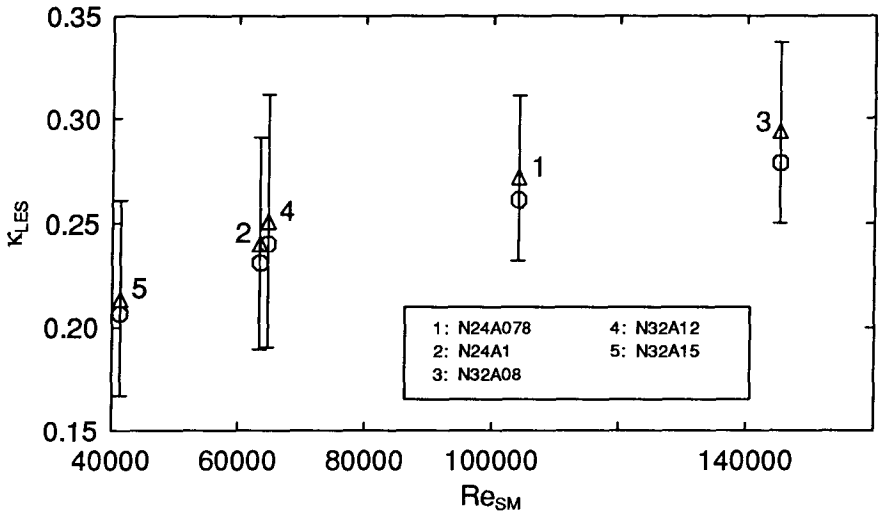

Figure 3.8: The von Kármán constant evaluated from LES for domain A; △, the value based on u_{*r}; ○, the value based on u_{*0}; the error-bars are from the averaging process of κ based on u_{*r}.

It is clearly demonstrated in figure 3.8 that, C_s is not the only parameter which determines κ_{LES}, while the parameter Re_{SM} is a good parameter for this purpose. For each one in N24A-cases, the value of κ_{LES} increases as C_s decreases; in N32A-cases, the same tendency is indicated. Case N32A08 adopts a larger value of C_s than case N24A078, for example, but the former gives a larger value of κ_{LES} than the latter, because the former case uses more mesh points than the latter so that the value of SM-Reynolds number of the former case is larger than that of the latter case. Another example is the comparison between case N24A1 and case N32A12: C_s in N32A12 is larger than that in N24A1, but both cases produce almost the same value of κ_{LES}; the reason is that they have almost the same value of Re_{SM}.

A question arising from the definition of Re_{SM} is that one could reduce the value of C_s to obtain a larger Re_{SM} with a fixed number of mesh points. In fact, if C_s is too small, RS turbulence cannot be dissipated properly and some of its energy is accumulated near the high-wavenumber end of energy spectra as grid-mode turbulence (Mason and Callen,

1986). This is generally adopted as a criterion for choosing the value of C_s.

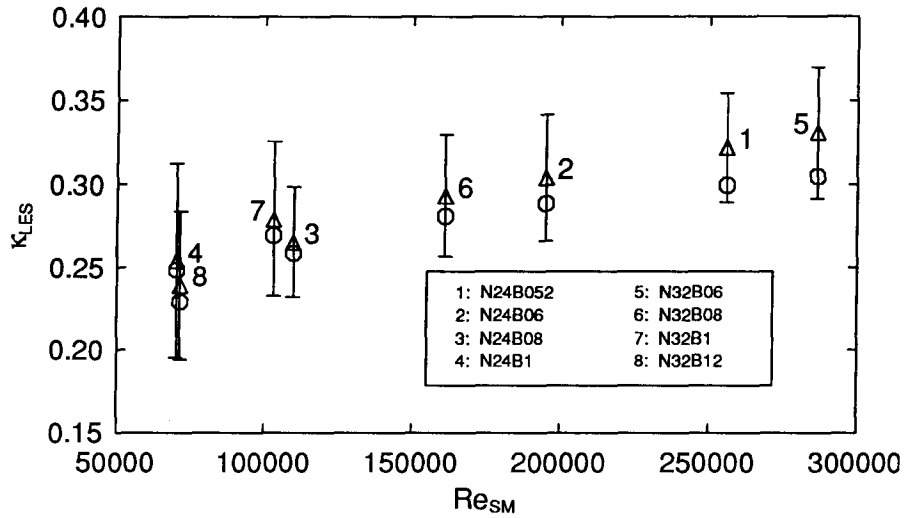

Figure 3.9: As in figure 3.8, but for domain B.

Figure 3.9 shows κ_{LES} vs. Re_{SM} for domain B. Two groups of cases are involved: N24B-cases adopt fewer mesh points than N32B-cases. The same results as those of domain A are found, which again support the proposal that SM-Reynolds number, rather than C_s is the unique dimensionless parameter for RS turbulence statistics when the domain size is fixed. A noticeable scatter occurred for the low SM-Reynolds number cases may be attributed to a poor statistical average, because those four cases only run for $1.8t_f$.

There is a significant difference between adopting u_{*r} and adopting u_{*0} when $Re_{SM} > 1.5 \times 10^5$, which implies that the value of u_{*0} is significantly smaller than that of u_{*r} in that range of Re_{SM}.

In figure 3.10, κ_{LES} vs. Re_{SM} for domain D is given. The trend of increasing κ_{LES} with Re_{SM} is the same as those observed in figure 3.8 for domain A and figure 3.9 for domain B. As SM-Reynolds number increases, the simulated value of κ_{LES} becomes progressively larger. Because of the large number of grid points for N64C-cases, the value

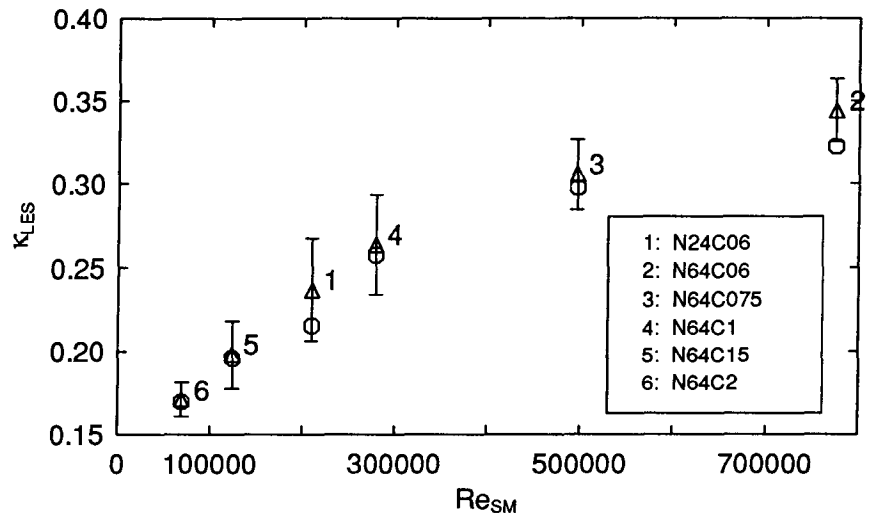

Figure 3.10: As in figure 3.8, but for domain C.

of Re_{SM} reaches as large as 7×10^5 for case N64C06. The value of κ_{LES} of this case is about 0.35, the largest among all cases in this study; however, this value is slightly overestimated because this case exhibits some grid-mode turbulence, which enhances turbulent transport in the whole layer and therefore increases the value of κ_{LES}. This is the same as the value obtained by Businger et al. (1971) from the Kansas observation data. It is unlikely that the value of κ_{LES} will reach 0.4 by extrapolating those points in figure 3.10 to the place where $Re_{SM} \sim 10^6$ or larger, but taking into account that u_{*r} is underestimated (see later in this chapter) this possibility cannot be excluded.

It is also found that variations of κ_{LES} with time (indicated by the lengths of the error bars) for domain D are smaller than those in results of domain A (see figure 3.8) and domain B (see figure 3.9). Furthermore, the difference between adopting u_{*r} and adopting u_{*0} is smaller than those in results of domain A and domain B. Although there are fairly large uncertainties (long error bars shown in these figures) for the estimates of κ_{LES}, there is an obvious relation between κ_{LES} and Re_{SM}: the value of κ_{LES} increasing with Re_{SM} for a fixed domain size.

The effects of domain size of κ_{LES}

The above discussion concerns the dependence of κ_{LES} on Re_{SM} for a fixed domain size. If the domain size varies, the domain Rossby number Ro_D changes (see table 3.5): a larger domain corresponds to a smaller Ro_D; the value of κ_{LES} might be influenced.

In figure 3.11, those points in figure 3.8 and in figure 3.9 are plotted together. In

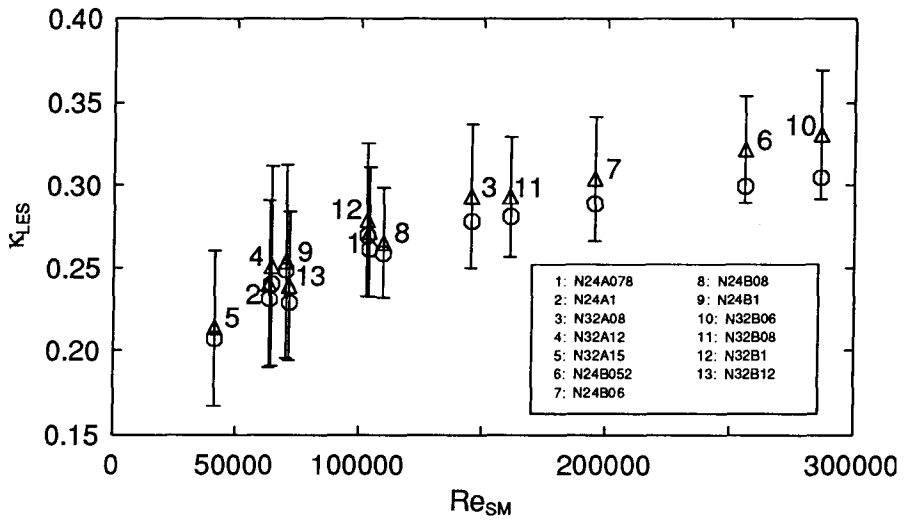

Figure 3.11: As in figure 3.8, but for domain A and domain B.

horizontal directions, domain B is 50% larger than domain A, but the results of κ_{LES} exhibit weak dependence on the domain size. Case N32A08 has almost the same value of κ_{LES} as case N32B08; case N24A1 and case N32A12 have almost the same value of κ_{LES} as case N24B1 and case N32B12, respectively; other cases fit one κ_{LES}-Re_{SM} relation very well.

In each horizontal direction, the dimension of domain C is four times of that of domain A. Big differences are seen in figure 3.12 between the LES cases in these two groups: as domain size increases, with the same value of SM-Reynolds number, the LES-estimated value of the von Kármán constant decreases. The same result can be seen in

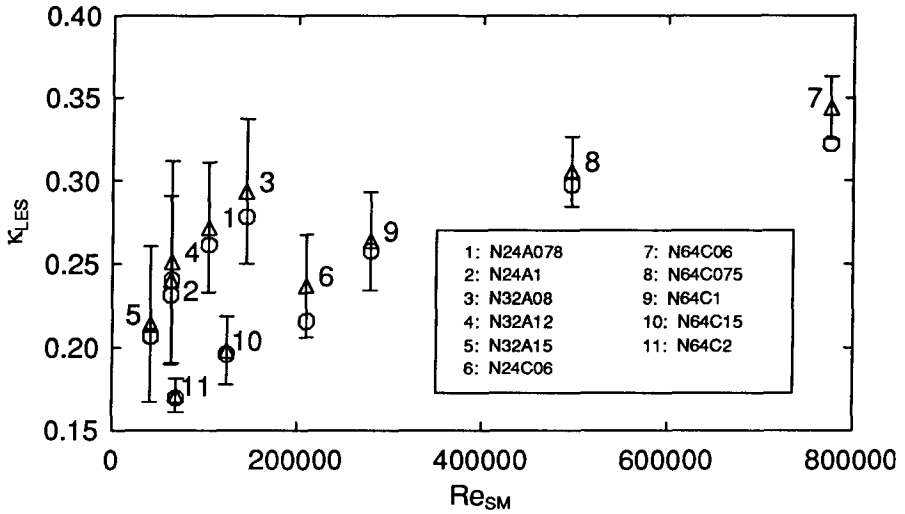

Figure 3.12: As in figure 3.8, but for domain A and domain C.

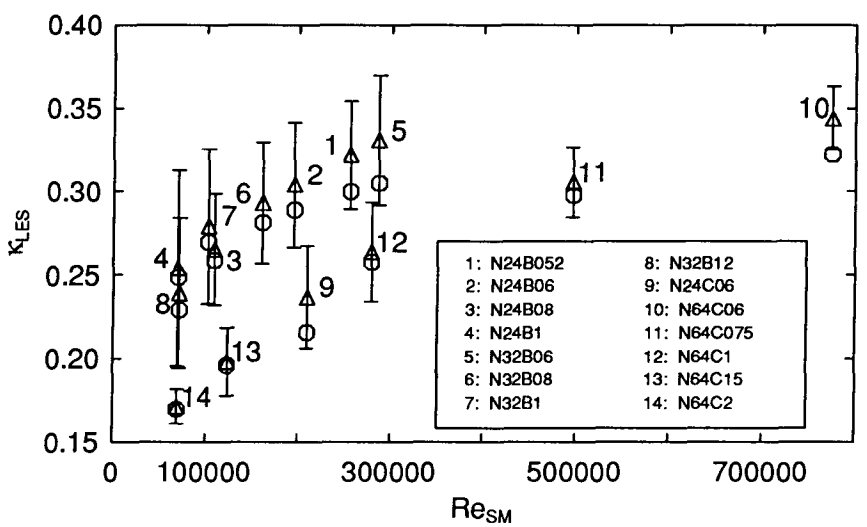

Figure 3.13: As in figure 3.8, but for domain B and domain C.

figure 3.13 between the cases for domain B and the cases for domain C. Considering that some cases exhibit differences between u_{*r} and u_{*0} and that a good correlation is seen between this difference and the value of C_s, the values of κ_{LES} based on u_{*0} (indicated by those circles in figures) becomes valuable. From figure 3.13, the indication from those circles is that the difference due to domain size decreases as Re_{SM} becomes larger.

3.3.3 Shear stress components

Figure 3.14 shows the effects of SM-Reynolds number on the shear stress component τ_{uw} for domain B. A very good Re_{SM}-dependence for profiles of τ_{uw} is found in this

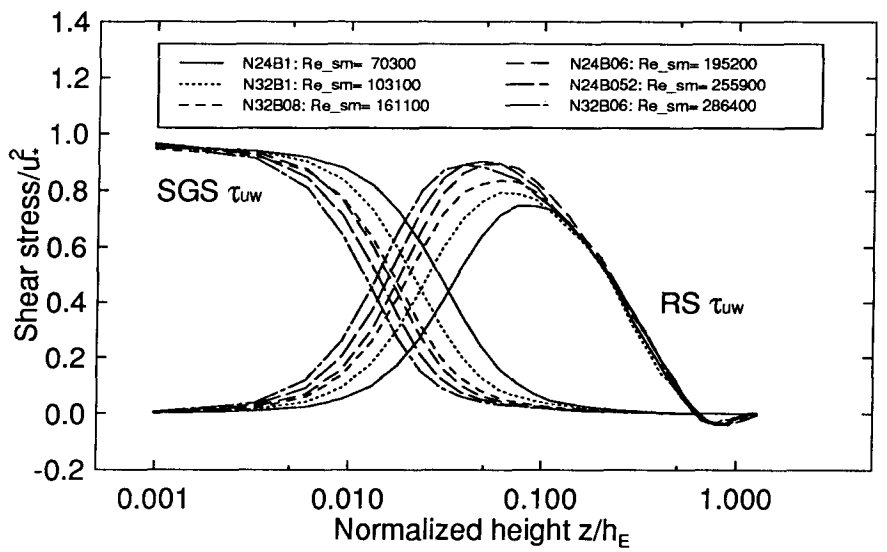

Figure 3.14: SGS stress $-\overline{u_s' w_s'}$, RS stress $-\langle \tilde{u}\tilde{w} \rangle$ for domain B.

figure. The peak value of RS τ_{uw}/u_* occurs at a lower elevation as Re_{SM} increases, while the maximum SGS τ_{uw}/u_* at the surface does not change with Re_{SM}. For a very small Re_{SM}, the peak value of RS τ_{uw} becomes very small and even is diminished as those RS eddies die out. SGS τ_{uw}, however, switches its profile to a lower elevation as Re_{SM} increases. The total shear stress component τ_{uw} = RS τ_{uw} + SGS τ_{uw} exhibits almost Re_{SM} independence, as shown in figure 3.15.

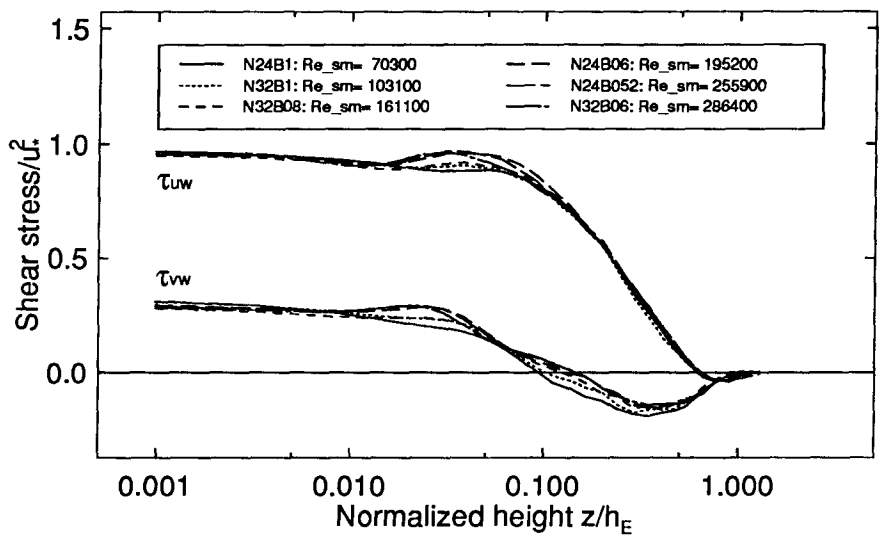

Figure 3.15: Total stress $-\overline{u_s' w_s'} - \langle \tilde{u}\tilde{w} \rangle$ and $-\overline{v_s' w_s'} - \langle \tilde{v}\tilde{w} \rangle$ for domain B.

For the shear stress component τ_{vw}, a very good Re_{SM}-dependence is also found for SGS part and RS part of τ_{vw} in the ASL for domain B, as shown in figure 3.16. The value of SGS τ_{vw} at the surface varies with Re_{SM}, corresponding to the turning angle between the shear stress vector at the surface and the geostrophic wind vector above the ABL. As expected, when Re_{SM} is very small (*e.g.*, case N24B1), RS τ_{vw} becomes very small compared with its SGS part, which implies that this case is by no means a good LES for surface layer turbulence. The total shear stress component τ_{vw} = RS τ_{vw} + SGS τ_{vw} also shows little dependence on Re_{SM} in figure 3.15.

Further indications of Re_{SM}-dependence of shear stresses can be found in figure 3.17 and figure 3.18, for domain A and domain C, respectively.

3.3.4 Standard deviations of velocity fluctuations

The value of SM-Reynolds number also affects the vertical distribution of $\sigma_{\tilde{u}}$, $\sigma_{\tilde{v}}$ and $\sigma_{\tilde{w}}$, which are the standard deviations of RS velocity fluctuations of u, v and w component, defined respectively by $\sigma_{\tilde{u}} = \sqrt{\langle \tilde{u}^2 \rangle}$, $\sigma_{\tilde{v}} = \sqrt{\langle \tilde{v}^2 \rangle}$ and $\sigma_{\tilde{w}} = \sqrt{\langle \tilde{w}^2 \rangle}$. Figure 3.19

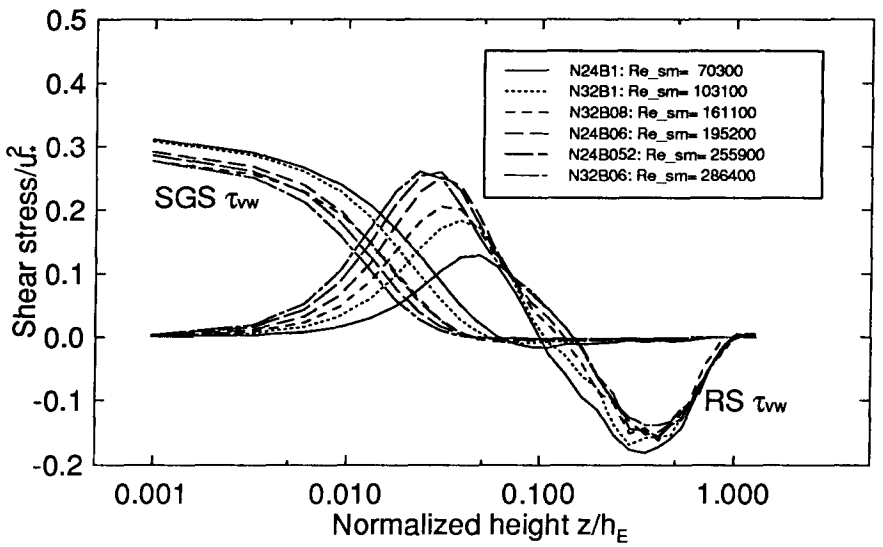

Figure 3.16: SGS stress $-\overline{v_s' w_s'}$, RS stress $-\langle \tilde{v}\tilde{w} \rangle$ for domain B.

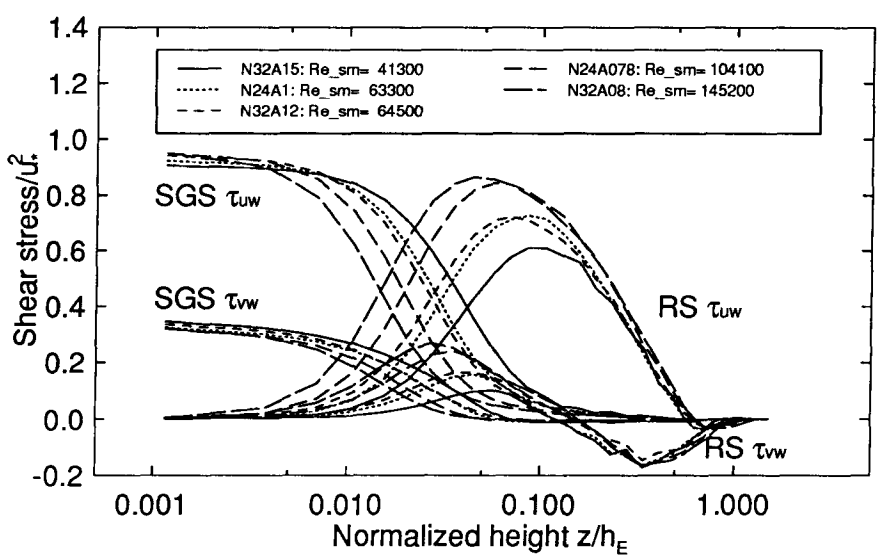

Figure 3.17: SGS stress $-\overline{u_s' w_s'}$ and $-\overline{v_s' w_s'}$, RS stress $-\langle \tilde{u}\tilde{w} \rangle$ and $-\langle \tilde{v}\tilde{w} \rangle$ for domain A.

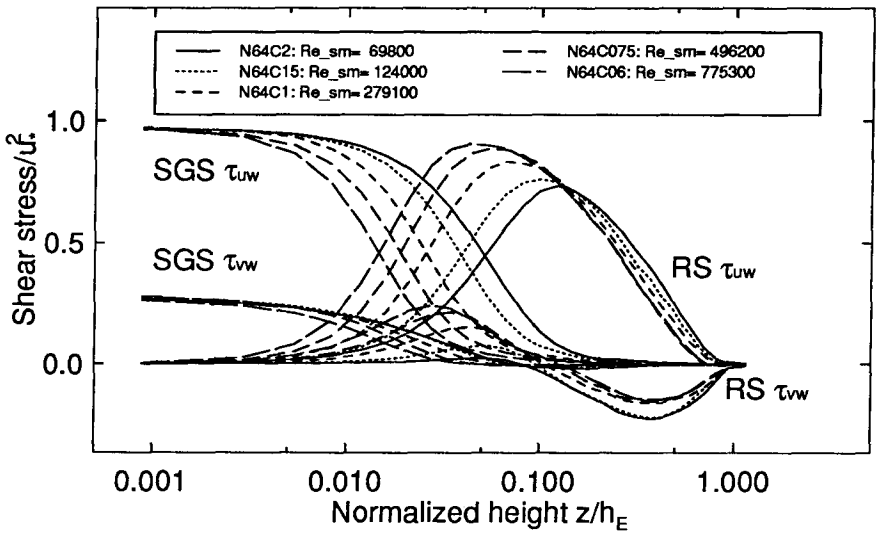

Figure 3.18: SGS stress $-\overline{u_s' w_s'}$ and $-\overline{v_s' w_s'}$, RS stress $-\langle \tilde{u}\tilde{w} \rangle$ and $-\langle \tilde{v}\tilde{w} \rangle$ for domain C.

presents the vertical profiles of $\sigma_{\tilde{u}}/u_*$, $\sigma_{\tilde{v}}/u_*$ and $\sigma_{\tilde{w}}/u_*$ for domain A. As SM-Reynolds number increases, $\sigma_{\tilde{u}}/u_*$ tends to peak at a lower elevation; similar trends can be seen for the $\sigma_{\tilde{v}}/u_*$ and $\sigma_{\tilde{w}}/u_*$. The height of maximum of $\sigma_{\tilde{w}}/u_*$ is larger than that of $\sigma_{\tilde{v}}/u_*$; the height of maximum of $\sigma_{\tilde{v}}/u_*$ is larger than that of $\sigma_{\tilde{u}}/u_*$. The peak value of $\sigma_{\tilde{u}}/u_*$ occurs in the region: $0.01 < z/h_E < 0.05$; that of $\sigma_{\tilde{v}}/u_*$ occurs in a higher region: $0.02 < z/h_E < 0.08$; that of $\sigma_{\tilde{w}}/u_*$ occurs in the region $0.1 < z/h_E < 0.2$. This implies that RS fluctuations of u component are least affected by the presence of the wall, those of v component are the second, and those of w component are most affected by the presence of the wall. In the range of Re_{SM} indicated by the legend figure 3.19, the maximum value of $\sigma_{\tilde{u}}/u_*$ is about 2.7; that of $\sigma_{\tilde{v}}/u_*$ is about 1.4; and that of $\sigma_{\tilde{v}}/u_*$ is about 0.95. In the SGS buffer layer, $\sigma_{\tilde{u}}/u_*$, $\sigma_{\tilde{v}}/u_*$ and $\sigma_{\tilde{w}}/u_*$ increase with the SM-Reynolds number, and all profiles show this dependence very well. One can see that a higher value of SM-Reynolds number will "erode" the SGS buffer layer more deeply and "squeeze" this buffer layer closer to the surface, while the outer layer is not significantly influenced.

A relation between the maximum value of $\sigma_{\tilde{u}}$ (denoted by $\sigma_{\tilde{u},max}$) normalized by u_*

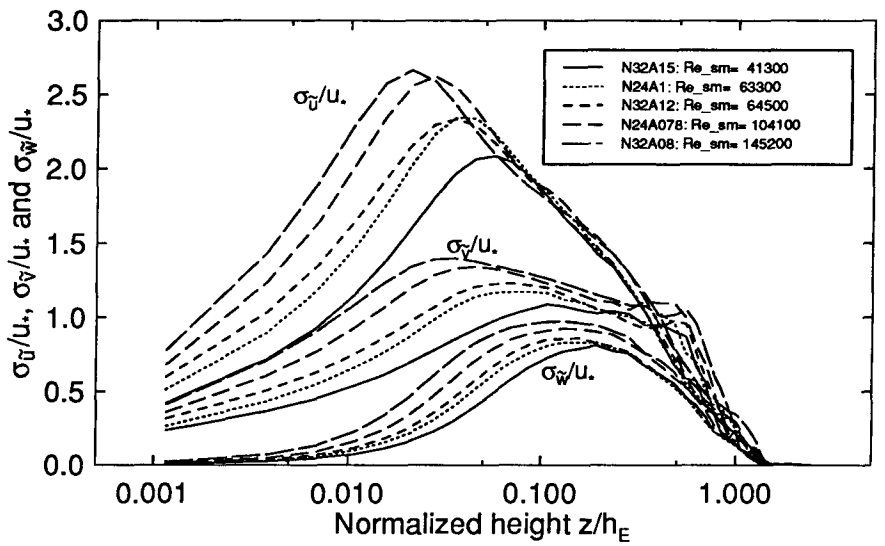

Figure 3.19: Profiles of $\sigma_{\tilde{u}}/u_*$, $\sigma_{\tilde{v}}/u_*$ and $\sigma_{\tilde{w}}/u_*$ for domain A.

and Re_{SM} can be found from LES results for domain A, shown in figure 3.20. Triangles denote the value of $\sigma_{\tilde{u},max}/u_{*r}$, while circles stand for the value of $\sigma_{\tilde{u},max}/u_{*0}$. The error bars represent the standard deviation with respect to time averaging (see averaging process for κ_{LES} on page 81). The value of $\sigma_{\tilde{u},max}/u_*$ increases with the SM-Reynolds number. The cases adopting more grid, i.e., N32A-cases, exhibit slightly smaller values of $\sigma_{\tilde{u},max}/u_*$ than N24A-cases, but the unique dependence of $\sigma_{\tilde{u},max}/u_*$ on Re_{SM} is still fairly good. Figure 3.21 shows the dependence of the value of RS $\sigma_{\tilde{v},max}/u_*$ on SM-Reynolds number for domain A. Figure 3.22 presents the value of RS $\sigma_{\tilde{w},max}/u_*$ as a function of SM-Reynolds number. It is found that $\sigma_{\tilde{w},max}/u_*$ slightly increases with Re_{SM} and the asymptote is about 0.95.

Figure 3.23 presents the vertical profiles of $\sigma_{\tilde{u}}/u_*$, $\sigma_{\tilde{v}}/u_*$ and $\sigma_{\tilde{w}}/u_*$ for domain B. Similar trends and Re_{SM}-dependence are observed for all three variables. In the range of Re_{SM} indicated by the legend figure 3.23, which is wider than that in figure 3.19, the maximum value of $\sigma_{\tilde{u}}/u_*$ is about 3.0, which is higher than that in figure 3.19; the maximum value of $\sigma_{\tilde{v}}/u_*$ is about 1.45, which is about the same as that in figure 3.19;

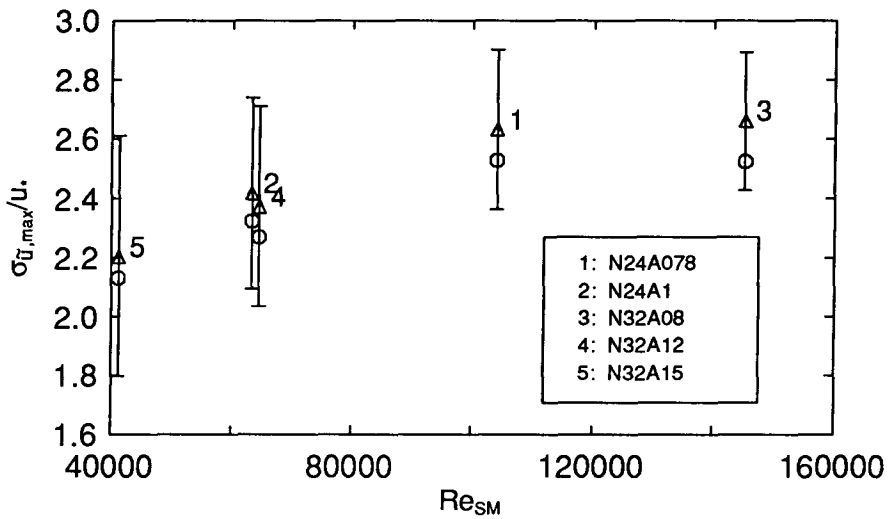

Figure 3.20: $\sigma_{\tilde{u},max}/u_*$ evaluated from LES; △, the value based on u_{*r}; ○, the value based on u_{*0}; the error-bars are from the averaging process of κ based on u_{*r}.

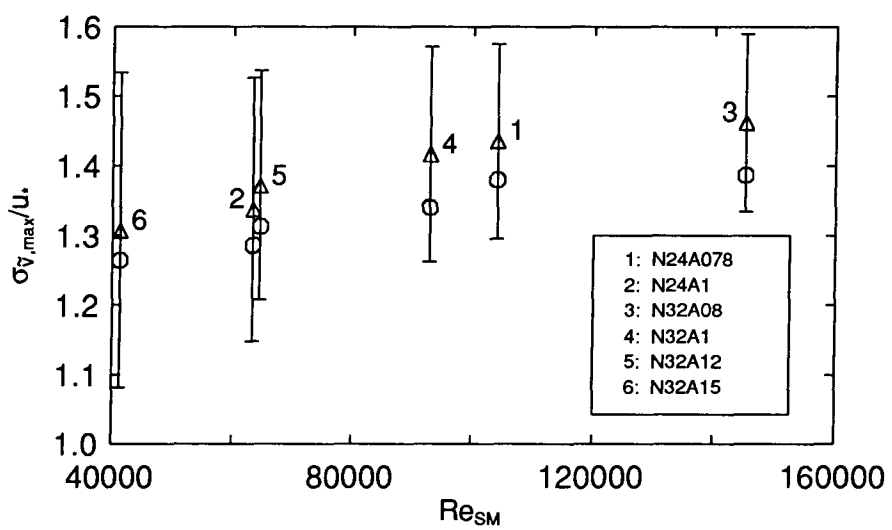

Figure 3.21: As in figure 3.20, but for $\sigma_{\tilde{v},max}/u_*$.

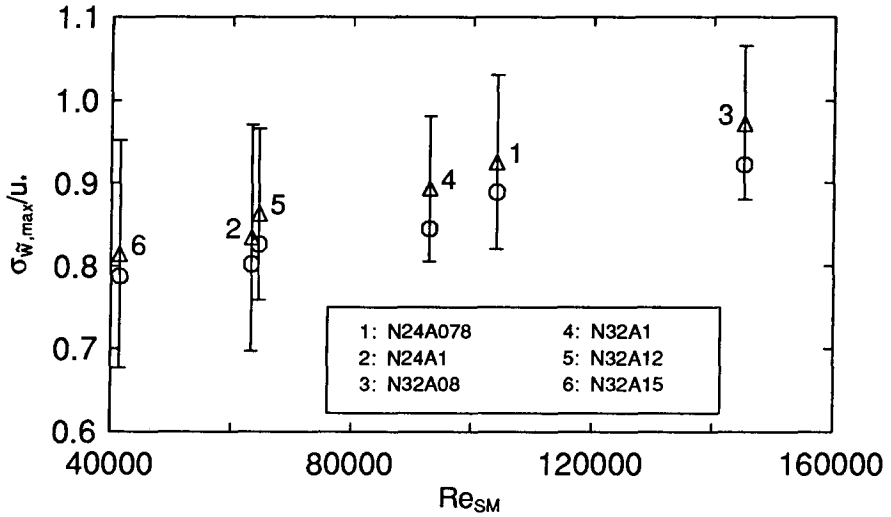

Figure 3.22: As in figure 3.20, but for $\sigma_{\tilde{w},max}/u_*$.

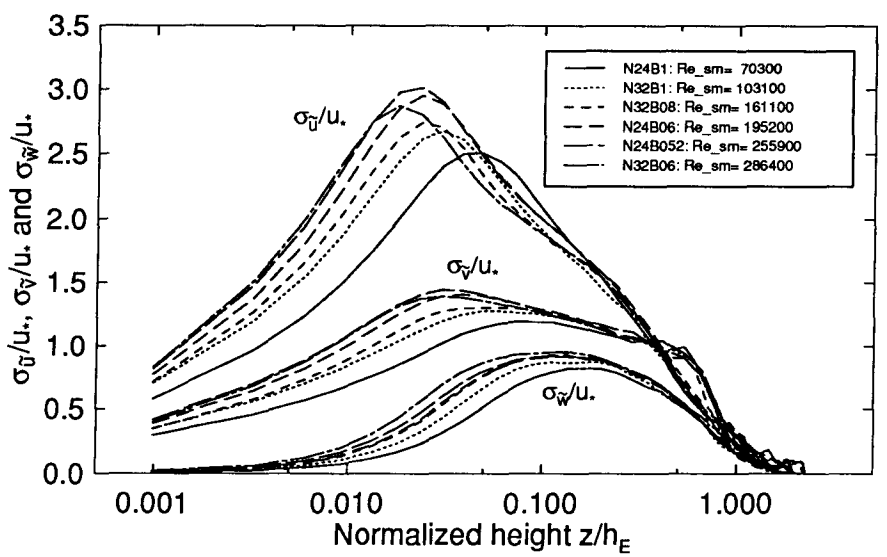

Figure 3.23: Profiles of $\sigma_{\tilde{u}}/u_*$, $\sigma_{\tilde{v}}/u_*$ and $\sigma_{\tilde{w}}/u_*$ for domain B.

and the maximum value of $\sigma_{\tilde{v}}/u_*$ is about 0.95, also about the same as that in figure 3.19.

Figure 3.24 shows the vertical profiles of $\sigma_{\tilde{u}}/u_*$, $\sigma_{\tilde{v}}/u_*$ and $\sigma_{\tilde{w}}/u_*$ for domain C. Similar trends and Re_{SM}-dependence are observed for all three variables. A noticeable

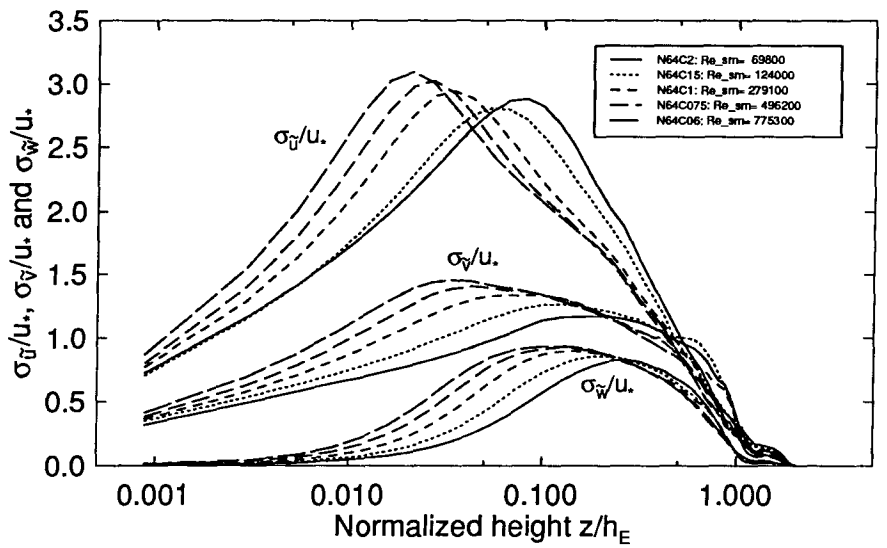

Figure 3.24: Profiles of $\sigma_{\tilde{u}}/u_*$, $\sigma_{\tilde{v}}/u_*$ and $\sigma_{\tilde{w}}/u_*$ for domain C.

characteristic is the peak values of $\sigma_{\tilde{u}}/u_*$: they do not vary too much (from 2.8 to 3.1) for the range of Re_{SM} from 0.65×10^5 to 7.17×10^5. An asymptote of $\sigma_{\tilde{u},max}/u_*$ for a sufficiently large value of Re_{SM} is about 3.1. The same characteristic for the peak values of $\sigma_{\tilde{w}}/u_*$ can also be seen from this figure.

As for the profiles of σ_u/u_*, σ_v/u_* and σ_w/u_* in the SGS buffer layer, LES can only parameterize them by using, for example, the eddy viscosity assumption. Mason and Thomson (1987) adopted two kinds of estimates for SGS σ_u. One is an isotropic estimate, given by

$$E_s = \frac{1}{2}\sum_{i=1}^{3}\overline{u'_{i,s}{}^2} = \frac{l^2 s^2}{C_E}, \tag{3.49}$$

where E_s is SGS TKE, $l = C_s\Delta$, s is the local velocity strain rate, and C_E is the stress-energy ratio, empirically taken as 0.3. This yields

$$\overline{u_s'^2} = \overline{v_s'^2} = \overline{w_s'^2} = \frac{2}{3}E_s = \frac{2}{3}\frac{l^2 s^2}{C_E}. \tag{3.50}$$

Another is an anisotropic estimate, in which the weights over three components are based on the observed values found in engineering shear flows near walls (Launder, Reece and Rodi, 1975), given by

$$\overline{u_s'^2} = \frac{2}{3}\frac{l^2 s^2}{C_E}[\alpha + 2.435(1-\alpha)], \tag{3.51}$$

$$\overline{v_s'^2} = \frac{2}{3}\frac{l^2 s^2}{C_E}[\alpha + 1.185(1-\alpha)], \tag{3.52}$$

$$\overline{w_s'^2} = \frac{2}{3}\frac{l^2 s^2}{C_E}[\alpha + 0.5(1-\alpha)], \tag{3.53}$$

where $0 \leq \alpha \leq 1$ is the matching parameter. If $\alpha = 1$, (3.51) to (3.53) all become (3.50) and can be applied to the interior where turbulence is more likely isotropic; if $\alpha = 0$, three different values indicate the degree of anisotropy and therefore they can be applied to the flow in the near-wall region. Parameterization (3.50) is definitely not valid in the near-wall region. Parameterizations (3.51) to (3.53) are based on engineering flow which is different from ABL turbulence. Mason's results show that none of them give a satisfactory profile in the near wall region in that profiles are not smoothly matched. His better estimates were obtained for $\sigma_{\bar{u}}/u_*$ at the surface even by the so-called "eye extrapolation". SGS part of σ_u/u_*, σ_v/u_* and σ_w/u_* is not presented here.

3.3.5 Spatial correlation functions of velocities

When the velocity fields have been obtained from LES, instantaneous two-point velocity correlations on horizontal planes can be calculated based on the RS velocity

fluctuations about the horizontal averages. For homogeneous turbulence, the correlation functions are defined as

$$R_{mn}(\vec{\xi};t) = \overline{u'_m(\vec{x};t)u'_n(\vec{x}+\vec{\xi};t)} \qquad m,n = 1,2,3. \tag{3.54}$$

For the present LES, the correlation functions are thus defined by

$$R_{mn}(\vec{\xi};z,t) = \frac{1}{N_x N_y}\sum_{\vec{x}\in S(z)} \tilde{u}_m(\vec{x};z,t)\tilde{u}_n(\vec{x}+\vec{\xi};z,t) \qquad m,n = 1,2,3 \tag{3.55}$$

where $S(z)$ denotes the set of grid points on a rectangular horizontal domain at height z:

$$S(z) = \{(x_i, y_j, z), i = 0,1,...,N_x, j = 0,1,...,N_y | x_i = i\Delta_x, y_j = j\Delta_y\} \tag{3.56}$$

and $\vec{\xi} \in S_1(z)$ with

$$\begin{aligned} S_1(z) = \{(\xi_{x,i}, \xi_{y,j}, z), i &= -\frac{N_x}{2}+1,...,-1,0,1,...,\frac{N_x}{2}, \\ j &= -\frac{N_y}{2}+1,...,-1,0,1,...,\frac{N_y}{2} \\ & \quad |\xi_{x,i} = i\Delta_x, \xi_{y,j} = j\Delta_y\}. \end{aligned} \tag{3.57}$$

One can define an extended horizontal domain using periodic extension so that some values of $\tilde{u}_m(\vec{x};t)$ and $\tilde{u}_n(\vec{x}+\vec{\xi};t)$ at outside of the rectangle region encountered in (3.55) become meaningful. The correlation functions have the properties:

$$R_{mm}(\vec{0};z,t) = [\tilde{u}_m^2(\vec{x};z,t)] \qquad m = 1,2,3 \tag{3.58}$$

$$R_{mm}(\vec{\xi};z,t) = R_{mm}(-\vec{\xi};z,t) \qquad m = 1,2,3 \tag{3.59}$$

$$\lim_{|\vec{\xi}|\to\infty} R_{mn}(\vec{\xi};z,t) = 0 \qquad m,n = 1,2,3. \tag{3.60}$$

The two-point correlation coefficients are defined by

$$r_{mn}(\vec{\xi};z,t) = \frac{R_{mn}(\vec{\xi};z,t)}{[\tilde{u}_m^2(\vec{x};z,t)]^{\frac{1}{2}}[\tilde{u}_n^2(\vec{x};z,t)]^{\frac{1}{2}}}. \tag{3.61}$$

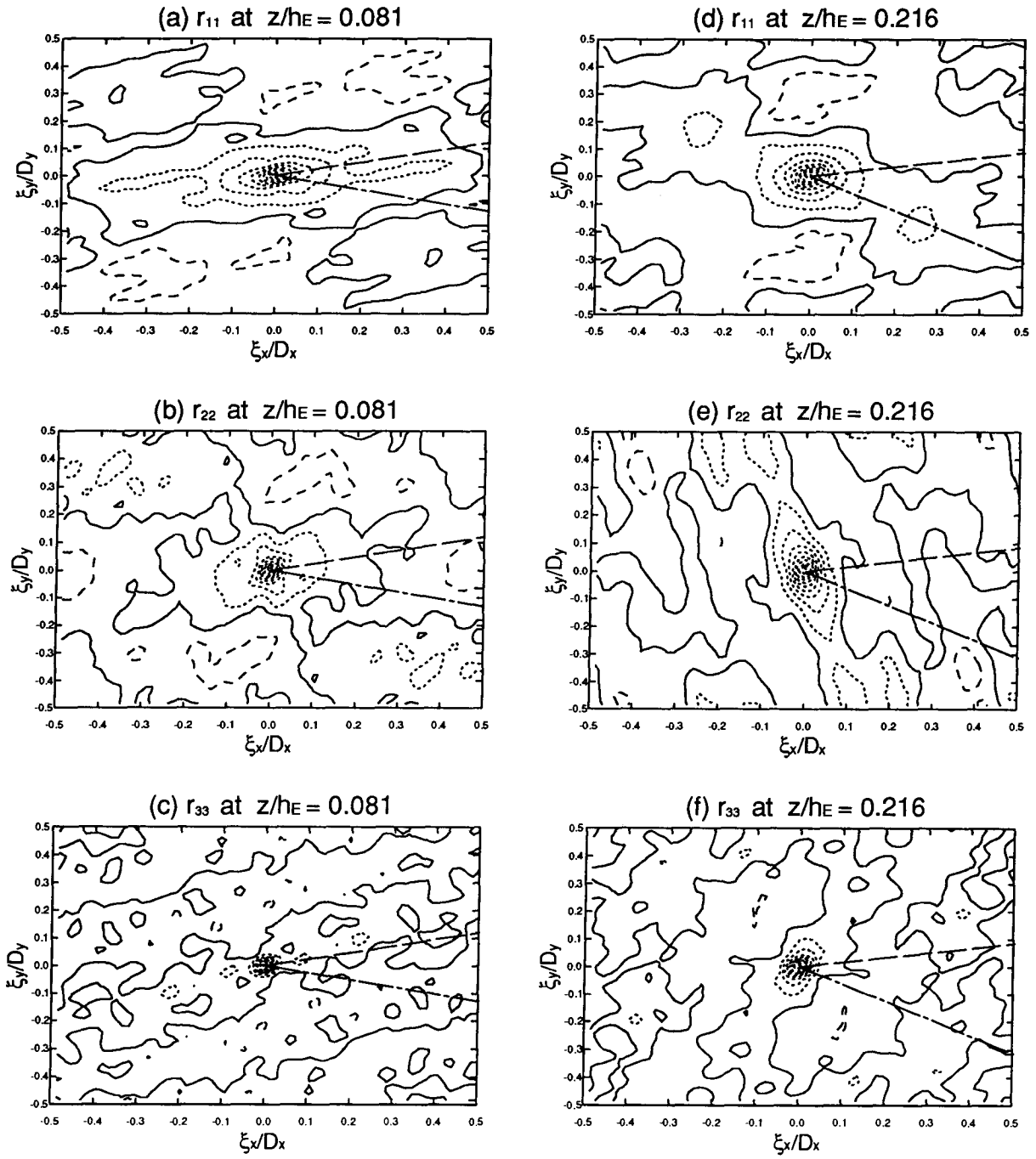

Figure 3.25: Contours of $r_{11}(\xi; z, t)$ at $t/t_f = 7.2$ for case N64C075. The solid curves are for $r_{ii} = 0$; Each increment of 0.1 from $r_{ii} = 0$ to $r_{ii} = 1$ is indicated by a dotted curve; each increment of -0.1 from $r_{ii} = 0$ to $r_{ii} = -1$ is indicated by a dashed curve. The long dashed line represents the mean wind direction; dot-dash line represents the direction of local RS shear stress.

The correlation coefficients have the properties:

$$r_{mm}(\vec{0}; z, t) = 1 \qquad m = 1, 2, 3 \tag{3.62}$$

$$r_{mm}(\vec{\xi}; z, t) = r_{mm}(-\vec{\xi}; z, t) \qquad m = 1, 2, 3 \tag{3.63}$$

$$\lim_{|\vec{\xi}| \to \infty} r_{mn}(\vec{\xi}; z, t) = 0 \qquad m, n = 1, 2, 3. \tag{3.64}$$

Since shear turbulence is anisotropic, the contour lines for $R_{mm}(\vec{\xi}; z, t)$ or $r_{mm}(\vec{\xi}; z, t)$ are not circles.

Figure 3.25 presents the correlation coefficients at the instant $t/t_f = 7.2$ and two different height levels: $z/h_E = 0.081$, which is within the USL, and $z/h_E = 0.216$, which is just above the ASL. Contours on the figure indicate the directional structure of ABL turbulence and the order of the integral length scale: purely isotropic turbulence would produce circular contours, and 2D horizontal rolls would produce parallel lines; for turbulence with a large integral length scale, contours of positive values of r_{ii} tend to spread widely, and for turbulence with a small integral length, these contours will be clustered. It is found in figure 3.25 that RS turbulence becomes increasingly isotropic with increasing height and has larger integral length scales. The w-component of turbulence has an extremely small integral length scale and the u-component has the largest scale among the three components. The correlation coefficient r_{11} is more elongated along the direction of the shear stress vector and the turning of the shear stress vector with height (shown in figure 3.45 on page 115) causes the corresponding change in the direction of the most highly correlated fluctuations.

3.4 LES results for a turbulent Ekman layer

In the last section, a broad range of results regarding to turbulence statistics in the USL were presented. Even though the concentration of this study was on the USL, the

numerical mesh has been set up to include the whole ABL, up to about 2 km. Previous LES work by Deardorff (1970a) and Mason and Thomson (1987) solved the whole ABL for their own purposes. The present LESs not only reproduce these results, but also investigate the effects of SM-Reynolds number on the results in the whole ABL.

3.4.1 Mean profiles of velocities and the Ekman spiral

Mean profiles and the Ekman spiral

Normalized mean velocities for domain A are presented as components in figure 3.26. The component curves are tightly clustered, and no indication of Re_{SM}-dependence of

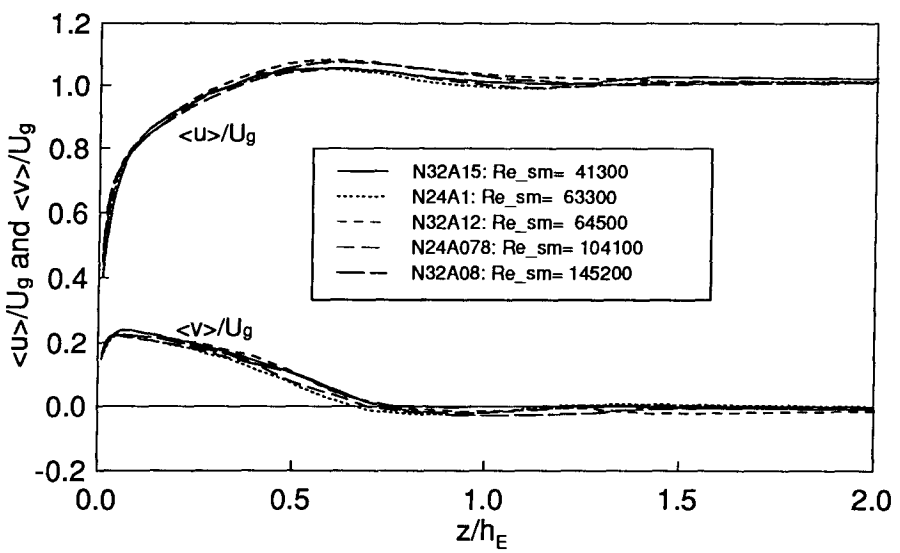

Figure 3.26: Profile of mean velocity components $\langle u \rangle / U_g$ and $\langle v \rangle / U_g$ for domain A.

the velocity profiles is shown in this figure. As discussed in the beginning of this chapter (see page 72), a major influence of the Coriolis force is on the inertial adjustment of the mean velocity components. If the time averaging interval is not large enough compared with the time scale of the Coriolis force, $2\pi/f \approx 62800$ second, mean velocity components may deviate their true profiles. A slight scatter occurred for the mean velocity profiles

in figure 3.26 and is attributed to the inertial oscillation due to the Coriolis force.

Figure 3.27 shows the normalized mean velocities for domain B, while figure 3.28 shows the normalized mean velocities for domain C. Also, Re_{SM}-dependence of the velocity profiles is hardly seen from either figure.

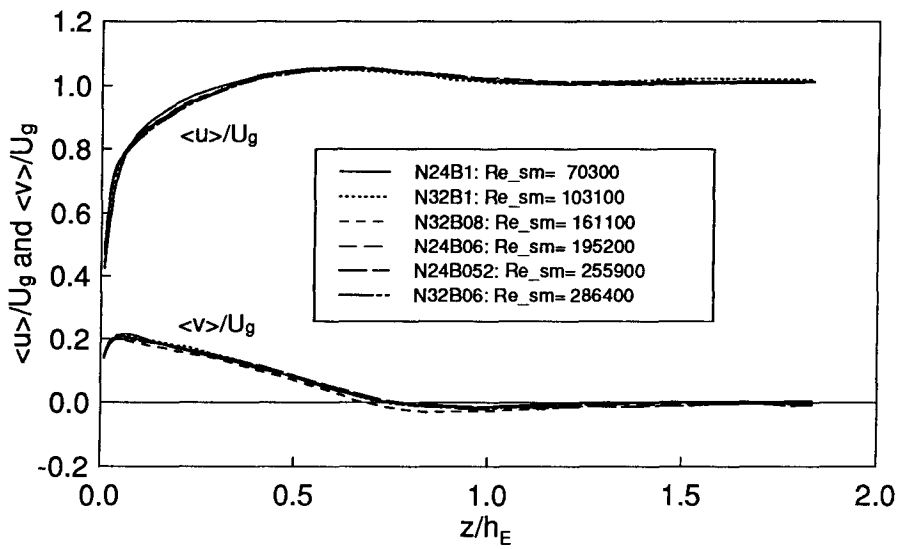

Figure 3.27: Profile of mean velocity components $\langle u \rangle / U_g$ and $\langle v \rangle / U_g$ for domain B.

The hodograph form of the mean velocities for domain C is shown in figure 3.29, together with the laminar solution of Ekman layer represented by equation (3.1) to (3.3). It is obvious that the turning angle between the shear stress vector at the surface and the geostrophic wind vector (x-axis) for the turbulent cases is much smaller than that of the laminar case. Among those turbulent cases, only small differences of this turning angle are observed. A scatter is seen in the upper Ekman layer, which is explained by the inertial oscillation due to the Coriolis force. The hodograph form of the mean velocities for domain A and that for domain B have similar results and therefore are not shown here.

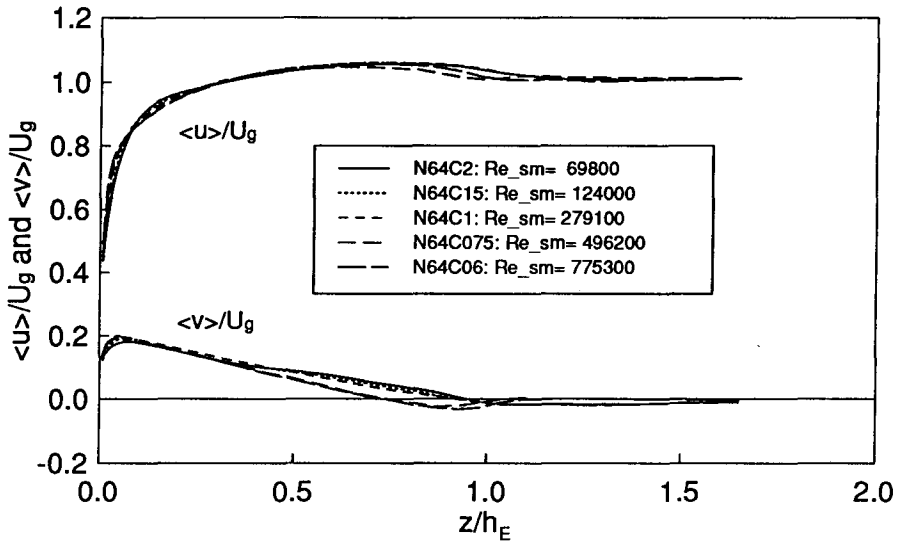

Figure 3.28: Profile of mean velocity components $\langle u \rangle / U_g$ and $\langle v \rangle / U_g$ for domain C.

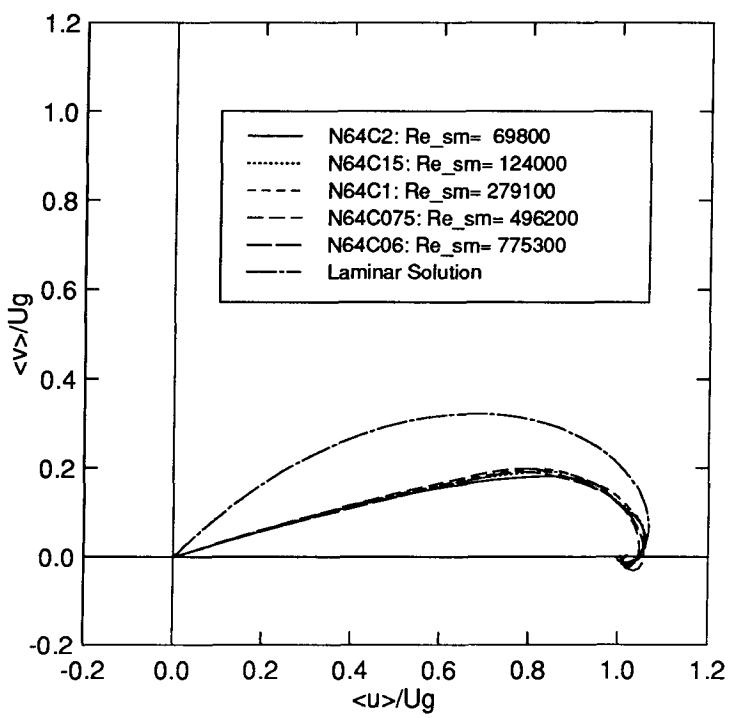

Figure 3.29: Hodograph of mean velocity components $\langle u \rangle / U_g$ and $\langle v \rangle / U_g$ for domain C; "Laminar Solution" represents the hodograph of velocity components for a laminar Ekman layer.

3.4.2 Mean profiles of shear stresses

In the preceding part of the text, h_E has been used to normalize z in many situations and its determination is now explained. This study derives h_E based on the mean profiles of shear stresses in the whole ABL, rather than giving an accurate definition. It is required that above h_E, $|\langle\tilde{u}\tilde{w}\rangle/u_*^2|$ and $|\langle\tilde{v}\tilde{w}\rangle/u_*^2|$ should be very small (*e.g.*, < 0.02), and that profiles of $-\langle\tilde{u}\tilde{w}\rangle/u_*^2$ and $-\langle\tilde{v}\tilde{w}\rangle/u_*^2$ should be collapse into one for all runs. Based on these criteria, this study found that the value of h_E mainly depends on domain size: $h_E \approx 830$ m for domain A, $h_E \approx 970$ m for domain B and $h_E \approx 1080$ m for domain C. These data have been listed in table 3.5.

In figure 3.30, normalized RS shear stress components for domain A are shown. The

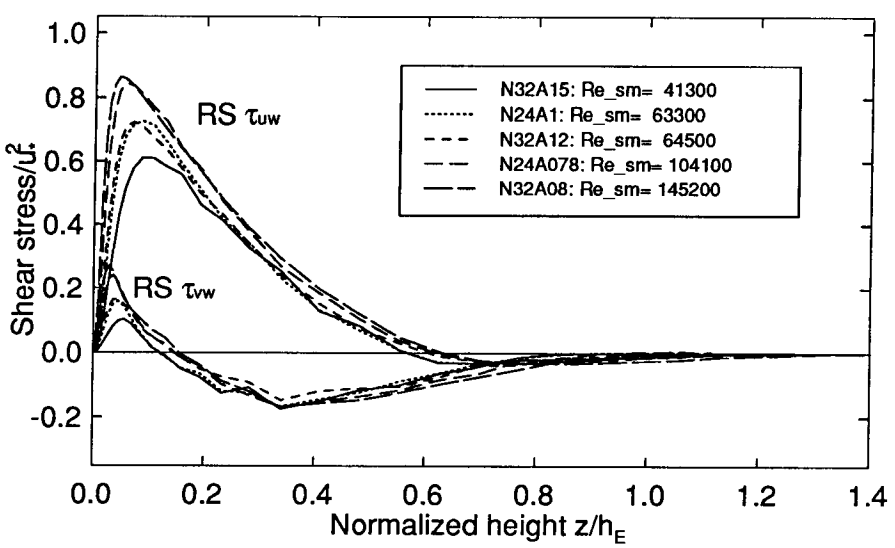

Figure 3.30: RS stress $-\langle\tilde{u}\tilde{w}\rangle$ and $-\langle\tilde{v}\tilde{w}\rangle$ for domain A.

Re_{SM}-dependence is not clearly shown except in the surface layer where $z < 0.1h_E$. The component τ_{uw} decreases with increasing height and changes its sign at $z/h_E \approx 0.6$. This characteristic can also been seen from the RS shear stresses for domain B, as shown in figure 3.31. In the cases of domain C, however, τ_{uw} decreases to zero without changing

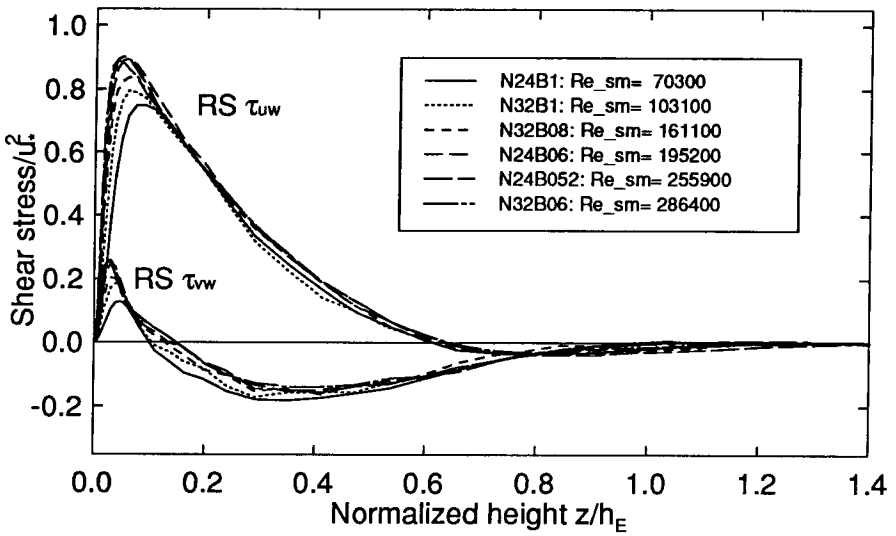

Figure 3.31: RS stress $-\langle\tilde{u}\tilde{w}\rangle$ and $-\langle\tilde{v}\tilde{w}\rangle$ for domain B.

sign, as illustrated by figure 3.32. In addition, the Re_{SM}-dependence of profile of RS τ_{uw} and τ_{vw} can be seen from this figure: as Re_{SM} becomes larger, the profile of RS τ_{uw} in the middle of the ABL tends to be smaller for a fixed height, while the value of RS τ_{uw} in the ASL increases; the same tendency occur to the profile of RS τ_{vw}.

Total shear stress components for domain A, domain B and domain C are shown in figure 3.33, figure 3.34 and figure 3.35, respectively. One common characteristic for the three groups of cases is that profiles are not smoothly connected in the ASL where transition from RS dominated flow to SGS dominated flow occurs. This has to be attributed to the poor performance of the Smagorinsky SGS model adopted by the present study: it underestimates the SGS shear stresses. Since it is very difficult to determine the amount of these underestimates, the "true" values of τ_{uw} and τ_{vw} are unknown. The "true" values of τ_{uw} and τ_{vw} are very important to determine u_*, and therefore are the key points for the success of LES. Most LES results in the present study are based on u_{*r}, which is obtained from the maximum value of τ_{uw} and τ_{vw}. From figure 3.33 to figure 3.35, if it is assumed that the surface values of τ_{uw} and τ_{vw} can be

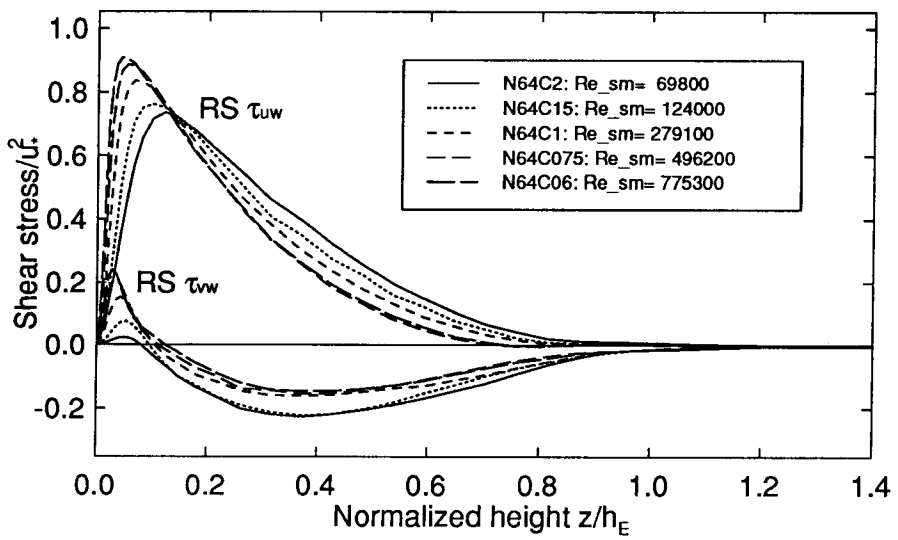

Figure 3.32: RS stress $-\langle\tilde{u}\tilde{w}\rangle$ and $-\langle\tilde{v}\tilde{w}\rangle$ for domain C.

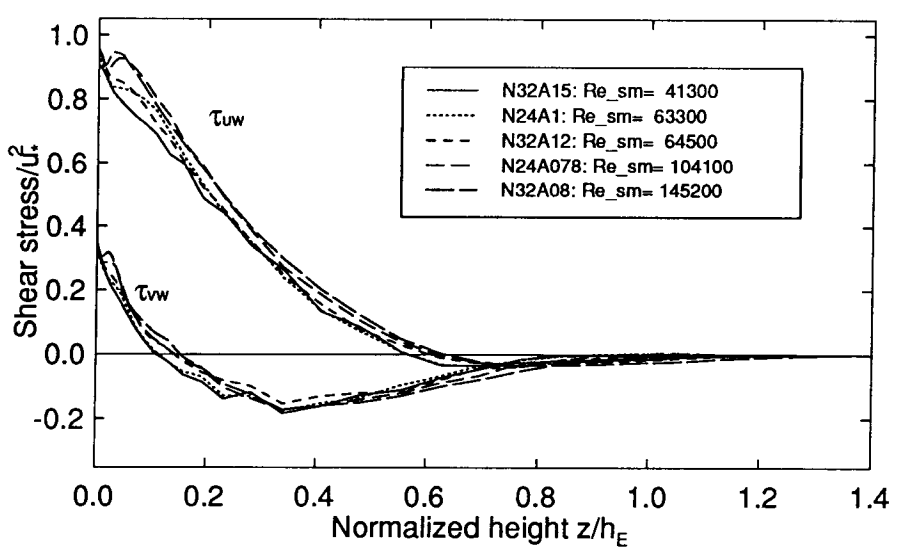

Figure 3.33: Total stress $-\overline{u_s' w_s'} - \langle\tilde{u}\tilde{w}\rangle$ and $\overline{v_s' w_s'} - \langle\tilde{v}\tilde{w}\rangle$ for domain A.

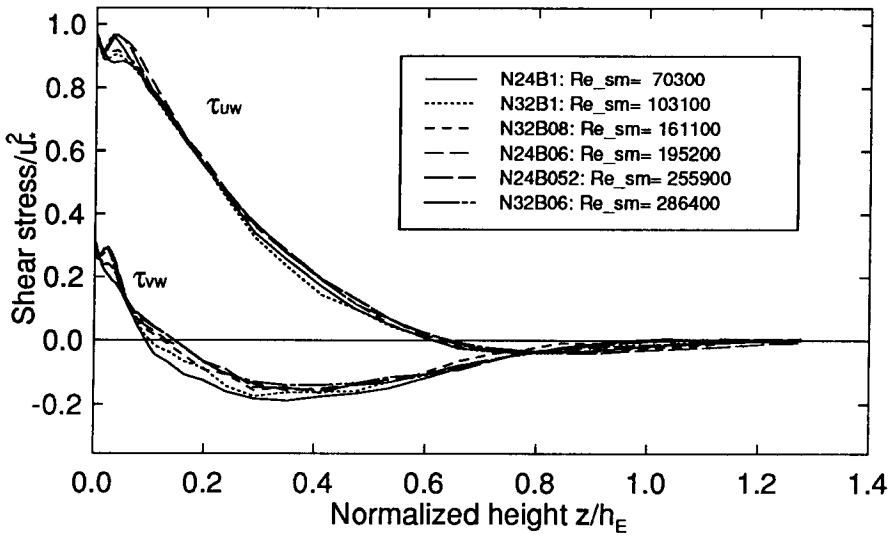

Figure 3.34: Total stress $-\overline{u_s' w_s'} - \langle \tilde{u}\tilde{w} \rangle$ and $-\overline{v_s' w_s'} - \langle \tilde{v}\tilde{w} \rangle$ for domain B.

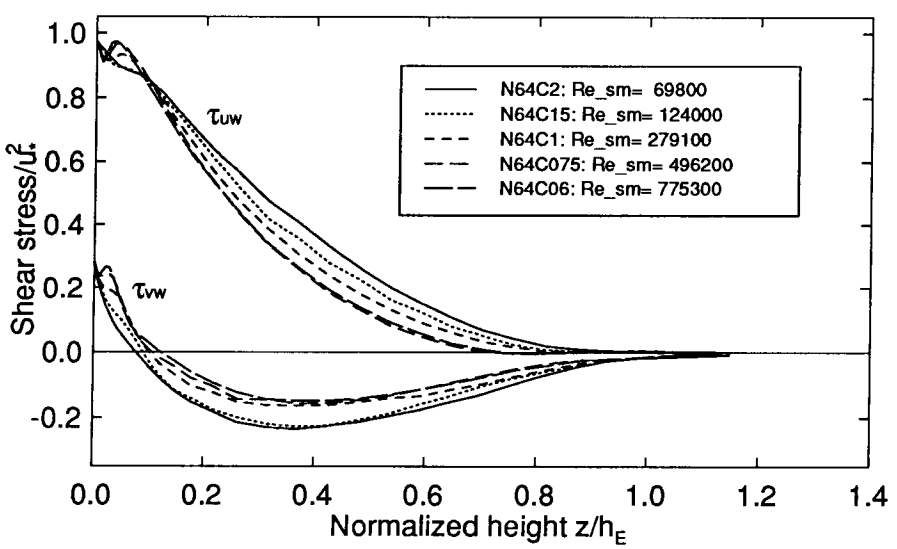

Figure 3.35: Total stress $-\overline{u_s' w_s'} - \langle \tilde{u}\tilde{w} \rangle$ and $-\overline{v_s' w_s'} - \langle \tilde{v}\tilde{w} \rangle$ for domain C.

obtained by smoothly extrapolating RS τ_{uw} and τ_{vw} down to the surface, it seems that the surface values of u_* are larger than $u_{*\tau}$ by from 10% to 20%.

In an EAM model of turbulent Ekman layer, an eddy viscosity closure is widely adopted, which writes

$$0 = -f(V_g - v) + \frac{\partial}{\partial z}\tau_{uw}, \tag{3.65}$$

$$0 = f(U_g - u) + \frac{\partial}{\partial z}\tau_{vw}, \tag{3.66}$$

$$\tau_{uw} = \nu_e \frac{\partial u}{\partial z}, \tag{3.67}$$

$$\tau_{vw} = \nu_e \frac{\partial v}{\partial z}. \tag{3.68}$$

Expressed in the form of vectors, (3.67) and (3.68) are

$$\vec{\tau} = \nu_e \frac{\partial \vec{v}}{\partial z}. \tag{3.69}$$

LES calculates the left-hand side term explicitly, as well as the velocity gradient $\partial\vec{v}/\partial z$ on the right-hand side of (3.69). One necessary condition for (3.69) to be satisfied is that the turning angles of both sides must be equal. In figure 3.36, the variation of the turning angle of total shear stress α_τ is shown, as well as the variation of the turning angle of velocity gradient, α_{dv}. All angles are measured with respect to the geostrophic wind vector, i.e., the x-axis. A wide scatter near the top of the ABL is due to the small values of local shear stresses since the turning angle is evaluated as $\alpha_\tau = \arctan(\tau_y/\tau_x)$. It can be seen that α_τ decreases almost linearly (turn in clockwise direction) with height and through much of the ABL, with nearly no dependence on SM-Reynolds number. From the height $z \approx 0.05h_E$ to $z \approx 0.6h_E$, in which RS turbulence plays an important role, the turning angles of mean velocity shear are systematically smaller than those of shear stress, with the former being parallel to the latter. If an average is taken over

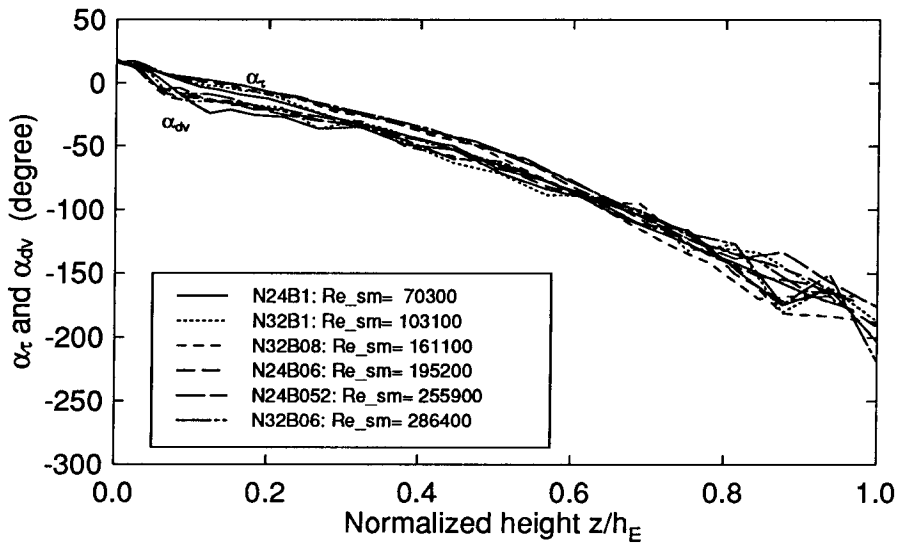

Figure 3.36: Turning angle between shear stress vector and the geostrophic wind vector, denoted by α_τ, and turning angle between velocity shear vector and the geostrophic wind vector, denoted by α_{dv}, for domain B, as functions of z/h_E.

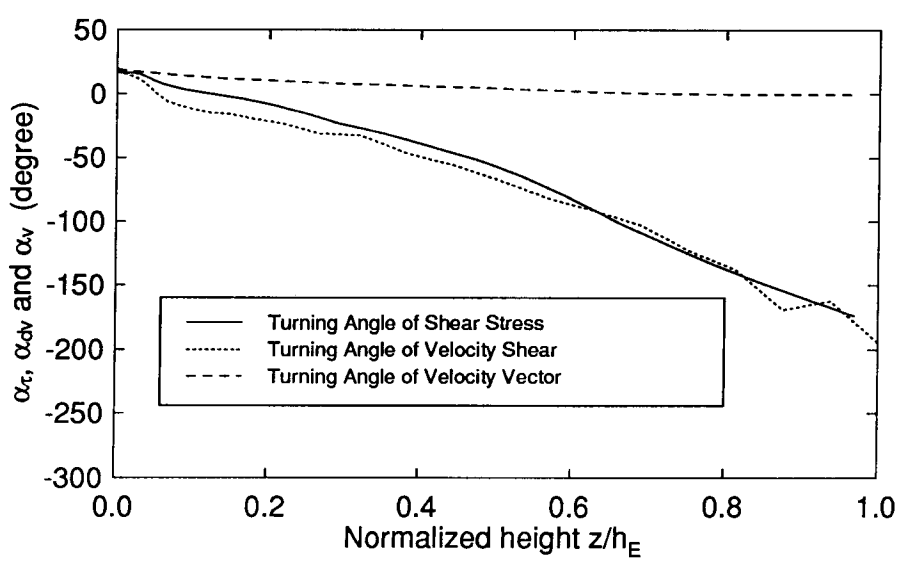

Figure 3.37: Case-averaged α_τ, α_{dv} and α_v as functions of z/h_E for domain B; α_v is the turning angle between the mean velocity vector and the geostrophic wind vector.

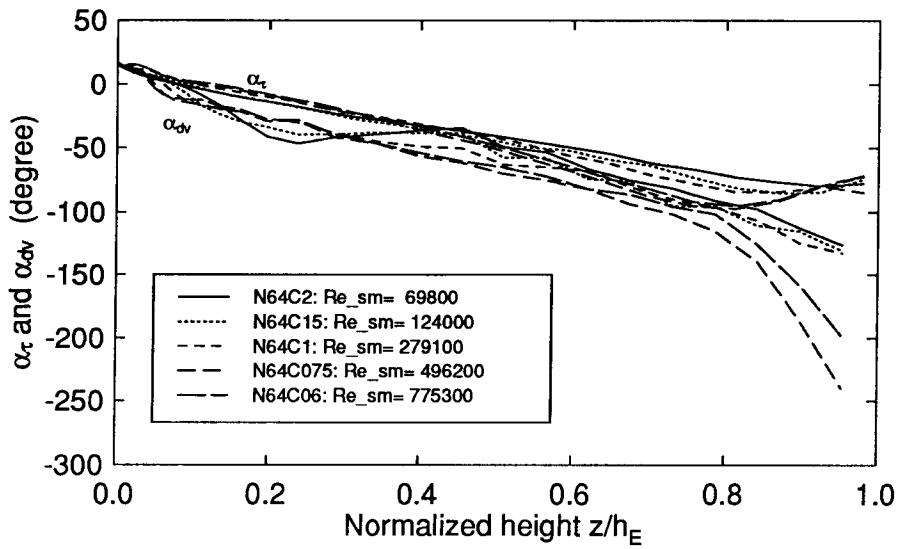

Figure 3.38: Turning angle α_τ and α_{dv} for domain C, as functions of z/h_E.

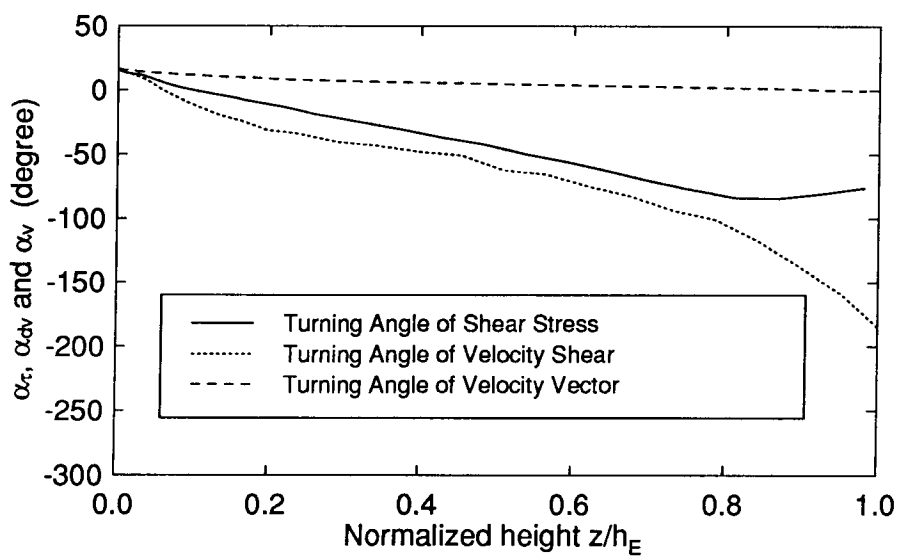

Figure 3.39: Case-averaged α_τ, α_{dv} and α_v as functions of z/h_E for domain C.

the six cases, as shown in figure 3.37, such a characteristic holds up to $z \approx 0.6h_E$. Similar situations are seen for domain C, as shown in figure 3.38 and figure 3.39. It is also indicated by figure 3.36 and figure 3.38 that the profile of turning angle of velocity gradient α_{dv} depends on Re_{SM}, and it is more parallel to that of α_τ when Re_{SM} becomes larger.

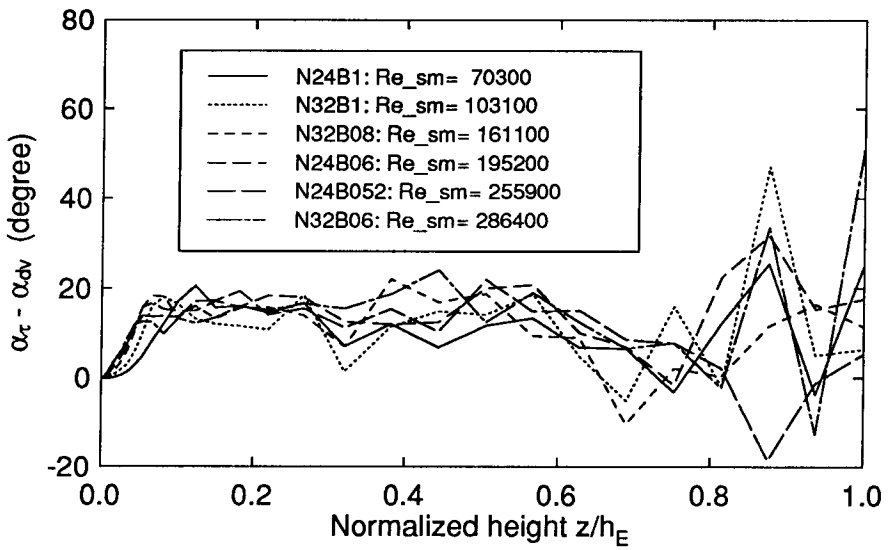

Figure 3.40: Difference $\alpha_\tau - \alpha_{dv}$ as a function of z/h_E for domain B.

Figure 3.40 and figure 3.41 present the difference between α_τ and α_{dv} for domain A and domain B. The differences are about 15° to 20°. In spite of some scatter above $z \approx 0.3h_E$, it seems that a positive value of $\alpha_\tau - \alpha_{dv}$ prevails in most of the ABL. This phenomenon can be stated as follows: with an increasing height, shear stress vector and velocity shear vector rotate in the clockwise direction, but the former lags behind the latter with an angle of about 20°. These significant differences in α_τ and α_{dv} imply that the eddy viscosity closure (3.69) is not appropriate for the turbulent Ekman layer.

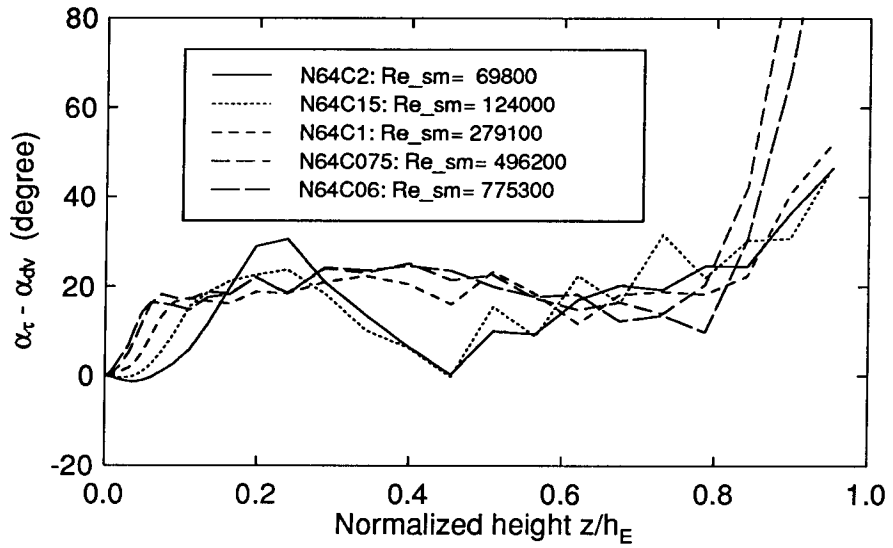

Figure 3.41: Difference $\alpha_\tau - \alpha_{dv}$ as a function of z/h_E for domain C.

3.4.3 Mean profiles of turbulence standard deviations

In this section, the vertical profiles of the components of RS turbulence energy, or standard deviations of the velocity fluctuations, are presented. It is noted that the heights above which SGS motions have small contributions (smaller than 5%) to total shear stresses are very low in the present LES runs (*e.g.*, see figure 3.14), usually lower than $0.1h_E$. If (3.50) or (3.51) to (3.53) are adopted, which are based on the assumption of constant stress-energy ratio, as a parameterization of SGS turbulence energy components, one can conclude that the components of SGS turbulence energy must be of the same order of those of SGS shear stresses, frequently less than 5% of RS parts.

Figure 3.42 presents vertical profiles of three components of standard deviations of velocity fluctuations, normalized by u_*, for domain A. One typical characteristic of these quantities is that they do not rapidly approach zero above the top of the Ekman layer. LES of the ABL by Mason and Thomson (1987), DNS of the Ekman layer by Coleman, Ferziger and Spalart (1990) and DNS of a Ekman-layer-like flow by Spalart (1989) gave

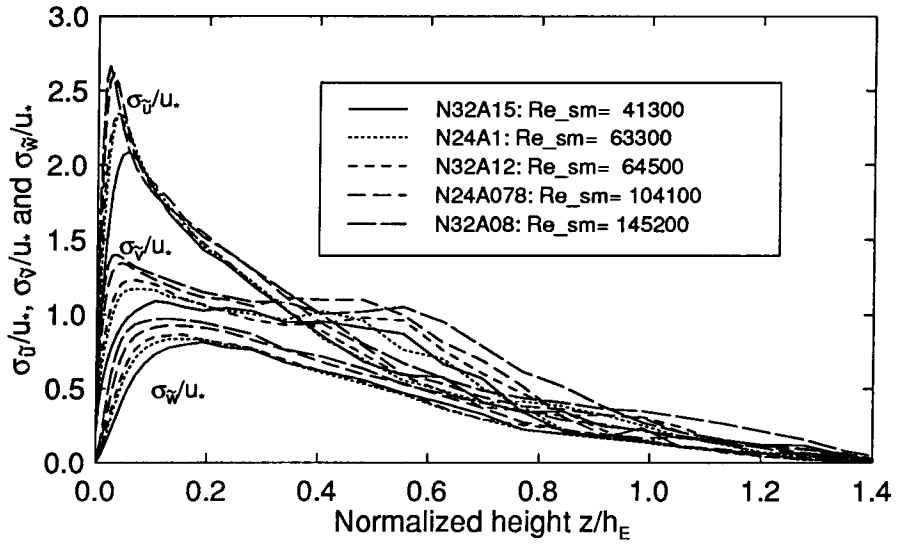

Figure 3.42: Profiles of $\sigma_{\tilde{u}}/u_*$, $\sigma_{\tilde{v}}/u_*$ and $\sigma_{\tilde{w}}/u_*$ for domain A.

similar results: shear stresses reach zeros but velocity standard deviations do not. This can be explained by the fact that there are some turbulent eddies above the height of the ABL, but the mean velocity components are almost constant so that a very small amount of momentum can be transferred across horizontal planes, thus causing small shear stresses. Some scatter is seen above $z > 0.5h_E$ for different SM-Reynolds numbers, but for z from 0.2 to 0.4, the three profiles are almost SM-Reynolds number independent. At heights above about $0.75h_E$, turbulence exhibits isotropy in that $\sigma_{\tilde{u}} \approx \sigma_{\tilde{v}} \approx \sigma_{\tilde{w}}$. When $0.4 < z/h_E < 0.75$, it is found from figure 3.42 that $\sigma_{\tilde{v}} > \sigma_{\tilde{u}} > \sigma_{\tilde{w}}$. Similar results were found in the DNS of the Ekman-layer-like flow by Spalart (1989) between $0.2 < z/h_E < 0.6$. The tendency for $\sigma_{\tilde{v}}$ to exceed $\sigma_{\tilde{u}}$ is observed at all Reynolds numbers. Since no such phenomenon is found in turbulent channel flows (Moin and Kim, 1982), nor in the TBL over a plate with zero pressure gradient (Spalart, 1988), this might be a real characteristic of a turbulent flow with a spiral, such as the Ekman layer (with the Ekman spiral) and the spiral flow dealt with by Spalart (1989). Coleman, Ferziger and Spalart (1990) obtained an interval of (0.4,0.75) in which $\sigma_{\tilde{v}} > \sigma_{\tilde{u}} > \sigma_{\tilde{w}}$ in their DNS

of Ekman layer turbulence, but the three values were very close which means that the turbulence is nearly isotropic in this interval. Figure 3.43 and figure 3.44 shows vertical

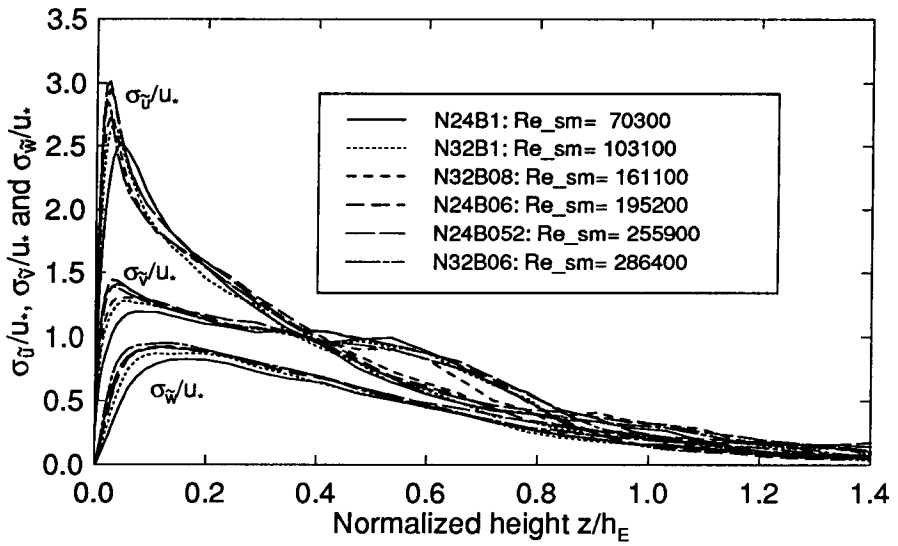

Figure 3.43: Profiles of $\sigma_{\tilde{u}}/u_*$, $\sigma_{\tilde{v}}/u_*$ and $\sigma_{\tilde{w}}/u_*$ for domain B.

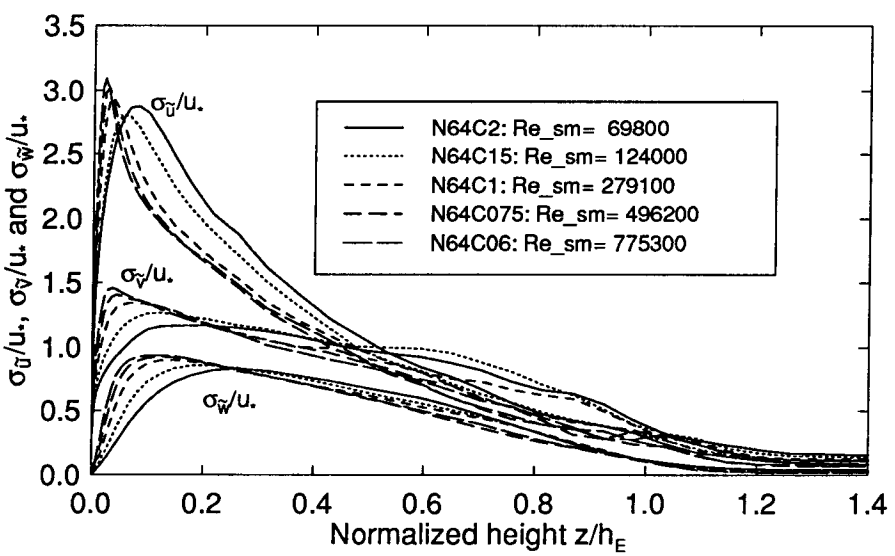

Figure 3.44: Profiles of $\sigma_{\tilde{u}}/u_*$, $\sigma_{\tilde{v}}/u_*$ and $\sigma_{\tilde{w}}/u_*$ for domain C.

profiles of $\sigma_{\tilde{u}}/u_*$, $\sigma_{\tilde{v}}/u_*$ and $\sigma_{\tilde{w}}/u_*$ for domain B and domain C, respectively. The Re_{SM}-dependence is hardly seen in most of the ABL in this group of simulations. The closer

to the ASL, the less isotropic the turbulence is. $\sigma_{\tilde{u}}/u_*$ rapidly climbs up to a value of 3, larger than 2.5 of Spalart (1989) and 2.25 of Coleman, Ferziger and Spalart (1990). The maximum value of $\sigma_{\tilde{v}}$ obtained by the present LES is about 1.5, which is also larger than that of Spalart (1989), of about 1.4, and that of Coleman, Ferziger and Spalart (1990), of about 1.1. In fact, it is generally accepted that for most wall turbulent flows, the close-wall values of σ_u, σ_v and σ_w increase with SM-Reynolds number. Therefore, the larger values obtained from the present LESs for the larger Reynolds number flows should not be much of a surprise. Another possibility is that underestimated shear stress or u_* at the surface (discussed in section 3.4.2) yields overestimated dimensionless quantities when normalized by u_*. The dependence of the surface values on SM-Reynolds number has been discussed in section 3.3.4.

3.4.4 Spatial correlation functions of velocities

Figure 3.45 shows the correlation coefficients at the instant $t/t_f = 7.2$ and two different height levels: $z/h_E = 0.537$, which is in the middle of the ABL, and $z/h_E = 0.814$, which is near the top of the ABL. Since purely isotropic turbulence would produce circular contour lines, the turbulence at these two heights is almost isotropic. In addition, the integral length scales for three velocity components are almost the same. It is found that the turning of the shear stress vector with height causes the corresponding change in direction of the most highly correlated fluctuations.

In section 2.2.3 on page 33, the criteria for domain size were discussed, and periodic boundary conditions were introduced for all variables in order to maintain turbulence. It is expected that as long as the horizontal domain size is large enough, the eddies in the center of the domain and those at the edge of the domain are nearly uncorrelated, and side-effects of the periodic boundary conditions can be greatly reduced. In fact, it is sufficient to require that the size be larger than $\mathcal{L}$, the order of integral length scale of

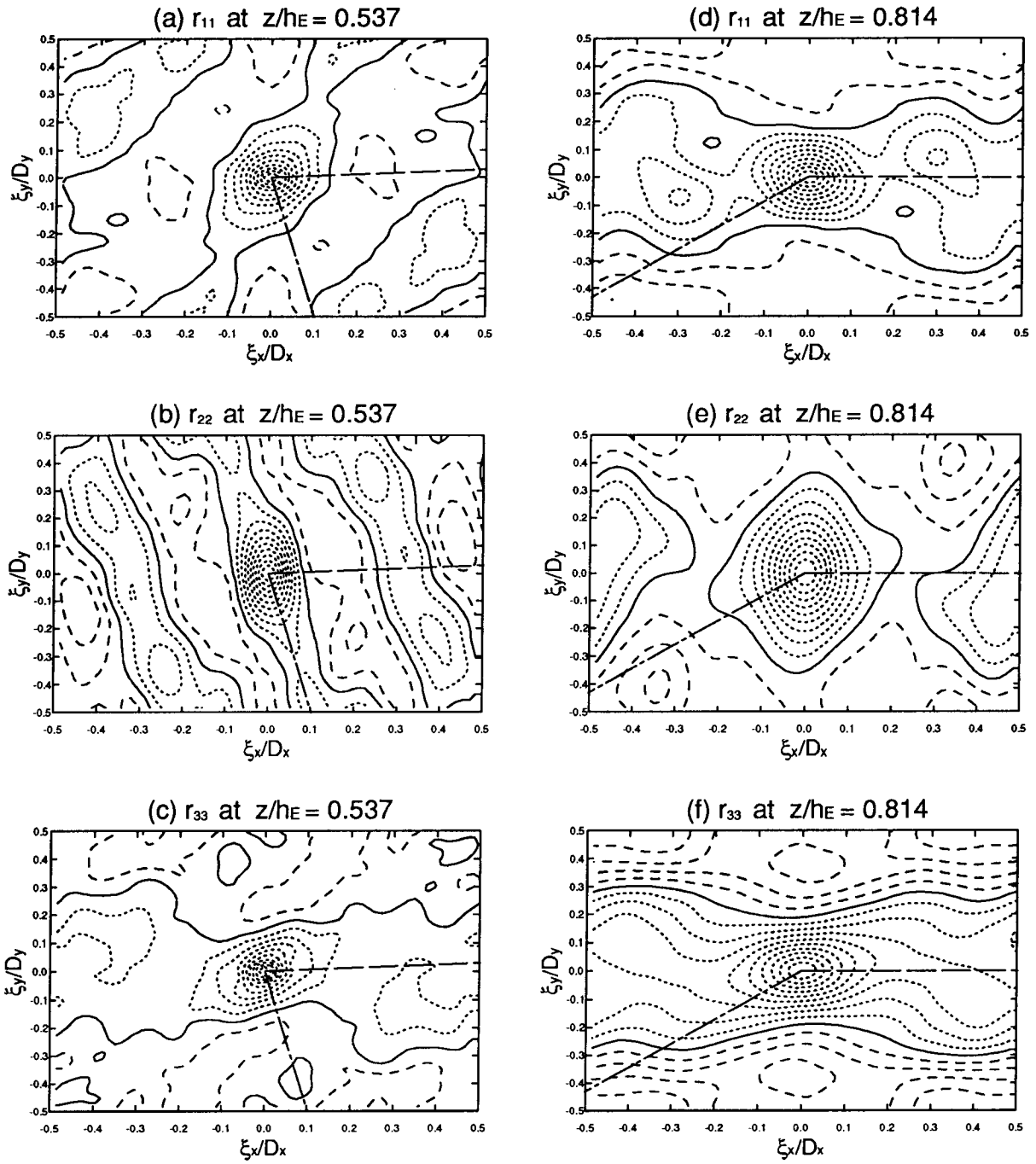

Figure 3.45: Contours of $r_{11}(\xi; z, t)$ at $t/t_f = 7.2$ for case N64C075. The solid curves are for $r_{ii} = 0$; Each increment of 0.1 from $r_{ii} = 0$ to $r_{ii} = 1$ is indicated by a dotted curve; each increment of -0.1 from $r_{ii} = 0$ to $r_{ii} = -1$ is indicated by a dashed curve. The long dashed line represents the mean wind direction; dot-dash line represents the direction of local RS shear stress.

the turbulence.

The $r_{ii} = 0.2$ contour has been suggested to be the criterion for LES domain size (Coleman, Ferziger and Spalart, 1990; Mason and Thomson, 1987): if it is closed within the simulation domain for several heights at which turbulence is well resolved, then the domain size is considered adequate. Figure 3.45 indicates that horizontal domain size of 3,840 m $\times$ 1,920 m is large enough.

Chapter 4

Large Eddy Simulation of an Unstable Atmospheric Boundary Layer

4.1 Scalings and dimensional analysis

4.1.1 Structure of an unstable ABL

In chapter 3, a horizontally homogeneous ABL under adiabatic, barotropic conditions was explored. Now, a positive turbulent sensible heat flux, denoted by $\overline{w'\theta'}_0$, is added at the surface so that the ABL becomes convectively unstable, most other conditions being the same as those described in chapter 3. When $\overline{w'\theta'}_0$ is sufficiently large, turbulence in the upper part of the ABL is dominated by buoyancy, and mean wind velocity and potential temperature profiles are nearly independent of height; this part of the ABL is referred to as the *mixed layer* (ML). The entire ABL is often called a "convective boundary layer", or CBL. In some cases, the term CBL is used to refer to a purely convective ABL in which there is no geostrophic wind and therefore no shear-generated turbulence. The present study uses the term CBL to represent an ABL which contains a ML.

In a real CBL, it is recognized that the elevation of the so-called *inversion base*, above which temperature[1] increases with height in the so-called *inversion layer*, often defines the ABL height, which is denoted by Z_i in this chapter. In general, Z_i shows strong diurnal variation, and typically reaches a height of about 1-2 km in afternoon of a sunny day in summertime, and mainly depends on $\overline{w'\theta'}_0$, vertical temperature profile in the

[1] "Potential temperature" hereafter is referred to as "temperature" unless otherwise specified.

inversion layer and the mean temperature in the ML. Moreover, temperature profiles in the inversion layer can be affected by synoptic processes (Garratt, 1992).

Sudden jumps of vertical profiles of temperature and other variables mark the *entrainment layer* (EL) or *interfacial layer* between the ML and the capping inversion layer. This sublayer is a result of the continuous penetrative convection at the inversion base by convective elements generated by surface heating which causes a turbulent transport of warm air downward into the ML, a process referred to as *entrainment.* Dominant processes in the EL are even more complicated than those in the ML, many remaining unsolved as yet (Driedonks and Tennekes, 1984).

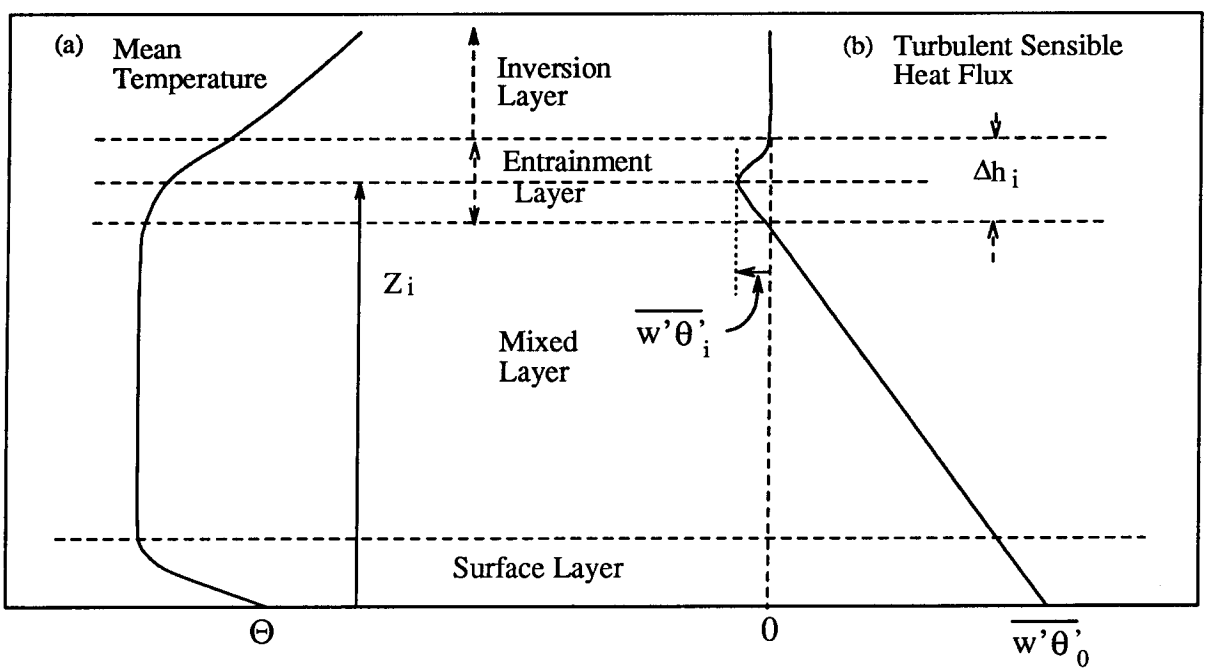

Figure 4.1: Sketch of (a) vertical profiles of mean temperature, and (b) heat flux in a CBL. Z_i is the height of the inversion base; $\overline{w'\theta'}_0$ is the surface heat flux; $\overline{w'\theta'}_i$ is the heat flux at the inversion base; Δh_i is the thickness of the entrainment layer.

The typical structure of a CBL can be shown through vertical profiles of mean temperature and turbulent sensible heat flux in figure 4.1. The ASL in a CBL is conventionally taken to be $0 \leq z \leq 0.1Z_i$, the height of the ASL being denoted by h_s. The depth of the

EL is denoted by Δh_i. The positive surface heat flux $\overline{w'\theta'}_0$ together with the negative entrainment heat flux $\overline{w'\theta'}_i$ will result in increasing ML temperature, while the negative surface momentum flux together with the positive entrainment momentum flux [2] will change the mean velocity in the ML.

For simplicity, the present study assumes that

1. there is no synoptical scale subsidence;

2. $\overline{w'\theta'}_0$ is specified as a constant; therefore, diurnal variation of $\overline{w'\theta'}_0$ is not considered here;

3. temperature profile in the inversion layer is a linear function of z:

$$\frac{\partial \Theta}{\partial z} = \Gamma \qquad z \geq Z_i, \tag{4.1}$$

where Γ is called *the environmental temperature lapse rate.*

4.1.2 Scaling in a CBL

Scalings in the upper part of the ML are very complicated. A simplified treatment of the effects due to entrainment is to choose $\overline{w'\theta'}_i$ as one external parameter. An alternative external parameter is Γ defined by (4.1), which is adopted in the present study; in other words, it is assumed that $\overline{w'\theta'}_i$ is not an independent external parameter and can be determined by Γ, $\overline{w'\theta'}_0$, Z_i and $\beta = g/\Theta_0$, the buoyancy parameter. For a CBL, there are seven external independent dimensional parameters: the Coriolis parameter f, the friction velocity u_*, the roughness length z_0, the buoyancy parameter β, the surface heat flux $\overline{w'\theta'}_0$, the capping inversion height Z_i and the temperature lapse rate Γ, i.e.,

$$(f, u_*, z_0, \beta, \overline{w'\theta'}_0, Z_i, \Gamma). \tag{4.2}$$

[2]Geostrophic wind speed in the inversion layer is usually larger than wind speed in the ML.

Three independent dimensional units are: length (L), time (T) and temperature (K). Based on the principle of dimensional analysis (see appendix B), there are *four* independent dimensionless external parameters; equivalently, there are *five* independent external length scales, *five* independent external time scales and *five* independent external temperature scales. One of the many possible choice of the five independent external length scales is:

$$(z_0, h_E, L, Z_i, \delta h_i), \tag{4.3}$$

where L is called the Monin-Obukhov length, defined by

$$L = -\frac{u_*^3}{\kappa\beta\overline{w'\theta'}_0}, \tag{4.4}$$

and δh_i is defined by

$$\delta h_i = \frac{w_*}{(\beta\Gamma)^{1/2}} = w_* t_N, \tag{4.5}$$

where $t_N = N_{BV}^{-1} = (\beta\Gamma)^{-1/2}$ is the reciprocal of the Brunt-Väisälä frequency, and w_* is called "convective velocity", defined by Deardorff (1970b) as follows:

$$w_* = (\frac{g\overline{w'\theta'}_0 Z_i}{\Theta_0})^{1/3}. \tag{4.6}$$

If one assumes that the vertical velocity of penetrative convection in the EL is of the order of w_* (Driedonks and Tennekes, 1984), then δh_i can be interpreted as the depth of the EL, i.e., $\delta h_i \sim \Delta h_i$.

One possible choices of the four independent dimensionless external parameters is:

$$(Ro = h_E/z_0, L/z_0, Z_i/L, \delta h_i/Z_i). \tag{4.7}$$

The last parameter represents the ratio of the depth of the EL to the depth of the CBL, denoted by δh_i^+:

$$\delta h_i^+ = \frac{\delta h_i}{Z_i} = \frac{t_N}{t_*}, \tag{4.8}$$

where t_* is the turn-over time of convective eddies:

$$t_* = \frac{Z_i}{w_*}. \tag{4.9}$$

Any field quantity, say ϕ (assumed to be a function of z only), must then be written as:

$$\frac{\phi}{\phi_0} = F(\frac{z}{L}; Ro, \frac{L}{z_0}, \frac{Z_i}{L}, \delta h_i^+), \tag{4.10}$$

where ϕ_0 is a power product of dimensional parameters and must have the same dimension as ϕ.

4.1.3 Monin-Obukhov similarity

The above system is very complicated since it has four independent dimensionless external parameters which implies that any field quantity must be a function of the four parameters plus spatial variables, as given by (4.10). Fortunately, if the following conditions are satisfied:

$$\frac{h_E}{|L|} \gg 1, \qquad \frac{Z_i}{|L|} \gg 1, \qquad \frac{z_0}{|L|} \ll 1 \qquad \text{and} \qquad \frac{z}{|L|} \approx 1. \tag{4.11}$$

then the function form in (4.10) becomes[3] asymptotically independent of all but $\zeta = z/L$:

$$\frac{\phi}{\phi_0} = F(\frac{z}{L}). \tag{4.13}$$

For mean velocity shear $\partial u/\partial z$, one obtains

$$\frac{z}{\kappa u_*}\frac{\partial u}{\partial z} = \phi_m(\zeta), \tag{4.14}$$

[3]Details are given as follows. In a sublayer where z is of the order of $|L|$, a flow quantity is asymptotically independent of z_0, Z_i, δh_i and h_E, and only three dimensional external parameters in (4.2) remain, namely, u_*, β and $\overline{w'\theta'}_0$. Adding ϕ and z into the parameter group yields

$$(\phi, z; u_*, \beta, \overline{w'\theta'}_0). \tag{4.12}$$

Applying corollary 2 in appendix B to this case yields (4.13).

which is called the *Monin-Obukhov similarity* formula for momentum flux. In (4.14), κ is conventionally introduced so that $\phi_m(0) = 1$ for the neutral case. More generally, dimensional analysis should lead to the conclusion that the quantities $\overline{u_i'u_j'}/u_*^2$ $(i, j = 1, 2, 3)$, $\overline{u_i'\theta'}/(u_* T_{*,s})$ and $\overline{\theta'^2}/T_{*,s}^2$ are also universal functions of $\zeta = z/L$ if (4.11) holds. In a real CBL, however, those quantities involving horizontal fluctuations u' and v' do not follow this similarity. It has been suggested by Panofsky et al. (1977) that $\overline{u'^2}$ and $\overline{v'^2}$ are strongly affected by large convective eddies of the scale length Z_i, and they are very little influenced by the distance to the surface z.

It is assumed that in a CBL, influence of Z_i dominates over that of h_E so that the latter is often ignored (Garratt, 1992). Under this assumption, the limit process discussed above still holds as long as the following conditions are satisfied:

$$\frac{Z_i}{|L|} \gg 1, \qquad \frac{z_0}{|L|} \ll 1 \qquad \text{and} \qquad \frac{z}{|L|} \approx 1. \tag{4.15}$$

4.1.4 Free convection layer

Under the assumption that the length scale h_E is unimportant, if (4.15) holds and, in addition,

$$Z_i \gg z \gg |L| \tag{4.16}$$

hold, then Z_i and L are not important at the height z. All external length scales drop out and the only remaining length scale is z. In this case, there are only three independent dimensional parameters:

$$(z; \beta, \overline{w'\theta'}_0). \tag{4.17}$$

Three independent dimensional units are: length (L), time (T) and temperature (K). Including a field quantity, $\partial\Theta/\partial z$, for example, allows use of corollary 1 of appendix B

to yield a power law for $\partial\Theta/\partial z$:

$$\frac{\partial\Theta}{\partial z} = -C' z^{-4/3}(\frac{g}{\Theta})^{-1/3}\overline{w'\theta'}_0^{2/3}, \tag{4.18}$$

where C' is a constant. An equivalent expression of (4.18) in terms of ζ is:

$$\frac{z}{\kappa T_{*,s}}\frac{\partial\Theta}{\partial z} = C_{\phi_h}(-\zeta)^{-1/3}. \tag{4.19}$$

This is referred to as the "minus one-third law" for temperature gradients. The region where (4.16) holds is referred to as the *free convective layer* (FCL).

The unique velocity scaling, temperature scaling and length scaling in the FCL are given by Wyngaard, Cote and Izumi (1971):

$$u_f = (z\beta\overline{w'\theta'}_0)^{1/3}, \tag{4.20}$$

$$\Theta_f = (\frac{\overline{w'\theta'}_0^2}{z\beta})^{1/3}, \tag{4.21}$$

$$z_f = z. \tag{4.22}$$

One can then derive other results in the FCL, such as:

$$\frac{\sigma_w}{u_f} = \text{constant}, \qquad \text{and} \qquad \frac{\sigma_\theta}{\Theta_f} = \text{constant}, \tag{4.23}$$

which are equivalent to

$$\frac{\sigma_w}{u_*} = \text{constant} \cdot \frac{u_f}{u_*} = C_{\sigma_w}(-\zeta)^{1/3}, \tag{4.24}$$

$$\frac{\sigma_\theta}{T_{*,s}} = \text{constant} \cdot \frac{\Theta_f}{T_{*,s}} = C_{\sigma_\theta}(-\zeta)^{-1/3}. \tag{4.25}$$

Similar results for σ_u/u_* and σ_v/u_* would be expected, but are not supported by observations (Panofsky et al., 1977). A more relevant length scaling is Z_i, associated with large convective eddies of the CBL.

A power law for velocity shear in the FCL derived from dimensional analysis is:

$$\frac{z}{\kappa u_*}\frac{\partial u}{\partial z} = \text{constant} \cdot (-\zeta)^{1/3}, \tag{4.26}$$

while observations indicate a *minus* one-third law (Carl, Tarbell and Panofsky, 1973), which is the same as that of temperature shear. Moreover, Lumley and Panofsky (1964) justified the derivation of a minus one-third law for velocity shear as follows. Two assumptions are involved: (i) the FCL is still within the constant-flux region; namely, both momentum flux and heat flux are almost constant in the FCL; (ii) the ratio of effective thermal diffusivity η_e to eddy viscosity ν_e is still constant in free convection. From (4.19) and the two assumption above, one can obtain

$$\eta_e = C_{\phi_h}^{-1} u_f z \qquad \text{and} \qquad \nu_e = A\eta_e = C_1 u_f z.$$

Applying $\nu_e \partial u/\partial z = u_*^2$ yields

$$\frac{z}{\kappa u_*}\frac{\partial u}{\partial z} = C_1^{-1}\frac{u_*}{u_f} = C_{\phi_m}(-\zeta)^{-1/3}. \tag{4.27}$$

4.1.5 Mixed layer

If the spatial variable z is large enough to satisfy

$$z \sim Z_i \gg L(\gg z_0), \tag{4.28}$$

one obtains ML similarity in which only z, δh_i and Z_i are important length scales. The relevant velocity scale w_* is defined by Deardorff (1970b) as in (4.6) and the temperature scale Θ_* as:

$$\Theta_* = -\frac{\overline{w'\theta'}_0}{w_*}. \tag{4.29}$$

All field quantities in the ML can be expressed as universal functions through these scalings. For example, σ_w/w_* can be written as

$$\frac{\sigma_w}{w_*} = F(\frac{z}{Z_i}, \frac{\delta h_i}{Z_i}). \tag{4.30}$$

4.2 Some measurements

Even though many careful field measurements have been made during the past three decades, a wide dispute over which empirical form of $\phi_m(\zeta)$ is correct continues amongst the meteorological community. Forms of $\phi_m(\zeta)$ proposed for the unstable case include the "KEYPS" equation (Panofsky, Blackadar and McVehil, 1960), the exponential profile (Swinbank, 1964), and a popular form called the Businger-Dyer relation:

$$\phi_m = (1 - a\zeta)^b \qquad \text{and} \qquad \phi_h = c(1 - a\zeta)^b, \tag{4.31}$$

where a, b and c are constants to be determined by measurement. Businger et al. (1971) proposed an empirical formula for $\phi_m(\zeta)$ based on the Kansas field experiment in which measurements were made from a 32 meter high tower:

$$\phi_m = (1 - 15\zeta)^{-1/4} \qquad \zeta \in (-2, 0) \tag{4.32}$$

It is noted that the range of applicability of (4.32) is constrained to small values of $|\zeta|$. A reanalysis of Kansas data by Wieringa (1980) suggested that $a = 22$ in (4.32) instead of 15, while Dyer and Bradley (1982) obtained an even larger value of $a = 28$ from wind profiles recorded during the 1976 International Turbulence Comparison Experiment (ITCE).

As to the value of b in (4.31), a number of experiments have pointed out that $\phi_m \sim (-\zeta)^{-1/3}$ as $-\zeta \to \infty$ to reach the asymptote of the free convection regime. Analysis of data measured on three different towers (with heights of 61 m, 96 m and 150 m) by Carl, Tarbell and Panofsky (1973), however, leads to a proposal that b in (4.31) must be $-1/3$ to be consistent with the asymptotic limit (4.27) for sufficiently large $|\zeta|$. Carl's formula is

$$\phi_m = (1 - 16\zeta)^{-1/3} \qquad \zeta \in (-10, -2). \tag{4.33}$$

Korrell, Panofsky and Rossi (1982) found that (4.33) can be extended to the range of their measurements at the Boulder Tower (300 m high), $\zeta \in (-0.6, 0)$ in which the form of Businger et al. (1971) overestimates ϕ_m. Measurements by Tsvang et al. (1985) (ITCE) on a low tower (32 m) also supported the $-1/3$ power relation for $\zeta \in (-0.7, -0.07)$. Other investigations, together with those mentioned above, are listed in Table 4.1. Among

Table 4.1: Estimates of $\phi_m(\zeta)$ from measurements for unstable surface layer

Source	$\phi_m(\zeta)$	
Panofsky *et al.* (1960)	$\phi_m^4 - 9\zeta\phi_m^3 = 1$	KEYPS formula
Dyer and Hicks (1970)	$(1-16\zeta)^{-1/4}$	$-1 \le \zeta \le 0$
Businger *et al.* (1971)	$(1-15\zeta)^{-1/4}$	$-2 \le \zeta \le 0$
Carl *et al.* (1973)	$(1-16\zeta)^{-1/3}$	$-10 \le \zeta \le -2$
Wieringa (1980)	$(1-22\zeta)^{-1/4}$	$-2 \le \zeta \le 0$
Dyer and Bradley (1982)	$(1-28\zeta)^{-1/4}$	$-4 \le \zeta \le -0.004$
Kai (1982)	$(1-7\zeta)^{-1/4} - 0.2$	$-0.1 \le \zeta \le 0$
Korrell *et al.* (1982)	$(1-15\zeta)^{-1/3}$	$-0.6 \le \zeta \le 0$
Foken and Skeib (1983)	1	$-0.06 \le \zeta \le 0$
	$(-\zeta/0.06)^{-1/4}$	$-2 \le \zeta \le -0.06$
Högström (1988)	$(1-19\zeta)^{-1/4}$	$-3 \le \zeta \le 0$
Frenzen and Vogel (1992)	$(1-22.6\zeta)^{-1/4}$	$-0.6 \le \zeta \le 0$
	$(1-15.1\zeta)^{-1/3}$	$-0.6 \le \zeta \le 0$

these results, recent measurements (Frenzen and Vogel, 1992b) obtained estimates for ϕ_m following the $-1/3$ power law:

$$\phi_m = (1 - 15.1\zeta)^{-1/3} \qquad \zeta \in (-0.6, 0). \tag{4.34}$$

Table 4.2: Estimates of σ_w/u_* from measurements for unstable surface layer

Source	σ_w/u_*	
Wyngaard, Cote and Izumi (1971)	$1.9(-\zeta)^{1/3}$	$-2 \leq \zeta \leq -1$
Haugen, Kaimal and Bradley (1971)	$[1.6 + (-2\zeta)^{2/3}]^{1/2}$	$-1.5 \leq \zeta \leq 0$
Merry and Panofsky (1976)	$1.3(\phi_m - 2.5\zeta)^{1/3}$	$-2 \leq \zeta \leq 0$
Panofsky et al. (1977)	$1.25(1 - 3\zeta)^{1/3}$	$-4 \leq \zeta \leq 0$
Bradley and Antonia (1979)	$[0.089 + 0.171(-\zeta)^{-2/3}]^{-1/2}$	$-2 \leq \zeta \leq -0.1$
Dyer and Bradley (1982)	$(1 - 14\zeta)^{1/4}$	$-4 \leq \zeta \leq -0.01$
Kai (1982)	$1.3(1 - 3\zeta)^{1/3}$	$-1 \leq \zeta \leq 0$

Table 4.2 gives a list of empirical formulas for σ_w/u_* based on observations. Most formulas in this table have asymptotes of $(-\zeta)^{1/3}$ as $-\zeta \to \infty$, which is consistent with (4.24).

In table 4.3, some examples of measuremental empirical formulas for $\sigma_\theta/T_{*,s}$ are listed. All of them have asymptotes of $C(-\zeta)^{-1/3}$ as $|\zeta| \to \infty$, even if some of them are only valid in small ranges of $|\zeta|$. These empirical formulas support the theoretical argument that $\sigma_\theta/T_{*,s}$ obeys a $-1/3$ power law for a large $|\zeta|$ (see section 4.1.4). Among three formulas given by Bradley and Antonia (1979), the first one was derived from the Kansas data, the second one from the Minnesota 1972 data, and the third one from the ITCE data.

As shown in figure 4.2, the dimensional analysis prediction of a $-1/3$ law for σ_w/u_* is supported by the observation given by Kaimal et al. (1982) which shows a good fit to $1/3$ power law for $|\zeta| > 1$. In addition, temperature variances behave as predicted for $-\zeta > 0.1$ (see figure 4.3).

Table 4.3: Estimates of $\sigma_\theta/T_{*,s}$ from measurements for unstable surface layer

Source	$\sigma_\theta/T_{*,s}$	
Wyngaard, Cote and Izumi (1971)	$0.95(-\zeta)^{-1/3}$	$-0.7 \leq \zeta \leq 0$
Tillman (1972)	$0.95(0.05-\zeta)^{-1/3}$	$-10 \leq \zeta \leq -0.1$
Monji (1973)	$0.92(-\zeta)^{-1/3}$	$-10 \leq \zeta \leq -0.1$
Bradley and Antonia (1979)	$[0.004+1.11(-\zeta)^{1/3}]^{-1}$	$-0.6 \leq \zeta \leq -0.2$
	$[0.13+0.84(-\zeta)^{1/3}]^{-1}$	$-3 \leq \zeta \leq -0.1$
	$[-0.22+1.28(-\zeta)^{1/3}]^{-1}$	$-2 \leq \zeta \leq -0.1$

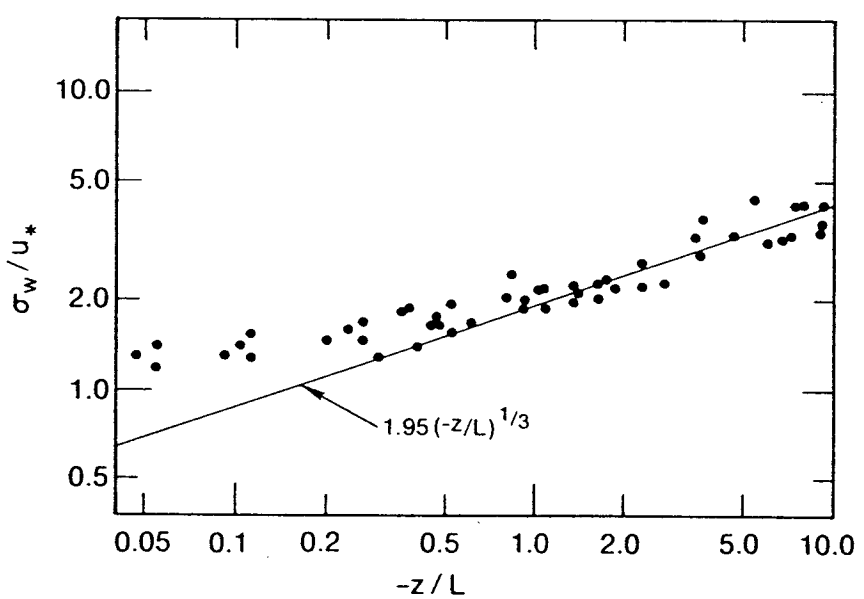

Figure 4.2: Universal function σ_w/u_* under very unstable conditions according to Kaimal *et al.* (1982).

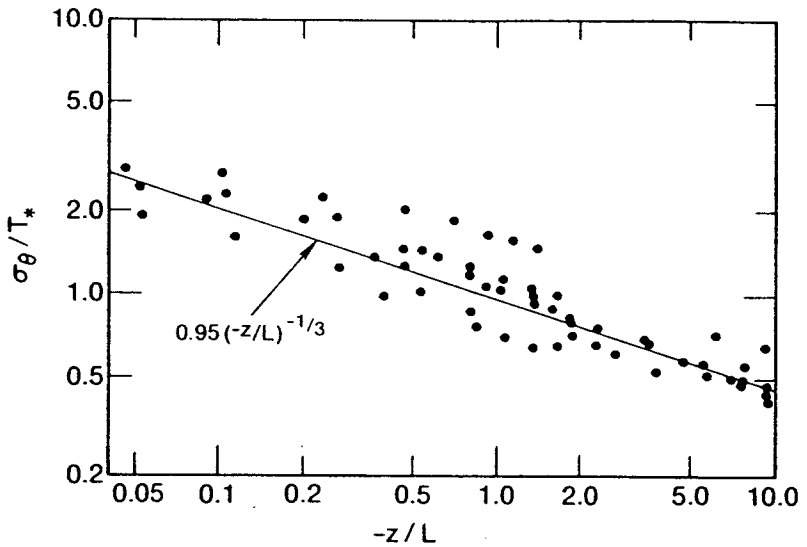

Figure 4.3: Universal function $\sigma_\theta/T_{*,s}$ under very unstable conditions according to Kaimal *et al.* (1982).

4.3 LES results for the upper surface layer

Four types of domain size (see table 4.4) have been adopted to examine LES results of resolved turbulent statistics in the USL. The parameters for model runs are shown in

Table 4.4: Specification of domain size and grid spacing for LESs of an unstable ABL. D_x, D_y and D_z are domain sizes in the x, y and z direction, respectively; N_x, N_y and N_z are the grid numbers in the x, y and z direction, respectively; Δ_x and Δ_y are the grid spaings in the x and y direction, respectively; kk is a few digits that stand for the value of $\overline{w'\theta'}_0$.

Run	Domain	D_x(m)	D_y(m)	D_z(m)	N_x	N_y	N_z	Δ_x(m)	Δ_y(m)
U16A2.kk	A	960	480	2140	16	16	50	60	30
U24B2.kk	B	1440	720	2140	24	24	50	60	30
U64C2.kk	C	3840	1920	2140	64	64	50	60	30
U32D2.kk	D	1920	960	2140	32	32	50	60	30

table 4.5. In these runs, $\overline{w'\theta'}_0$ is specified at the first vertical grid elevation; L is derived from its definition (4.4), in which $\kappa = 0.35$, and u_* and $\beta(= g/\Theta_0)$ are calculated from

LES output (u_{*0} is adopted to be u_* and Θ_0 is the horizontally averaged temperature at

Table 4.5: Parameters for each run. $\Delta_x = 60$ m and $\Delta_y = 30$ m; C_s is the Smagorinsky sub-grid model constant; $\overline{w'\theta'}_0$ is the turbulent sensible heat flux at the surface; L is the Monin-Obukhov length scale; Z_i is the height of the CBL; $-Z_i/L$ is a measure of stability of a CBL; Re_{SM} is the SM-Reynolds number; w_* is the convective velocity of a CBL; t_* is the time scaling of convective thermals.

Run	C_s	$\overline{w'\theta'}_0$	L	Z_i	$-Z_i/L$	Re_{SM}	w_*	t_*
U16A2.1	0.20	0.10	-55.5	1500	-27.0	13700	1.72	0.243
U16A2.15	0.20	0.15	-40.7	1480	-36.4	13600	1.96	0.210
U24B2.05	0.20	0.05	-136.3	1240	-9.1	20700	1.29	0.268
U24B2.1	0.20	0.10	-78.1	1360	-17.4	22000	1.67	0.227
U24B2.2	0.20	0.20	-44.5	1420	-31.9	22600	2.13	0.185
U32D2.01	0.20	0.01	-433.6	1060	-2.4	27300	0.71	0.412
U32D2.2	0.20	0.20	-47.1	1480	-31.4	34200	2.16	0.191
U64C2.1	0.20	0.10	-66.5	1300	-19.5	79000	1.64	0.220
U64C2.15	0.20	0.15	-50.8	1360	-26.8	81400	1.91	0.198

the surface); Z_i is estimated from LES output of vertical profile of mean heat flux (see details later); w_* is derived from (4.6) while t_* from (4.9); Θ_* is the temperature scaling in the ML, defined as

$$\Theta_* = \frac{\overline{w'\theta'}_0}{w_*}, \tag{4.35}$$

not to be confused with the temperature scaling in the ASL, defined as

$$T_{*,s} = \frac{\overline{w'\theta'}_0}{u_*}. \tag{4.36}$$

The initial velocity fields have been disturbed with the same magnitudes of random numbers to the mean velocities as those for the neutral cases (see chapter 3), but the effects of the velocity perturbations are overwhelmed by imposed buoyancy. For simplicity, the initial vertical temperature profile within the ABL is given by a constant value of

284° K. To save computation, it is reasonable to run one case with a moderate $\overline{w'\theta'}_0$ for a certain length of time, say $t/t_* \approx 10$, with all other runs starting with the output from this run as their initial conditions, but with the different surface heat flux $\overline{w'\theta'}_0$. This type of initialization is called a "hot start". With a hot start, RS turbulent eddies in the CBL can adjust themselves into a new equilibrium state very fast and this transition period must be shorter than that in a run through a "cold start".

Determination of Z_i

Figure 4.4 presents the vertical distributions of RS turbulent sensible heat fluxes for different cases. Very clear linear distributions of $\langle \tilde{w}\tilde{\theta} \rangle$ in most of the CBL are shown

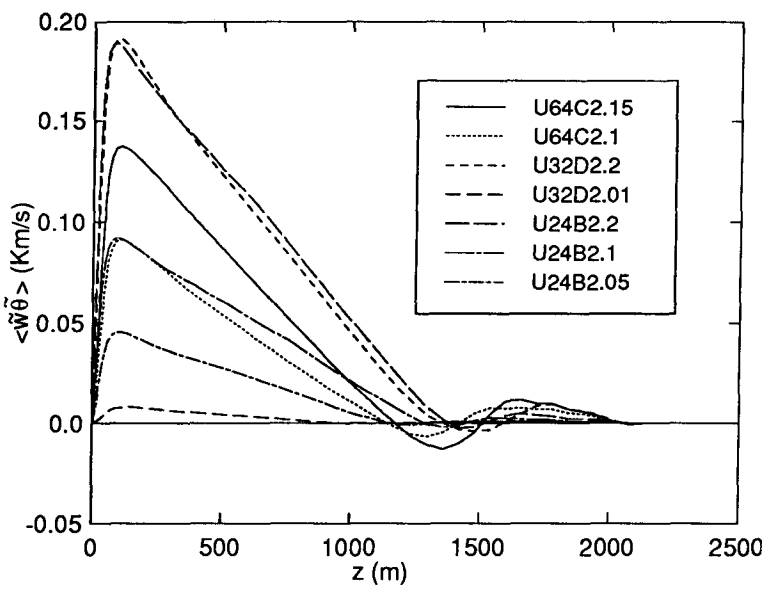

Figure 4.4: Profiles of RS turbulent sensible heat fluxes in the CBL.

except for the near-surface region where RS heat fluxes are suppressed to zero. Extrapolating these linear portions to the surface yields the intercepted values shown in table 4.6. These values are very close to the imposed values of $\overline{w'\theta'}_0$ at the surface (see table 4.6).

In all runs, as shown in figure 4.4, $\langle \tilde{w}\tilde{\theta} \rangle$ deceases linearly to zero at a height near

Table 4.6: Intercepts at the surface by extrapolating the linear portions of $\langle \tilde{w}\tilde{\theta} \rangle$.

U64C2.15	U64C2.1	U32D2.2	U32D2.01	U24B2.2	U24B2.1	U24B2.05
0.1547	0.1006	0.2036	0.0095	0.1996	0.09894	0.04946

the top of the CBL and overshoots to a negative value. Passing a negative minimum, it turns to increase to a positive maximum and then approaches zero at a sufficiently large z. This characteristic is consistent with observations (*e.g.*, Stull and Eloranta (1983)). The portion of negative $\langle \tilde{w}\tilde{\theta} \rangle$ implies a downward heat flux which is associated with the inversion layer aloft, where temperature increases with height; in other words, hot air is entrained downward in this region. The present study defines the height at which $\langle \tilde{w}\tilde{\theta} \rangle$ is a negative minimum as Z_i for LES runs. Since these LESs are started from slightly different initial conditions, the values of Z_i are different. It is noted that the ratio of $\langle \tilde{w}\tilde{\theta} \rangle_{z=Z_i}$ (the buoyancy entrainment heat flux at Z_i) to $\overline{w'\theta'}_0$ (the surface heat flux) is larger than the observational value, -0.2. This may be partially attributed to the big value of Γ ($= 0.011°$ K/m, see page 136) adopted by the present study.

Unsteadiness of the CBL height Z_i

Since the surface heat flux provides a continuous energy input to the simulated boundary layer, the total energy in the domain will increase unless there is the same (or larger) amount of energy flowing out of the upper part of the domain. The boundary condition at the upper layer does not necessarily provide such an energy flux. The Rayleigh damping layer (see appendix A) consumes some energy, but the specification of this layer is such that it cannot have a significant influence on the energy balance, because the position of this layer is much higher than Z_i. The consequence is that total

energy in the ABL accumulates in an obviously unsteady process. The unsteadiness can be illustrated by a mean quantity such as the mean temperature. Since the vertical profile of turbulent sensible heat flux is nearly linear in the vertical direction throughout the ABL and it distributes heat energy almost evenly to every elevation, the mean temperature is therefore almost constant but continuously increasing with time. The height of inversion base is also unsteady as a consequence of the temperature increase and entrainment process. The change rate of the inversion base $\partial Z_i/\partial t$ is referred to as *entrainment rate.*

The present study, however, proposes at least two reasons to neglect the effects of this unsteadiness on turbulent processes in the CBL. Firstly, if most of the energy stays in the form of heat and does not convert to kinetic energy, one can thus assume that the processes only involving kinetic energy are steady, admitting that mean quantities such as mean temperature are increasing with a certain rate. Secondly, the entrainment rate is insignificantly small when compared with the convective velocity scale of the CBL turbulence w_* when only turbulence statistics are dealt with. The proof follows five assumptions: (a) temperature in the ML, Θ, is constant, varying with time only; (b) the relation between the rate of change of Θ and the rate of change of Z_i is

$$\frac{\partial Z_i}{\partial t} \approx \frac{\partial Z_i}{\partial \Theta}\frac{\partial \Theta}{\partial t} = \frac{1}{\Gamma}\frac{\partial \Theta}{\partial t}; \tag{4.37}$$

(c) heat flux at the interfacial layer $\overline{w'\theta'}_i = R\overline{w'\theta'}_0$ where R is a function of δh_i^+; (d) $\overline{w'\theta'}$ is a linear function of z; (e) other sources affecting temperature in the ML are ignored. An estimate for the variation of mean temperature based on the simplified equation of (2.100) is:

$$\frac{\partial \Theta}{\partial t} \approx \frac{\partial \overline{w'\theta'}}{\partial z} = \frac{\overline{w'\theta'}_0 - \overline{w'\theta'}_i}{Zi} = [1 - R(\delta h_i^+)]\frac{\overline{w'\theta'}_0}{Z_i}.$$

Therefore, the ratio of $\partial Z_i/\partial t$ to w_* can be estimated:

$$\frac{\partial Z_i/\partial t}{w_*} \approx \frac{\partial \Theta/\partial t}{\Gamma w_*} \approx \frac{[1 - R(\delta h_i^+)]\overline{w'\theta'}_0}{Z_i \Gamma w_*}. \tag{4.38}$$

Applying (4.8) and (4.5) to (4.38) yields

$$\frac{\partial Z_i/\partial t}{w_*} \approx [1 - R(\delta h_i^+)](\delta h_i^+)^2. \tag{4.39}$$

Let $R \approx -0.2$, $\overline{w'\theta'}_0 = 0.15°$ Km/s, $\Theta = 300°$ K, $Z_i = 1500$ m and $\Gamma = 0.003°$ K/m (these are typical values in a CBL), and the value of dimensionless depth of the EL is about $\delta h_i^+ \approx 0.131$. Therefore, $(\partial Z_i/\partial t)/w_* \approx 0.02$; this estimate shows that the unsteadiness of Z_i is unimportant when only turbulence statistics are investigated. It is expected that those turbulence statistics are almost steady.

Time scaling of the convective eddies

Because $t_*(= Z_i/w_*)$ represents approximately the time during which convective eddies move from the bottom to the top of the CBL, the time scale of $2t_*$ to πt_* must be associated with a complete cycle of those convective motions.[4] Figure 4.5 shows the time variation of the domain-averaged RS TKE, $E_R(t)$, for case U64C2.1. $E_R(t)$ was not developed until $t \approx 1000$ sec (or $t/t_* \approx 1.3$); then it oscillates with a period of about 1800 to 2140 sec (or $2.3t_*$ to $2.8t_*$), which demonstrates the importance of convective eddies in a CBL. This type of time scale exists throughout the simulation. The oscillation is purer in the on-set period, which implies that only large eddies are dominant, and becomes more chaotic as smaller eddies are superimposed on the persisting large eddies, thus revealing a cascading process.

Averaging time interval

Figure 4.6 shows that effects of the Coriolis force on the oscillation of mean velocity profile, and therefore on the variation of total KE, $E_M(t)$, still exist in an unstable ABL

[4]A complete cycle of an up-and-down convective eddy is $2t_*$, while a complete cycle of a circularly moving convective eddy is πt_*. Therefore, a real convective eddy may move along an ellipse which takes a period of between $2t_*$ and πt_*.

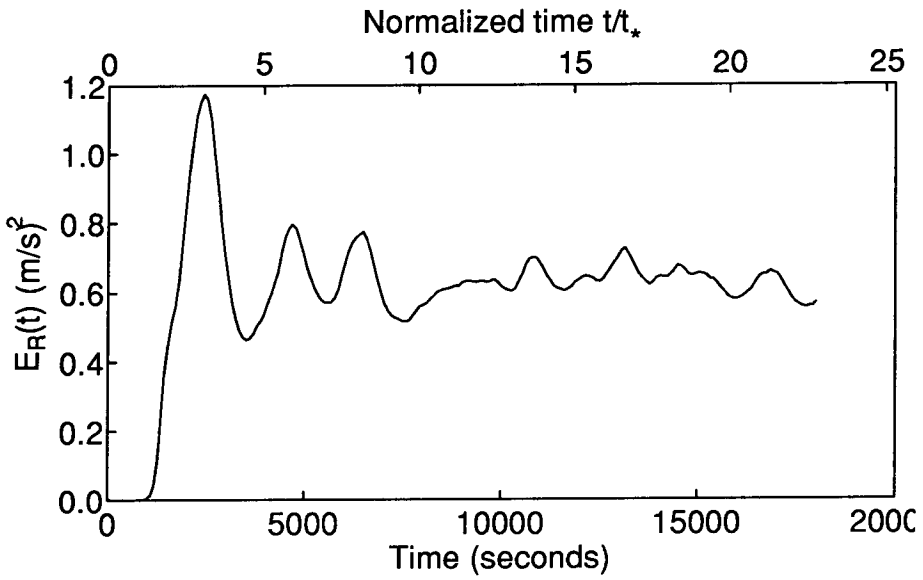

Figure 4.5: Variation of RS TKE (averaged over the numerical domain) with time for case U64C2.1.

(only 18000 second, about 1/4 of the oscillation with period of $2\pi/f$, is shown). As discussed in chapter 3, this effect is negligible if one is only interested in turbulence statistics.

The conclusion is that compared with the time scale of the convective eddies ($\sim 10^3$ sec) which play the most important role in CBL turbulence, the time scale of the Coriolis force ($\sim 2\pi 10^4$ sec) can be ignored[5] and the time scale due to the unsteadiness of Z_i ($\sim 10^4$ sec) can also be ignored.[6] This is the reason that the simulation duration for the cases in this chapter can be shorter than those in chapter 3, while still being long enough to obtain stable statistics for convective eddies. Figure 4.5 shows that LES output for analysis must be taken after $t/t_* > 12$ or so, and the time interval

[5]This time scale can be expressed by $t_f = 2\pi/f$. A complete cycle of convective eddies is πt_*. Therefore, $\pi t_*/t_f = fZ_i/2w_* \approx 0.05$ if $f = 10^{-4}$ sec, $Z_i = 1000$ m and $w_* = 1$ m/s.

[6]This time scale can be expressed by $t_i = (Z_i^{-1}\partial Z_i/\partial t)^{-1}$. Applying (4.39) and definition of t_* in (4.9) yield $t_*/t_i \approx [1 + R(\delta h_i^+)](\delta h_i^+)^2$, which is very small if δh_i^+ takes its typical value of about 0.2.

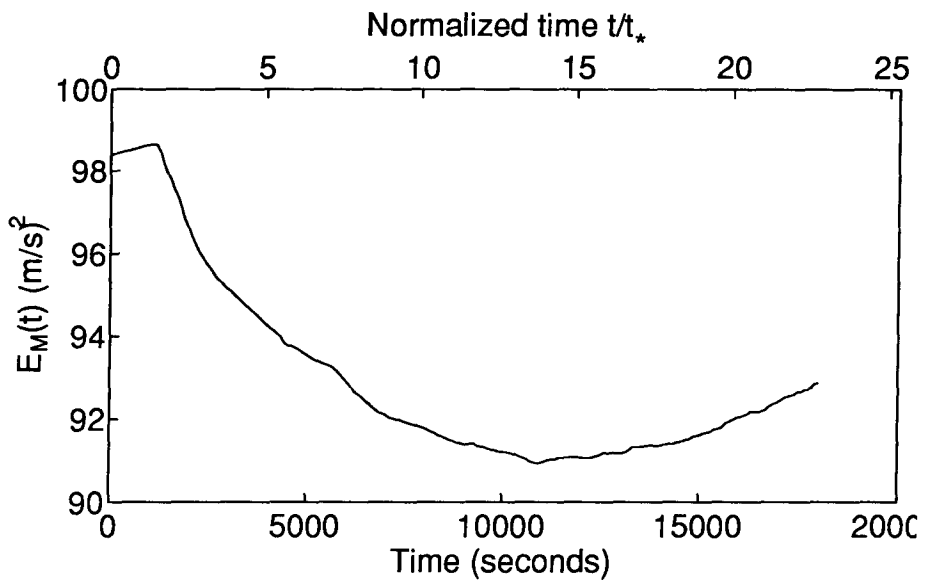

Figure 4.6: Variation of total KE (averaged over the numerical domain) with time for case U64C2.1.

in which temporal averaging procedure is implemented must be *much larger than* t_* in order to obtain a stable statistics. Some previous LES approaches, such as Mason (1989), Schmidt and Schumann (1989) and Nieuwstadt et al. (1991), adopted one t_* as the time-averaging interval to avoid unsteadiness due to $\partial Z_i/\partial t$. This procedure may result in non-representative statistics. These authors adopted $\Gamma = 0.003°$ K/m, which yields large values of δh_i^+, and therefore a large degree of unsteadiness represented by $(\partial Z_i/\partial t)/w_*$ in (4.39). To obtain better average statistics and reduce the influence of the unsteadiness of Z_i, the present study uses the value of $\Gamma = 0.011°$ K/m. This value is rather large, but reduces the value of $(\partial Z_i/\partial t)/w_*$ by about three quarters while only halving values of δh_i^+. In the present study, LES results with $\Gamma = 0.011°$ K/m, the unsteadiness of Z_i is hardly seen within a time interval of several t_*'s, so a time-averaging procedure over

up to $10t_*$ can be used.[7]

C_s and Re_{SM}

In a neutral case the only turbulence production term is shear instability which requires a large value of Re_{SM} (small SGS dissipation) to retain RS motions. In an unstable ABL, a positive buoyancy production term is added to produce extra RS TKE, thus relaxing the requirement of large Re_{SM}. In his investigation of a pure CBL, Mason (1989) adopted values of C_s of 0.2 to 0.46, and addressed the size of C_s in a LES (with the Smagorinsky SGS model). He found that the factors which proved to be critical were the mesh resolution and the implied SGS constant C_s. If a value of C_s as small as those for the neutral cases (*e.g.*, 0.08) is still used, extra RS TKE will be accumulated at the wavenumber of grid spacing (see the footnote on page 12).

The values of C_s (= 0.2) employed in this chapter are much larger than those employed in chapter 3, and therefore the SM-Reynolds numbers Re_{SM} in this chapter are much smaller than those in the neutral cases.

The SGS model for a CBL must be modified to include buoyancy effects on the SGS

[7]Suppose that Z_i vary $K\%$ within $\Delta t = Nt_*$ is required, i.e.,

$$\frac{\Delta t \partial Z_i/\partial t}{Z_i} \leq K\% \qquad \Leftrightarrow \qquad \frac{Nt_* \partial Z_i/\partial t}{Z_i} = N\frac{\partial Z_i/\partial t}{w_*} \leq K\%.$$

Applying (4.39) to the above inequality yields

$$N \leq \frac{K\%}{(1-R)(\delta h_i^+)^2}.$$

Substitution of typical values of $R \approx -0.2$, $\overline{w'\theta'}_0 = 0.15°$ Km/s, $\Theta = 300°$ K, $Z_i = 1500$ m and (i) $\Gamma = 0.003°$ K/m; (ii) $\Gamma = 0.011°$ K/m into the above inequality gives

$$\text{(i) } N \leq 48K\%; \qquad \text{(ii)} N \leq 178K\%.$$

If $K\% = 5\%$ is required, then for (i), $N \leq 2.4$; for (ii) $N \leq 9$.

eddy viscosity, and is expressed by the following equations (Lilly, 1962):

$$\tau_{ij}^{(s)} = -\frac{2}{3}E_s\delta_{ij} + 2\nu_s s_{ij}, \tag{4.40}$$

$$s_{ij} = \frac{1}{2}(\frac{\partial \bar{u}_i}{\partial x_j} + \frac{\partial \bar{u}_j}{\partial x_i}), \tag{4.41}$$

$$\nu_s = (C_s\Delta)^2 s(1 - R_{f,s}), \tag{4.42}$$

$$s^2 = 2s_{ij}s_{ij}, \tag{4.43}$$

where E_s is SGS TKE, and $R_{f,s}$ is the SGS flux Richardson number, defined by

$$R_{f,s} = \frac{g/\Theta_0 \partial\Theta/\partial z}{Pr_s s^2}. \tag{4.44}$$

The parameter Pr_s is the SGS Prandtl number, which is defined by

$$Pr_s = \frac{\nu_s}{\eta_s}, \tag{4.45}$$

where η_s is the SGS eddy thermal diffusivity for temperature. In the present study, the SGS Prandtl number is taken as 1/3 as suggested by Deardorff (1972). The modified form (4.42) has a larger value of viscosity under an unstable situation. Mason (1989) concluded from his LES runs for a pure CBL that the SGS Prandtl number had very little effect on the results, and adopted $Pr_s = 0.5$ in most of his cases.

Determination of h_b

To analyze the output of LES, one must exclude the SGS buffer layer since RS quantities are poorly represented in this region (see the discussion in section 3.3.1 on page 73). In the ASL of a CBL, one more length scale L is present than that in a neutral ABL. Therefore, in a LES model of an unstable surface layer, relevant length scales include the Monin-Obukhov length scale L, the roughness length z_0, the height of the

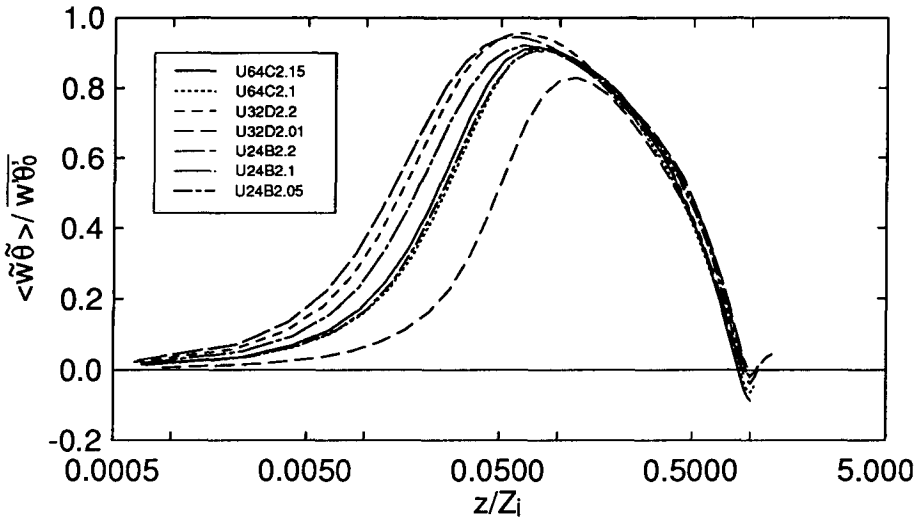

Figure 4.7: Profiles of RS turbulent sensible heat fluxes in a CBL. Height is normalized by Z_i and $\overline{w'\theta'}$ is normalized by its surface value $\overline{w'\theta'}_0$.

SGS buffer layer h_b, and spatial variable z. In this chapter h_b is arbitrarily defined as the height from the surface where the RS heat flux $\langle\tilde{w}\tilde{\theta}\rangle = 0.8\overline{w'\theta'}_0$ for the first time, or where $\langle\tilde{w}\tilde{\theta}\rangle$ is a maximum if $\max\langle\tilde{w}\tilde{\theta}\rangle < 0.8\overline{w'\theta'}_0$. This definition is found to be appropriate for the unstable cases. As shown in figure 4.7, h_b/Z_i is about 0.03 to 0.09, depending on $|Z_i/L|$, domain size and the SGS parameterization. With other parameters fixed, h_b decreases with $|Z_i/L|$; the effect of a larger SGS diffusivity (either by increasing the value of C_s or adopting a larger grid spacing) is to enhance the value of h_b; the influence of domain size is also to raise h_b.

Scaling regimes

The value of L can indicate the type of turbulent processes in a region above h_b and below $h_s \approx 0.1Z_i$. Since L is defined by

$$L = -\frac{\Theta_0 u_*^3}{\kappa g \overline{w'\theta'}_0}, \tag{4.46}$$

with other parameter unchanged, $|L|$ must be decreased if $\overline{w'\theta'}_0$ becomes larger.

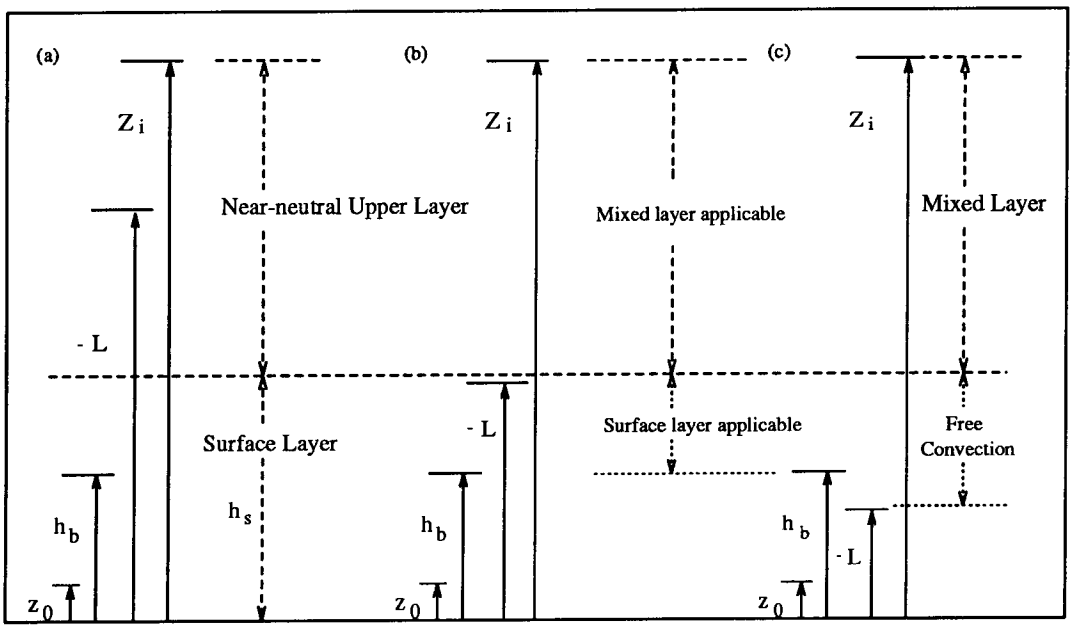

Figure 4.8: Sketch of length scales in a simulated CBL. h_b is the height of the SGS buffer layer; Z_i is the height of the inversion base; z_0 is the surface roughness length; L is the Monin-Obukhov length; z_0 is the surface roughness length (z_0 is drawn vertically for illustrative purpose only and should not be interpreted as the vertical extent of any physical object). (a) weak convection case; (b) moderate convection case; (c) strong convection case.

Figure 4.8 illustrates some possible situations with variation of $|L|$. In case (a), when $|L| \gg h_s$ ($|L|$ may be larger than, or smaller than Z_i), the value of $z/|L|$ in the surface layer is very small; therefore turbulence production by buoyancy is weak in this region and shear turbulence dominates. The processes in the so-called "near-neutral upper layer" (Holtslag and Nieuwstadt, 1986) are not strongly mixing. This case corresponds to a near-neutral ABL, or a weak CBL. In case (b), when $|L| \sim h_s$, the ML is well developed, most mean variables being almost constant. In the top of the surface layer, turbulence production by buoyancy is as important as that by velocity shear, but there is no free convection layer, which requires that $z/L \gg 1$ and $z/Z_i \ll 1$. In case (c), when $|L| \ll h_s$ (it could be smaller than h_b), the region in which the turbulence production by velocity shear dominates is squeezed to a very shallow layer (it could be within the SGS buffer layer). A free convection layer emerges near the top of the surface layer. In the present LES cases, due to the presence of the SGS buffer layer, the region in which surface layer similarity analysis is applicable to the LES output must be above $z = h_b$ and below $z = h_s$, as shown in figure 4.8. Therefore, the output of case (a) in the applicable region are applied for small $-\zeta$ ($= -z/L \ll 1$), the output of case (b) for $-\zeta = -z/L \sim 1$, and the output of case (c) for large $-\zeta$ ($= -z/L \gg 1$). In a real ABL, case (c) in figure 4.8 rarely happens which requires a strong surface heat flux and a weak wind.

Figure 4.9 shows a plot of z/Z_i against the stability parameter $-Z_i/L$, first given by Holtslag and Nieuwstadt (1986). LES applicable region occupies the upper part of the ASL ($h_b \leq z \leq 0.1Z_i$), while the lower part of the ASL is the SGS buffer layer. As $-Z_i/L$ increases up to 10, the USL transits to FCL. From table 4.5, those cases with C_s greater than 0.1 satisfy the condition of $-Z_i/L > 10$, and therefore LES output of these cases can be adopted for FCL analysis.

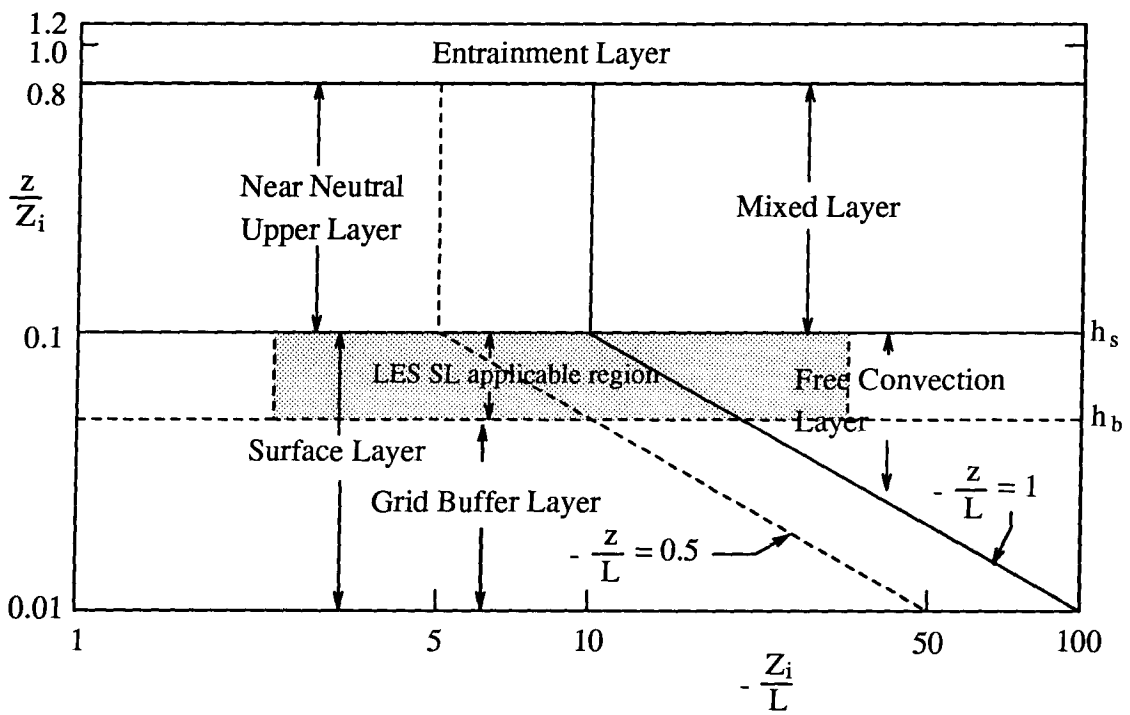

Figure 4.9: Sketch of scaling regimes in a CBL after Holtslag and Nieuwstadt (1986) and the present LES applicable region, which is indicated by shaded area.

Mean velocity components and the friction velocity

Vertical profiles of velocity components in the surface layer are averaged over a time interval $10t_*$. Figure 4.10 and figure 4.11 show a vertical mean speed profile for

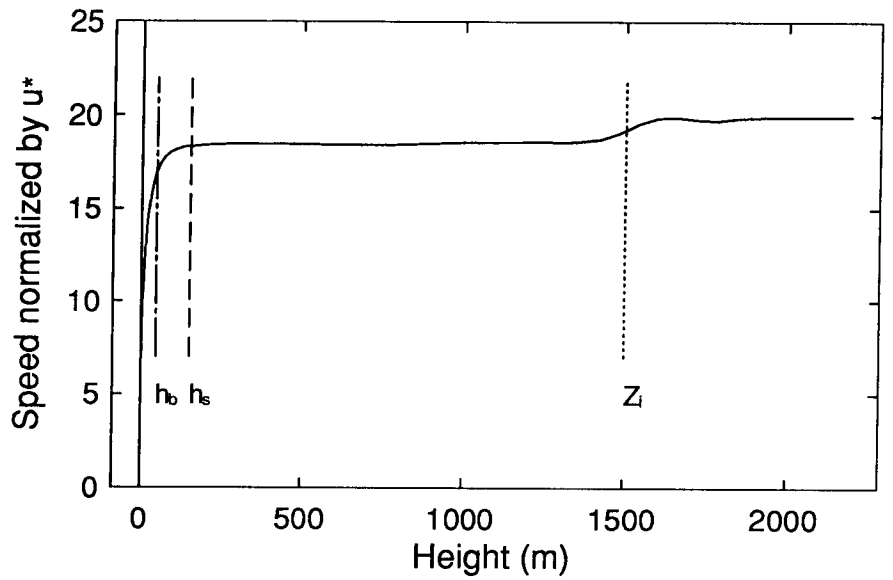

Figure 4.10: Vertical profile of the wind speed for case U64C2.1.

case U64C2.1 under two different coordinates. The profiles are very different from those in a neutral case shown in figure 3.3 on page 73, for example. In most of the CBL, the mean speed is almost constant, with a very large shear in the near surface region. Near the inversion base ($z \sim 1500$ m), the mean velocity components have moderate shears and adjust themselves to the geostrophic wind aloft. The Coriolis force affects the mean velocity distribution at the inversion base.

4.3.1 Momentum flux profile in the USL

The dimensionless momentum flux $\phi_m(\zeta)$ in the USL can be calculated from the velocity profiles in the region $z \in (h_b, h_s)$, where $h_s = 0.1Z_i$. In fact, the U32E-cases are not suitable for surface layer similarity because the region (h_b, h_s) for these cases disappears

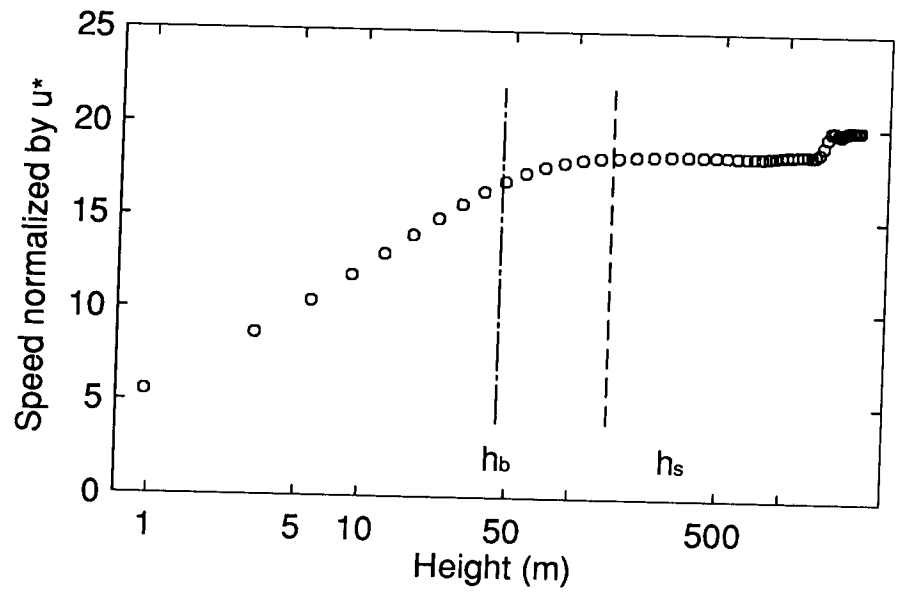

Figure 4.11: Vertical profile of the wind speed for case U64C2.1 under a semi-log coordinate.

as $h_b > h_s$ (see figure 4.7). To obtain the dimensionless momentum flux $\phi_m(\zeta)$ in the USL, the following evaluation procedure is adopted:

- the time interval of evaluation, $[t_1, t_2]$, is divided into N sub-intervals, each of length t_*, which is the time scaling of convective eddies; time averages are taken for velocity profiles at each i-th sub-interval; based on the averaged profiles, $\phi_m(\zeta)$ is evaluated in this time sub-interval:

$$\phi_m^{(i)}(\zeta) = \frac{\kappa z}{u_{*0}}[(\frac{\partial u^{(i)}}{\partial z})^2 + (\frac{\partial v^{(i)}}{\partial z})^2]^{1/2} \qquad z \in (h_b, h_s) \tag{4.47}$$

  where $^{(i)}$ indicates the i-th time interval; $u^{(i)}$ and $v^{(i)}$, are mean velocity components averaged over this time interval in the x and y direction, respectively; the value of ζ is then calculated based on the definition of L in (4.4), in which the value of κ is taken as 0.35, and u_{*0}, the friction velocity evaluated at the surface, and Θ_0, the temperature at the surface, are adopted.

- a further time averaging process is taken over these N sub-intervals to obtain a value for ϕ_m:

$$\phi_m = \frac{1}{N}\sum_i \phi_m^{(i)}. \tag{4.48}$$

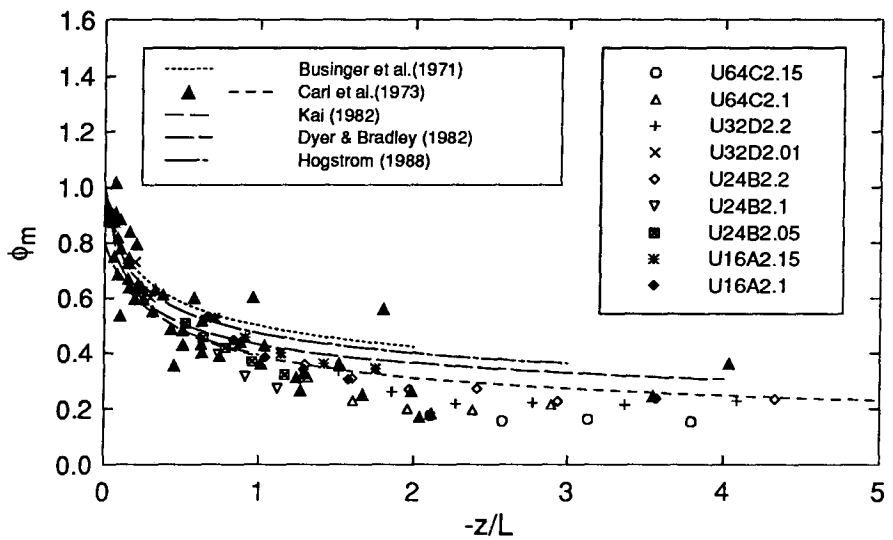

Figure 4.12: Momentum flux profile ϕ_m as a function of $-z/L$ from the LES output, indicated by symbols, together with measurement points from Carl *et al.* (1973), indicated by solid triangle, and empirical formulas for ϕ_m based on observations, indicated by lines.

In figure 4.12, momentum flux profile ϕ_m from the LES output, together with empirical formulas for ϕ_m, are presented as a function of $-z/L$. Case U24B2.2 is in very close agreement with the empirical formula proposed by Carl, Tarbell and Panofsky (1973) in the region $-4 < \zeta < -2$, while other cases in this range of ζ give smaller values. Case U64C2.1 and U64C2.15 show the smallest ϕ_m in the region of $-4 < \zeta < -1.6$, which seems to demonstrates that a larger domain size produces a smaller value of ϕ_m. This might be explained by the fact that a larger domain brings more influence of the convective eddies on the momentum transfer in the USL, and therefore flattens the mean velocity profiles. For small $-\zeta(\sim 1)$, LES results also show smaller values of ϕ_m compared with those empirical formulas, but two cases with relatively small number of grids,

case U16A2.1 and U16A2.15, give fairly good results in agreement with observations.

Some measurement points (indicated by solid triangles) are also plotted in figure 4.12. These data are collected from four different sites by Carl, Tarbell and Panofsky (1973), who proposed the $-1/3$ formula of (4.33). There are many data points in $-\zeta \in (1,2)$ that fall into the same range of ϕ_m values as the LES results, while only two points are above all empirical formulas. Unfortunately, there is no measurement data in the region of $-\zeta \in (2.1, 3.5)$.

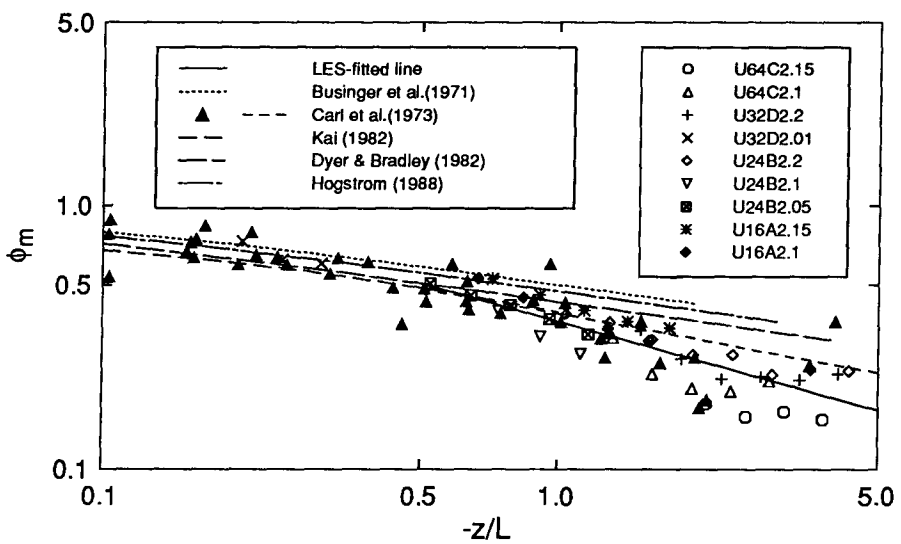

Figure 4.13: As in figure 4.12, but in log-log coordinates.

In figure 4.13, the same results are plotted in log-log coordinates. The formulas given by Businger et al. (1971), Högström (1988), Dyer and Bradley (1982) and Kai (1982) fit Carl's data (indicated by solid triangles) very well in the region of $-\zeta \in (0.1, 0.8)$, but overestimate the value of ϕ_m when $-\zeta > 0.8$. Most measurement points in $-\zeta \in (1,2)$, together with most of LES results in this region, are below Carl's empirical line. The slope derived from LES results is generally steeper than $-1/3$, indicated by solid line in figure 4.13. This LES-fitted line by the least square method is given by the following

formula:

$$\phi_m = 0.363(-\zeta)^{-0.482}. \tag{4.49}$$

4.3.2 Standard deviation of temperature fluctuations in the USL

From equation (4.25) on page 123, the standard deviation of temperature fluctuations $\sigma_{\tilde{\theta}}/T_{*,s}$ follows $-1/3$ law in the FCL for very large values of $|\zeta|$. In addition, observations

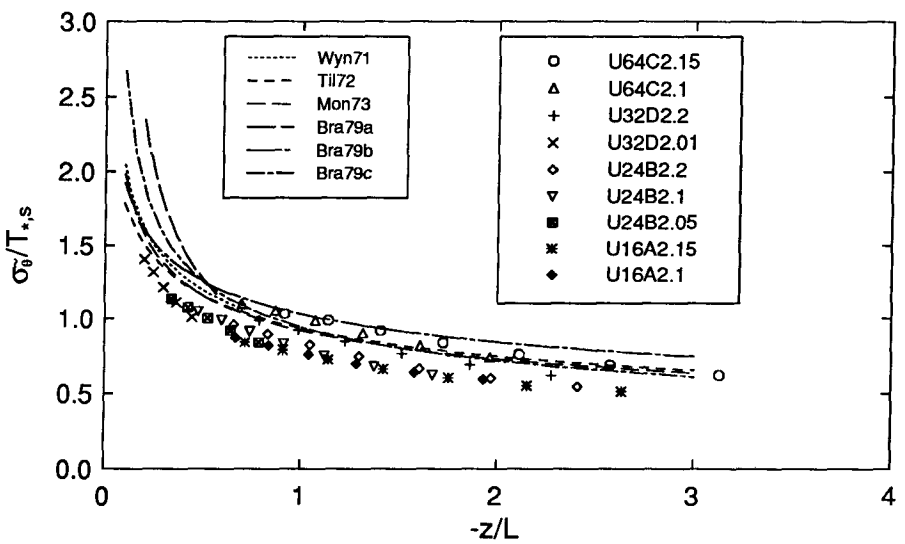

Figure 4.14: Standard deviation of RS temperature fluctuations $\sigma_{\tilde{\theta}}$, normalized by $T_{*,s}$, as a function of z/L from the LES output, indicated by symbols, together with empirical formulas for $\sigma_{\theta}/T_{*,s}$ based on observations. Wyn71: Wyngaard *et al.* (1971); Til72: Tillman (1972); Mon73: Monji (1973); Bra79: Bradley and Antonia (1979).

illustrated by table 4.3 or figure 4.3 on page 129 surprisingly suggest that the $-1/3$ law remains valid even for small values of $|\zeta|$, although the theoretical argument does not support this form.

Figure 4.14 presents the LES results for $\sigma_{\tilde{\theta}}/T_{*,s}$, together with the empirical formulas listed in table 4.3. U64C-cases agree with the empirical formulas fairly well, while the cases representing smaller domains show smaller values of $\sigma_{\tilde{\theta}}/T_{*,s}$. The effects due to the

domain size can be seen from this figure: the smaller the domain size is, the lower value of $\sigma_{\tilde{\theta}}/T_{*,s}$ will be. However, the differences between U16A-cases and U24B-cases are very small.

Figure 4.15 shows the same LES results for $\sigma_{\tilde{\theta}}/T_{*,s}$, but plotted in log-log coordinates. The agreement with $-1/3$ law, given by Wyngaard, Cote and Izumi (1971), is fairly good,

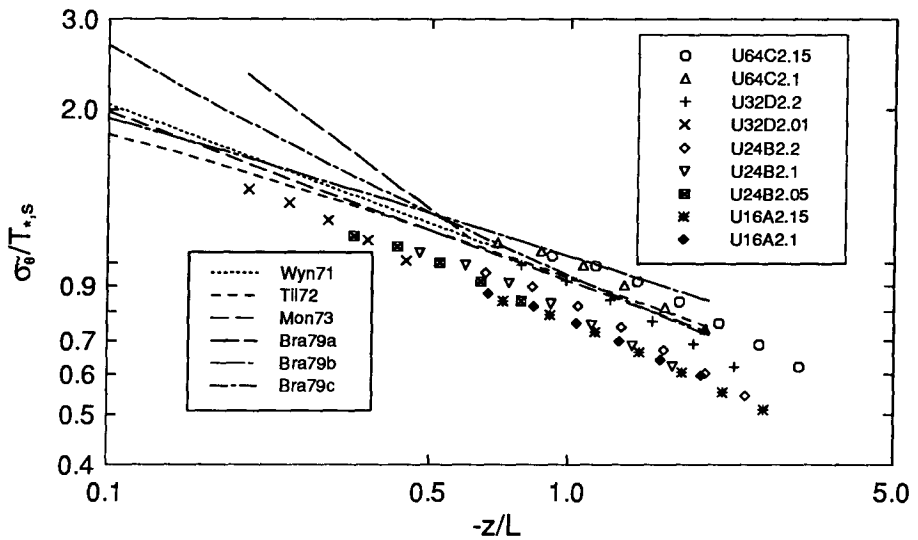

Figure 4.15: As in figure 4.14, but plotted in log-log coordinates.

even though the points of U32D- and U24B-cases are parallel to but smaller than the empirical curves. This is attributed to the lack of representation of large eddies due to the smaller domain size than that of U64C-cases. If θ' has no relation to large eddies, $\sigma_{\tilde{\theta}}/T_{*,s}$ should not have such a strong dependence on domain size. Figure 4.15 also shows a very weak dependence of LES output on the surface heat flux $\overline{w'\theta'}_0$, except for the case U32D2.01 which has an extremely small $\overline{w'\theta'}_0$. For large value of $-\zeta$, it seems that a little steeper slope can be fit for LES results than those of the empirical curves. The values of the power n obtained by fitting the linear sections of LES output are given in

Table 4.7: Coeffient $C_{\sigma_{\tilde{\theta}}}$ and power n from least-square fit of the LES output to the formula $\sigma_{\tilde{\theta}}/T_{*,s} = C_{\sigma_{\tilde{\theta}}}(-\zeta)^n$.

Run	Fitted $C_{\sigma_{\tilde{\theta}}}$	Fitted n	Run	Fitted $C_{\sigma_{\tilde{\theta}}}$	Fitted n
U16A2.1	0.762	−0.365	U32D2.01	0.726	−0.420
U16A2.15	0.755	−0.394	U32D2.2	0.909	−0.443
U24B2.05	0.779	−0.365	U64C2.1	0.987	−0.393
U24B2.1	0.787	−0.425	U64C2.15	1.030	−0.424
U24B2.2	0.821	−0.443	Average	0.840	−0.408

table 4.7. The power law for temperature fluctuations as derived from the LES is:

$$\frac{\sigma_{\tilde{\theta}}}{T_{*,s}} = 0.84(-\zeta)^{-0.408} \tag{4.50}$$

4.3.3 Standard deviation of vertical velocity fluctuations in the USL

From LES output, one can examine the portion of $\sigma_{\tilde{w}}/u_*$ that follows the 1/3 power law. This portion for each single run is very short in space since $\tilde{w}$ is remarkably suppressed by the presence of the wall and by the SGS effects. However, the appropriateness of identifying this portion is supported by consistency with the 1/3 law for different runs as shown in figure 4.16. Case U64C2.1 and U64C2.15 are not shown here because they produce small values of $\sigma_{\tilde{w}}/u_*$. Agreement with the empirical formulas is good for cases shown in figure 4.16. In figure 4.17, those cases together with case U64C2.1 and U64C2.15 are plotted on log-log coordinates. For U32D- and U24B-cases, this portion of LES output consistently follows the 1/3 power line, with magnitudes a little smaller than the empirical formula proposed by Wyngaard, Cote and Izumi (1971). The effects of $\overline{w'\theta'}_0$ is insignificant. This result reveals that with a small domain size which may lose accuracy of the ML, LES can still show some properties in lower part of the CBL. It is

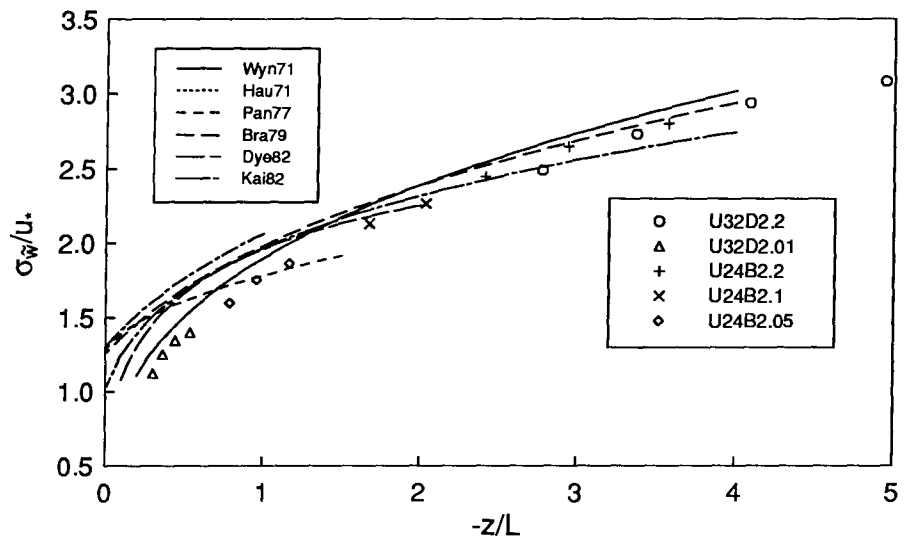

Figure 4.16: Standard deviation of RS vertical velocity fluctuations, $\sigma_{\tilde{w}}$, normalized by u_*, as a function of $-z/L$ from the LES output, indicated by symbols, together with empirical formulae based on observations. Wyn71: Wyngaard *et al.* (1971); Hau71: Haugen *et al.* (1971); Pan77: Panofsky *et al.* (1977); Bra79: Bradley and Antonia (1979); Dye82: Dyer and Bradley (1982); Kai82: Kai (1982).

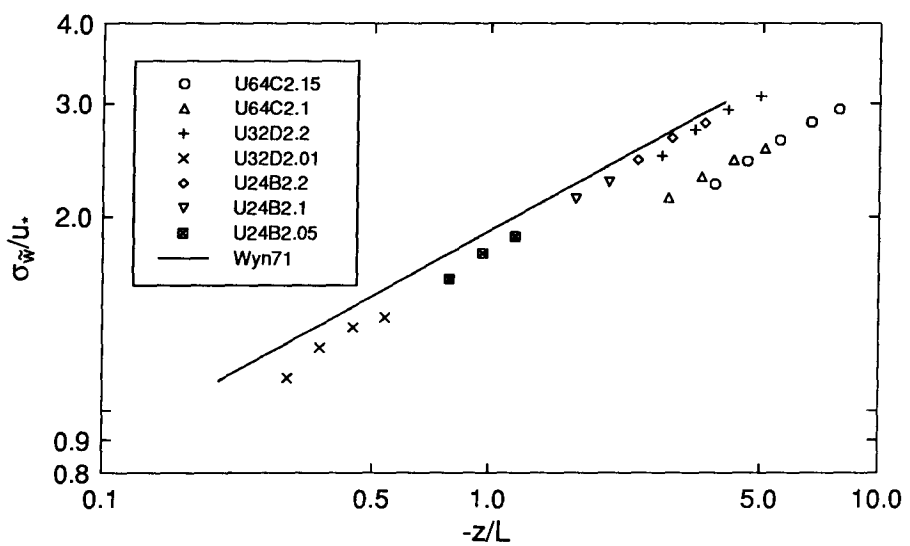

Figure 4.17: Standard deviation of RS vertical velocity fluctuations, $\sigma_{\tilde{w}}$, normalized by u_*, as a function of z/L from the LES output, indicated by symbols, together with empirical formula by Wyngaard *et al.* (1971) based on observations: $\sigma_w/u_* = 1.9(-\zeta)^{1/3}$.

surprising that with a large domain size, U64C-cases present smaller values of $\sigma_{\tilde{w}}/u_*$.

4.3.4 Spatial correlation functions of velocity fluctuations

Instantaneous spatial two-point correlations and correlation coefficients of RS velocity fluctuations on horizontal planes can be derived from LES output through (3.55) and (3.61). Figure 4.18 gives contours of correlation coefficient $r_{11}(\vec{\xi}, z, t)$, $r_{22}(\vec{\xi}, z, t)$ and $r_{33}(\vec{\xi}, z, t)$ for $t/t_* = 22.76$ at two higher levels: $z/Z_i = 0.082$ and $z/Z_i = 0.217$ which are located in the ASL and just above the ASL, respectively. Compared with figure 3.25 on page 98, which shows contours of correlation function $r_{ii}(\vec{\xi}, z, t)$ under neutral conditions, very different features are demonstrated in the unstable cases. Firstly, integral length scale of turbulence is much larger than that in a neutral case. In figure 3.25, positive contours (corresponding to dotted curves) are clustered; in figure 4.18, however, these dotted contours here spread widely, which represents a larger integral length scale. In figure 3.25, horizontal fluctuations are more directionally elongated with shear stress direction, indicated by dot-dash line, than those illustrated in figure 4.18. In other words, horizontal velocity fluctuations becomes more isotropic with an increasing surface heat flux. Contours of $r_{ii} = 0$ (represented by the solid curve) indicate that simulation domain size is large enough to resolve the eddies at least near top of the ASL. The vertical velocity fluctuations have elongated structure near top of the ASL ($z/Z_i = 0.082$), but velocity fluctuations in the x direction do not show this property, neither velocity fluctuations in the y direction. Above the ASL, r_{11} presents a very good horizontal isotropy; r_{22} is almost isotropic but stretched along the y-direction; and r_{33} does not display a strong elongated structure anymore, yet shows some anisotropy, stretched along wind direction.

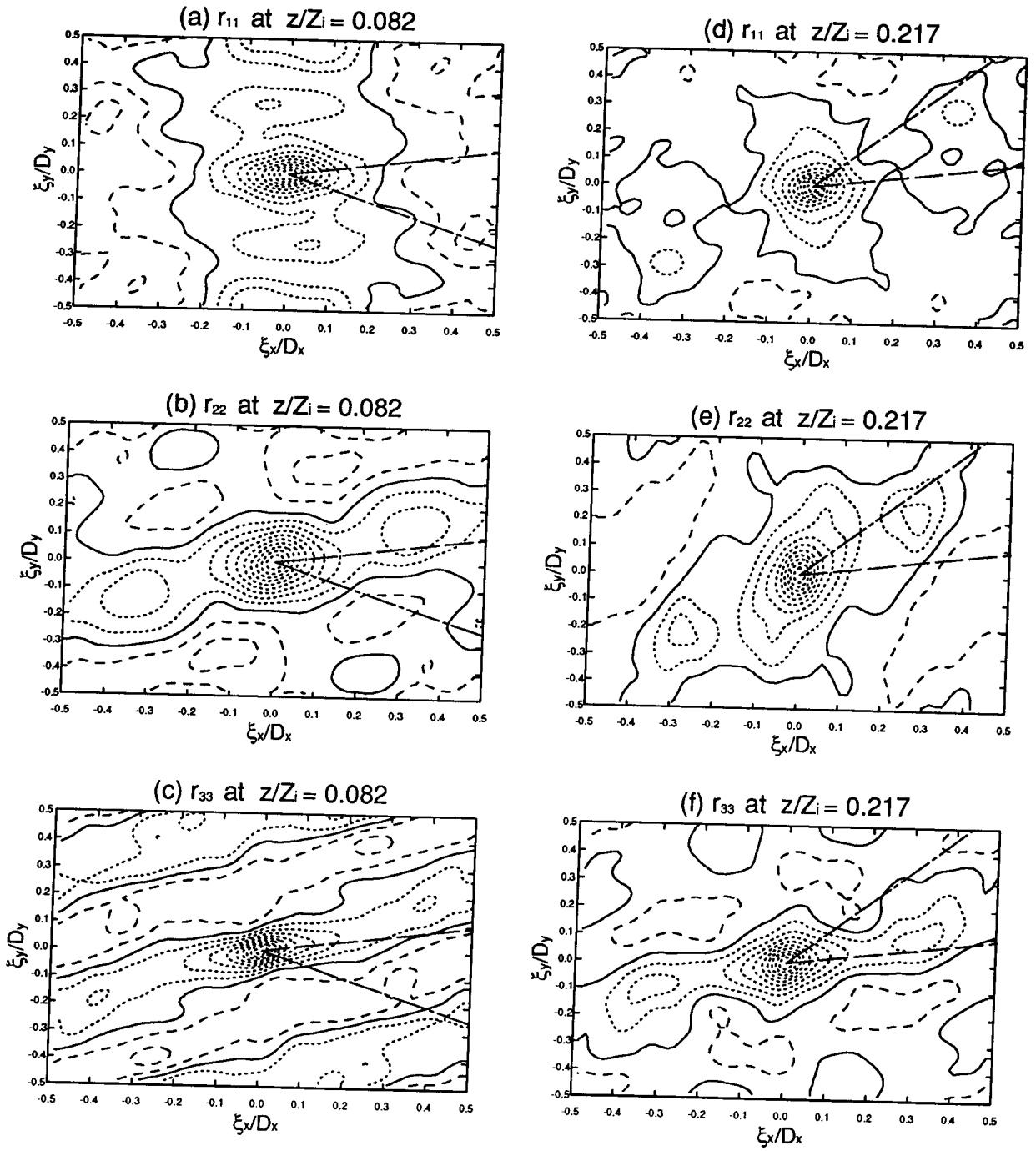

Figure 4.18: Contours of $r_{11}(\xi; z, t)$ at $t/t_* = 22.76$ for case U64C2.1. The solid curves are for $r_{ii} = 0$; Each increment of 0.1 from $r_{ii} = 0$ to $r_{ii} = 1$ is indicated by a dotted curve; each increment of -0.1 from $r_{ii} = 0$ to $r_{ii} = -1$ is indicated by a dashed curve. The long dashed line represents the mean wind direction; dot-dash line represents the direction of local RS shear stress.

Chapter 5

Conclusions

5.1 The Smagorinsky-model Reynolds number

In the present study, the Smagorinsky-model Reynolds number is proposed for a LES adopting the Smagorinsky SGS model. This number is shown to be an independent model parameter based on the assumption that the velocity scale and the length scale in the strain-rate of the RS field are of the order of U_g and D, respectively. When the Rossby number and the simulation domain is fixed, i.e., D_x/h and D_y/h are fixed, the SM-Reynolds number determines the statistics of RS turbulence in a LES of a neutral ABL.

The criteria for a LES are listed as follows:

CR1 grid size must fall into the ISR of the turbulence simulated so that the Smagorinsky SGS model can be employed properly;

CR2 Re_{SM} must be larger than $Re_{SM,cr}$ so that the model runs in a turbulent regime and the RS fields are fully turbulent;

CR3 C_s must be large enough so as to eliminate grid-mode TKE accumulation.

As long as the grid spacing is determined under the first criterion **CR1**, the second criterion **CR2** can be established either by increasing the number of grids, or by reducing the value of C_s while checking if the third criterion **CR3** is satisfied.

If D_x/h and D_y/h vary, these two parameters enter the external parameter group and LES results must depend on them. For a horizontally homogeneous ABL, LES results are independent of D_x/h and D_y/h if they are sufficiently large. For a neutral ABL, the present study shows that when $D_x/h_E \geq 1$ and $D_y/h_E \geq 1$, LES results are satisfactory and less dependent on D_x/h_E and D_y/h_E. The reason is that turbulent eddies whose sizes are comparable to h_E are of small magnitude under neutral conditions.

The present study adopts grid spacings falling into the ISR of ABL turbulence (60 m and 30 m in x and y direction, respectively) in order to meet the assumption of the Smagorinsky SGS model. Other specifications of grid spacing are also used in order to show the influence of grid spacing (or domain size) and the validity of the SM-Reynolds number. Three groups of LES runs have been conducted:

1. fixing mesh configuration and varying C_s;
2. fixing C_s, D_x/h and D_y/h, and varying N_x and N_y;
3. fixing C_s, Δ_x and Δ_y, and varying N_x and N_y.

The first two groups are used to check the validity of the SM-Reynolds number, while the third group of LESs are used to examine the effects of D_x/h and D_y/h.

5.2 A defect of LES in the ABL — the SGS buffer layer

Near wall region is one of the toughest problems that LES faces. Unlike the near-wall region in engineering flows, the atmospheric LES has no resolution in the so-called "low Reynolds number region"; in the present study, the first vertical grid point is at $z \approx 2$ m, where turbulence is already fully developed. For a few vertical grid points from the surface, all fluxes are virtually subgrid scale due to the nature of LES — no RS fluctuations at the first vertical grid point near the surface, which can be considered

as "boundary conditions" for all RS velocity components. At this height in the ABL, horizontal grid spacings are too large to fall into the ISR of turbulence. The Smagorinsky SGS model fails to describe the SGS turbulence, which now includes energy-containing eddies. Poor representation of the SGS momentum flux extends up to a certain height h_b, above which RS motions dominate the flow. The defined "numerical" sublayer (called the SGS buffer layer), from the surface to h_b, is intrinsic in LES of wall turbulence with a very large Reynolds number. By analogy with low-Reynolds number wall turbulence, which has a shallow genuine buffer layer[1] in the near-wall region, the SGS buffer layer has low local SM-Reynolds number layer if D in the definition of Re_{SM} is replaced by h_b. RS turbulence is relaminarized due to the small local SM-Reynolds number. This buffer layer does not show the real logarithmic velocity profile and it "buffers" the momentum connection between the logarithmic region and the surface. In the logarithmic region, RS eddies can sense the presence of the wall and therefore form the logarithmic velocity profile. The value of h_b depends mainly on Re_{SM}, and also on the stability parameter Z_i/L for unstable ABL simulation.

5.3 Neutral-static-stability ABL

The present work shows that a LES can be employed to study statistical properties of turbulence in the upper surface layer. A neutral ABL turbulent flow has been simulated by LES, the largest computation involving $64 \times 64 \times 50$ grids. Results show that, for a LES with the Smagorinsky SGS Model, a logarithmic wind profile is obtained above the SGS buffer layer and below $0.1h_E$. The von Kármán constant calculated from slope of the logarithmic profile is found to be dependent on the proposed SM-Reynolds number (rather than on C_s) and domain ratio D_x/h_E and D_y/h_E. The present study shows that

[1]This buffer layer is sometimes called the low local Reynolds number layer, not to be confused with the low-Reynolds number wall turbulence.

a domain size of 3840 m $\times$ 1920 m $\times$ 2140 m gives a satisfactory results. An asymptotic value of the von Kármán constant is observed to approach about 0.35 as Re_{SM} becomes large. In addition, when the domain configuration 3840 m $\times$ 1920 m $\times$ 2140 m with $64 \times 64 \times 50$ grid points is adopted, C_s can be as small as 0.06 while a negligible amount of grid-mode TKE is observed in the x direction only.

The dependence of the vertical profiles of some RS quantities on Re_{SM} and domain ratios in the USL has also been examined. These quantities are: dimensionless shear stress components τ_{uw}/u_*^2 and τ_{vw}/u_*^2, and dimensionless standard deviations of RS velocity fluctuations $\sigma_{\tilde{u}}/u_*$, $\sigma_{\tilde{v}}/u_*$ and $\sigma_{\tilde{w}}/u_*$. These results show that for a fixed domain ratio, Re_{SM} is the parameter on which the vertical profiles of RS quantities depend. When D_x/h_E is large enough (≥ 2.5, *e.g.*, for domain C), asymptotes for the maxima of $\sigma_{\tilde{u}}/u_*$, $\sigma_{\tilde{v}}/u_*$ and $\sigma_{\tilde{w}}/u_*$ are about 0.3, 1.47 and 0.96, respectively.

In contrast to that in the USL, turbulence statistics in the whole boundary layer show a little dependence on Re_{SM} and D_x/h_E. The vertical profiles of mean velocity components normalized by the geostrophic wind speed and the RS shear stress components normalized by u_*^2 for different values of Re_{SM} collapse into a cluster. The eddy viscosity closure scheme in an EAM is shown not to be appropriate for the neutral ABL by an angle difference of about 20° between the RS shear stress vector and the mean velocity shear vector in almost whole ABL.

5.4 Unstable ABL

The present study also explores the extent to which LES resolves the upper surface layer and derives the surface layer similarity formulas. Horizontal grid spacings adopted fall into the ISR of turbulence ($\Delta_x = 60$ m and $\Delta_y = 30$ m), but the domain size is small owing to limitation of the total number of grids; LES results have shown that

momentum flux in the upper surface layer is generally smaller than all empirical formulas for $-\zeta > 1$. The closest empirical formula to LES results is the one given by Carl, Tarbell and Panofsky (1973), which were derived from high-tower data. The present study also shows that the power law exponent of $\phi_m(\zeta)$ is about -0.48 for $-\zeta > 1$, which is much smaller than $-1/3$. LES results of $\sigma_{\tilde{\theta}}/T_{*,s}$ fit the empirical formulas fairly well, and derive a power law exponent of about -0.4, which is also smaller than $-1/3$. In addition, the present study produces the standard deviation of RS vertical velocity fluctuations in the USL and the results are in agreement with the empirical power law proposed by Wyngaard, Cote and Izumi (1971).

5.5 Future work

It is worth noting that most of the present work was accomplished on an IBM workstation. Therefore, this practice gives us a promising future of conducting LES with more grid points to get better results for more complicated cases, perhaps even considering some cases with real terrain or time varying forcing. As an illustration, the largest computation of the present study is with the grid points $64 \times 64 \times 50$. It takes about 24 seconds of CPU time on an IBM RISC 6000/560 workstation for one time step. It is therefore not difficult to run an unstable case for several t_*'s. Even though it takes a large amount of CPU time to run a neutral case for even one $2\pi f^{-1}$, such a LES is still possible.

This work, as the first trial of resolving part of the ASL by LES, demonstrated that it is possible to adopt a relatively small number of grid points to reveal some important features of USL turbulence. From the comparisons among different cases, better solution of the SL turbulence mainly depends on better grid resolution. An ideal LES of an ABL excluding the ASL is: Δ_0 falls into the ISR of the ABL turbulence; D is larger than the

most energetic eddies; $C_s \approx 0.17$. This requires 10^6 or more grid points in the simulation domain. Based on the definition of Re_{SM}, as grid resolution becomes finer, the value of Re_{SM} will be larger; when D/Δ_0 is large enough, adopting the theoretical value of $C_s \approx 0.17$ suitable for homogeneous turbulence will give a large value of Re_{SM}. An ideal LES of an ABL including the ASL is: Δ_x and Δ_y fall into the ISR of turbulence at the height desired to resolve the ASL; D is larger than the most energetic eddies in the whole ABL; and $C_s \approx 0.17$. This LES would require many more than 10^6 grid points. It is expected that a value of κ evaluated from such a LES will be made more accurate by adopting such a fine resolution, a task that can be accomplished in the near future.

Appendix A

Code and numerical scheme

The numerical code used is the Regional Atmospheric Modeling System (CSU-RAMS), which is a highly versatile numerical code developed by scientists at Colorado State University for simulating and forecasting meteorological phenomena (Walko and Tramback, 1991). This model is constructed around the full set of primitive dynamical equations which govern atmospheric motions, and supplements these equations with optional parameterizations for turbulent diffusion, solar and terrestrial radiation, moist processes, multiple soil layers, the kinematic effects of terrain, and cumulus convection. RAMS is fundamentally a limited-area model, while there is no lower limit to the domain size or to the mesh cell size of the model's finite difference grid. RAMS has been successfully applied to several large-eddy simulations (Chen and Cotton, 1986; Cotton et al., 1987; Hadfield, Cotton and Pielke, 1991; Hadfield, Cotton and Pielke, 1992; Walko, Cotton and Pielke, 1992). All finite differencing is carried out on the staggered grid described by Tripoli and Cotton (1982). Acoustically active terms are integrated with a small time step, while other terms are integrated on a large time step. This separation is called the "time split" technique (Klemp and Wilhelmson, 1978). The leap-frog method is employed for time advancement, operating on advection, buoyancy and Coriolis terms. Horizontal turbulence terms are integrated in a forward sense along the two time-step leap of the leapfrog advection scheme while the vertical part of the turbulence term is integrated on a small time step for stability. A second-order scheme is used for the

advection terms. For any variable ϕ, the advection term is given by:

$$\frac{\partial}{\partial x_j}(\rho_0 u_j \phi) - \phi \frac{\partial}{\partial x_j}(\rho_0 u_j).$$

It is written as the difference between a mass flux divergence term and a momentum divergence term to increase numerical conservation. To minimize restrictions of the Courant restriction on time step Δt, calculations are carried on in a frame moving at the mean velocity of the initial velocity field prescribed in the whole domain.

In the upper part of the computational domain, a damping layer is prescribed by adding a friction term $-\alpha_R u_i$ to the equation (2.99) to absorb gravity waves so that they will not reflected back into the ABL. The value of the Rayleigh friction relaxation coefficient α_R is taken as:

$$\alpha_R = \begin{cases} 0 & z < z_r \\ \alpha_R^{(0)}(z - z_r)/(D_z - z_r) & z \geq z_r \end{cases} \tag{A.1}$$

where $\alpha_R^{(0)} = 50\ s^{-1}$ and $z_r = 1840$ m. The damping layer is of particular importance in simulating a diabatic ABL.

RAMS model adopts the so-called Exner function as the equivalent quantity to the pressure p. Exner function is defined as

$$\Pi = C_p(\frac{p}{p_0})^{R_d/C_p} = C_p \frac{T}{\Theta}. \tag{A.2}$$

Through this variable substitution, the pressure gradient term in the momentum equation (2.99) can be written as

$$-\frac{1}{\rho_0}\frac{\partial p}{\partial x_i} = -\Theta_0 \frac{\partial \Pi}{\partial x_i}. \tag{A.3}$$

Therefore, the momentum equation (2.99) can be written as

$$\begin{aligned} \frac{\partial u_i}{\partial t} + \frac{\partial u_i u_j}{\partial x_j} &= -\Theta_0 \frac{\partial \Pi}{\partial x_i} + g\frac{\Theta}{\Theta_0}\delta_{i3} - f(G_j - u_j)\epsilon_{ij3} \\ &\quad + \nu \frac{\partial^2 u_i}{\partial x_j^2} + \frac{\partial \tau_{ij}^{(s)}}{\partial x_j}. \end{aligned} \tag{A.4}$$

Appendix B

Fundamentals of dimensional analysis and similarity

Theorem 1 (The Buckingham Π theorem (Buckingham, 1914)) *It is assumed that the physical quantities $x_1, x_2, ..., x_n$ involve m independent fundamental dimensional units (f.d.u.s), say $u_1, u_2, ..., u_m$ $(m \leq n)$; the dimension of x_i, denoted by $[x_i]$, is a product of powers of the f.d.u.s, i.e., $[x_i] = u_1^{b_{1i}} u_2^{b_{2i}} \cdots u_m^{b_{mi}}$, where $\mathbf{b_i} = (b_{1i}, b_{2i}, \cdots, b_{mi})^T$ is the dimension vector of x_i, or the i-th column of the dimension matrix*

$$B = \begin{bmatrix} b_{11} & b_{12} & \cdots & b_{1n} \\ \vdots & \vdots & & \vdots \\ b_{m1} & b_{m2} & \cdots & b_{mn} \end{bmatrix}$$

and the rank of matrix B is denoted by k. If $x_1, x_2, ..., x_n$ are related by a physical background and the relationship is written as

$$f(x_1, x_2, ..., x_k, x_{k+1}, ..., x_n) = 0, \tag{B.1}$$

then (1) can be simplified as

$$F(\pi_1, \pi_2, ..., \pi_{n-k}) = 0, \tag{B.2}$$

where $\pi_1, \pi_2, ..., \pi_{n-k}$ are dimensionless power products of $x_1, x_2, ..., x_n$.

Proof of the theorem is found in, for example, Bluman and Cole (1974).

For two special cases, the following corollaries are obtained:

Corollary 1 *If $n = k + 1$ in the Π theorem, then a power law can be obtained which relates $x_1, x_2, ..., x_n$:*

$$x_1^{\alpha_1} \cdot x_2^{\alpha_2} \cdot \cdots \cdot x_n^{\alpha_n} = C, \tag{B.3}$$

$$\textit{or} \qquad x_1 = C_1 \cdot x_2^{\beta_2} \cdot \cdots \cdot x_n^{\beta_n}. \tag{B.4}$$

An example of this case is the Kolmogoroff spectrum law for homogeneous turbulence in the ISR.

Corollary 2 *If $n = k + 2$ in the Π theorem, then a single variable function can be obtained which relates $x_1, x_2, ..., x_n$:*

$$F(\pi_1, \pi_2) = 0, \tag{B.5}$$

$$\textit{or} \qquad \pi_1 = f(\pi_2). \tag{B.6}$$

A good example of this category is the Monin-Obukhov similarity theory in the atmospheric surface layer.

Bibliography

Antonopaulos-Domis, M., 1981: Large-eddy simulation of a passive scalar in isotropic turbulence, *J. Fluid Mech.*, **104**, 55–79.

Arya, S. P. S., 1975: Geostrophic drag and heat transfer relations for the atmospheric boundary layer, *Quart. J. Roy. Meteorol. Soc.*, **101**, 147–163.

Bader, D. C. and T. W. Horst, 1988: Large-eddy simulation of concentration fluctuations. *Proc. of 8th Symp. on Turb. and Diff.*, pp. 5–7.

Batchelor, G. K., 1960: *The Theory of Homogeneous Turbulence*, Cambridge Univ. Press, London.

Bluman, G. and J. Cole, 1974: *Similarity Methods for Differential Equations*, Springer-Verlag.

Bradley, E. F. and R. A. Antonia, 1979: Structure parameters in the atmospheric surface layer, *Q.J.R. Meteorol. Soc.*, **105**, 695–705.

Brost, R. A. and F. T. M. Nieuwstadt, 1986: Large eddy simulation of convective turbulence decay. *Proc. of 7th Symp. on Turb. and Diff.*, pp. 342–344.

Brown, G. L. and A. Roshko, 1974: On density effects and large structure in turbulent mixing layers, *J. Fluid Mech.*, **64**, 775–816.

Brown, R. A., 1974: *Analytical Methods in Planetary Boundary-Layer Modelling*, Adam Hilger, London.

Buckingham, E., 1914: *Phys. Rev.*, **4**, 345.

Businger, J. A., 1986: Evaluation of the accuracy with which dry deposition can be measured with current micrometeorological techniques, *J. Appl. Meteorol.*, **25**, 1100–1124.

Businger, J. A., J. C. Wyngaard, Y. Izumi and E. F. Bradley, 1971: Flux profile relationships in the atmospheric surface layer, *J. Atmos. Sci.*, **28**, 181–189.

Cantwell, B., 1989: Future directions in turbulence research and the role of organized motion. *Whither Turbulence? Turbulence at the Crossroads*, J. L. Lumley, Ed., **Vol.357, Lecture Notes in Physics**, Ithaca, New York, pp. 97–131.

Carl, D. M., T. C. Tarbell and J. A. Panofsky, 1973: Profiles of wind and temperature from towers over homogeneous terrain, *J. Atmos. Sci.*, **30**, 788–794.

Chasnov, J. R., 1991: Simulation of the Kolmogorov inertial subrange using an improved subgrid model, *Phys. Fluids*, **A3**, 188–200.

Chen, C. and W. R. Cotton, 1986: A three-dimensional large-eddy simulation. *Proc. of 7th Symp. on Turb. and Diff.*, pp. 345–348.

Clark, J. H., J. H. Ferziger and W. C. Reynolds, 1978: Evaluation of subgrid-scale models using an accurately simulated turbulent flow, *J. Fluid Mech.*, **91**, 1–6.

Clarke, R. H., A. J. Dyer, R. R. Brook, D. G. Reid and A. J. Troup, 1971: *The Wangara experiment: boundary layer data*, Div. Meteorol. Phys., CSIRO, Tech. Paper No.19, Australia.

Coleman, G. N., J. H. Ferziger and P. R. Spalart, 1990: A numerical study of the turbulent Ekman layer, *J. Fluid Mech.*, **213**, 313–348.

———, 1992: Direct simulation of the stably stratified turbulent Ekman layer, *J. Fluid Mech.*, **244**, 677–712.

Constantin, P., C. Foias, O. P. Manley and R. Temam, 1985: Determining modes and fractal dimension of turbulent flows, *J. Fluid Mech.*, **150**, 427–440.

Cotton, W. R., R. A. Pielke, C. Chen, M. G. Hadfield, C. J. Tremback and R. L. Walko, 1987: *Large-eddy simulations of plume transport and dispersion over flat and hilly terrain*, Final Rep. for EPRI Contract #1630-53, Dept. of Atmos. Sci., Colorado State Univ..

Dang, K. and C. Teissedre, 1989: Spectral transfer analysis for subgrid-scale modelling. *Proc. of 7th Symp. on Turbulent Shear Flows*, pp. 30.5.1–6.

Deardorff, J. W., 1970a: A three-dimensional numerical investigation of the idealized planetary boundary layer, *Geophys. Fluid Dyn.*, **1**, 377–410.

———, 1970b: Convective velocity and temperature scales for the unstable planetary boundary layer and for Rayleigh convection, *J. Atmos. Sci.*, **27**, 1211–1213.

———, 1970c: A numerical study of three-dimensional turbulent channel flow at large Reynolds numbers, *J. Fluid Mech.*, **41**, 453–480.

———, 1971: On the magnitude of the subgrid scale eddy coefficient, *J. Comp. Phys.*, **7**, 120–133.

———, 1972: Numerical investigation of neutral and unstable planetary boundary layers, *J. Atmos. Sci.*, **29**, 91–115.

———, 1973: An explanation of anomalously large Reynolds stresses within the convective planetary boundary layer, *J. Atmos. Sci.*, **30**, 1070–1076.

———, 1974a: Three-dimensional numerical study of turbulence in an entraining mixed layer, *B-L Meteorol.*, **7**, 199–226.

———, 1974b: Three-dimensional numerical study of the height and mean structure of a heated planetary boundary layer, *B-L Meteorol.*, **7**, 81–106.

———, 1980: Stratocumulus-capped mixed layers derived from a three-dimensional model, *B-L Meteorol.*, **18**, 495–527.

Driedonks, A. G. M. and H. Tennekes, 1984: Entrainment effects in the well-mixed atmospheric boundary layer, *J. Atmos. Sci.*, **30**, 75–105.

Dyer, A. J., 1974: A review of flux-profile relationship, *B-L Meteorol.*, **7**, 363–372.

Dyer, A. J. and E. F. Bradley, 1982: An alternative analysis of flux-gradient relationships at the 1976 ITCE, *B-L Meteorol.*, **22**, 3–19.

Dyer, A. J., J. R. Garratt and R. J. Francey, 1981: *The International Turbulence Comparison Experiment (Australia, 1976) — Central Core Data*, CSIRO Div. Atmos. Physics, Tech. Paper No.38, 43 pp..

Dyer, A. J. and B. B. Hicks, 1970: Flux gradient transport of heat and water vapor in an unstable atmosphere, *Quart. J. Roy. Meteorol. Soc.*, **93**, 501–508.

Ebert, E. E., U. Schumann and R. Stull, 1989: Nonlocal Turbulent mixing in the convective boundary layer evaluated from large-eddy simulation, *J. Atmos. Sci.*, **46, No.14**, 2178–2207.

Ferziger, J. H., 1977: Large-eddy simulation of turbulent flows, *AIAA J.*, **15**, 1261–1267.

Ferziger, J. H. and D. C. Leslie, 1979: *Large-eddy simulation — A predictive approach to turbulent flow computation*, AIAA Paper 79-1441.

Foken, T. and G. Skeib, 1983: Profile measurements in the atmospheric near-surface layer and the use of suitable universal functions for the determination of the turbulent energy exchange, *B-L Meteorol.*, **25**, 55–62.

Francey, R. J. and J. R. Garratt, 1981: Interpretation of flux-profile observations at ITCE (1976), *J. Appl. Meteorol.*, **20**, 603–618.

Frenzen, P., 1973: The observed relation between the Kolmogorov and von Karman constants in the surface boundary layer, *B-L Meteorol.*, **3**, 348–358.

———, 1974: On the response of low-inertia cup anemometers in real turbulence; a reply, *B-L Meteorol.*, **6**, 523–526.

Frenzen, P. and R. J. Hart, 1983: A further note on the Kolmogorov-von Kármán product and the values of the constants. *Proc. of 6th Symp. on Turb. and Diff.*, Boston, Mass., pp. 24–27.

Frenzen, P. and C. A. Vogel, 1992a: A new study of the TKE budget in the surface layer. Part 1: the von Karman Constant and rates of TKE production. *Proc. of 10th Symp. on Turb. and Diff.*, Portland, Oregon, pp. 157–160.

———, 1992b: The turbulent kinetic energy budget in the atmospheric surface layer: a review and an experimental reexamination in the field, *B-L Meteorol.*, **60**, 49–76.

Garratt, J. R., 1974: Note on a paper by Frenzen (1973): the observed relation between the Kolmogorov and von Kármán constants in the surface boundary layer, *B-L Meteorol.*, **6**, 519–521.

———, 1977: Review of drag coefficient over oceans and continents, *Monthly Weather Rev.*, **105**, 915–929.

———, 1992: *The Atmospheric Boundary Layer*, Cambridge.

Garratt, J. R., R. J. Francey, I. C. McIlroy, A. J. Dyer, I. Helmond, E. F. Bradley and O. T. Denmead, 1979: *The International Turbulence Comparison Experiment (Australia, 1976) — Micrometeorological Support Data*, CSIRO Div. Atmos. Physics, Tech. Paper No.37, 23 pp..

Gerz, T., U. Schumann and S. E. Elghobashi, 1989: Direct numerical simulation of stratified homogeneous turbulent shear flows, *J. Fluid Mech.*, **200**, 563–594.

Goddard, W. B., 1970: A floating drag-plate lysimeter for atmospheric boundary layer research, *J. Appl. Meteorol.*, **9**, 373–378.

Gollub, J. P., S. V. Benson and J. Steinman, 1979: A subharmonic route to turbulent convection, *Ann. New York Acad. Sci.*, **357**, 22–27.

Grant, A. L. M., 1986: Observations of boundary layer structure made during the KONTUR experiment, *Quart. J. Roy. Meteorol. Soc.*, **112**, 825–841.

Hadfield, M. G., W. R. Cotton and R. A. Pielke, 1991: Large-eddy simulation of thermally forced circulations in the convective boundary layer. Part I: a small-scale circulation with zero wind, *B-L Meteorol.*, **57**, 19–114.

———, 1992: Large-eddy simulation of thermally forced circulations in the convective boundary layer. Part II: the effect of changes in wavelength and wind speed, *B-L Meteorol.*, **58**, 307–327.

van Haren, L. and F. T. M. Nieuwstadt, 1989: The behavior of passive and buoyant plumes in a convective boundary layer, as simulated with a large-eddy model, *J. Appl. Meteorol.*, **28**, 818–832.

Haugen, D. A., J. C. Kaimal and E. F. Bradley, 1971: An experimental study of Reynolds stress and heat flux in the atmospheric surface layer, *Quart. J. Roy. Meteorol. Soc.*, **97**, 168–180.

Herring, J. R., 1979: Subgrid Scale modelling – an introduction and review. *Proc. of 1st Symp. on Turbulent Shear Flows*, **I**, pp. 347–353.

Hicks, B. B., 1970: The measurement of atmospheric fluxes near the surface: a generalized approach, *J. Appl. Meteorol.*, **9**, 386–388.

———, 1976: Reply to comments by J.J. Shreffler, *B-L Meteorol.*, **10**, 237–240.

Hinze, J. O., 1975: *Turbulence* (second Edition), McGraw-Hill, New York.

Högström, U., 1974: A field study of the turbulent fluxes of heat, water vapor and momentum at a 'typical' agricultural site, *Quart. J. Roy. Meteorol. Soc.*, **100**, 624–639.

———, 1985: Von Kármán constant in atmospheric boundary layer flow: reevaluated, *J. Atmos. Sci.*, **42**, 263–270.

———, 1986: Reply, *J. Atmos. Sci.*, **43**, 2131–2134.

———, 1988: Nondimensional wind and temperature profiles in the atmospheric surface layer: A re-evaluation, *B-L Meteorol.*, **42**, 55–78.

Holmes, P., 1989: Can dynamical systems approach turbulence?. *Whither Turbulence? Turbulence at the Crossroads*, J. L. Lumley, Ed., **Vol.357, Lecture Notes in Physics**, Ithaca, New York, pp. 195–249.

Holt, S. E., J. R. Koseff and J. H. Ferziger, 1989: The evolution of turbulence in the presence of mean shear and stable stratification. *Proc. of 7th Symp. on Turbulent Shear Flows*, pp. 12.2.1–6.

Holtslag, A. A. M. and F. T. M. Nieuwstadt, 1986: Scaling the atmospheric boundary layer, *B-L Meteorol.*, **36**, 201–209.

Izumi, Y. and S. J. Caughey, 1976: *Minnesota 1973 Atmospheric Boundary Layer Experiment Data Report*, AFCRL, 28 pp..

Kai, K., 1982: *Statistical characteristics of turbulence and the budget of turbulent energy in the surface boundary layer*, Environmental Research Center Paper No.1, Univ. of Tsukuba.

Kaimal, J. C., R. A. Eversole, D. J. Lenschow, B. B. Stankov, P. H. Kahn and J. A. Businger, 1982: Spectral characteristics of the convective boundary layer over uneven terrain, *J. Atmos. Sci.*, **39**, 1098–1114.

Kaimal, J. C., J. C. Wyngaard, D. A. Haugen, O. R. Cote, Y. Izumi, S. J. Caughey and C. J. Readings, 1976: Turbulent structures in the convective boundary layer, *J. Atmos. Sci.*, **33**, 2152–2169.

Kaimal, J. C., J. C. Wyngaard, Y. Izumi and O. R. Cote, 1972: Spectral characteristic of surface layer turbulence, *Quart. J. Roy. Meteorol. Soc.*, **98**, 563–589.

Keefe, L., P. Moin and J. Kim, 1992: The dimension of attractors underlying periodic turbulent Poiseulle flow, *J. Fluid Mech.*, **242**, 1–29.

Kim, J., P. Moin and R. D. Moser, 1987: Turbulence statistics in fully developed channel flow at low Reynolds number, *J. Fluid Mech.*, **177**, 133–166.

Klemp, J. B. and R. B. Wilhelmson, 1978: The simulation of three-dimensional convective storm dynamics, *J. Atmos. Sci.*, **35**, 1070–1096.

Kline, S. J., B. Cantwell and G. K. Lilley, 1981. *Proc. 1980-81 AFOSR-HTTM-Stanford Conf. on Complex Turbulent Flows*, Stanford.

Kline, S. J., W. C. Reynolds, F. A. Schraub and P. W. Rundstadler, 1967: The structure of turbulent boundary layers, *J. Fluid Mech.*, **30**, 741–773.

Kondo, J. and T. Sato, 1982: The determination of the von Karman constant, *J. Meteorol. Soc. Japan*, **60**, 461–471.

Korrell, A., H. A. Panofsky and R. J. Rossi, 1982: Wind profiles at the Boulder Tower, *B-L Meteorol.*, **22**, 295–312.

Krettenauer, K. and U. Schumann, 1992: Numerical simulation of turbulent convection over wavy terrain, *J. Fluid Mech.*, **237**, 261–299.

Ladyzhenskaya, O. A., 1969: *The Mathematical Theory of Viscous Incompressible Flow* (second English Edition), Bordon and Breach Science Publishers, New York.

Launder, B. E., 1989: Phenomenological modelling: present ... and future?. *Whither Turbulence? Turbulence at the Crossroads*, J. L. Lumley, Ed., **Vol.357, Lecture Notes in Physics**, Ithaca, New York, pp. 439–485.

Launder, B. E., G. J. Reece and W. Rodi, 1975: Progress in the development of a Reynolds-stress turbulence closure, *J. Fluid Mech.*, **68**, 537–566.

Leith, C. E., 1990: Stochastic backscatter in a subgrid-scale model: Plane shear mixing layer, *Phys. Fluids*, **A2**, 297–299.

Leonard, A., 1974: Energy cascade in large-eddy simulations of turbulent fluid flows, *Adv. in Geophys.*, **18A**, 237–248.

Lesieur, M., O. Metais and H. Laroche, 1989: Numerical simulations of turbulent stably-stratified and free shear flows. *Proc. of 8th Symp. on Turbulence and diffusion*, pp. 57–60.

Leslie, D. C. and G. L. Quarini, 1979: The application of turbulence theory to the formulation of subgrid modelling procedures, *J. Fluid Mech.*, **91**, 65–91.

Lettau, H. H. and B. Davidson, 1957: *Exploring the Atmosphere First Mile*, **1-2**, Pergamon Press.

Liapunov, A. M., 1966: *Stability of Motion*, **30**, Mathematics in Science and Engineering, Academic Press, Ner York.

Lichtenberg, A. J. and M. A. Lieberman, 1982: *Regular and Stochastic Motion*, Springer, New York.

Lilly, D. K., 1962: On the numerical simulation of buoyant convection, *Tellus; a quarterly journal of geophysics*, **14**, 148–171.

———, 1967: The representation of small-scale turbulence in numerical simulation experiments. *Proc. IBM Sci. Comput. Symp. on Environ. Sci.*, **IBM Form 320-1951**, pp. 195–210.

Lorenz, E. N., 1963: Deterministic non-periodic flow, *J. Atmos. Sci.*, **20**, 130–141.

Love, M. D. and D. C. Leslie, 1977: Studies of sub-grid modelling with classical closure and Burger's equation. *Proc. of 1st Symp. on Turbulent Shear Flows*, **I**, pp. 14.1–10.

Lumley, J. L. and H. A. Panofsky, 1964: *The Structure of Atmospheric Turbulence*, John Wiley & Sons, New York.

Mansour, N. N., W. C. Reynolds and J. H. Ferziger, 1979: Improved method for large-eddy simulation of turbulence. *Proc. of 1st Symp. on Turbulent Shear Flows*, **I**, pp. 387–400.

Mason, P. J., 1989: Large-eddy simulation of the convective atmospheric boundary layer, *J. Atmos. Sci.*, **46**, 1492–1516.

———, 1990: Large-eddy simulation of the stably-stratified atmospheric boundary layer, *B-L Meteorol.*, **53**, 117–162.

Mason, P. J. and N. S. Callen, 1986: On the magnitude of the subgrid-scale eddy coefficient in large-eddy simulation of turbulent channel flow, *J. Fluid Mech.*, **162**, 439–462.

Mason, P. J. and D. J. Thomson, 1987: Large-eddy simulation of the neutral-static-stability planetary boundary, *Quart. J. Roy. Meteorol. Soc.*, **113**, 413–443.

———, 1992: Stochastic backscatter in large-eddy simulations of boundary layers, *J. Fluid Mech.*, **242**, 51–78.

McMillan, O. J. and J. H. Ferziger, 1979: Direct testing of subgrid-scale models, *AIAA J.*, **17**, 1340–1346.

Merry, M. and H. A. Panofsky, 1976: Statistics of vertical motion over land and water, *Quart. J. Roy. Meteorol. Soc.*, **102**, 255–260.

Miyake, Y., T. Kajishima and K. Hamaogi, 1989: A discussion on turbulence model by means of LES. *Proc. of 7th symp. on Turbulent Shear Flows.*

Moeng, C. -H., 1984: A large-eddy simulation model for the study of planetary boundary layer turbulence, *J. Atmos. Sci.*, **41**, 2052–2062.

———, 1986a: Large-eddy simulation of a stratus-topped boundary layer, Part I: structure and budgets, *J. Atmos. Sci.*, **43**, 2886–2900.

———, 1986b: Large-eddy simulation of a stratus-topped boundary layer, Part II: Implications for mixed-layer modelling, *J. Atmos. Sci.*, **44**, 1605–1614.

Moeng, C. -H. and D. A. Randall, 1984: Problems in simulation the stratocumulus-topped boundary layer with a third-order closure model, *J. Atmos. Sci.*, **41**, 1588–1600.

Moeng, C. -H. and J. C. Wyngaard, 1984: Statistics of conservative scalars in the convective boundary layer, *J. Atmos. Sci.*, **41**, 3161–3169.

———, 1986: An analysis of closures for pressure-scalar covariances in the convective boundary layer, *J. Atmos. Sci.*, **43**, 2499–2513.

———, 1988: Spectral analysis of large-eddy simulation of the convective boundary layer, *J. Atmos. Sci.*, **45**, 3573–3587.

———, 1989: Evaluation turbulent transport and dissipation closures in second-order modeling, *J. Atmos. Sci.*, **46**, 2311–2330.

Moin, P. and J. Kim, 1982: Numerical investigation of turbulent channel flow, *J. Fluid Mech.*, **118**, 341–377.

———, 1985: The structure of the vorticity field in turbulent channel flow, *J. Fluid Mech.*, **155**, 441–464.

Moin, P., W. C. Reynolds and J. H. Ferziger, 1978: *Large-eddy simulation of incompressible turbulent channel flow*, Rep. No.TF-12.

Monji, N., 1973: Budgets of turbulent energy and temperature variance in the transition zone from forced to free convection, *J. Meteorol. Soc. Japan*, **2**, 133–145.

Nicholls, S., 1985: Aircraft observations of the Ekman layer during the Joint Air-Sea Interaction Experiment, *Quart. J. Roy. Meteorol. Soc.*, **111**, 391–426.

Nieuwstadt, F. T. M. and R. A. Brost, 1986: The decay of convective turbulence, *J. Atmos. Sci.*, **43**, 532–546.

Nieuwstadt, F. T. M. and H. van Dop, 1982: *Atmospheric Turbulence and Air-pollution Modelling*, D. Reidel Publishing Co..

Nieuwstadt, F. T. M., P. J. Mason, C. -H. Moeng and U. Schumann, 1991: Large-eddy simulation of the convective boundary layer: a comparison of four computer codes. *Proc. of 8th Symp. on Turbulent Shear Flows* (in press), F. Durst and et al., Eds., Springer-Verlag.

Nieuwstadt, F. T. M. and J. P. J. M. M. de Valk, 1987: A large-eddy simulation of buoyant and non-buoyant plume dispersion in the atmospheric boundary layer, *Atmos. Environ.*, **21**, 2573–2587.

Panchev, S., 1971: *Random Functions and Turbulence*, Pergamon Press.

Panofsky, H. A., A. K. Blackadar and G. E. McVehil, 1960: The Diabatic wind profile, *Quart. J. Roy. Meteorol. Soc.*, **86**, 495–503.

Panofsky, H. A. and J. A. Dutton, 1984: *Atmospheric Turbulence: Models and Methods for Engineering Applications*, John Wiley & Sons.

Panofsky, H. A., H. Tennekes, D. H. Lenschow and J. C. Wyngaard, 1977: The characteristics of turbulent velocity components in the surface layer under convective conditions, *B-L Meteorol.*, **11**, 355–361.

Patankar, S. V., 1980: *Numerical Heat Transfer and Fluid Flow*, McGraw-Hill, New York.

Paulson, C. A., 1970: The mathematical representation of wind speed and temperature profiles in the unstable atmospheric surface layer, *J. Appl. Meteorol.*, **9**, 857–861.

Pielke, R. A., 1984: *Mesoscale Meteorological Modeling*, Academic Press, Orlando.

Pruitt, W. O., D. L. Morgan and F. J. Lourence, 1973: Momentum and mass transfers in the surface boundary layer, *Quart. J. Roy. Meteorol. Soc.*, **99**, 370–386.

Reynolds, W. C., 1989: The potential and limitations of Direct and Large Eddy Simulations. *Whither Turbulence? Turbulence at the Crossroads*, J. L. Lumley, Ed., **Vol.357, Lecture Notes in Physics**, Ithaca, New York, pp. 313–343.

Rodi, W., 1980: *Turbulence Models and their Application in Hydraulics*, International Association for Hydraulic Research.

Ruelle, D., 1980: Strange attractors, *Math. Intelligencer*, **2**, 126–137.

Schlichting, H., 1979: *Boundary-layer Theory* (translated by J. Kestin, 7th edition), McGraw-Hill, Jamburg.

Schmidt, H. and U. Schumann, 1989: Coherent structure of the convective boundary layer derived from large-eddy simulation, *J. Fluid Mech.*, **200**, 511–562.

Schumann, U., 1975: Subgrid scale model for finite difference simulations of turbulent flows in plane channels and annuli, *J. Comp. Phys.*, **18**, 376–404.

———, 1989: Large-eddy simulation of turbulent diffusion with chemical reactions in the convective boundary layer, *Atmos. Environ.*, **23**, 1713–1727.

Shaw, R. H. and U. Schumann, 1992: Large-eddy simulation of turbulent flow above and within a forest, *B-L Meteorol.*, **61**, 47–64.

Shirasawa, K., 1981: The stress of wind on ice, *Low Temperature Sci.*, **40**, 101–118.

Smagorinsky, J., 1963: General circulation experiments with the primitive equations: 1. The basic experiment, *Monthly Weather Rev.*, **91**, 99–164.

Smolarkiewicz, P. K. and T. L. Clark, 1985: Numerical simulation of the evolution of a three-dimensional field of cumulus clouds, Part I: Model description, comparison with observations and sensitivity studies, *J. Atmos. Sci.*, **42**, 502–522.

———, 1986: The multidimensional positive definite advection transport algorithm with small implicit diffusion: Further development and applications, *J. Comp. Phys.*, **67**, 396–438.

Sorbjan, Z., 1989: *Structure of the Atmospheric Boundary Layer*, Prentice Hall, New Jersey.

Spalart, P. R., 1988: Direct simulation of a turbulent boundary layer up to $R_\theta = 1410$, *J. Fluid Mech.*, **187**, 61–98.

———, 1989: Theoretical and numerical study of a three-dimensional turbulent boundary layer, *J. Fluid Mech.*, **205**, 319–340.

Sreenivasan, K. R., 1985: Transition and turbulence in fluid flows and low-dimensional chaos. *Frontiers of Fluid Mechanics*, S. H. Davis and J. L. Lumley, Eds., Springer, pp. 41–67.

Stull, R. B., 1984: Transilient turbulence theory, Part I: The concept of eddy mixing across finite distance, *J. Atmos. Sci.*, **41**, 3351–3367.

———, 1988: *An Introduction to Boundary Layer Meteorology*, Kluwer Acad. Publishers, Dordrecht.

Stull, R. B. and E. W. Eloranta, 1983: Boundary layer experiment, *Bull. American Meteorological Society*, **65**, 450–456.

Stull, R. B. and T. Hasagawa, 1984: Transilient turbulence theory, Part II: Turbulent adjustment, *J. Atmos. Sci.*, **41**, 3368–3379.

Swinbank, W. C., 1964: The exponential profile, *Quart. J. Roy. Meteorol. Soc.*, **90**, 119–135.

Sykes, R. I. and D. S. Henn, 1989: Large-eddy simulation of turbulent sheared convection, *J. Atmos. Sci.*, **46**, 1106–1118.

Sykes, R. I., D. S. Henn and W. S. Lewellen, 1993: Surface-layer description under free-convection conditions, *Quart. J. Roy. Meteorol. Soc.*, **119**, 409–422.

Sykes, R. I., W. S. Lewellen and D. S. Henn, 1988: Large-eddy simulation of concentration fluctuations. *Proc. of 8th Symp. on Turb. and Diff.*, pp. 8–11.

Telford, J. W., 1982: A theoretical value for von Kármán constant, *Pure Appl. Geophysics*, **120**, 648–661.

Tennekes, H. and J. L. Lumley, 1972: *A First Course in Turbulence*, The MIT Press.

Thuillier, R. H. and V. O. Lappe, 1964: Wind and temperature profile characteristics from observations on a 1400 ft tower, *J. Appl. Meteorol.*, **3**, 299–306.

Tillman, J. E., 1972: The indirect determination of stability, heat and momentum fluxes in the atmospheric boundary layer from simple scalar variables during dry unstable conditions, *J. Appl. Meteorol.*, **11**, 783–792.

Tripoli, G. J. and W. R. Cotton, 1982: The Colorado State University three-dimensional cloud/mesoscale model — 1982, Part I: General theoretical framework and sensitivity experiments, *J. de Rech. Atmos.*, **16**, 185–220.

Tsvang, L. R., A. L. Zubkovskii, B. A. Kader, M. A. Kallistratova, T. Foken, V. Gerstmann, A. Przadka, Y. Pretel and Y. Zeleny, 1985: International Turbulence comparison experiment (ITCE-81), *B-L Meteorol.*, **31**, 325–348.

Voke, P. R., 1983: Large-eddy simulation — Retro- and pro-spect review, *Physicochemical Hydrodynamics*, **4**, 119.

Walko, R. L., W. R. Cotton and R. A. Pielke, 1992: Large-eddy simulation of the effects of hilly terrain on the convective boundary layer, *B-L Meteorol.*, **58**, 133–150.

Walko, R. L. and C. J. Tramback, 1991: RAMS: The Regional Atmospheric Modeling System, Version 2c, User's Guide.

Wieringa, J., 1980: A reevaluation of the Kansas mast influence on measurements of stress and cup anemometer overspeeding, *B-L Meteorol.*, **18**, 411–430.

———, 1982: Reply , *B-L Meteorol.*, **22**, 251–255.

Wyngaard, J. C., 1984a: Top-down and bottom-up diffusion of a scalar in a convective boundary layer, *J. Atmos. Sci.*, **41**, 102–112.

———, 1984b: Toward convective boundary layer parameterization: a scalar transport module, *J. Atmos. Sci.*, **41**, 1959–1969.

———, 1984c: *Large-eddy Simulation: Guidelines for its application to planetary boundary layer research*, DTIC, AD-A146381.

———, 1985: Structure of the planetary boundary layer and implications for its modeling, *J. Appl. Meteorol.*, **24**, 1131–1142.

Wyngaard, J. C., J. A. Businger, J. C. Kaimal and S. E. Larson, 1982: Comment on "A reevaluation of the Kansas mast influence on measurements of stress and cup anemometer overspeeding", *B-L Meteorol.*, **22**, 245–250.

Wyngaard, J. C. and O. R. Cote, 1971: The budgets of turbulent kinetic energy and temperature variance in the atmospheric boundary layer, *J. Atmos. Sci.*, **28**, 190–201.

Wyngaard, J. C., O. R. Cote and Y. Izumi, 1971: Local free convection, similarity, and the budgets of shear stress and heat flux, *J. Atmos. Sci.*, **28**, 1171–1182.

Yoshizawa, A., 1986: Large-eddy simulation of turbulent flows. *Encyclopedia of Fluid Mechanics*, N. P. Cheremisinoff, Ed., **Vol.6**, Houston, Golf, pp. 1277–1297.

Young, G. S., 1988: Convection in the atmospheric boundary layer, *Earth-Sience Reviews*, **25**, 179–198.

Zhang, S. F., 1988: *A critical evaluation of the von Kármán constant from a new atmospheric surface layer experiment*, Ph.D. thesis, University of Washington.